

MECHANISM OF C₂H₄ DEHYDROGENATION TO C₂H₂
ON THE Ni(111) SURFACE

by

Mimi Elizabeth Lam

Submitted in partial fulfillment of the requirements
for the degree of Doctor of Philosophy

at

Dalhousie University
Halifax, Nova Scotia
July 1995

© Copyright by Mimi Elizabeth Lam, 1995



National Library
of Canada

Acquisitions and
Bibliographic Services Branch

395 Wellington Street
Ottawa, Ontario
K1A 0N4

Bibliothèque nationale
du Canada

Direction des acquisitions et
des services bibliographiques

395, rue Wellington
Ottawa (Ontario)
K1A 0N4

Your file *Votre référence*

Our file *Notre référence*

The author has granted an irrevocable non-exclusive licence allowing the National Library of Canada to reproduce, loan, distribute or sell copies of his/her thesis by any means and in any form or format, making this thesis available to interested persons.

L'auteur a accordé une licence irrévocable et non exclusive permettant à la Bibliothèque nationale du Canada de reproduire, prêter, distribuer ou vendre des copies de sa thèse de quelque manière et sous quelque forme que ce soit pour mettre des exemplaires de cette thèse à la disposition des personnes intéressées.

The author retains ownership of the copyright in his/her thesis. Neither the thesis nor substantial extracts from it may be printed or otherwise reproduced without his/her permission.

L'auteur conserve la propriété du droit d'auteur qui protège sa thèse. Ni la thèse ni des extraits substantiels de celle-ci ne doivent être imprimés ou autrement reproduits sans son autorisation.

ISBN 0-612-15953-1

Canada

To my parents,
Kenneth Yok Keung and Shum Chee Lam

謹獻給父母
林煜強 林趙深智

TABLE OF CONTENTS

LIST OF FIGURES	viii
LIST OF TABLES	xv
ABSTRACT	xvi
LIST OF ABBREVIATIONS AND SYMBOLS	xvii
ACKNOWLEDGEMENTS	xxi
Chapter 1: INTRODUCTION	1
Chapter 2: BACKGROUND	5
A. Experimental	5
1. Surface-Analysis Techniques and Probes	5
a. Geometrical Structure	7
1. Low-Energy Electron Diffraction (LEED)	8
2. Vibrational Spectroscopy	9
a. Reflection/Absorption Infrared Spectroscopy (RAIRS)	10
b. High-Resolution Electron-Energy-Loss Spectroscopy (HREELS)	10
c. Time-Resolved HREELS	11
3. X-Ray-Based Electron Spectroscopies	12
a. Near-Edge X-ray Absorption Fine Structure (NEXAFS)	12
b. Surface-Extended X-ray Absorption Fine Structure (SEXAFS) and X-ray Photoelectron Diffraction (XPD)	13
c. Scanned-Energy-Mode Photoelectron Diffraction (PD)	14
b. Chemical Composition and Electronic Structure	14
1. Auger Electron Spectroscopy (AES)	15
2. Photoelectron or Photoemission Spectroscopy	17
c. Thermodynamic and Kinetic Properties	19
1. Desorption Kinetics	19
2. Electron Work-Function Changes	21
2. Related Work	22
a. C ₂ H ₄ and C ₂ H ₂ on Ni(111)	22
1. Adsorption of C ₂ H ₄ and C ₂ H ₂ on Ni(111)	22
2. Thermal Decomposition of C ₂ H ₄ to C ₂ H ₂ on Ni(111)	25
3. Thermal Evolution of C ₂ H ₂ on Ni(111)	28
b. C ₂ H ₄ and C ₂ H ₂ on Pt(111)	29
c. C ₂ H ₄ and C ₂ H ₂ on Pd(111)	31
d. C ₂ H ₄ and C ₂ H ₂ on Ni(100)	32
e. C ₂ H ₄ and C ₂ H ₂ on Ni(110)	33

B. Theoretical	35
1. Methodologies	35
a. Semiempirical Methods	35
1. Hückel and Extended-Hückel (EH) Molecular-Orbital (MO) Theories	35
2. Atom-Superposition and Electron-Delocalization Molecular-Orbital (ASED-MO) Theory	39
b. Density-Functional Theory (DFT)	42
1. Hohenberg-Kohn (HK) Formulation	42
2. Kohn-Sham (KS) Method	44
2. Related Work	48
a. C ₂ H ₄ and C ₂ H ₂ on Ni(111)	48
1. Semiempirical Methods	48
2. <i>Ab initio</i> , X α (or HFS), and Density-functional Studies	49
b. C ₂ H ₄ and C ₂ H ₂ on Related Surfaces	50
Chapter 3: COMPUTATIONAL DETAILS AND PRELIMINARIES	54
A. Theoretical Method	54
1. Atom-Superposition and Electron-Delocalization Molecular-Orbital (ASED-MO) Calculations	54
a. Parameter Choice	55
b. Symmetry Constraints	59
c. Error Estimates	59
2. Density-Functional Theory (DFT) Computations	61
a. Self-Consistent-Field (SCF) Convergence	63
B. Cluster Model	65
1. Adsorption Sites	68
a. Layer Dependence	75
b. Lateral Extent	76
c. Configuration and Symmetry	77
d. Spin Configuration	86
2. Coordinate Variable Changes	100
Chapter 4: RESULTS AND DISCUSSION	108
A. ASED-MO Calculations	108
1. Adsorption Sites of Ethylene and Acetylene	108
a. Single Adsorbate Molecules	109
1. Ethylene: Ni _n (C ₂ H ₄)	109
2. Acetylene: Ni _n (C ₂ H ₂)	134
b. Two Adsorbate Molecules in (2×2) Overlayer Structure	158
1. Ethylene: Ni _n (C ₂ H ₄) ₂	158
2. Acetylene: Ni _n (C ₂ H ₂) ₂	165

2.	Dehydrogenation Mechanism	165
a.	$\text{Ni}_n(\text{C}_2\text{H}_4)_2$: $n = 30, 51, 72$	171
1.	Concerted Parametric Stretch of <i>trans</i> C–H Bonds	171
2.	Constrained Coupled Rotation of the C_2H_4 's about ϕ_C and ϕ_{CH_2}	172
3.	Rotation of the C_2H_4 's about ϕ_C	176
4.	Concerted Stretch of <i>trans</i> C–H Bonds after Rotation about ϕ_C	181
5.	Incremental Shortening of $r(\text{H}–\text{H})$ along Line Connecting their Centres	182
6.	Shortening of $r(\text{H}–\text{H})$ while Optimizing H's	182
b.	$\text{Ni}_{30}(\text{C}_2\text{H}_4)_2\text{H}_2$: Preliminary Calculations	183
1.	Elimination of <i>trans</i> H's	183
c.	$\text{Ni}_n(\text{C}_2\text{H}_4)_2\text{H}_2$: $n = 30, 51, 72$	186
1.	Rotation of C_2H_4 's about ϕ_r	186
2.	Parametric Shortening (and Lengthening) of $r(\text{H}–\text{H})$	187
3.	Tunnelling of Intermolecular H's	197
3.	Final Adsorption Sites of Decomposition Products	213
a.	$\text{Ni}_{72}(\text{C}_2\text{H}_2)_2$: Rotation of C_2H_2 's about ϕ_C Followed by Dissociative Chemisorption of H_2	215
b.	$\text{Ni}_{72}[2\text{C}_2\text{H}_2+3\text{H}_2]$: Simultaneous C_2H_2 Rotation and H_2 Dissociation	215
c.	$\text{Ni}_{72}(\text{C}_2\text{H}_2)_2\text{H}_4$: H_2 Dissociation Followed by C_2H_2 Rotation	218
4.	Cluster Spin-Configuration Dependence of Dehydrogenation Mechanism Results	223
5.	Dehydrogenation Mechanism in the Atop Adsorption Site	223
6.	Comparative Study of the Pt(111)/ C_2H_4 System	229
a.	Adsorption Sites	230
b.	Dehydrogenation Mechanism	230
B.	DFT Calculations	232
1.	Geometry Optimization of Adsorbate Molecules on a Ni_4 Cluster	233
a.	Ethylene: $\text{Ni}_4(\text{C}_2\text{H}_4)$	233
b.	Acetylene: $\text{Ni}_4(\text{C}_2\text{H}_2)$	235
2.	Single-Point Energy Calculations along Various Coordinate Variable Changes	235
a.	Elongation of C–H bonds, $\Delta r(\text{C}–\text{H})$	235
b.	Rotation about $\Delta\phi_C$	236
3.	Conclusions Based on the DFT Study	239
Chapter 5: CONCLUSIONS		240
Chapter 6: FURTHER INVESTIGATIONS		245
REFERENCES		251

LIST OF FIGURES

Chapter 3

<p>Figure 3.1 Quadratic fits and coefficients, a_2, a_1, and a_0, of the experimental and theoretical, both ASED-MO and DFT, C–C bond lengths, $r(\text{C}–\text{C})$'s, of C_2H_2, C_2H_4, and C_2H_6 as a function of their states of hybridization, sp^n, $n = 1, 2$, and 3, respectively.</p>	58
<p>Figure 3.2 Comparison of calculated binding energies, E_B's, for C_2H_4 in five adsorption sites on Pt(111) using (a) parameter set of Ref. [5] and (b) parameter adjustment of original data set analogous to that used for Ni(111).</p>	58
<p>Figure 3.3 Bulk cluster models of the Ni(111) surface, Ni_n, for $n = 14, 20, 26, 44, 62$, and 80 total number of Ni atoms, corresponding, respectively, to $d = 4, 7, 9, 14, 19$, and 24 number of atoms in the topmost layer, and ranging from $\ell = 1 \rightarrow 4$ number of layers. The cluster designations, $(n_1/n_2/\dots/n_\ell)$, reflecting the number of atoms in each layer, and the two principal azimuthal directions are indicated.</p>	67
<p>Figure 3.4 Energy level diagrams for the $\ell = 1$; $d = 4, 14$, and 24 series of clusters, Ni_n: (a) full set of $9 \times n$ levels with d bands highlighted (other levels comprise the broad and overlapping s and p bands) and (b) expanded view of the d bands with the cluster Fermi levels, ϵ_F's, indicated.</p>	69
<p>Figure 3.5 Energy level diagrams for the $d = 14$ series of clusters, Ni_n, $n = 14, 22, 30$, and 44, as $\ell = 1 \rightarrow 4$: (a) full set of $9 \times n$ levels and (b) expanded view of the cluster d bands.</p>	70
<p>Figure 3.6 Mulliken population analysis (MPA) for the $d = 4, 14$, and 24 Ni clusters: (a) Ni–Ni overlap populations; and atomic orbital occupations for Ni (b) s, d_{z^2}, $d_{x^2-y^2}$, and (c) d_{xy}, d_{xz}, d_{yz}</p>	71
<p>Figure 3.7 MPA for the $d = 14$ series of Ni clusters as $\ell = 1 \rightarrow 4$: (a) Ni–Ni overlap populations; and atomic orbital occupations for Ni (b) s and d_{z^2}, (c) $d_{x^2-y^2}$ and d_{xy}, and (d) d_{xz} and d_{yz}.</p>	72
<p>Figure 3.8 Five bonding configurations (and corresponding adsorption sites) investigated, shown for the $n = 44, d = 14, \ell = 4$, or (14/8/8/14) cluster model: (a) π (onfold atop); (b) di-σ (twofold aligned bridging); (c) di-σ/π (threefold triangular or Δ) – hcp; (d) di-σ/π (threefold triangular or Δ) – fcc; (e) μ/π (threefold bridging/atop) – hcp; (f) μ/π (threefold bridging/atop) – fcc; and (g) di-$\sigma/\text{di-}\pi$ (fourfold bridging or μ). Hcp and fcc denote threefold sites over second-layer atoms and hollows, respectively.</p>	74
<p>Figure 3.9 Cluster layer dependence of adsorbate relative site stabilities: binding energy, E_B, as a function of the number of layers of Ni atoms, $\ell = 1 \rightarrow 4$, for five bonding configurations of (a) C_2H_4 and (b) C_2H_2 on the $d = 4$ series of clusters, Ni_n, $n = 4, 7, 10$, and 14, symmetric about the centre of a unit cell of the extended lattice.</p>	78

Figure 3.10 E_B as a function of $\ell = 1 \rightarrow 4$ for (a) C_2H_4 and (b) C_2H_2 on the $d = 14$ series of clusters, Ni_n , $n = 14, 22, 30,$ and 44 , symmetric about the centre of a unit cell of the extended lattice.	79
Figure 3.11 E_B as a function of $\ell = 1 \rightarrow 4$ for (a) C_2H_4 and (b) C_2H_2 on the $d = 24$ series of clusters, Ni_n , $n = 24, 40, 56,$ and 80 , symmetric about the centre of a unit cell of the extended lattice.	80
Figure 3.12 Cluster layer dependence of adsorbate structure: C–C bond distance, $r(C-C)$, as a function of the number of layers of Ni atoms, $\ell = 1 \rightarrow 4$, for five bonding configurations of (a) C_2H_4 and (b) C_2H_2 on the $d = 4$ series of clusters, Ni_n , $n = 4, 7, 10,$ and 14	81
Figure 3.13 $r(C-C)$ as a function of $\ell = 1 \rightarrow 4$ for (a) C_2H_4 and (b) C_2H_2 on the $d = 14$ series of Ni_n , $n = 14, 22, 30,$ and 44	82
Figure 3.14 $r(C-C)$ as a function of $\ell = 1 \rightarrow 4$ for (a) C_2H_4 and (b) C_2H_2 on the $d = 24$ series of Ni_n , $n = 24, 40, 56,$ and 80	83
Figure 3.15 Cluster layer dependence of adsorbate relative site stabilities: E_B as a function of $\ell = 1 \rightarrow 4$ for (a) C_2H_4 and (b) C_2H_2 on the $d = 19$ series of clusters, Ni_n , $n = 19, 31, 43,$ and 62 , symmetric about an individual atom of the extended lattice.	84
Figure 3.16 Cluster layer dependence of adsorbate structure: $r(C-C)$ as a function of $\ell = 1 \rightarrow 4$ for (a) C_2H_4 and (b) C_2H_2 on the $d = 19$ series of Ni_n , $n = 19, 31, 43,$ and 62	85
Figure 3.17 Effect of spin unpairing on adsorbate relative site stabilities: net energy change upon adsorption, ΔE_{spin} , as a function of the number of unpaired electrons, s , for five bonding configurations of (a) C_2H_4 and (b) C_2H_2 on the $d = 4$, $\ell = 1$ cluster, Ni_4	88
Figure 3.18 ΔE_{spin} as a function of s for (a) C_2H_4 and (b) C_2H_2 on the $d = 14$, $\ell = 1$ cluster, Ni_{14}	89
Figure 3.19 ΔE_{spin} as a function of s for (a) C_2H_4 and (b) C_2H_2 on the $d = 24$, $\ell = 1$ cluster, Ni_{24}	90
Figure 3.20 ΔE_{spin} as a function of s for (a) C_2H_4 and (b) C_2H_2 on the $d = 14$, $\ell = 2$, (14/8) cluster, Ni_{22}	91
Figure 3.21 ΔE_{spin} as a function of s for (a) C_2H_4 and (b) C_2H_2 on the $d = 14$, $\ell = 3$, (14/8/8) cluster, Ni_{30}	92
Figure 3.22 ΔE_{spin} as a function of s for (a) C_2H_4 and (b) C_2H_2 on the $d = 14$, $\ell = 4$, (14/8/8/14) cluster, Ni_{44}	93
Figure 3.23 Effect of cluster spin unpairing on adsorbate structure: C–C bond distance, $r(C-C)$, as a function of the number of unpaired electrons, s , for five bonding configurations of (a) C_2H_4 and (b) C_2H_2 on the $d = 4$, $\ell = 1$ cluster, Ni_4	94
Figure 3.24 $r(C-C)$ as a function of s for (a) C_2H_4 and (b) C_2H_2 on the $d = 14$, $\ell = 1$ cluster, Ni_{14}	95
Figure 3.25 $r(C-C)$ as a function of s for (a) C_2H_4 and (b) C_2H_2 on the $d = 24$, $\ell = 1$ cluster, Ni_{24}	96

Figure 3.26 $r(\text{C}-\text{C})$ as a function of s for (a) C_2H_4 and (b) C_2H_2 on the $d = 14$, $\ell = 2$, (14/8) cluster, Ni_{22} .	97
Figure 3.27 $r(\text{C}-\text{C})$ as a function of s for (a) C_2H_4 and (b) C_2H_2 on the $d = 14$, $\ell = 3$, (14/8/8) cluster, Ni_{30} .	98
Figure 3.28 $r(\text{C}-\text{C})$ as a function of s for (a) C_2H_4 and (b) C_2H_2 on the $d = 14$, $\ell = 4$, (14/8/8/14) cluster, Ni_{44} .	99
Figure 3.29 Cluster layer and lateral extent dependence along parametric coordinate variable changes: relative energy change, ΔE , as a function of C-H bond stretch, $\Delta r(\text{C}-\text{H})$, for C_2H_4 on two series of Ni clusters, Ni_n , for $\ell = 1 \rightarrow 4$, (a) $d = 4$, $n = 4, 7, 10$, and 14 , and (b) $d = 14$; $n = 14, 22, 30$, and 44 .	102
Figure 3.30 $r(\text{C}-\text{C})$ as a function of $\Delta r(\text{C}-\text{H})$ for C_2H_4 on two series of Ni_n , $\ell = 1 \rightarrow 4$: (a) $d = 4$; $n = 4, 7, 10$, and 14 , and (b) $d = 14$; $n = 14, 22, 30$, and 44 .	103
Figure 3.31 ΔE as a function of rotation about an axis through the centre of the C-C bond and perpendicular to the surface, $\Delta\phi_{\text{C}}$, for di- σ -bonded C_2H_4 on two $\ell = 1 \rightarrow 4$ series of Ni_n : (a) $d = 4$; $n = 4, 7, 10$, and 14 ; and (b) $d = 14$; $n = 14, 22, 30$, and 44 .	104
Figure 3.32 $r(\text{C}-\text{C})$ as a function of $\Delta\phi_{\text{C}}$ for C_2H_4 on two $\ell = 1 \rightarrow 4$ series of Ni_n : (a) $d = 4$ and (b) $d = 14$.	105
Figure 3.33 ΔE as a function of $\Delta\phi_{\text{C}}$ for di- σ -bonded C_2H_2 on two $\ell = 1 \rightarrow 4$ series of Ni_n : (a) $d = 4$ and (b) $d = 14$.	106
Figure 3.34 $r(\text{C}-\text{C})$ as a function of $\Delta\phi_{\text{C}}$ for C_2H_2 on two $\ell = 1 \rightarrow 4$ series of Ni_n : (a) $d = 4$ and (b) $d = 14$.	107

Chapter 4

Figure 4.1 $\text{Ni}_{80}(\text{C}_2\text{H}_4)$ adsorption system: optimized geometries and binding energies for (a) - (g) five bonding configurations (and corresponding adsorption sites) of C_2H_4 on the $n = 80$, $\ell = 4$, $d = 24$ or (24/16/16/24) cluster model. hcp and fcc denote threefold sites over second-layer atoms and hollows, respectively.	114
Figure 4.2 Mulliken population analysis (MPA) of di- σ -bonded C_2H_4 on Ni_n for the $d = 4, 14$, and 24 series of clusters: (a) C-C overlap populations and π and π^* molecular orbital (MO) occupations; (b) Ni-C and Ni-Ni overlap populations; and atomic orbital (AO) occupations for Ni (c) s , d_{z^2} , and $d_{x^2-y^2}$; and (d) d_{xy} , d_{xz} and d_{yz} .	127
Figure 4.3 MPA of di- σ -bonded C_2H_4 on Ni_n for the $d = 14$ series of clusters as $\ell = 1 \rightarrow 4$: (a) C-C overlap populations and π and π^* MO occupations; (b) Ni-C and (c) Ni-Ni overlap populations; and AO occupations for Ni (d) s , d_{z^2} , (e) $d_{x^2-y^2}$, d_{xy} , (f) d_{xz} and d_{yz} .	129

Figure 4.4 Adsorbate MO energy level diagram for C_2H_4 adsorbed on Ni_{80} : C_2H_4 MO energies compared for the gaseous and the distorted molecule when adsorbed in five binding sites. The highest occupied (HOMO) and lowest unoccupied (LUMO) molecular orbitals, π and π^* , are drawn, while the lowest energy levels, $1a_g$ and $1b_{3u}$, corresponding to overlap of the neglected inner-shell C $1s$ AO's, are omitted.	132
Figure 4.5 MO energy level diagram for $Ni_{80}(C_2H_4)$: chemisorption bonding interaction for C_2H_4 in five adsorption sites. The relative placement of the π and π^* frontier orbitals of gaseous C_2H_4 with respect to the Fermi level, ϵ_F , and d band of the Ni_{80} cluster is indicated.	133
Figure 4.6 $Ni_{80}(C_2H_2)$ adsorption system: optimized geometries and binding energies for (a) - (g) five bonding configurations of C_2H_2 on the (24/16/16/24) cluster.	137
Figure 4.7 MPA of di- σ/π -bonded C_2H_2 on Ni_n for the $d = 4, 14,$ and 24 series of clusters: (a) C-C overlap populations and $\pi_y, \pi_z, \pi_z^*,$ and π_y^* MO occupations; (b) Ni-C and (c) Ni-Ni overlap populations; and AO occupations for Ni (d) $s, d_{z^2},$ (e) $d_{x^2-y^2}, d_{xy},$ (f) d_{xz} and d_{yz}	150
Figure 4.8 MPA of di- σ/π -bonded C_2H_2 on Ni_n for the $d = 14$ series of clusters as $\ell = 1 \rightarrow 4$: (a) C-C overlap populations and $\pi_y, \pi_z, \pi_z^*,$ and π_y^* MO occupations; (b) Ni-C and (c) Ni-Ni overlap populations; and AO occupation for Ni (d) $s, d_{z^2},$ (e) $d_{x^2-y^2}, d_{xy},$ (f) d_{xz} and d_{yz}	153
Figure 4.9 Adsorbate MO energy level diagram for C_2H_2 adsorbed on Ni_{80} : C_2H_2 MO energies compared for the gaseous and the distorted molecule when adsorbed in five adsorption sites. The HOMO's, π_y and π_z , and LUMO's, π_z^* and π_y^* , are drawn, while the lowest energy levels, $1\sigma_g$ and $1\sigma_u$, corresponding to overlap of the neglected C $1s$ AO's, are omitted, as for C_2H_4	156
Figure 4.10 MO energy level diagram for $Ni_{80}(C_2H_2)$: chemisorption bonding interaction for C_2H_2 in five adsorption sites. The relative placement of the π_y, π_z, π_z^* and π_y^* frontier orbitals of gaseous C_2H_2 with respect to ϵ_F and the d band of the Ni_{80} cluster is indicated.	157
Figure 4.11 $Ni_{72}(C_2H_4)_2$ adsorption system: optimized geometries and binding energies for (a) - (e) five bonding configurations of two C_2H_4 's in (2×2) overlayer structure on the (30/21/21) cluster.	160
Figure 4.12 $Ni_{72}(C_2H_2)_2$ adsorption system: optimized geometries and binding energies for (a) - (e) five bonding configurations of two C_2H_2 's in (2×2) overlayer structure on the (30/21/21) cluster.	166
Figure 4.13 Concerted cleavage of <i>trans</i> C-H bonds from each C_2H_4 of the $Ni_{30}(C_2H_4)_2$ system: relative energy change, ΔE , and intermolecular H-H distance, $r(H-H)$, as functions of C-H bond stretch, $\Delta r(C-H)$, for (a) unrestricted ϕ_C rotation relative to the Ni lattice and (b) $\phi_C = 0.0^\circ$, i.e., C-C bond axis fixed along direction (di- σ site).	174

Figure 4.14 Constrained coupled rotation of adjacent C_2H_4 's about an axis through the centre of each C–C bond and perpendicular to the surface, $\Delta\phi_C$, and counter-rotation of the $-CH_2$ groups, $\Delta\phi_{CH_2}$, for $Ni_{30}(C_2H_4)_2$: (a) clockwise (+) and (b) counterclockwise (-) rotation about $\Delta\phi_C$ for both clockwise (+) and counterclockwise (-) rotation about $\Delta\phi_{CH_2}$ (viewing down the C–C axis).	175
Figure 4.15 Concerted rotation of C_2H_4 's about $\Delta\phi_C$ for $Ni_{30}(C_2H_4)_2$: (a) clockwise (+) rotation under C_2 local molecular symmetry constraint and (b) counterclockwise (-) rotation under C_2 and C_1 symmetry constraints.	177
Figure 4.16 Molecular symmetry constraint and cluster layer dependences for $Ni_n(C_2H_4)_2$ of ΔE and $r(H-H)$ as functions of $\Delta\phi_C(+)$: (a) $n = 51$, $\ell = 2$, C_2 and C_1 symmetries; and (b) $n = 30, 51$, and 72 , corresponding to $\ell = 1, 2$, and 3 , under C_2 symmetry.	178
Figure 4.17 Concerted, coupled and independent rotations of two C_2H_4 's about $\Delta\phi_C(+)$ for $Ni_{30}(C_2H_4)_2$: (a) ΔE and (b) $r(H-H)$	180
Figure 4.18 Parametric lengthening of <i>trans</i> C–H bonds after rotation about $\Delta\phi_C$ for $Ni_{30}(C_2H_4)_2$: $\Delta\phi_C$ fixed at 21.0° , corresponding to the structure of Figure 4.15 (a) which yielded a minimum in the intermolecular H–H separation distance, $r_{min}(H-H)$	181
Figure 4.19 Incremental shortening of $r(H-H)$, $\Delta r(H-H)$, along line connecting nuclear centres, otherwise fixing H positions while optimizing C_2H_2 components of $Ni_n(C_2H_4)_2$: $n = 30$, $\ell = 1$ and $n = 51$, $\ell = 2$	184
Figure 4.20 Parametric shortening of $r(H-H)$ optimizing coordinates of both anticipated dehydrogenation products, H_2 and C_2H_2 , for $Ni_{30}(C_2H_4)_2$: C_2H_2 's optimized under C_1 and C_2 symmetry with and without translations, ΔX and ΔY , along the surface, respectively.	184
Figure 4.21 Concerted stretch of <i>trans</i> C–H bonds of each C_2H_4 of the $Ni_{30}(C_2H_4)_2H_2$ model system, with $\Delta\phi_C$ (a) optimized and (b) fixed at 0.0°	185
Figure 4.22 Initial rotation in the dehydrogenation mechanism of di- σ -bonded C_2H_4 for the $Ni_{72}(C_2H_4)_2H_2$ model system: relative energy change, ΔE , and intermolecular H–H distance, $r(H-H)$, as functions of clockwise rotation about an axis through the centre of each C–C bond and perpendicular to the surface, $\Delta\phi_C$, with optimized structures shown for (a) $\Delta\phi_C = 0.0^\circ$ and (b) $\Delta\phi_C = 16.0^\circ$	188
Figure 4.23 Cluster layer dependence of initial C_2H_4 rotation illustrated in Figure 4.22 for $Ni_n(C_2H_4)_2H_2$, $n = 30, 51$, and 72 , corresponding to $\ell = 1, 2$, and 3 : (a) ΔE and (b) $r(H-H)$ as functions of $\Delta\phi_C$	189
Figure 4.24 Concerted dehydrogenation step for rotated, di- σ -bonded C_2H_4 's of $Ni_{72}(C_2H_4)_2H_2$: ΔE and <i>trans</i> C–H bond lengths, $r(C-H)$, as functions of decreasing intermolecular H–H distance, $\Delta r(H-H)$, with optimized structures shown for (a) $\Delta r(H-H) = 0.640 \text{ \AA}$ and (b) $\Delta r(H-H) = 1.000 \text{ \AA}$	191
Figure 4.25 Cluster layer dependence of the dehydrogenation step illustrated in Figure 4.24 for $Ni_n(C_2H_4)_2H_2$, $n = 30, 51$, and 72 , corresponding to $\ell = 1, 2$, and 3 : (a) ΔE and (b) $r(C-H)$ as functions of $\Delta r(H-H)$	192

Figure 4.26 Structural changes as functions of $\Delta r(\text{H-H})$ induced by the dehydrogenation step to form the intermediate decomposition products, $2\text{C}_2\text{H}_2 + 3\text{H}_2$, from $\text{Ni}_{72}(\text{C}_2\text{H}_4)_2\text{H}_2$: (a) C-C bond distance, $r(\text{C-C})$, and rotation angle from the $[\bar{1}10]$ lattice direction, ϕ_{C} , of C_2H_2 ; and (b) centre-of-mass height, $z_{\text{CM}}(\text{H}_2)$, and inclination angle, θ_{H_2} , of physisorbed H_2 relative to the cluster surface.	194
Figure 4.27 Cluster layer dependence of constrained sampling of configuration space for $\text{Ni}_n(\text{C}_2\text{H}_4)_2\text{H}_2$: ΔE as a function of the parametric decrease, $\Delta r(\text{H-H})^-$, and increase, $\Delta r(\text{H-H})^+$, of $r(\text{H-H})$ for (a) $n = 30$, $\ell = 1$ and (b) $n = 72$, $\ell = 3$	195
Figure 4.28 Dehydrogenation mechanism for $\text{Ni}_{72}(\text{C}_2\text{H}_4)_2\text{H}_2$ parametrized by the single reaction coordinate, $r(\text{H-H})$, specifying critical configurations and $E_a = \Delta E_{\text{max}}^{\text{rot}}$	196
Figure 4.29 (a) Qualitative behaviour of time-dependent occupation probabilities for the lower, $n_l(t)$, and upper, $n_u(t)$, states of eqns. (4.34) and (4.35), shown for $r_1 = 0.05 r_2 = 0.01 r_2 = 1 \text{ s}^{-1}$, with expanded time scale in inset validating SSA. Estimated values of $r_1 = 10^{-6} r_2 = 10^{-14} r_2 = 10^{-4} \text{ s}^{-1}$ yield indiscernible features: $n_l(t)$ exhibits a steep initial decline followed by a gradual decay, while $n_u(t)$ rises sharply, quickly peaks, and then decays slowly, under approximate steady-state conditions. (b) Progression of $n_l(t)$ and $n_u(t)$ with increasing r_2 , for $r_1 = 100 r_2 = 0.01 \text{ s}^{-1}$, in the approach towards the predicted curves of eqns. (4.38) and (4.39).	209
Figure 4.30 Low-energy electron diffraction (LEED) pattern from Ref. [10] of the final decomposition products, C_2H_2 and coadsorbed H, following C_2H_4 dehydrogenation on Ni(111): \circ 's are Ni's; \bullet 's are C's of C_2H_2 observed with the C-C axis rotated counterclockwise by $\phi_{\text{C}} \sim 10^\circ$ from the direction of μ site; \circ 's are C's of an ideal C_2H_2 overlayer commensurate with the underlying lattice in the μ binding sites; and the H's are not detectable. The \uparrow 's, $+$'s, and $-$'s indicate the Ni first- and second-layer lateral ($l_{1,2} \leq 0.1 \text{ \AA}$) and buckling ($b_1 \leq 0.04 \text{ \AA}$ and $b_2 \leq 0.07 \text{ \AA}$) reconstructions.	215
Figure 4.31 Counterclockwise acetylene rotation for $\text{Ni}_{72}(\text{C}_2\text{H}_2)_2$: ΔE as a function of $\Delta\phi_{\text{C}}(-)$, with optimized structures shown for (a) $\Delta\phi_{\text{C}} = 0.0^\circ$ (di- σ site) and (b) $\Delta\phi_{\text{C}} = -90.0^\circ$ (μ site).	216
Figure 4.32 Cluster layer dependence of counterclockwise C_2H_2 rotation from the di- σ to μ sites, illustrated in Figure 4.31, for $\text{Ni}_n(\text{C}_2\text{H}_2)_2$ ($n = 30, 51, \text{ and } 72$ ($\ell = 1 \rightarrow 3$)): ΔE as a function of $\Delta\phi_{\text{C}}(-)$	217
Figure 4.33 Simultaneous counterclockwise C_2H_2 rotation and H_2 optimization following C_2H_4 dehydrogenation of $\text{Ni}_{72}(\text{C}_2\text{H}_4)_2\text{H}_2$ to $\text{Ni}_{72}[2\text{C}_2\text{H}_2 + 3\text{H}_2]$ from $\Delta\phi_{\text{C}} = -20.0^\circ$ with respect to the di- σ site, <i>i.e.</i> , the approximate system configuration of Figure 4.24 (b) following the tunnelling step.	217

Figure 4.34 Counterclockwise C_2H_2 rotation followed by H_2 dissociation after C_2H_4 dehydrogenation of $Ni_n(C_2H_4)_2$ to $Ni_n(C_2H_2)_2H_4$ for (a) $n = 72$; $l = 3$ and (b) $n = 30, 51, \text{ and } 72$; $l = 1 \rightarrow 3$. Figure 4.35 shows the geometries optimized nearby the two local minima at $\Delta\phi_C = -95.0^\circ$ and -165.0°	219
Figure 4.35 Adsorption sites of the final decomposition products, C_2H_2 and coadsorbed H, for $Ni_{72}(C_2H_2)_2H_4$: optimized C_2H_2 geometries with (a) $\Delta\phi_C = -5.5^\circ$ from the μ site, stabler by $\Delta E = 0.09$ eV than (b) $\Delta\phi_C = 15.0^\circ$ from the di- σ site. Two perspectives are shown: view down the surface normal and edge-on parallel to the surface plane.	221
Figure 4.36 Cluster spin-configuration dependence of the critical configurations in the dehydrogenation mechanism for $Ni_{72}(C_2H_4)_2H_2$, $\Delta\phi_C = 0.0^\circ$ and 16.0° and $\Delta r(H-H) = 0.640$ and 1.000 Å: (a) ΔE and (b) $r(C-C)$ and $r(H-H)$ as functions of the number of unpaired electrons, s	224
Figure 4.37 Cluster spin-configuration dependence of critical configurations in the adsorption study of the decomposition products for $Ni_{72}(C_2H_2)_2$ ($\Delta\phi_C = 0.0^\circ$ and -90.0°) and $Ni_{72}(C_2H_2)_2H_4$ ($\Delta\phi_C = -95.0^\circ$ and -165.0°): (a) ΔE and (b) $r(C-C)$ as functions of s	225
Figure 4.38 Initial rotation in the dehydrogenation mechanism for π -bonded C_2H_4 in the atop site of the $Ni_{37}(C_2H_4)_2H_2$ model system: ΔE and $r(H-H)$ as functions of $\Delta\phi_C$, with optimized structures shown for (a) $\Delta\phi_C = 0.0^\circ$ and (b) $\Delta\phi_C = 21.0^\circ$	227
Figure 4.39 Concerted dehydrogenation step for rotated, π -bonded C_2H_4 of $Ni_{37}(C_2H_4)_2H_2$: ΔE and <i>trans</i> $r(C-H)$ as functions $\Delta r(H-H)$, with optimized structures shown for (a) $\Delta r(H-H) = 0.600$ Å and (b) $\Delta r(H-H) = 0.925$ Å.	228
Figure 4.40 Dehydrogenation mechanism for di- σ -bonded C_2H_4 of a $Pt_{30}(C_2H_4)_2H_2$ model of the Pt(111)/ C_2H_4 system: (a) ΔE and $r(H-H)$ as functions of $\Delta\phi_C$ and (b) ΔE and <i>trans</i> $r(C-H)$ as functions $\Delta r(H-H)$	232
Figure 4.41 Comparative density-functional theoretical (DFT) single-point and ASE-D-MO single-point and optimized (opt) ΔE 's as functions of single (1 C-H) and concerted <i>trans</i> (2 C-H's) C-H bond stretch, $\Delta r(C-H)$, for (a) isolated C_2H_4 and (b) C_2H_4 di- σ -bonded on Ni_4	237
Figure 4.42 Comparative DFT and ASE-D-MO ΔE 's as functions of $\Delta\phi_C$ for (a) C_2H_4 and (b) C_2H_2 di- σ -bonded on Ni_4 . The DFT single-point ΔE 's implemented two techniques to enhance SCF convergence, damping plus smearing ($\alpha + \omega$) and level shifting (ϵ_{SHIFT}), while ASE-D-MO single-point and optimized (opt) ΔE 's were computed.	238

LIST OF TABLES

Chapter 3

Table 3.1 Atomic Parameters ^a Used in the ASED-MO Calculations	56
Table 3.2 Structural Parameters of Isolated Hydrocarbons, C ₂ H _x , x = 2, 4, 6	57
Table 3.3 Convergence Criteria and Estimated Errors in the ASED-MO Calculations	60
Table 3.4 Basis Sets Used in the Density-Functional Calculations	62

Chapter 4

Table 4.1 Optimized Adsorption Parameters for Ni _n (C ₂ H ₄) for Three Series of Clusters: d = 14, 19, 24 ^a ; l = 1, 2, 3, 4	116
Table 4.2 Ni ₈₀ (C ₂ H ₄) Chemisorption Bonding Indices (Mulliken Population Analyses or MPA's) for Five Binding Sites of Central Ni ₄ Unit Cell	124
Table 4.3 Optimized Adsorption Parameters for Ni _n (C ₂ H ₂) for Three Series of Clusters: d = 14, 19, 24 ^a ; l = 1, 2, 3, 4	139
Table 4.4 Ni ₈₀ (C ₂ H ₂) Chemisorption Bonding Indices (MPA's) for Five Binding Sites of the Central Ni ₄ Unit Cell	147
Table 4.5 Optimized Adsorption Parameters for Ni _n (C ₂ H ₄) ₂ for Three Series of Clusters: d = 19, 30, 37 ^a ; l = 1, 2, 3	162
Table 4.6 Optimized Adsorption Parameters for Ni _n (C ₂ H ₂) ₂ for Two Series of Clusters: d = 19, 30 ^a ; l = 1, 2, 3	168
Table 4.7 Cluster Layer Dependence of Dehydrogenation Mechanism Calculations for Ni _n (C ₂ H ₄) ₂ H ₂ Model Systems: n = 30, 51, 72; l = 1, 2, 3 .	170
Table 4.8 Cluster Layer Dependence of Tunnelling Parameters for Di-σ- and π-bonded C ₂ H ₄ for Ni _n (C ₂ H ₄) ₂ H ₂ Model ^a Systems: n = 30, 51, 72 and n = 37 .	199
Table 4.9 Optimized Adsorption Parameters ^a for Ni _n (C ₂ H ₂) ₂ H ₄ : n = 30, 51, 72; l = 1, 2, 3	222
Table 4.10 Optimized DFT and ASED-MO Adsorption Parameters for Ni ₄ C ₂ H ₄ and Ni ₄ C ₂ H ₂	234

ABSTRACT

The thermal-induced decomposition of ethylene, C_2H_4 , to acetylene, C_2H_2 , on the Ni(111) surface has been treated theoretically within both a semiempirical, modified extended-Hückel framework, the atom-superposition and electron-delocalization molecular-orbital (ASED-MO) method, supplemented with selected density-functional theoretical (DFT) calculations, and a non-equilibrium, statistical mechanical, master-equation formalism. As a preliminary step, adsorbate geometries and binding energies were optimized for one and two molecules of each hydrocarbon species adsorbed in various sites on rigid cluster models of the Ni substrate: on the largest, four-layered, eighty-atom cluster, C_2H_4 favours the di- σ bonding configuration, while C_2H_2 prefers the di- σ/π , or triangular binding site. A fragmentation pathway, entailing the concerted tunnelling of interior intermolecular H's from a transient, bimolecular complex comprised of two rotated C_2H_4 's, is proposed which rationalizes the observed second-order kinetics.

In the dehydrogenation mechanism advanced, each di- σ -bonded C_2H_4 rotates, at elevated temperatures, relative to the Ni substrate, bringing the two interior H's on adjacent molecules closer to each other and a corresponding surface Ni atom; the resultant H-H and metal-H interactions weaken the respective C-H bonds, which lengthen and eventually rupture. The intermolecular H's tunnel, in a process fast compared with the rate of thermal activation, through the potential barrier arising along the shortening of their internuclear distance to form the decoupled dehydrogenation products, C_2H_2 fragments and an intermediate, chemisorption precursor, physisorbed H_2 . The C_2H_2 's rotate to the fourfold bridging or μ site, oriented along the $[\bar{1}\bar{1}2]$ direction, from which they are slightly perturbed by the subsequent dissociation of the metastable, molecular H_2 to atomic H's chemisorbed in the threefold sites of the Ni lattice.

LIST OF ABBREVIATIONS AND SYMBOLS

ABBREVIATIONS

AES	Auger electron spectroscopy
AO	atomic orbital
ARUPS	angle-resolved ultraviolet photoelectron spectroscopy
ASED	atom-superposition and electron-delocalization
DFT	density-functional theory
EELS	electron-energy-loss spectroscopy
EH	extended-Hückel
FEM	field-emission microscopy
fcc	face-centred cubic
HF	Hartree-Fock
HFS	Hartree-Fock-Slater ($X\alpha$)
HK	Hohenberg-Kohn
HOMO	highest occupied molecular orbital
HREELS	high-resolution electron-energy-loss spectroscopy
hcp	hexagonal close-packed
IR	infrared
KS	Kohn-Sham
LCAO	linear combination of atomic orbitals
LCGTO	linear combination of Gaussian-type orbitals
LDA	local-density approximation
LDF	local-density functional
LEED	low-energy electron diffraction
LID	laser-induced desorption
LSDA	local-spin-density approximation
LUMO	lowest unoccupied molecular orbital
ML	monolayer
MO	molecular orbital
MPA	Mulliken population analysis
NEXAFS	near-edge X-ray absorption fine structure
NL	non-local
<i>npf</i>	non-perfectly-following
PD	photoelectron diffraction
<i>pf</i>	perfectly-following
RAIRS	reflection/absorption infrared spectroscopy
SCF	self-consistent-field

SEXAFS	surface-extended X-ray absorption fine structure
SIMS	secondary-ion mass spectrometry
SSA	steady- or stationary-state approximation
STM	scanning tunnelling microscopy
TDS	thermal desorption spectroscopy
TPD	temperature-programmed desorption
TPRS	temperature-programmed reaction spectroscopy
TPSSIMS	temperature-programmed static secondary-ion mass spectroscopy
UHV	ultrahigh vacuum
UPS	ultraviolet photoelectron spectroscopy
VSIP	valence-state ionization potential
VWN	Vosko-Wilk-Nusair
WKB	Wentzel-Kramers-Brillouin
XPD	X-ray photoelectron diffraction
XPS	X-ray photoelectron spectroscopy

SYMBOLS

a	lattice constant
$\equiv\text{CH}$	methylidyne
$=\text{CH}_2$	methylene
$-\text{CH}_3$	methyl
$-\text{C}\equiv\text{CH}$	ethynyl (acetylide)
$=\text{C}=\text{CH}$	vinylidene
$\equiv\text{C}-\text{CH}_3$	ethylidyne
$-\text{CH}=\text{CH}_2$	vinyl
C_2H_2	acetylene (ethyne)
C_2H_4	ethylene (ethene)
C_2H_6	ethane
C_x	Dirac exchange energy coefficient
d	number of atoms in topmost layer of cluster; inter-layer spacing
$\Delta d_{1,2}$	first-/second-layer expansion
$d(\text{Ni}-\text{C})$	distance between nearest Ni of cluster or surface and C of hydrocarbon adsorbate
E_a	activation energy
E_B	binding energy of an adsorbate
$E_{xc}[\rho]$	exchange-correlation energy functional
ϵ_F	Fermi level
$\epsilon_c(\rho)$	uniform-gas correlation energy per particle
ϵ_i	electron ionization energy

$J[\rho]$	classical electron-electron repulsion energy
k_B	Boltzmann constant
ℓ	number of layers in cluster model
μ	chemical potential; reduced mass
N	number of electrons
n	total number of atoms in cluster
$n_\nu(t)$	time-dependent occupation probability of microstate ν
n_ℓ	number of atoms in ℓ^{th} layer of cluster
nn	nearest-neighbour distance
nnn	next-nearest-neighbour distance
ν	pre-exponential or frequency factor, or prefactor; microstate label
ν_{eff}	effective prefactor
P^{WKB}	Wentzel-Kramers-Brillouin tunnelling probability
$P_{t.a.}$	Boltzmann probability of thermal activation
R_d	desorption rate
r	rate constant
r_{eff}	effective rate constant
r_i	spatial coordinates of i^{th} electron
$r_{\nu\nu'}$	transition probability per unit time or transition rate from microstate ν to microstate ν'
r_\uparrow	excitation rate from the ground state to state of energy E
r_\downarrow	decay rate from state of energy E to the ground state
r_t	tunnelling rate
$r_{t,a}$	rate of thermal activation
$r(\text{C}-\text{C})$	hydrocarbon adsorbate carbon-carbon bond length
$r(\text{C}-\text{H})$	hydrocarbon adsorbate carbon-hydrogen bond length
$r(\text{H}-\text{H})$	intermolecular hydrogen-hydrogen internuclear separation
$r_{\text{min}}(\text{H}-\text{H})$	minimum intermolecular hydrogen-hydrogen internuclear separation
$\rho(\mathbf{r})$	ground-state electron number density
$\rho'(\mathbf{r})$	trial electron density
s	number of unpaired electrons in cluster
s_i	spin coordinates of i^{th} electron
T	temperature
T_c	decomposition temperature for thermal activation to be rate-limiting
$T_s[\rho]$	kinetic-energy component in Kohn-Sham noninteracting reference system
$T[\rho]$	kinetic-energy functional
t	time
$V_{ee}[\rho]$	electron-electron repulsion energy functional
$V_{ne}[\rho]$	nuclear-electron attraction energy functional
$v(\mathbf{r})$	scalar local external potential
$v_{\text{eff}}(\mathbf{r})$	Kohn-Sham effective potential
$v_s(\mathbf{r})$	potential in Kohn-Sham reference system
$v_{xc}(\mathbf{r})$	exchange-correlation potential

Φ	bare-metal electron work function
$\Delta\Phi$	adsorbate-induced change in electron work function
ϕ_C	rotation angle about an axis through the centre of the C–C bond and perpendicular to the surface
ϕ_{CH_2}	asymmetric twist distortion or axial counter-rotation angle of $-CH_2$ groups about the C–C bond
x_i	spin and spatial coordinates of i^{th} electron
Ψ	ground-state N -electron wave function
Ψ_s	ground-state wave function in Kohn-Sham reference system
ψ_i	i^{th} Kohn-Sham orbital
Z	atomic number
z	adsorbate coordinate perpendicular to the surface
$z_{CM}(H_2)$	centre-of-mass height of physisorbed H_2 molecule above the surface

ACKNOWLEDGEMENTS

Now as my stint as a graduate student nears its end, I wish to acknowledge those who have moulded it into a rich and rewarding experience, albeit an arduous one, amidst the academic and personal challenges it afforded. Foremost thanks go to my research supervisors, Dr. Russell J. Boyd and Dr. H. Jürgen Kreuzer, for their scientific input and guidance, which they gave whilst maintaining sufficient flexibility to let me make and learn from my mistakes; their complementary approaches to research and perspectives have influenced and broadened my own. I am obliged to Dr. Peter G. Kusalik, for his unwavering willingness to assist me in my endeavours throughout my programme. To the members of the Physics Department who have instructed me, thank you, but I am especially indebted to Dr. M.G. Calkin and Dr. J.G. Cordes for their patient tutelage. I extend my appreciation to Dr. R.L.C. Wang, Dr. L.A. Eriksson, and Dr. R. Fournier for their computational advice and to A. Evans for his dedication in the Computer Centre. I must thank all members, past, interim, and present, of the two research groups with which I have been affiliated, but, in particular, my "adopted family" over much of the last four plus years, including Dr. Susan L. Boyd for adding the cohesive gel: Natalie M. Cann, Jing Kong, Ann Lucasius, Jaime M. Martell, Dr. Zheng Shi, and Jian Wang (especially in the critical stages of the thesis preparation), for their daily camaraderie, assistance, and support, without which I would have undoubtedly succumbed to the pressures of graduate studies. A special, warm note of thanks goes to my conversational companions and sports buddies, for unveiling to me how to have fun yet still be a diligent academic; previously, the elusive balance had always escaped me.

Although not here with me during my doctoral studies, my family played a supporting role by being with me in spirit. Without doubt, I owe a huge thanks to my parents, who, by never questioning my obstinacy in my academic pursuits, provided an environment most conducive to study throughout my earlier years of education. Only after I left home did I realize and appreciate how much they did and sacrificed for me.

Lastly, the financial assistance of the Natural Sciences and Engineering Research Council of Canada (NSERC), the Walter C. Sumner Foundation, and Dalhousie University is gratefully acknowledged.

Chapter 1: INTRODUCTION

Adsorption phenomena on solid surfaces [1] have applications in diverse fields of surface science, encompassing heterogeneous catalysis, electrolysis, corrosion, and adhesion and friction; inherent in each is the role of chemical reactions, charge-transfer processes, and/or intermolecular forces at surfaces. Academically, the study of adsorption is motivated by the dual quest to understand in detail the fundamental interactions which occur on solid surfaces, as well as the two-dimensional equilibria and phase transitions unique to adsorption complexes. In the structural and dynamic elucidation of these systems, the absence of translational symmetry in the direction perpendicular to the surface plane not only challenges, but provides impetus for theoretical descriptions beyond those invoking idealized, semi-infinite, uniform substrate models, while the demand for ultrahigh vacuum (UHV) conditions and surface-specific probes spurs on experimental activity as empirical techniques evolve.

Unsaturated hydrocarbons chemisorbed on well-characterized, transition-metal, single-crystal surfaces [2,3] afford a versatile and instructive vehicle in the research of adsorption phenomena on solid surfaces, particularly processes in heterogeneous catalysis. The spectroscopic identification, under static conditions, of a wealth of chemisorbed species, on both the distinct crystal faces of a given metal and a specific crystal face for varying metals, reflects the interplay between surface geometrical and electronic factors, *i.e.*, the atomic arrangements of the exposed crystal face and sites and the electronic configuration of the metal substrate. As well, multiple bonding

configurations ensue from the charge redistributions of the adsorbed hydrocarbon, due to the variable hybridization states of the carbon atoms, while numerous structural transitions between the equilibrium phases occur as functions of temperature and adsorbate coverage. Reactivity studies reveal a diversity of thermal-activated processes, by which the hydrocarbon surface species may restructure, decompose, and/or react with each other, on a surface which may itself reconstruct. The varying activities of dissimilar metals and crystal faces towards C–C and C–H bond scission and rearrangement offer insight into the molecular interactions and conversions at the microscopic level, once the chemical nature, geometry, and relative surface location of the hydrocarbon adsorbate have been identified.

Experimental [4] and, to a lesser extent, theoretical [5] studies on the adsorption and reactivity of the simplest of the unsaturated, straight-chain hydrocarbons, ethylene (C_2H_4) and acetylene (C_2H_2), chemisorbed on low-Miller-index planes of Group VIII face-centred cubic (fcc) metals, *e.g.*, the Ni, Pd, and Pt series, permeate the surface science literature, as they represent elementary analogues of metal-catalyzed reactions of higher hydrocarbons in industrial syntheses. Both C_2H_4 and C_2H_2 undergo structural distortions and electronic redistributions upon chemisorption on a metal substrate. The low-temperature, molecularly adsorbed, ethylene species are often either di- σ -bonded to two metal atoms or π -bonded to one, with bond orders intermediate between one and two, indicating strong rehybridization of the C atoms. At elevated temperatures, loss of H atoms leads to dissociatively adsorbed intermediates, such as the ethylidyne and acetylenic species. Whether an ethylene thermal-decomposition product or a low-

temperature species of nondissociative adsorption, acetylene adsorbs generally via either a di- σ/π bond to three metal centres or a di- $\sigma/\text{di-}\pi$ bond to four, with bond-order reductions ranging from one to two, reflecting multiple bonding to the surface.

The specific chemical system on which this thesis focuses is the surface-catalyzed dehydrogenation, by thermal-induced decomposition, of C_2H_4 to C_2H_2 on Ni(111), the model heterogeneous reaction first detected by ultraviolet photoemission spectroscopy [6]. Ethylene has been hypothesized to chemisorb in a distorted di- σ configuration [7], in which a pair of *trans* C–H bonds lying parallel to the surface are postulated to undergo facile thermal bond cleavage, a consequence of the direct electronic metal–H interaction deduced by electron-energy-loss spectroscopy (EELS) [8]. Molecularly adsorbed acetylene has been proposed, based on an early low-energy electron diffraction (LEED) analysis [9], to bond via a di- $\sigma/\text{di-}\pi$ interaction to four Ni atoms, while the LEED pattern of the decomposition products, C_2H_2 and coadsorbed H [10], also identifies the C_2H_2 C's in neighbouring threefold hollow sites of the Ni lattice, but with the C–C axis preferentially rotated counterclockwise by an angle of $\phi_{\text{C}} \sim 10^\circ$ with respect to the $[\bar{1}\bar{1}2]$ direction connecting next-nearest-neighbour surface atoms. Time-resolved, high-resolution EELS experiments [11] have revealed a second-order process for the dehydrogenation, in contrast to the expected first-order kinetics of a unimolecular fragmentation scheme, as was measured for isobutene ($\text{CH}_2=\text{C}(\text{CH}_3)_2$) conversion to di- σ/π isobutenylidene ($=\text{C}=\text{C}(\text{CH}_3)_2$) on the same surface [12] and C_2H_4 decomposition to vinyl ($-\text{CH}=\text{CH}_2$) on Ni(100) [13]. A recent scanned-energy-mode photoelectron diffraction study determined for the local adsorption

reactant and product hydrocarbons [14] contrasting azimuthal alignment of the respective bond axes, thereby eliminating all but two possible pathways for a concerted reaction mechanism: either a 90° -rotation of the C–C axis, or a 30° -rotation with a concomitant translation, the bond axis remaining essentially parallel to the surface in both fragmentation scenarios.

Motivated by the forementioned experimental observations, the present theoretical study advances a mechanism for C_2H_4 dehydrogenation to C_2H_2 on the Ni(111) surface both compatible with the deduced local adsorption geometries and specifying the nature of the intermediate, bimolecular complex necessitated by the second-order reaction kinetics. An overview of the pertinent experimental and theoretical techniques and methods, as well as a literature survey of previous work on related systems, are given in Chapter 2, as background for the subsequent discussion of the calculated results. Computational details are examined in Chapter 3, where the appropriateness and limitations of the theoretical methods and cluster models employed are also assessed. Chapter 4 presents and discusses the results of atom-superposition and electron-delocalization molecular-orbital and preliminary density-functional calculations on C_2H_4 and C_2H_2 adsorption and C_2H_4 dehydrogenation on the Ni substrate. Concluding remarks are summarized in Chapter 5, while suggestions for areas of future investigation are explored in Chapter 6.

Chapter 2: BACKGROUND

The synergistic interplay between theory and experiment pervades surface science, with advances in one fuelling developments in the other. The research topic of this thesis bears no exception, but rather, the interdependence weaves a central and recurring theme. Hence, relevant experimental and theoretical techniques and methods are overviewed and previous work on related systems surveyed, structuring both a framework and perspective for the present study, as elaborated in the ensuing chapters.

A. Experimental

1. Surface-Analysis Techniques and Probes [15]

The identity, concentration, and geometric and electronic structures of a species present at a solid surface govern its physics and chemistry; thus, of fundamental importance is the characterization of clean and adsorbate-covered surface properties by various surface-analysis methods. Gross structural information on the unit mesh of regular arrays of adsorbed species is provided by diffraction techniques, while vibrational and X-ray-based electron spectroscopies, in conjunction with surface microscopies, identify the adsorbate binding site, orientation relative to the surface, and local molecular configuration. The chemical composition and electronic structure of adsorption systems are revealed predominantly by electron spectroscopies. Thermodynamic and kinetic

parameters are routinely extracted from investigations of thermal excitation processes and conversions, such as desorption, as well as work-function-change measurements. Adsorption interactions, both between the adsorbate and substrate and among the adsorbates, may be inferred indirectly from a variety of the above methods.

Low-energy (slow) electrons (10 - 200 eV), owing to their short penetration or escape depths within solids, wavelengths comparable to atomic lattice spacings, and chemical specificity, constitute a highly sensitive probe for surface investigations, as, *e.g.*, in low-energy electron diffraction (LEED), electron-energy loss spectroscopy (EELS), and Auger electron spectroscopy (AES). The scattering mechanisms by which slow electrons can interact with a solid and its surface include elastic, quasi-elastic, and inelastic scattering. Elastic scattering (diffraction), the basis of LEED, is attributable primarily to the ion cores, comprised of the nucleus and the strongly bound or core electrons. Because of the small energy exchange (10 - 100 meV) involved, quasi-elastic scattering, a consequence of the thermal motion of the ion cores (lattice vibrations), influences only the angular distribution of the scattering process (differential scattering cross-section), leading to a strong layer dependence in diffracted beam and Auger intensities. Inelastic scattering induces excitation of adsorbate vibrational modes, as in EELS; excitation or ionization of inner-shell electrons, as in AES; and valence (conduction) electron excitation of bulk and surface excitons and plasmons, which not only probes substrate and adsorbate electronic distributions and states, but also attenuates (in conjunction with elastic back-scattering) the incident beam intensity, resulting in a short, inelastic-scattering, electron mean-free-path and hence surface specificity. The



strong interaction between slow electrons and condensed matter imposes experimental limitations on the methods, requiring UHV conditions and a surrounding gaseous environment and specimen inert to the electron beam (*viz.*, beam-induced sample charging, dissociation, desorption, adsorption, carbon contamination buildup, etc.).

a. Geometrical Structure

Characterization of adsorbate structure, *i.e.*, the local molecular configuration, the adsorption site, and lateral arrangement of the adsorbed species, hinges on identifying the number and relative saturation densities of binding states, as well as the long-range adsorbate periodicity. Adsorbate structural models may be constructed from supplementary information, *e.g.*, differentiation of atomic and molecular states, binding energies, sticking coefficients, and dipole moments, combined with either a complete diffraction analysis or spectroscopic information on bonding and electronic structures. This section focuses on the physical principles of LEED and vibrational and X-ray-based electron spectroscopies salient to the system under investigation. Though not elaborated upon, various microscopies and particle scattering experiments also probe local surface topography: both scanning tunnelling (STM) and field-emission, *i.e.*, field-ion (FIM) and -electron (FEM) microscopies exploit electron tunnelling from metal tips, induced by either a high electric field or low fixed-bias voltage coupled with a microscopic tunnel junction, to yield direct, real-space images which reflect atomic positions and thermal disorder; whereas low- (LEEM) and high-energy, or transmission (TEM) electron

microscopies, as well as classical scattering by light atoms and ions, image the surface through electron and particle scattering, or diffraction, respectively.

1. Low-Energy Electron Diffraction (LEED) [16,17]

Coherent interference between electron waves elastically back-scattered from surface atoms of crystalline solids constitutes the basis of low-energy electron diffraction (LEED). The kinematical theory of LEED considers only the production of diffracted waves by the unattenuated (Bragg scattering) or attenuated (primarily due to inelastic scattering) incident wave, while neglecting the rediffraction of diffracted waves (*i.e.*, double and multiple scattering). In contrast, the dynamical theory also incorporates multiple scattering, absorption due to strong inelastic scattering, and the reduction of beam intensities due to quasi-elastic scattering. The theory of low-energy electron scattering, and thus the utility of LEED, are limited by the lack of a quantitative description of exchange and correlation effects, *i.e.*, spin-spin interactions between, and polarization of, incident and ion-core electrons, and their clouds, respectively.

Governed by the two-dimensional periodicity parallel to the diffracting surface, LEED is restricted to the study of surfaces with sufficient lateral periodicity, *e.g.*, those of single crystals, fibrous-textured specimens, and layered materials with disorder normal to the surface. By revealing the structure of the Fourier transform of the surface-charge density, LEED yields information on the symmetry and long-range order of regular arrays of surface atoms. Clean-surface lateral periodicity, *i.e.*, the size and orientation

of the surface unit mesh, the extent of the periodicity or degree of order, and atom locations within the repeat unit, are routinely determined from diffraction-beam spot positions, widths, and intensities, respectively. Similarly, both adlayer structure, including domain size distributions, and processes which alter its lateral periodicity or order (*e.g.*, order-disorder and commensurate-incommensurate phase transitions, and decomposition, adsorption or condensation processes), as well as inter-adsorbate interactions from beam-intensity variations with coverage, can be investigated by LEED. While revealing the relative pattern and spacings of adsorbed species, LEED cannot unambiguously differentiate, without detailed intensity/voltage measurements, between varying adsorption sites or relative surface orientations of the adsorbate.

2. Vibrational Spectroscopy [4,18,19]

Elucidation of both the local structure and chemical composition of adsorption complexes by vibrational spectroscopic techniques permits detailed analysis of adsorbate site symmetry, bonding, and adsorption geometry. The local electric field at the adsorbate site couples to the dipole moment generated by the intra-adsorbate nuclear motion associated with the excited vibrational mode. Dipole selection rules, established from group-theoretical arguments, state that the transition probability has non-vanishing matrix elements only when the vibrational mode belongs to the same irreducible representation of the adsorbate point group as at least one Cartesian component of the electric dipole operator. Reviewed below are the two principal forms of vibrational

spectroscopy used to identify the molecular configurations of hydrocarbon complexes chemisorbed on single-crystal, metal surfaces: reflection/absorption infrared spectroscopy and electron-energy-loss spectroscopy; other surface vibrational spectroscopies include incoherent inelastic neutron scattering (IINS), surface-enhanced Raman spectroscopy (SERS), and inelastic electron tunnelling spectroscopy (IETS).

a. Reflection/Absorption Infrared Spectroscopy (RAIRS)

Reflection/absorption infrared spectroscopy (RAIRS) elicits the absorption of an infrared (IR) photon by a molecule adsorbed on a flat metal surface, which generates an oscillating vibrational dipole moment in the adsorbate, followed by subsequent reflection of the IR beam from the surface. Vibrational dipoles oriented parallel to the surface are effectively cancelled in the IR regime by the corresponding motions of induced virtual images of opposite sign in the metal, while those perpendicular to the surface are enhanced by a factor of two. The following metal-surface selection rule results: only vibrations leading to dynamic dipoles or dipole-components perpendicular to the surface are detectable by absorption; hence, only totally symmetric modes are excited [4].

b. High-Resolution Electron-Energy-Loss Spectroscopy (HREELS)

In electron-energy-loss spectroscopy (EELS), monoenergetic electrons reflected from a metal surface lose energy in discrete amounts due to the absorption of vibrational

quanta by the adsorbate, with quanta of different magnitudes corresponding to the excitation of individual modes of molecular vibration. Two primary excitation mechanisms have been invoked: dipole scattering, which proceeds via a long-range interaction of the electric dipole field, associated with the approaching or receding electron, with a vibrational dipole of the adsorbed species; and impact scattering, which arises from a direct, short-range interaction of the electron with the local adsorbate potential; while a third, resonance mechanism can occur for specific incident electron energies. Dipole scattering follows the same metal-surface selection rule of IR absorption, with reflection of electrons predominantly in the specular direction (where the angle of incidence equals the angle of reflection), while impact scattering, subject to different selection rules [4], yields complementary vibrational information by also exciting non-dipole-active modes, *i.e.*, vibrational atomic motions parallel to the surface, with electrons reflected hemispherically. By distinguishing dipole and impact-excited modes, the angular dependence of specular and non-specular EELS loss intensities identifies not only the symmetry properties of the relevant normal vibrational modes, and thus the adsorbed species, but also the molecular adsorption geometry and orientation.

c. Time-Resolved HREELS [11]

Time-resolved HREELS monitors selected loss peak heights, after a controlled temperature rise, to follow the increase (decrease) of forming (decomposing) species as a function of time. Utilized in studies of dynamic surface processes, *e.g.*, adsorption and

thermal decomposition, it yields kinetic parameters, *i.e.*, pre-exponentials, activation energies, and orders of reactions, of the elementary, intermediate steps in molecular conversions (*cf.* Sect. 2.A.1.c.1. on desorption kinetics). Of the two existing modes of operation, fast repetitive scans of a single loss peak or narrow group of peaks and continuous monitoring of the maximum intensity of a selected loss peak invariant in shape and position to the fragmentation process, the latter, being easier to perform, is preferred, as both give essentially the same results within the experimental error. Requisite for quantitative measurements is the linearity of the signal peak intensity with the density of scatterers at the surface, *i.e.*, the adsorbate coverage.

3. X-Ray-Based Electron Spectroscopies [20]

a. Near-Edge X-ray Absorption Fine Structure (NEXAFS)

Based on atomic, X-ray, core-level, absorption edges (photoionization thresholds), the near-edge X-ray absorption fine structure (NEXAFS) or X-ray absorption near-edge structure (XANES) technique elucidates the adsorbate orientation with respect to the substrate, *i.e.*, the local structure of the adsorption complex. The method probes the absorption properties of adsorbed molecules within ~ 50 eV of a core absorption edge; the NEXAFS absorption cross-sections are dominated by simple intra-molecular resonant transitions to unoccupied and virtual (or quasi-) bound states, the latter being continuum states just above the vacuum level. For hydrocarbon adsorbates, both the C–C orbital

symmetry or orientation relative to the metal surface and the degree of π^* -antibonding-orbital filling through metal back-donation can be ascertained from measured C core-level absorption cross-section dependences upon the incident-beam polarization or molecular symmetry, as selection rules may preclude absorption into σ - or π -symmetry final states.

b. Surface-Extended X-ray Absorption Fine Structure (SEXAFS) and X-ray Photoelectron Diffraction (XPD)

Both surface-extended X-ray absorption fine structure (SEXAFS) and X-ray photoelectron diffraction (XPD) employ X-ray photons to eject core-level electrons from adsorbate atoms, as a means to gain local surface structure information (*e.g.*, bond lengths, angles, coordination, etc.). SEXAFS measures the Auger electron (see Sect. 2.A.1.b.1) or fluorescence yield following core-hole production, while XPD measures the direct photoelectron current. SEXAFS monitors the total absorption coefficient hundreds of eV above core-level edges as a function of incident photon energy and hence photoelectron wave vector. Adsorption bond length and site information can be extracted by Fourier inversion of the small-amplitude oscillations (fine structure) the absorption coefficient exhibits due to back-scattering and diffraction of ejected photoelectrons by atoms neighbouring the photoionized atoms. XPD plots of the polar and azimuthal dependence of the photoemission intensity display characteristic interference maxima and minima consistent with the substrate symmetry, from which the location of an adsorbate relative to a substrate may be determined upon comparison with intensities calculated for

different geometries. Averaging over all possible XPD final-state emission angles eliminates the method's restriction to adsorption on single-crystal surfaces and insensitivity to adsorbate positional variations normal to the surface for heights $> 1 \text{ \AA}$.

c. Scanned-Energy-Mode Photoelectron Diffraction (PD) [14]

Structural parameters of adsorbed molecules, which need not exhibit long-range order (*cf.* LEED), can be deduced via scanned-energy-mode photoelectron diffraction (PD). The intensities of a core-level photoemission peak of an adsorbate atom (*e.g.*, C 1s) are measured at fixed emission angles as functions of photon energy, and hence photoelectron kinetic energy. Interference between the primary photoelectron wave and secondary waves scattered by neighbouring substrate atoms modulate the diffraction spectra, *i.e.*, plots of core-level photoelectron intensities *vs.* energy. Encoded in the modulations, information on the scattering path lengths, and thus local bonding geometry, *i.e.*, the surface site and distances to nearest-neighbour substrate atoms, is extracted by comparing the experimental and calculated (using multiple-scattering theory) diffraction spectra.

b. Chemical Composition and Electronic Structure

The electronic energy level spectrum of a clean surface following its interaction with a foreign particle may be characterized via electron spectroscopic techniques, which associate a specific bonding (electronic) configuration with each spectrum. In such

electron emission processes, the emitted electrons are energy-analyzed and the initial state is inferred from the measured final-state energy and probe characteristics: Auger electron and photoelectron (or photoemission) spectroscopies use an incident beam of electrons or photons as the external probe, whereas field-emission (FES) and ion-neutralization (INS) spectroscopies (not described) employ an applied field and a low-energy ion beam, respectively. Their theoretical descriptions often invoke a one-electron picture which assumes an unrelaxed ionic core (Koopmans' theorem), thereby not distinguishing between the ionization potential, or binding energy, required to eject the electron and the gas-phase, orbital energies of the neutral species. This relaxation energy, along with any surface-induced relaxation, must then be imposed ad hoc when interpreting the experimental energy distributions. An alternative probe of surface chemical composition and concentrations, notably of adsorbed compounds and decomposition products, as well as the local adsorption-complex configuration, secondary-ion mass spectrometry (SIMS) bombards a solid surface with medium-energy (> 1 keV) ions and mass-spectrometrically detects and identifies the secondary ions sputtered off the surface.

1. Auger Electron Spectroscopy (AES) [17]

In Auger electron spectroscopy (AES), bombardment of electrons (> 1 keV), X-ray photons, or energetic ions or neutrals on a solid surface ejects core electrons i , their vacancies being filled by valence electrons j . The liberated energy is radiated as

characteristic X-ray radiation or transferred to a second valence electron k , which is subsequently emitted as an "Auger electron". This latter, two-stage radiationless Auger emission process may be summarized, for an atom A , by



and



or energetically, with minimal incorporation of relaxation phenomena, by

$$E_{kin}^{ijk} = E_i(Z) - E_j(Z) - E_k(Z+\Delta Z) , \quad (2.3)$$

where E_{kin}^{ijk} is the kinetic energy of the Auger electron, $E_i(Z)$ the binding energy of the i^{th} electron in an atom of atomic number Z , and $E_k(Z + \Delta Z)$ that of the Auger electron ejected from the singly charged ion, approximated as a neutral atom of atomic number $Z + \Delta Z$, with $0.5 \leq \Delta Z \leq 1$. The electrons are liberated with kinetic energies (10 – 2000 eV) characteristic of the emitter, with a nearly isotropic angular distribution.

In condensed matter, the free-atom valence levels are broadened into bands and shifted in energy, giving broad peaks rather than narrow lines in the Auger energy distribution. The proportionality between the peak intensity and number of excited species makes AES a potentially quantitative, analytical tool for surface chemical composition and processes involving changes in such. However, inelastic scattering in condensed samples strongly attenuates Auger electrons, and hence peak intensities, thereby restricting quantitative AES to systems of either known or two-dimensional distribution, as varying sample depths yield variable intensities. This attenuation may

instead be exploited to gain structural information on perpendicular surface concentration gradients, as in depth profiling. The strong, localized disturbance induced by the Auger emission process elicits dynamic and static relaxations, *i.e.*, atomic rearrangements accompanying ionization and the j^{th} -electronic transition into the i^{th} hole, respectively, with the latter decomposable into intra- and extra-atomic relaxations, describing the respective responses of the free atom and the atomic environment in the solid to the formation of the j^{th} hole, all of which must be accounted for in an accurate calculation of the Auger energy, E_{kn}^{pk} . Practically, identification of surface chemical elements is aided by catalogued Auger spectra, which enable AES to serve as a standard fingerprint, though destructive, technique and monitor of surface cleanliness. Complementary to LEED, AES requires neither a periodic nor a flat surface, valuable in the characterization of polycrystalline and amorphous surfaces not amenable to LEED, and elucidates the surface chemical composition requisite for interpretation of LEED data.

2. Photoelectron or Photoemission Spectroscopy [21]

In photoelectron spectroscopy, excitation by an incident photon elastically and/or inelastically scatters electrons, which may subsequently escape from the solid and be energy-analyzed. X-ray and far-ultraviolet radiation eject core and valence electrons, respectively, corresponding to X-ray (XPS) and ultraviolet (UPS) photoelectron spectroscopy, with XPS also named electron spectroscopy for chemical analysis (ESCA). Ejection of a photoelectron i from an adsorbate-covered metal surface can be described

energetically by the modified Einstein photoelectric equation:

$$\begin{aligned}
 E_{kin}^i &= h\nu - \epsilon_i, & \text{with } \epsilon_i &= E_b^i + \Phi + \Delta\Phi \\
 & & &= \epsilon_i^g - \Delta\epsilon_i^R + \Delta\epsilon_i^b;
 \end{aligned}
 \tag{2.4}$$

where E_{kin}^i is the measured kinetic energy; $h\nu$ is the incident photon energy; E_b^i is the deduced binding energy (relative to the Fermi level) of the emitted electron; ϵ_i , ϵ_i^g , $\Delta\epsilon_i^R$, and $\Delta\epsilon_i^b$ are the adsorbate and gas-phase ionization energies (vacuum-level reference), and relaxation and chemical bonding shifts, respectively; and Φ and $\Delta\Phi$ are the bare-metal and adsorbate-induced change in the substrate work function. The surface species can be identified upon comparison with tabulated gaseous ionization energies, while adsorbate-induced differences in emission intensity curves monitor more subtle orbital bonding interactions and chemical-state changes of adsorbate complexes. A probe of surface elemental and electronic structure, photoelectron spectroscopy can yield information on adsorbate site and orbital symmetry. However, relaxation effects ($\Delta\epsilon_i^R$'s, due to image-charge screening of the final hole state, molecular polarization and charge transfer upon adsorption, and orbital relaxation of the ionic core; see also Sect. 2.A.b.1) complicate the correlation between observed adsorbate (ϵ_i) and gas-phase (ϵ_i^g) ionization energies often made to extract particular orbital bonding interactions from chemical (π -orbital, for unsaturated hydrocarbons) bonding shifts ($\Delta\epsilon_i^b$). The angular dependence of the photoemitted electron energy distribution, measured in angle-resolved ultraviolet photoelectron spectroscopy (ARUPS), yields structural information via the spatial symmetry of excited orbitals in adsorbate-covered surfaces.

c. Thermodynamic and Kinetic Properties

1. Desorption Kinetics [22,23]

Desorption, or the rupture of the adsorption bond and consequent removal of adparticles from the surface, may be achieved thermally; by impact of electrons, photons, and ions or fast neutrals; and by the application of high electrostatic fields. Monitoring desorption phenomena probes the identities, populations, and binding energies of adsorbate states; the shapes of ground-state potential curves; the existence of and transitions to and from excited electronic adsorbate states; as well as lateral interactions between the adparticles. The temperature-programmed desorption (TPD) or thermal desorption spectroscopy (TDS) method employs elevated temperatures at which a significant fraction of adparticles has energies exceeding the desorption energy, thus exploiting thermal desorption, and measures the desorption rate as a function of temperature while the substrate is continuously heated. Determined by the temperature and amount of gas remaining on the surface, the desorption rate is maximal when the increase due to the temperature rise equals the decrease from the diminished coverage. Hydrocarbon and/or hydrogen desorption as a function of temperature in TPD studies can reveal information about the desorbing species and/or the overall CH_x composition of the remaining adsorbed hydrocarbon.

Thermal desorption peak positions and shapes, in principle, directly yield binding states, relative saturation densities, and desorption rate parameters, though

interpretational ambiguities may preclude unravelling this information, especially if peaks overlap. The desorption rate, R_d , or number of desorbing particles per unit time, is a function of both the temperature, T , and the adsorbate coverage, Θ , *i.e.*, the number of adsorbed particles, normalized to the maximum number at monolayer (ML) coverage or the number of surface adsorption sites:

$$R_d = -d\Theta/dt = f(T, \Theta). \quad (2.5)$$

The rate of desorption, being a thermally activated process, is phenomenologically parametrized by an Arrhenius or Polanyi-Wigner equation:

$$R_d = r\Theta^m = \nu e^{-E_a/k_B T} \Theta^m, \quad (2.6)$$

where r is the rate constant, ν the (dynamic) pre-exponential or frequency factor, or simply prefactor, and E_a the (static) activation or desorption energy (frequently summed as the binding plus activation energies of adsorption), all of which depend on the formal order of the reaction, m , with k_B being the Boltzmann constant. Often, the only coverage dependence is assumed to reside in the Θ^m term, related to the number of particles participating in the critical step, and the temperature dependence, in the exponential term, which represents the relative number of attempts by the system, having the necessary minimum energy, E_a , to undergo reaction, with the pre-exponential, ν , equal to the frequency of such attempts; in general, though, both E_a and ν , and hence r , may be coverage- and temperature-dependent. While no simple correspondence between mechanism and order exists, the measured order is traditionally interpreted as indicative of the molecularity of the rate-determining elementary step.

2. Electron Work-Function Changes [15,24]

The electron work function, *i.e.*, the minimum energy required to transport an electron from the bulk of a solid to a macroscopic distance from the surface, equals the energy difference between the Fermi level (bulk chemical potential) and the vacuum level just outside the surface (surface electrostatic barrier). The latter reflects the effect of the surface on the binding energy of an electron, *i.e.*, the surface contribution to the work function, equivalent to the work that must be done to move an electron through the electric field prevailing in the surface electrical double layer. Both the double layer and a net macroscopic surface charge, if inequivalent crystal faces exist, arise from asymmetrical distortions of the surface electronic charge distribution, caused both by electron spill-out of a clean metal or by the presence of an adsorbed particle, and ionic displacements, from ideal Bravais lattice positions, in surface unit cells. Measurement of the work function for clean surfaces, Φ , yields information on the surface potential, while monitoring adsorbate-induced changes, $\Delta\Phi$, as a function of coverage can not only elucidate the corresponding surface-adsorbate electronic interaction, different binding sites, and saturation densities, but also derive adsorption-induced adparticle dipole moments and polarizabilities, related in turn to their mutual interaction and that with the surface.

2. Related Work

a. C_2H_4 and C_2H_2 on Ni(111)

1. Adsorption of C_2H_4 and C_2H_2 on Ni(111)

The long-range ordering behaviours of ethylene and acetylene on Ni(111) were studied by joint kinematical LEED and EELS measurements [25]: each system forms three ordered phases as functions of temperature and exposure, with the hydrocarbon symmetry and adsorption site preserved during structural phase transitions. At exposures of ~ 2 L (where $1 \text{ L} = 10^{-6} \text{ torr sec}$), both C_2H_4 ($T < 200 \text{ K}$) [26] and C_2H_2 ($T = 200 - 370 \text{ K}$) [26,27] give well-ordered (2×2) LEED patterns, corresponding to coverages of $\Theta \sim 0.25$. The observation of only commensurable LEED structures implies a high-symmetry substrate site, which was deduced, for both molecules, as the triangular (Δ) binding site, with the C atoms in neighbouring bridge positions in a $di-\sigma/\pi$ bonding configuration. (Various hydrocarbon bonding configurations and adsorption sites are displayed in Figure 3.8 on p. 74.) In contrast, a full dynamical LEED analysis [9] of the Ni(111)/ (2×2) - C_2H_2 structure, at 0.5 L exposure and $T = 250 \text{ K}$, favoured the fourfold bridging or μ site, with the molecular axis parallel to the surface plane, a C-C bond length of $r(C-C) = 1.50 \text{ \AA}$, and a Ni-C distance of $d(Ni-C) = 2.1 \text{ \AA}$, consistent with subsequent HREELS and PD results. (Structural parameters for the gas-phase hydrocarbons, C_2H_x , where $x = 2, 4$, and 6, are documented in Table 3.2 on p. 57.)

From vibrational modes observed in HREELS studies of normal and deuterated ethylene at $T = 150$ K, Lehwald and Ibach deduced a local molecular di- σ -bonding configuration with near- sp^3 rehybridization [28], suggestive of nonplanar adsorption, with an adsorbate-complex point group symmetry lower than C_{2v} , *i.e.*, C_s , C_2 , or C_1 , [8,29], which requires additional tilting or twisting of the molecule in a high-symmetry site. An analysis by Felter and Weinberg [30] of UPS ionization level shifts, $\Delta\epsilon_i$'s, and EELS data, using free, ground- and first-excited state molecular analogues, predicted a similarly twisted chemisorption geometry: $r(\text{C}-\text{C}) = 1.41$ Å, $\theta_{\text{CCH}} = 107^\circ$, $\theta_{\text{HCH}} = 105^\circ$, and a methylene ($-\text{CH}_2$) asymmetric twist distortion or axial counter-rotation, *i.e.*, opposite-directional twisting of the $-\text{CH}_2$ groups about the C-C bond, of $\phi_{\text{CH}_2} = 39^\circ$. In contrast, earlier UPS spectra interpreted by Demuth in a free-molecule (ground-state) approximation, *i.e.*, by correlation of observed relative $\Delta\epsilon_i$'s between chemisorbed and gaseous molecules with those computed theoretically for distorted and equilibrium structures, suggested a weakly distorted, π -bonded species [31]: $r(\text{C}-\text{C}) = 1.39$ Å, $\theta_{\text{CCH}} = 120^\circ$, $\theta_{\text{HCH}} = 117^\circ$, and $\phi_{\text{CH}_2} \leq 10^\circ$ [32]. A softened and broadened C-H stretch mode observed in EELS spectra at high coverages [8] indicates that two of the H atoms lie closer to, directly interacting electronically with the metal, reminiscent of H bonding. From a TPD, LEED, and UPS study of the conversion of C_2H_4 to C_2H_2 on Ni(111) [26], geometric models proposed for ethylene bonding (and dehydrogenation) place the C_2H_4 molecules in either the di- σ/π (Δ) or di- $\sigma/\text{di-}\pi$ (μ) binding sites, with potential asymmetric axial twisting of C_2H_4 in the μ site suggested, to correlate with the above EELS observation. Methylene counter-rotation

to rationalize the H-bridge bonding was also invoked by Hammer and Müller [7], who proposed a distorted di- σ -bonding configuration to next-nearest-neighbour Ni atoms. The local C_2H_4 adsorption geometry deduced from a recent scanned-energy-mode PD analysis [14] orients the C–C axis parallel to the surface along the $\langle 110 \rangle$ set of directions, with the two C's almost atop Ni atoms in an aligned bridging or di- σ configuration, giving a perpendicular distance from the surface of $z(C) = (1.90 \pm 0.02) \text{ \AA}$, $r(C-C) = (1.60 \pm 0.18) \text{ \AA}$, and a Ni first-/second-layer expansion of $\Delta d_{12} = (0.15 \pm 0.10) \text{ \AA}$.

Demuth and Ibach [33] reported, from HREELS measurements of normal and deuterated C_2H_2 on Ni(111), a strongly distorted molecular configuration with $\sim sp^{2.5} - sp^3$ hybridization (reflecting an estimated $r(C-C)$ of 1.45 – 1.49 \AA); this contrasted with previous UPS studies, which proposed a π -adsorbed species without any significant rehybridization [34,31], but was subsequently corroborated by a refined UPS analysis, which suggested $r(C-C) = 1.38 - 1.44 \text{ \AA}$ and $\theta_{CCH} = 120 - 130^\circ$ [32]. The UPS/EELS work by Felner and Weinberg predicted di- σ bonding, sp^3 hybridization, $r(C-C) = 1.5 - 1.6 \text{ \AA}$, and $\theta_{CCH} \sim 109^\circ$ [30], while a NEXAFS study of both C_2H_4 (which decomposes to C_2H_2) and C_2H_2 on Ni(111) at $T = 300 \text{ K}$ [35] deduced $r(C-C) = (1.45 \pm 0.04) \text{ \AA}$, with the molecular axis parallel to the surface. The bonding geometry proposed from the HREELS study [33] positions the C atoms above two adjacent, inequivalent threefold hollow sites, *i.e.*, in the μ binding site of the Ni lattice, as originally suggested from an UPS, TPD, and LEED analysis [36], with the C–C bond axis slightly tilted ($10 - 17^\circ$), and the molecular plane normal with respect to the surface. Alternatively, an HREELS, LEED, $\Delta\Phi$, and TPD investigation of C_2H_4

adsorption at room temperature suggested a triangular surface chemisorption site for the flat-lying, nearly sp^3 -hybridized C_2H_2 dehydrogenation product, with two σ bonds and one π bond to three Ni atoms in a bent HCCH arrangement ($\theta_{CCH} \sim 155^\circ$) [37], later supported by the LEED/EELS result reported previously [25]. The C_1 point group symmetry of the C_2H_2 surface complex, as deduced from angular profiles of EELS loss intensities [38], restricts the possible bonding geometries to those with no element of symmetry. Corroborating the early dynamical LEED [9] and HREELS [33] investigations already mentioned, a scanned-energy-mode PD determination of the local C_2H_2 adsorption structure [39] confirmed the orientation of the C–C axis along one of the $\langle 211 \rangle$ set of azimuths, *i.e.*, the μ binding site, with $z(C) = (1.36/1.37 \pm 0.04)$ Å (fcc/hcp site), $r(C-C) = 1.44$ Å, and surface-layer contraction of $\Delta d_{12} = -(0.01 \pm 0.06)$ Å. The unpublished LEED results of Heinz *et al.* [10] predict C_2H_2 , when coadsorbed with H as a product of C_2H_4 decomposition (see below), is axially twisted by $\phi_C \sim 10^\circ$ from the $[\bar{1}\bar{1}2]$ Ni lattice direction, with $r(C-C) = 1.33$ Å and $z(C) = 1.34$ Å; Ni first- and second-layer lateral ($l_{1,2} \leq 0.1$ Å) and buckling ($b_1 \leq 0.04$ Å and $b_2 \leq 0.07$ Å, respectively) reconstructions were detected.

2. Thermal Decomposition of C_2H_4 to C_2H_2 on Ni(111)

Ethylene, upon heating to $T \sim 230$ K, undergoes a thermally activated dehydrogenation to acetylene on Ni(111), as originally detected by Demuth and Eastman [6] by comparing the resultant UPS spectrum with that of chemisorbed C_2H_2 . A

subsequent UPS, TPD, and LEED analysis revealed that the thermal dehydrogenation to C_2H_2 of a (2×2) submonolayer saturation coverage of chemisorbed C_2H_4 on Ni(111) is accompanied by both the formation of chemisorbed atomic hydrogen and molecular desorption of some chemisorbed C_2H_4 [26]. Geometric models of asymmetric, axially twisted C_2H_4 molecules easily rationalize the observed weak metal-H interaction, proposed to facilitate thermal C-H bond cleavage [8], with subsequent H loss leading to chemisorbed H bonded in nearby threefold sites [26]. Strong isotopic and coverage dependences in the desorption and decomposition steps of molecular ethylene were observed by temperature-programmed static (TPS) SIMS, TPD, and AES: C-H (D) bond-breaking was concluded, from the isotope effect in the onset bond-cleavage temperature, to be involved in the rate-determining step in the conversion of C_2H_4 to C_2H_2 , while molecular desorption of weakly π -bonded C_2H_4 was determined to be induced by decomposition of the di- σ -bonded species [40].

The kinetics of the thermally induced fragmentation on Ni(111) of C_2H_4 , adsorbed at $T = 90$ K, to C_2H_2 and coadsorbed H at $T \sim 180$ K, has been investigated by time-resolved HREELS [11,12], whereas previous kinetic studies of the Ni(111)/ C_2H_4 system focused on the dissociative adsorption [41,42] and thermal decomposition [43] of the room temperature phase. In the time-resolved HREELS study by Hammer *et al.*, both decomposition steps, *i.e.*, including the second step, dehydrogenation of acetylene, were described by second-order Langmuir kinetics: for the first decomposition step, an activation energy of $E_a = (0.35 \pm 0.04)$ eV and effective frequency factor of $\nu = 10^{8 \pm 2}$ s⁻¹, with subsequent, updated values of $E_a = (0.30/0.31 \pm 0.02)$ eV and $\nu = 10^{6 \pm 2}$ s⁻¹

[44], were obtained; while results for the second decomposition step are discussed in the next section. The HREELS intensity curves were fitted with the temperature-dependent decay functions for first- and second-order decomposition mechanisms:

$$\begin{aligned}
 \text{reactant:} \quad I(t) &= I_0 f_T(t) + I_b \\
 \text{product:} \quad I(t) &= I_\infty + (I_0 - I_\infty) f_T(t) + I_b, \quad (2.7) \\
 \text{with} \quad f_I(t) &= e^{-t/\tau} \quad (1^{\text{st}}\text{-order}) \quad \text{and} \quad f_T(t) = \frac{\tau}{t + \tau} \quad (2^{\text{nd}}\text{-order}),
 \end{aligned}$$

where the characteristic time constant, τ , and the inelastic background intensity, I_b , were taken as free parameters, determined by the method of least-mean-square deviation, and I_0 and I_∞ are the initial and saturation intensities, *i.e.*, at $t = 0$ and $t \rightarrow \infty$. A thermal-activated process was assumed, relating the time constant to the activation energy via

$$\tau(T) = \nu^{-1} e^{E_a/k_B T}, \quad (2.8)$$

from which E_a and ν were extracted from an Arrhenius plot of $\ln \tau(T)$ vs. T^{-1} . In contrast, the first decomposition step of the thermal-induced fragmentation of isobutene to di- σ/π isobutenylidene (dimethylvinylidene) on Ni(111) was deduced to proceed by a first-order process, with $E_a = (0.30 \pm 0.03)$ eV and $\nu = 10^7$ s⁻¹ [12]. Cleavage of methylene hydrogens bridge-bonded to the surface, the respective C–H bonds weakened by the metal–H interaction, has been invoked in both cases [7].

The dehydrogenation of C₂H₄ to C₂H₂ on Ni(111) was most recently analyzed by scanned-energy-mode PD [14], whereby the local adsorption geometries of the reactant and product molecules were determined. The PD study found the C–C axis essentially parallel to the surface for both molecules, but aligned along the two different principal

azimuths, while LEED results predicted C_2H_2 to be rotated by $\phi_C \sim 10^\circ$ with respect to the $[\bar{1}\bar{1}2]$ lattice direction [10]. The change in hydrocarbon adsorption site eliminates all but two possible pathways for a concerted reaction mechanism: either a 90° -rotation of the C–C axis or a 30° -rotation with a concomitant translation, accompanied in both scenarios by $\Delta r(C-C) \sim 0.15 \text{ \AA}$ and $\Delta z(C) \sim 0.50 \text{ \AA}$ upon dehydrogenation.

3. Thermal Evolution of C_2H_2 on Ni(111)

Acetylene on Ni(111) fragments, upon completion of a (2×2) overlayer [36] or warming to $T > 400 \text{ K}$ [28], to methylidyne ($\equiv CH$), as observed by UPS and HREELS, respectively; at $T > 450 \text{ K}$, the CH converts to a CH_2 -containing species [45], while above 500 K , only surface C remains [28]. A subsequent, time-dependent HREELS study [43] detected both CH and ethynyl or acetylide ($-C \equiv CH$) after flashing a high exposure and hence saturation coverage of a room-temperature C_2H_4 sample, with the following measured kinetic parameters for the respective dehydrogenation reactions: $E_a(CH) = (12 \pm 3) \text{ kcal/mol}$, *i.e.*, $(0.52 \pm 0.13) \text{ eV}$; $E_a(CCH) = (8 \pm 3) \text{ kcal/mol}$, *i.e.*, $(0.35 \pm 0.13) \text{ eV}$; and $\nu = 10^{3 \pm 1} \text{ s}^{-1}$ for both the slow and fast, CH and CCH, respectively, dissociation processes, assumed to be first-order. The decomposition of C_2H_2 exhibits a strong coverage dependence, as observed by TPSSIMS, TPD, and AES [40]: at low coverages, both CCH and CH result from the respective C–H and C–C bond cleavages, while at high coverages, ethylidyne ($\equiv C-CH_3$) is formed additionally.

The time-resolved HREELS study by Hammer *et al.* [11] described both the second dehydrogenation step of C_2H_4 and the fragmentation of a submonolayer coverage ($\Theta = 0.25$) of directly adsorbed C_2H_2 , with eventual nickel carbide formation, by second-order Langmuir kinetics, with $E_a = (1.36 \pm 0.06)$ eV and $\nu = 10^{17 \pm 2}$ s⁻¹, while a later analysis from the same group deduced, for coverages of $\Theta < 0.25$, a first-order process, with $E_a = (1.20 \pm 0.01)$ eV and $\nu = 10^{14 \pm 1}$ s⁻¹ [44].

b. C_2H_4 and C_2H_2 on Pt(111)

The low-temperature ($T \sim 140 - 260$ K), non-dissociatively adsorbed species of C_2H_4 on Pt(111) bonds, as on Ni(111), via a di- σ configuration, indicative of $\sim sp^3$ hybridization, with local C_{2v} symmetry [46], which distorts to lower symmetry at higher coverages [29] and orders to a (2×2) LEED pattern upon electron beam exposure [47]. Structural parameters deduced for this phase include: $r(C-C) = 1.52$ Å, $\theta_{CCH} = 110^\circ$, and $\theta_{HCH} = 108^\circ$, from UPS [32]; $r(C-C) = 1.49$ Å, $\theta_{CCH} = 114^\circ$, and $\theta_{HCH} = 112^\circ$, from UPS and EELS [30]; and $z(C) \sim 2.0$ Å, with the C-C axis parallel to the surface, from NEXAFS [48]. Conversely, the low-temperature ($T \sim 150 - 300$ K) C_2H_2 species adsorbs, according to HREELS results, via a di- σ/π bonding configuration [49] to three metal atoms, with C_s symmetry, $\sim sp^2$ hybridization, a bond order of ~ 1.4 , $r(C-C) \sim 1.45$ Å, $\theta_{CCH} \sim 120^\circ$ [46], and from a dynamical LEED analysis, with the C-C axis parallel to the surface at a height of $z(C) = (2.45 \pm 0.10)$ Å, though the atop site was deduced [50]. This contrasts with the UPS conclusions of Demuth, who reported $r(C-C) \sim 1.34 - 1.39$ Å and $\theta_{CCH} = 122 - 132^\circ$ [32], as well as the

UPS/EELS results of Felter and Weinberg, $r(\text{C}-\text{C}) \sim 1.35 \text{ \AA}$ and $\theta_{\text{CCH}} \sim 120^\circ$ [30]. At $T = 300 \text{ K}$, $\text{Pt}(111)/\text{C}_2\text{H}_2$ gives a well-ordered (2×2) LEED pattern at low coverages [51,52].

Both molecules, C_2H_4 at room temperature and C_2H_2 at $T = 350 - 400 \text{ K}$ and in the presence of H, undergo a chemical and structural transformation to the ethylidyne complex ($\equiv\text{C}-\text{CH}_3$) [53], as characterized by LEED [54,47], UPS [55,56], HREELS and TPD [57], SIMS [58], NEXAFS [48], and STM [59]. The ethylidyne species bonds in a fcc threefold hollow site with its molecular axis oriented perpendicular to the surface, hence possessing C_{3v} symmetry [53], with $r(\text{C}-\text{C}) = 1.49 \text{ \AA}$, corresponding to near- sp^3 hybridization, and a Pt-C distance of $d(\text{Pt}-\text{C}) = 1.91 \text{ \AA}$ [60]. The decomposition kinetics of C_2H_4 and CCH_3 on $\text{Pt}(111)$ were investigated using SSIMS, TPSSIMS, and TPD, yielding the following kinetic parameters for the assumed first-order processes: $E_a = 17 \pm 1 \text{ kcal/mol}$ ($0.74 \pm 0.04 \text{ eV}$) and $\nu = 1 \times 10^{12 \pm 1} \text{ s}^{-1}$ for CCH_3 formation; and $E_a = 27 \pm 2 \text{ kcal/mol}$ ($1.17 \pm 0.08 \text{ eV}$) and $\nu = 6 \times 10^{11 \pm 1} \text{ s}^{-1}$ for CCH_3 decomposition [61]. A recent temperature-programmed reaction spectroscopy (TPRS) study found normal kinetic isotope effects and tunnelling to be unimportant in the first-order C-H bond activation of C_2H_4 and CCH_3 , with $E_a = 22.4 \pm 0.6 \text{ kcal/mol}$ ($0.97 \pm 0.03 \text{ eV}$) and $\nu = (3.1 \pm 2.5) \times 10^{16} \text{ s}^{-1}$ for CCH_3 formation; and $E_a = 37.3 \pm 1.7 \text{ kcal/mol}$ ($1.17 \pm 0.07 \text{ eV}$) and $\nu = (2.9 \pm 2.6) \times 10^{16} \text{ s}^{-1}$ for CCH_3 decomposition [62].

c. C_2H_4 and C_2H_2 on Pd(111)

The adsorption and thermal evolution of ethylene and acetylene on Pd(111) have been extensively studied by Gates and Kesmodel, primarily with angle-dependent EELS. EELS spectra of the low-temperature ($T = 150$ K) disordered phase of ethylene on Pd(111) [63] were interpreted in terms of a weakly bound π -complex (*cf.* di- σ complex on the (111) faces of Ni and Pt), with C_s (or higher) symmetry, in the threefold bridging/atop or μ/π site, the tilted C–C axis with respect to the surface leading to a direct electronic metal–H interaction, as on Ni(111) [8]. As on Pt(111), strongly distorted C_2H_4 and C_2H_2 species were predicted from UPS data [32], with the following structural parameters: $r(C-C) \sim 1.47$ Å, $\theta_{CCH} = 112^\circ$, and $\theta_{HCH} = 108^\circ$ for C_2H_4 ; and $r(C-C) \sim 1.34 - 1.39$ Å and $\theta_{CCH} = 122 - 132^\circ$ for C_2H_2 . Angle-dependent EELS and LEED measurements at $T = 150$ K showed acetylene chemisorbed on Pd(111) to be strongly rehybridized ($\sim sp^{2.5}$), with an estimated $r(C-C) = (1.42 \pm 0.03)$ Å, and having either C_s or C_2 symmetry [64]. The C_2H_2 bonding geometry proposed for the observed $(\sqrt{3} \times \sqrt{3})R30^\circ$ LEED structure is a planar, *cis*-bent, di- σ/π -bonded species in the threefold triangular (Δ) site, with its bond axis parallel to the surface and molecular plane slightly tilted relative to the surface normal. At room temperature, both ethylene [65] and acetylene [65], the latter in the presence of residual surface hydrogen and via a postulated vinylidene ($=C=CH_2$) intermediate, decompose on Pd(111) to ethynidyne bonded in the threefold Δ site and oriented perpendicular to the surface, as on Pt(111) [53]. Acetylene evolves thermally at $T \sim 400$ K to ethynyl ($-C \equiv CH$) [66],

previously characterized as CH formation from C–C bond scission of acetylene [65], while acetylene hydrogenation to ethylene [67,68] and cyclotrimerization to benzene [67,68,69] have also been observed.

d. C_2H_4 and C_2H_2 on Ni(100)

The non-dissociatively adsorbed species of ethylene on Ni(100) has been proposed to be H-bonded and tilted with respect to the surface, based on HREELS results [70], with possible twisting of the molecule about the C–C bond axis, from ARUPS data [71], and oriented with the molecular axis parallel to, and the molecular plane tilted 50° from the surface, with $r(C-C) = 1.46 \text{ \AA}$, as concluded from a NEXAFS study [72]. Conversely, a TPD, HREELS, and time-resolved laser-induced desorption (LID) analysis [13] deduced the low-temperature ($T \leq 150 \text{ K}$) complex to be π -bonded with little rehybridization, which corroborates the weakly distorted geometry proposed from UPS data [32]: $r(C-C) \sim 1.39 \text{ \AA}$, $\theta_{CCH} = 114^\circ$, and $\theta_{HCH} = 117^\circ$. For coverages below 0.4 ML, C_2H_4 undergoes unimolecular, stepwise dehydrogenation at $T = 170 \text{ K}$ to vinyl ($-CH=CH_2$) and H, exhibiting a strong kinetic isotope effect, with a first-order rate constant of $r = (8.0 \pm 2.0) \times 10^{-2} \text{ s}^{-1}$, pre-exponential factor of $\nu = 10^{(9.8 \pm 0.5)} \text{ s}^{-1}$, and activation energy of $E_a = (8.4 \pm 0.4) \text{ kcal mol}^{-1}$, *i.e.*, $(0.36 \pm 0.02) \text{ eV}$, (*cf.* $E_a = (0.30/0.31 \pm 0.02) \text{ eV}$ and $\nu = 10^{6 \pm 2} \text{ s}^{-1}$ for Ni(111)); above half-saturation coverages, the desorption and decomposition rates are competitive [13]. Both the acetylenic

fragment formed at $T = 230$ K as a decomposition product of the CHCH_2 intermediate [73] and the molecularly chemisorbed, sp^3 -hybridized acetylene species at $T = 90$ K dehydrogenate to CCH at $T \sim 325$ K and yield C residues above 400 K [73], in discord with an early UPS/TPD finding of a CH species at room temperature [74]. Angle-dependent EELS measurements determined the low-temperature acetylene species to be di- σ /di- π -bonded with $sp^{2.6}$ hybridization, in a *cis*-distorted arrangement possessing C_s symmetry, with its molecular plane tilted with respect to the surface and mirror plane aligned along the $\langle 110 \rangle$ set of directions [75]. Weak structural distortions were determined from UPS [32]: $r(\text{C}-\text{C}) \sim 1.30 - 1.36$ Å and $\theta_{\text{CCH}} = 130 - 140^\circ$. At saturation coverages for $T = 80 - 370$ K, both C_2H_4 and C_2H_2 exhibit $c(2 \times 2)$ LEED patterns, which convert, either upon prolonged exposures or at elevated temperatures, to $p(2 \times 2)$ structures, indicating the formation of carbonaceous overlayers [76,71].

e. C_2H_4 and C_2H_2 on Ni(110)

Molecular adsorption and thermal evolution of ethylene and acetylene on Ni(110) have also been intensively investigated. On- and off-specular EELS spectra of C_2H_4 at $T = 110$ K were interpreted in terms of a di- σ -bonded species with its molecular axis parallel to the surface [77], later corroborated by HREELS, LEED, and TPD data, which also suggested that C_2H_4 adsorbed at $T = 80$ K is $\sim sp^3$ -hybridized, with a site symmetry lower than C_{2v} , [78]. Contrarily, the UPS results of Demuth [32] predict a weakly distorted species: $r(\text{C}-\text{C}) \sim 1.39$ Å, $\theta_{\text{CCH}} = 120^\circ$, and $\theta_{\text{HCH}} = 117 - 120^\circ$.

A recent ARUPS, TPD, LEED, and linear combination of Gaussian-type orbitals local-density functional (LCGTO-LDF) cluster-model study of a dilute C_2H_4 layer [79] also favoured, from calculated binding energies, the π -bonding configuration, with the molecular plane parallel to the surface and C–C axis preferentially aligned along the $[1\bar{1}0]$ azimuth, *i.e.*, along the top-layer rows; the deduced C_1 adsorption-complex symmetry implies either imperfect azimuthal alignment or slight twisting of the molecule in a low-symmetry adsorption site. At saturation coverages, the C_2H_4 's of neighbouring rows are displaced by half a lattice vector along the $[1\bar{1}0]$ direction, with the two-dimensional band structure dominated by interadsorbate interactions, as revealed by a subsequent LEED, ARUPS, NEXAFS, and extended-Hückel analysis [80]. The low-temperature ($T = 110 - 120$ K) C_2H_2 species is proposed, from EELS results, to be between sp^2 - to sp^3 -hybridized and di- σ/π -bonded to three metal centres [81], with its C–C axis either tilted or parallel to the surface in a *cis*- or *trans*-bent molecular configuration [78]; in contrast, the bonding model stemming from an UPS/TPD analysis [74] has the molecular axis oriented along the $[001]$ azimuth in a twofold aligned bridging site. The UPS results of Demuth [32] suggest weak distortions: $r(C-C) \sim 1.27 - 1.32$ Å and $\theta_{CCH} = 145 - 150^\circ$. Upon heating to $T > 200$ K, C_2H_4 , characterized by a complex $c(2 \times 4)$ LEED pattern at saturation, decomposes to CCH intermediates, which further dissociate to CH and atomic C below half-saturation coverages, while molecular desorption predominates above; C_2H_2 exhibits a $c(2 \times 2)$ LEED pattern and complex decomposition [78] to form CCH, CH_2 , and CH species [74].

B. Theoretical

1. Methodologies

While varying levels of sophistication exist in the quantum theory of electronic structure, for practical problems, a compromise between the theoretical accuracy and a realistic model description of the system dictates the applicable theoretical method. One-electron, semiempirical, molecular-orbital methods, such as the Hückel, extended-Hückel, and related atom-superposition and electron-delocalization theories, invoke only valence electrons in their descriptions of chemical bonding, neglect interelectronic repulsions, and introduce empirical parameters. Contrastingly, within the density-functional framework, systems of interacting particles are treated, in principle, exactly, offering a parameter-free computational scheme for both simple and extended systems, otherwise perhaps inaccessible by conventional *ab initio* methods. A common thread of both the Hückel and density-functional approaches is the electron density, which permits the Hückel theory to be formulated as an approximate density-functional theory [82].

a. Semiempirical Methods

1. Hückel and Extended-Hückel (EH) Molecular-Orbital (MO) Theories [83]

The Hückel theory for planar, unsaturated hydrocarbons, particularly conjugated and

aromatic systems, makes two fundamental assumptions: neglect of electron correlation in a one-electron approximation; and σ - π separability, translating into the π -electron approximation, which assumes inactivity of the σ orbitals. The σ electrons are described in terms of localized, hybrid bond orbitals and the π electrons, by molecular wave functions extending over each of the atoms donating a π electron. The delocalized π electrons move in the fixed, electrostatic, effective potential set up by the σ molecular framework. They satisfy

$$\hat{H}_\pi \Psi_\pi = E_\pi \Psi_\pi , \quad (2.9)$$

with

$$\hat{H}_\pi = \sum_{i=1}^{n_\pi} \hat{H}^{eff}(i) \quad (2.10)$$

and

$$\Psi_\pi = \prod_{i=1}^{n_\pi} \psi_i , \quad (2.11)$$

which yield the n_π one-electron Schrödinger equations:

$$\hat{H}^{eff}(i) \psi_i = \epsilon_i \psi_i , \quad i = 1, \dots, n_\pi , \quad (2.12)$$

where n_π is the number of π electrons and

$$\psi_i = \sum_j c_{ji} \phi_j \quad (2.13)$$

is the i^{th} π -electron molecular orbital (MO), written as a linear combination of atomic orbitals (LCAO), ϕ_j , of π symmetry and localized on atom j with coefficient c_{ji} . The

linear variational problem defined by eqns. (2.17) and (2.13):

$$\sum_j c_j (H_{jk}^{eff} - S_{jk} \epsilon_i) = 0 , \quad (2.14)$$

yields the $(n_\pi \times n_\pi)$ secular determinantal equation:

$$|H_{jk}^{eff} - S_{jk} \epsilon_i| = 0 , \quad (2.15)$$

the solution of which amounts to evaluating the integrals H_{jk}^{eff} and S_{jk} . The assumed orthonormality of the ϕ_j 's translates into the following expression for the overlap integral:

$$S_{jk} = \langle \phi_j | \phi_k \rangle = \delta_{jk} ; \quad (2.16)$$

i.e., overlap between orbitals centred on different atoms is ignored, since for $j \neq k$, $S_{jk} = 0$, and for $j = k$, $S_{jk} = 1$. The integrals involving the effective Hamiltonian yield, on a given atom j , the Coulomb integrals:

$$H_{jj}^{eff} = \langle \phi_j | \hat{H}_{eff} | \phi_j \rangle = \alpha_j , \quad (2.17)$$

where α_j is an empirical constant; while over two different atoms j and k , the two-centre resonance or exchange integrals result:

$$H_{jk}^{eff} = \langle \phi_j | \hat{H}_{eff} | \phi_k \rangle = \beta_{jk} , \quad (2.18)$$

where β_{jk} is a negative parameter related to the overlap between orbitals ϕ_j and ϕ_k for neighbouring atoms, and is zero otherwise. The total energy of the π electrons is set equal to the sum of their one-electron orbital energies, ϵ_i :

$$E_\pi = \sum_i \epsilon_i . \quad (2.19)$$

In the extended-Hückel (EH) treatment [84] of planar and nonplanar molecules, all valence electrons, including those of σ symmetry, are incorporated into a one-electron theory applicable to both saturated and unsaturated, organic and inorganic compounds. It invokes the valence-electron approximation, which treats valence and core electrons separately, and neglects interelectronic and internuclear repulsions to write the valence-electron Hamiltonian as the sum of effective one-electron Hamiltonians:

$$\hat{H}_{val} = \sum_{i=1}^{n_{val}} \hat{H}^{eff}(i) . \quad (2.20)$$

A series of one-electron Schrödinger equations analogous to eqn. (2.12) ensues, but with i running from 1 to n_{val} , the number of valence electrons, the MO's being again approximated as LCAO's as in eqn. (2.13), where j now spans all the fixed-orbital-exponent Slater-type orbitals (STO's) in the basis set of valence atomic orbitals. The resulting linear variational problem and $(n_{val} \times n_{val})$ secular equation are in accordance with eqns. (2.14) and (2.15). The diagonal matrix elements, H_{jj}^{aa} , are equated to the negative of the corresponding experimental valence-state ionization potential, VSIP, of the j^{th} valence level on atom a , while the off-diagonal elements on atom a are zero by orthogonality of the valence-orbital basis states:

$$H_{jk}^{aa} = -\delta_{jk} (VSIP)_j^a . \quad (2.21)$$

The off-diagonal Hamiltonian matrix elements on different atoms a and b , H_{jk}^{ab} , are given by the Wolfsberg-Helmholz formula [85]:

$$H_{jk}^{ab} = K \times \left[\frac{H_{jj}^{aa} + H_{kk}^{bb}}{2} \right] S_{jk}^{ab} , \quad (2.22)$$

with the constant K set equal to 1.75 and where the overlap integral:

$$S_{jk}^{ab} = \langle \phi_j^a | \phi_k^b \rangle \quad (2.23)$$

between the j^{th} atomic orbital on atom a and the k^{th} orbital on atom b is explicitly calculated, in contrast with eqn. (2.16) of simple Hückel theory. Thus, within the EH formalism, the total valence-electron energy is the sum of the occupied MO energies:

$$E_{\text{val}} = \sum_i \epsilon_i , \quad (2.24)$$

obtained by diagonalizing the Hamiltonian,

$$\hat{H}^{\text{eff}}(i) = \sum_{j,a} H_{jj}^{aa} | \phi_j^a \rangle \langle \phi_j^a | + \sum_{a \neq b, j \neq k} H_{jk}^{ab} | \phi_j^a \rangle \langle \phi_k^b | . \quad (2.25)$$

The method, yielding reasonably good equilibrium bond angles and angular deformation energies, has its prime utility in qualitative conformational studies, while the poorly predicted bond lengths invalidate its potential surfaces for stretching motions [84,86].

2. Atom-Superposition and Electron-Delocalization Molecular-Orbital (ASED-MO) Theory

The atom-superposition and electron-delocalization molecular-orbital (ASED-MO) method [87,88] approximates the total molecular energy as the sum of a two-body

atomic repulsive term and a modified extended-Hückel configurational energy. The exact electronic charge-density distribution of a molecule or solid, ρ , is partitioned into the sum of spherical, atomic, perfectly-following (*pf*) charge densities, ρ_a , centred on the N nuclei a , and a non-spherical, non-perfectly-following (*npf*) contribution, ρ_{npf} , due to charge redistribution [89], with the formalism of Refs. [87,89] generalized as follows:

$$\rho(r, \mathbf{R}^N) = \sum_a^N \rho_a(r - \mathbf{R}_a) + \rho_{npf}(r, \mathbf{R}^N) , \quad (2.26)$$

where r and \mathbf{R} are electronic and nuclear coordinates with respect to an arbitrary origin and $\mathbf{R}^N = (\mathbf{R}_a, \mathbf{R}_b, \dots)$. Integration of the sum of the Hellmann-Feynman electrostatic forces [90,91] on any nucleus a due to the other nuclei b and the delocalized electrons:

$$\mathbf{F}_a(\mathbf{R}^N) = \sum_{b \neq a}^N \mathbf{F}_{ab}(\mathbf{R}_a, \mathbf{R}_b, \rho_a, Z_a, Z_b) + \mathbf{F}_a(\mathbf{R}_a, \rho_{npf}) , \quad (2.27)$$

yields the total molecular energy as the sum, E_R , of pairwise atomic repulsion energies and an attractive electron-delocalization energy from the *npf* charge density, E_{npf} [92]:

$$E(\mathbf{R}^N) = E_R(\mathbf{R}^N) + E_{npf}(\mathbf{R}^N) . \quad (2.28)$$

The repulsive component, E_R , arising from the superposition of N rigid atoms into a molecular configuration, is the sum of the two-body, electrostatic interaction energies, E_{ab} , between any nucleus a and both the nucleus and *pf* electronic charge density of each of the other fixed, neutral atoms b , taken as the more electronegative of the pair:

$$E_R(\mathbf{R}^N) = \sum_a^N \sum_{b \neq a}^N E_{ab}(\mathbf{R}_a, \mathbf{R}_b) = \sum_a^N \sum_{b \neq a}^N \frac{Z_a}{2} \left[\frac{Z_b}{|\mathbf{R}_b - \mathbf{R}_a|} - \int \frac{\rho_b(\mathbf{r})}{|\mathbf{r} - \mathbf{R}_a|} d\mathbf{r} \right], \quad (2.29)$$

where $\rho_b(\mathbf{r})$ is the electronic charge density on atom b and Z_a and Z_b are the atomic numbers of a and b . The atomic charge densities, and hence E_R , are easily derived from AO wave functions. Conversely, the total attractive electrostatic energy between the nuclei and the npf component of the electronic charge density after bond formation:

$$E_{npf}(\mathbf{R}^N) = - \int_{\infty}^{|\mathbf{R}_a|} \dots \int_{\infty}^{|\mathbf{R}_N|} \sum_a^N \frac{d}{d\mathbf{R}_a'} \frac{Z_a}{|\mathbf{r} - \mathbf{R}_a'|} \rho_{npf}(\mathbf{r}, \mathbf{R}'^N) d\mathbf{r} d\mathbf{R}'^N, \quad (2.30)$$

requires knowledge of the \mathbf{R} -dependence of ρ_{npf} , which is only attainable from exact quantum mechanical calculations. Instead, E_{npf} is approximated as the sum of one-electron energies obtained by solving an EH-like Hamiltonian, with the modified off-diagonal matrix elements:

$$H_{jk}^{ab} = 2.25 \times \frac{1}{2} (H_j^{aa} + H_k^{bb}) S_{jk}^{ab} e^{-0.13R_{ab}}, \quad (2.31)$$

where R_{ab} is the internuclear distance between atoms a and b . Thus, the total molecular energy within the ASED-MO method is given by

$$E = E_R + E_{npf} \simeq E_R + \text{modified extended-Hückel energy}, \quad (2.32)$$

whereby molecular electronic properties, structures, vibrational force constants, relative binding energies, as well as reaction energies and pathways, can be estimated from empirical atomic data.

b. Density-Functional Theory (DFT) [93,94]

1. Hohenberg-Kohn (HK) Formulation

Density-functional theory (DFT), the exact theoretical treatment of an interacting inhomogeneous many-electron system in terms of the electron density distribution, was formulated by Hohenberg and Kohn (HK) [95]. The first of two HK theorems sanctions using, as the basic variable, the ground-state electron number density, which, in terms of the N -electron ground-state wave function, $\Psi(\mathbf{x}_1, \dots, \mathbf{x}_N)$, is

$$\rho(\mathbf{r}) = N \int \dots \int |\Psi(\mathbf{x}_1, \mathbf{x}_2, \dots, \mathbf{x}_N)|^2 ds dx_2 \dots dx_N , \quad (2.33)$$

where the \mathbf{x}_i denote both spin, s_i , and spatial, \mathbf{r}_i , electronic coordinates. Based on the minimum-energy principle for the ground state, it proves that the external potential $v(\mathbf{r})$ is determined, to within a trivial additive constant, by $\rho(\mathbf{r})$, and conversely. Since $v(\mathbf{r})$ completely fixes the Hamiltonian for an N -electron system and $\rho(\mathbf{r})$ integrates to N , *i.e.*,

$$N = N[\rho(\mathbf{r})] = \int \rho(\mathbf{r}) d\mathbf{r} , \quad (2.34)$$

ρ uniquely determines, as N and v do in conventional wave-function theory, all the ground-state electronic properties of the system, including Ψ and the energy, E . Thus, the total energy can be written as a functional of $\rho(\mathbf{r})$:

$$E_v[\rho] = T[\rho] + V_{ee}[\rho] + V_{ne}[\rho] = F_{HK}[\rho] + \int v(\mathbf{r})\rho(\mathbf{r})d\mathbf{r} , \quad (2.35)$$

where $T[\rho]$, $V_{ee}[\rho]$, and $V_{ne}[\rho] = \int v(\mathbf{r})\rho(\mathbf{r})d\mathbf{r}$ are the electronic kinetic, electron-electron repulsive, and nuclear-electron attractive energies, respectively, and $F_{HK}[\rho]$ is

a universal functional of $\rho(r)$, defined as

$$F_{HK}[\rho] \equiv T[\rho] + V_{ee}[\rho] = T[\rho] + J[\rho] + \text{nonclassical term} , \quad (2.36)$$

with $J[\rho]$ the classical electrostatic component of $V_{ee}[\rho]$, the nonclassical term being dominated by the exchange-correlation energy.

The second HK theorem, the DFT energy-variational principle, states that, for a trial density $\rho'(r)$, where $\rho'(r) \geq 0$ and $\int \rho'(r) dr = N$, the ground-state energy, E , satisfies

$$E \leq E_v[\rho'] , \quad (2.37)$$

where $E_v[\rho']$ is the energy functional of eqn. (2.35); this contrasts with the variational principle of wave mechanics, expressed in terms of $\Psi(x_1, \dots, x_N)$. With the assumed differentiability of $E_v[\rho]$, eqn.(2.37) requires that ρ satisfy the stationary principle,

$$\delta\{E_v[\rho] - \mu[\int \rho(r) dr - N]\} = 0 , \quad (2.38)$$

which gives the Euler-Lagrange equation:

$$\mu = \frac{\delta E_v[\rho]}{\delta \rho(r)} = v(r) + \frac{\delta F_{HK}[\rho]}{\delta \rho(r)} , \quad (2.39)$$

where the Lagrangian multiplier, μ , is the chemical potential. Eqn. (2.39), the basic working equation of DFT, can be solved, together with the constraint of constant N , eqn. (2.34), and the resulting ρ inserted into eqn. (2.35) to yield the total energy, $E_v[\rho]$.

By definition, a v -representable electron density is associated with the antisymmetric Ψ of a Hamiltonian of the form,

$$\hat{H} = \sum_{i=1}^N \left(-\frac{1}{2} \nabla_i^2\right) + \sum_{i=1}^N v(r_i) + \sum_{i < j}^N \frac{1}{r_{ij}} , \quad (2.40)$$

with some scalar external potential $v(r_i)$. The first HK theorem may then be restated: v -representable ρ 's map uniquely to Ψ 's; while the second HK theorem asserts that, for all trial v -representable densities, $\rho'(r)$,

$$E_v[\rho'] \equiv F_{HK}[\rho'] + \int v(r)\rho'(r)dr \geq E_v[\rho] . \quad (2.41)$$

Alternatively, an N -representable ρ is obtainable from some antisymmetric Ψ , which requires nonnegative, normalized, and continuous densities, *i.e.*,

$$\rho(r) \geq 0 , \quad \int \rho(r)dr = N , \quad \text{and} \quad \int |\nabla\rho^{1/2}(r)|^2 dr < \infty ; \quad (2.42)$$

any such ρ 's can be decomposed uniquely into N orthonormal orbitals [96]. DFT can be reformulated requiring the trial densities, in functionals and variational principle, to satisfy the N -, instead of the original, stronger v -representability condition.

2. Kohn-Sham (KS) Method

The method of Kohn and Sham (KS) [97] invokes a non-interacting quasi-particle reference system, with Hamiltonian,

$$\hat{H}_s = \sum_i^N \left(-\frac{1}{2} \nabla_i^2 \right) + \sum_i^N v_s(r) , \quad (2.43)$$

for which the ground-state electron density is exactly

$$\rho(r) = \sum_i^N \sum_s |\psi_i(r, s)|^2 , \quad (2.44)$$

and the ground-state wave function is the Slater determinant,

$$\Psi_s = \frac{1}{\sqrt{N!}} \det[\psi_1 \cdots \psi_N] , \quad (2.45)$$

where ψ_i are the N lowest eigenstates or orbitals of the one-electron Hamiltonian, *i.e.*,

$$\hat{h}_s \psi_i = \left[-\frac{1}{2} \nabla^2 + v_s(r) \right] \psi_i = \epsilon_i \psi_i . \quad (2.46)$$

The resulting N Kohn-Sham orbital equations treat the dominant part of the true kinetic energy indirectly but exactly by defining

$$T_s[\rho] = \langle \Psi_s | \sum_i^N \left(-\frac{1}{2} \nabla_i^2 \right) | \Psi_s \rangle = \sum_{i=1}^N \langle \psi_i | -\frac{1}{2} \nabla^2 | \psi_i \rangle , \quad (2.47)$$

leaving a small residual correction to be handled separately. They have the same single-particle form as the Hartree equations, but, in principle, incorporate exactly the electron exchange-correlation effects absent in both the Hartree and Hartree-Fock (HF) equations.

To achieve the desired partitioning of the kinetic-energy functional, $T[\rho]$, with $T_s[\rho]$ as the kinetic-energy component, the universal functional of eqn. (2.36) is rewritten as

$$F[\rho] = T[\rho] + V_{ee}[\rho] = T_s[\rho] + J[\rho] + E_{xc}[\rho] , \quad (2.48)$$

where

$$E_{xc}[\rho] \equiv T[\rho] - T_s[\rho] + V_{ee}[\rho] - J[\rho] \quad (2.49)$$

is the exchange-correlation energy, *i.e.*, the residual correction to $T[\rho]$ plus the nonclassical part of $V_{ee}[\rho]$. The corresponding Euler eqn. becomes

$$\mu = \frac{\delta E[\rho]}{\delta \rho(r)} = v_{eff}(r) + \frac{\delta T_s[\rho]}{\delta \rho(r)} , \quad (2.50)$$

where the local KS effective potential is defined by

$$\begin{aligned} v_{\text{eff}}(\mathbf{r}) &= v_s(\mathbf{r}) = v(\mathbf{r}) + \frac{\delta J[\rho]}{\delta \rho(\mathbf{r})} + \frac{\delta E_{xc}[\rho]}{\delta \rho(\mathbf{r})} \\ &= v(\mathbf{r}) + \int \frac{\rho(\mathbf{r}')}{|\mathbf{r} - \mathbf{r}'|} d\mathbf{r}' + v_{xc}(\mathbf{r}), \end{aligned} \quad (2.51)$$

with the exchange-correlation potential,

$$v_{xc}(\mathbf{r}) = \frac{\delta E_{xc}[\rho]}{\delta \rho(\mathbf{r})}. \quad (2.52)$$

For a given $v_{\text{eff}}(\mathbf{r})$, the density is obtained by solving the N KS orbital eqns.:

$$\left[-\frac{1}{2}\nabla^2 + v_{\text{eff}}(\mathbf{r})\right]\psi_i = \epsilon_i \psi_i, \quad (2.53)$$

and setting the electron density as in eqn. (2.44). Self-consistent solution of the KS equations, eqns. (2.44) and (2.51) - (2.53), begins with a guessed $\rho(\mathbf{r})$, whereby $v_{\text{eff}}(\mathbf{r})$ is constructed via eqn. (2.51), and a new $\rho(\mathbf{r})$ is computed from eqns. (2.53) and (2.44); the procedure is continued iteratively towards self-consistency. The total energy may then be determined from the energy functional, rewritten in terms of the N KS orbitals:

$$\begin{aligned} E[\rho] &= T_s[\rho] + J[\rho] + E_{xc}[\rho] + \int v(\mathbf{r})\rho(\mathbf{r})d\mathbf{r} \\ &= \sum_i^N \sum_s \int \psi_i^*(\mathbf{r})\left(-\frac{1}{2}\nabla^2\right)\psi_i(\mathbf{r})d\mathbf{r} + J[\rho] + E_{xc}[\rho] + \int v(\mathbf{r})\rho(\mathbf{r})d\mathbf{r}. \end{aligned} \quad (2.54)$$

Specification of the KS equations requires an explicit form for $E_{xc}[\rho]$, the simplest being the local-density approximation (LDA) for the exchange and correlation energy,

$$E_{xc}^{LDA}[\rho] = \int \epsilon_{xc}(\rho)\rho(\mathbf{r})d\mathbf{r}, \quad (2.55)$$

where $\epsilon_{xc}(\rho)$ is the exchange and correlation energy per particle of a uniform electron gas of density ρ . The corresponding exchange-correlation potential becomes

$$v_{xc}^{LDA}(\mathbf{r}) = \frac{\delta E_{xc}^{LDA}}{\delta \rho(\mathbf{r})} = \epsilon_{xc}(\rho(\mathbf{r})) + \rho(\mathbf{r}) \frac{\delta \epsilon_{xc}(\rho)}{\delta \rho} \quad (2.56)$$

and the KS orbital equations read

$$\left[-\frac{1}{2} \nabla^2 + v(\mathbf{r}) + \int \frac{\rho(\mathbf{r}')}{|\mathbf{r} - \mathbf{r}'|} d\mathbf{r}' + v_{xc}^{LDA}(\mathbf{r}) \right] \psi_i = \epsilon_i \psi_i . \quad (2.57)$$

Self-consistent solution of eqn. (2.57) constitutes the KS LDA, which extracts $E_{xc}[\rho]$ for a nonuniform system from the uniform spin-compensated electron gas result of $\epsilon_{xc}(\rho)$ applied to infinitesimal portions, each having $\rho(\mathbf{r})d\mathbf{r}$ electrons, of the inhomogeneous electron distribution, with the individual contributions, $\epsilon_{xc}(\rho)\rho(\mathbf{r})d\mathbf{r}$, summed over all space. The function $\epsilon_{xc}(\rho)$ can be partitioned into exchange and correlation contributions:

$$\epsilon_{xc}(\rho) = \epsilon_x(\rho) + \epsilon_c(\rho) ; \quad (2.58)$$

the exchange part, $\epsilon_x(\rho)$, is given by the Dirac exchange-energy functional:

$$\epsilon_x(\rho) = -C_x \rho(\mathbf{r})^{1/3} , \quad C_x = \frac{3}{4} \left[\frac{3}{\pi} \right]^{1/3} = 0.7386 , \quad (2.59)$$

while the most accurate analytic form available for the uniform-gas correlation energy per particle, $\epsilon_c(\rho)$, comes from interpolations by Vosko, Wilk, and Nusair [98] of the quantum Monte Carlo calculations of Ceperley and Alder [99] to yield the VWN local functional. Note that the X_α or Hartree-Fock-Slater (HFS) method proposed by Slater [100] corresponds to the LDA with correlation neglected and $\alpha = 2/3$, which was unity in Slater's original formulation and subsequently often an adjustable parameter.

Beyond the LDA, nonlocal (NL) or gradient corrections to the exchange functional proposed by Perdew and Wang [101] or Becke [102] are typically used together with Perdew's NL correlation functional [103]. While the KS orbital equations formally incorporate many-body effects, their exact solution reflects only the accuracy of the inherently approximate, exchange-correlation and corresponding energy functionals.

Spin-density-functional theory generalizes DFT to include the electronic spin degrees of freedom by permitting spin dependence in $v_{eff}(r)$, in analogy to the unrestricted HF method. The basic variables become the α - and β -electron densities, $\rho^\alpha(r)$ and $\rho^\beta(r)$, or equivalently, the total electron density, $\rho(r)$, and the electron spin density, $Q(r) = \rho^\alpha(r) - \rho^\beta(r)$. The local-spin-density approximation (LSDA) incorporates this dual-spin resolution of the density in a more accurate $E_{xc}[\rho]$, the exchange-correlation energy of the homogeneous spin-polarized electron gas, $E_{xc}^{LSDA}[\rho^\alpha, \rho^\beta]$.

2. Related Work

a. C₂H₄ and C₂H₂ on Ni(111)

1. Semiempirical Methods

Theoretical investigations of C₂H₄ and C₂H₂ adsorption and reactivity on Ni(111) have utilized primarily the semiempirical ASED- and EH-MO cluster approaches to chemisorption and surface catalysis. In the pioneering ASED-MO study by Anderson

[104], both C_2H_4 and C_2H_2 preferred the di- σ bridging position on two- and thirteen-atom ($n = 2$ and 13), the latter being two-layered ($\ell = 2$), low-spin configuration Ni(111) clusters. Computed structural parameters include: for C_2H_4 , $r(C-C) = 1.7 \text{ \AA}$ (corresponding to a stretch of $\Delta r(C-C) = 0.22 \text{ \AA}$ from the calculated gas-phase structure), $r(C-H) = 1.17 \text{ \AA}$, $z(C) = 2.0 \text{ \AA}$, $d(Ni-C) = 2.04$, and a $\theta_{CH_2} = 45^\circ$ angle of bend of the CH_2 groups from planarity; while for C_2H_2 , $r(C-C) = 1.5 \text{ \AA}$ ($\Delta r(C-C) = 0.2 \text{ \AA}$), $r(C-H) = 1.14 \text{ \AA}$, $z(C) = 1.9 \text{ \AA}$, $d(Ni-C) = 1.96 \text{ \AA}$, and a CCH angular distortion of $\Delta\theta_{CCH} = 55^\circ$, or angle of bend of the CH groups from the surface. A subsequent, more extensive examination of C_2H_2 adsorption on Ni(111) [105] found, employing $n = 4$, $\ell = 1$ and $n = 13$ and 31 , $\ell = 2$ cluster models; a modified set of parameters, with atomic ionization energy shifts to counteract excessive charge transfer to the C_2H_2 C's; and spin unpairing in the cluster, with each d -band level at least singly occupied: a site stability ordering of $\mu/\pi > \text{di-}\sigma \sim \text{di-}\sigma/\pi > \pi \sim \mu$, with $\Delta r(C-C) = 0.17 \text{ \AA}$, $z(C) = 1.6/1.8 \text{ \AA}$, and $\Delta\theta_{CCH} = 50^\circ$ for the favoured (by 0.3 eV) μ/π site.

In the first EH study of C_2H_4 on Ni(111) [86], the surface was modelled as an $n = 10$, $\ell = 2$ cluster, with C_2H_4 in an atop binding site and the molecular plane fixed at a height of $z(C) = 2.0 \text{ \AA}$; the calculated energy levels accounted qualitatively for the shift of the π toward the σ levels observed in the experimental UPS spectrum [6]. Adopting Anderson's ASED-MO C_2H_4 di- σ bridging orientation and chemisorption geometry results [104], a fragment-molecular-orbital extended-Hückel-theory (FMO-EHT) analysis [106] showed that both the π and π^* orbitals of C_2H_4 interact with the d bands of the two-layered clusters. The two predominant interactions were a four-electron

interaction involving the π -bonding orbital of C_2H_4 and the matching orbital of the metal d -band and a two-electron interaction involving the π^* -antibonding orbital of C_2H_4 . Total energy minimization by the method of steepest descents in an EH study of C_2H_2 on Ni(111) [107], which employed a Ni_4 cluster and allowed only rigid-body degrees of freedom and θ_{CCH} variation, *i.e.*, a planar species with $r(C-C) = 1.20 \text{ \AA}$ and $r(C-H) = 1.06 \text{ \AA}$, found little to distinguish energetically the five sites investigated.

2. *Ab initio*, $X\alpha$ (or HFS), and Density-functional Studies

Chemisorption properties have been extrapolated from *ab initio*, $X\alpha$ (or HFS), and density-functional studies of primitive surface-model and transition-metal/ligand complexes: $Ni_n(C_2H_x)$, where $n = 1 - 4$ and $x = 2$ or 4. Generalized-valence-bond and configuration-interaction (GVB-CI) calculations of C_2H_4 and C_2H_2 π -coordinated to a single Ni-atom surface model [108] found geometries only slightly distorted from those of the free molecules, with the following optimized triplet-state parameters ($r(C-H)$'s fixed at gas-phase values): for $Ni(C_2H_4)$, $r(C-C) = 1.36 \text{ \AA}$, $d(Ni-C) = 2.07 \text{ \AA}$, $\theta_{CH_2} = 2^\circ$, and a binding energy of $E_B = 14.2 \text{ kcal/mol}$; while for $Ni(C_2H_2)$, $r(C-C) = 1.21 \text{ \AA}$, $d(Ni-C) = 2.01 \text{ \AA}$, $\Delta\theta_{CCH} = 5^\circ$, and $E_B = 16.7 \text{ kcal/mol}$. A complete-active-space self-consistent-field and contracted CI (CASSCF-CI) investigation of the lowest-lying singlet and triplet potential energy surfaces of the $Ni(C_2H_4)$ complex established the singlet as the ground state, with $r(C-C) = 1.45 \text{ \AA}$, a 21° angle of tilt of the H atoms from the C-C axis, and a corrected E_B of 20 kcal/mol [109]. An SCF- $X\alpha$ -

scattered-wave (SCF-X α -SW) analysis, with a model surface complex comprised of C₂H₄ fixed in its equilibrium geometry at $d(\text{Ni}-\text{C}) = 2.0 \text{ \AA}$ from the nearest Ni of a Ni dimer [110], favoured the π - over the di- σ -chemisorbed species. The interaction of C₂H₂ with the Ni(111) surface was examined by the HFS-LCAO method with core pseudopotentials and $n = 1 - 4$ cluster models [111]; correlation of calculated results for different structures with measured UPS and EELS data yielded the di- σ/π configuration or triangular binding site (denoted μ_3 in their notation), with $d(\text{Ni}-\text{C}) = 1.9 \text{ \AA}$ and $\theta_{\text{CCH}} \leq 150^\circ$, as the most probable of the four investigated adsorption sites.

Non-local (NL) DFT optimized geometries and binding energies of the binary transition-metal/ligand complex, Ni(C₂H₄), [112] were obtained for the singlet ground state: $r(\text{C}-\text{C}) = 1.439 \text{ \AA}$, $r(\text{C}-\text{H}) = 1.108 \text{ \AA}$, $d(\text{Ni}-\text{C}) = 1.878 \text{ \AA}$, $\theta_{\text{HCH}} = 114.4^\circ$, $\theta_{\text{NiCH}} = 112.1^\circ$, and $E_B = 39.8 \text{ kcal/mol}$ (cf. experimental $E_B^{\text{expt}} = 35.5 \pm 5 \text{ kcal/mol}$ and calculated extended coupled-cluster and coupled-pair functional $E_B \sim 27.5 \text{ kcal/mol}$ [113] results); while for the triplet state $r(\text{C}-\text{C}) = 1.394 \text{ \AA}$, $r(\text{C}-\text{H}) = 1.105/1.102 \text{ \AA}$, $d(\text{Ni}-\text{C}) = 1.997/2.158 \text{ \AA}$, $\theta_{\text{HCH}} = 115.1/116.5^\circ$, $\theta_{\text{NiCH}} = 105.4/106.9^\circ$, and $E_B = 8.9 \text{ kcal/mol}$. An analogous NL (Becke/Perdew gradient-corrected) DFT study of the monoligand complex, Ni(C₂H₂), gave for the singlet ground state: $r(\text{C}-\text{C}) = 1.293 \text{ \AA}$, $r(\text{C}-\text{H}) = 1.091 \text{ \AA}$, $d(\text{Ni}-\text{C}) = 1.823 \text{ \AA}$, $\theta_{\text{CCH}} = 151.0^\circ$, and $E_B = 42.8 \text{ kcal/mol}$ (cf. $E_B^{\text{expt}} = 44 \text{ kcal/mol}$); whereas for the triplet state, $r(\text{C}-\text{C}) = 1.313 \text{ \AA}$, $r(\text{C}-\text{H}) = 1.096/1.097 \text{ \AA}$, $d(\text{Ni}-\text{C}) = 1.804/1.962 \text{ \AA}$, $\theta_{\text{CCH}} = 147.4/138.9^\circ$, C-C tilt angle of 7.4° , and $E_B = 11.3 \text{ kcal/mol}$ [114].

b. C₂H₄ and C₂H₂ on Related Surfaces

A brief synopsis of theoretical work on the related surfaces, Pt(111), Ni(100), Ni(110), is also documented. ASED-MO studies of the adsorption and structural rearrangements of C₂H₄ and C₂H₂ on Pt(111) [5], employing originally $n = 4$ and later $n = 19$ cluster models, found that C₂H₄, which is di- σ -bonded, twists during dehydrogenation, while C₂H₂ favours the di- σ/π (Δ) and di- σ configurations. The Pt(111)/C₂H₂ system has been extensively analyzed by EHT [115,107]: on $n = 9 - 11$, $\ell = 2$ clusters, C₂H₂ prefers a linear over a bent arrangement in the di- σ bonding mode, with a site stability ordering of di- $\sigma > \pi > \text{di-}\sigma/\pi \sim \mu/\pi > \mu$. The adsorption and dehydrogenation of C₂H₄ on the flat (111), (100), and (110) and stepped (112) Pt surfaces were also investigated with an EH-type tight-binding method [116], though structural distortions were not addressed.

The self-consistent, two-electron, semiempirical complete-neglect-of-differential-overlap (CNDO)/2 study of C₂H₄ and C₂H₂ interacting with the Ni(100) surface [117], modelled as an $n = 8$, $\ell = 1$ cluster, found: C-C and C-H bond weakening coupled with Ni-C and Ni-H bond formation; π -adsorbed (planar) C₂H₄ and (linear) C₂H₂ species most stable of the four and two, respectively, parallel geometries investigated in single-point energy calculations at various $z(\text{C})$; probable dehydrogenation of twisted C₂H₄ to C₂H₂. Geometric and electronic effects of the di- σ and π complexes of C₂H₄ on Ni(100) were examined in a discrete variational (DV)-X α approach, which employed a Ni₅ cluster model and fixed both C₂H₄ at its gas-phase geometry and

$d(\text{Ni}-\text{C})$ extrapolated from that of $\text{Ni}-\text{C}_2\text{H}_4$ complexes [118]. LCGTO-LDF partial geometry optimizations of a dilute layer of C_2H_4 , constrained to C_{2v} symmetry, on Ni(110) [79] yielded, for the π (di- σ)-bonded species on a Ni_{25} (Ni_{24}) cluster: $r(\text{C}-\text{C}) = 1.42$ (1.41) Å, $d(\text{Ni}-\text{C}) = 2.01$ (2.06) Å, $\gamma_{\text{CH}_i} = 23^\circ$, and $E_B = 1.80$ (1.26) eV.

Chapter 3: COMPUTATIONAL DETAILS AND PRELIMINARIES

A. Theoretical Method

1. Atom-Superposition and Electron-Delocalization Molecular-Orbital (ASED-MO) Calculations

Adsorbate structures and binding energies were optimized within the semiempirical, modified extended-Hückel, ASED-MO method. The modified version [119] that was employed of the "ASED" program of A.B. Anderson *et al.* [86-88] implements the method of steepest descents in its optimizing procedure to compute numerical gradients, *i.e.*, first derivatives of the energy with respect to the nuclear coordinates being varied. The input configuration can bias the geometry optimized, as multiple local minima and saddle points exist as stationary points in the potential energy hypersurface, corresponding, respectively, to possible adsorption and transition states.

The surface was modelled as a cluster of Ni atoms fixed at their ideal bulk lattice positions (lattice constant $a_{\text{Ni}} = 3.52 \text{ \AA}$ [120]; nearest-neighbour distance $nn_{\text{Ni}} = 2.48 \text{ \AA}$; next-nearest-neighbour distance $nnn_{\text{Ni}} = 4.30 \text{ \AA}$; inter-layer spacing $d_{\text{Ni}} = 2.025 \text{ \AA}$). Only slight C_2H_2 -induced lateral ($l_{1,2} \leq 0.1 \text{ \AA}$) and buckling ($b_1 \leq 0.04 \text{ \AA}$ and $b_2 \leq 0.07 \text{ \AA}$) reconstructions were detected in the LEED analysis of the decomposition products [10], while the PD study measured displacements of $\Delta d_{12} = -(0.01 \pm 0.06) \text{ \AA}$ and $\Delta d_{12} = (0.15 \pm 0.10) \text{ \AA}$ for C_2H_2 and C_2H_4 adsorption, respectively [14]. The applicability and

limitations of both the theoretical method and cluster model are scrutinized to gauge the reliability of the calculated results in describing the actual physical system.

a. Parameter Choice

To partially counterbalance the method's overestimate of electron transfer from the metal to the adsorbed hydrocarbons, the parameter adjustment of Anderson *et al.* [98] was adopted, whereby, as listed in Table 3.1, the valence-state ionization potentials (VSIP's) of the H and C atoms were decreased, and that of Ni and Pt increased by 1.0 eV. Such parameter adjustments mimic self-consistent charge transfer [121], but at the expense of a systematic overestimate of C–C single, double, and triple, as well as C–H bond lengths, by ~ 0.2 , 0.15, 0.1, and 0.1 Å, respectively [122], as revealed by the structural parameters in Table 3.2. Approximate states of hybridization, sp^n , and corrected C–C bond lengths, $r(\text{C–C})$, of the adsorbate hydrocarbons were interpolated from quadratic fits, displayed in Figure 3.1, of the experimental and theoretical, both ASED-MO and DFT, $r(\text{C–C})$'s of C_2H_2 , C_2H_4 , and C_2H_6 , as a function of sp^n . The sensitivity of the results on the parameter choice was analyzed by comparing, as in Figure 3.2, relative binding energies, E_B 's, determined with two different parameter sets, that of Ref. [5] (implemented in the subsequent, comparative Pt study) and adjustment of the original data set as above, but for the Pt(111)/ C_2H_4 system; while the quantitative results may differ, the qualitative trends remain essentially unaltered.

Table 3.1 Atomic Parameters^a Used in the ASED-MO Calculations

Atom	n^b		VSIP ^c / eV	ζ_1^d / a.u.	ζ_2^d / a.u.	c_1^e	c_2^e
H	1	<i>s</i>	-12.600 (-13.600)	1.2000			
C	2	<i>s</i>	-19.000 (-20.000)	1.6583			
	2	<i>p</i>	-10.260 (-11.260)	1.6180			
Ni	4	<i>s</i>	-8.635 (-7.635)	1.8000			
	4	<i>p</i>	-4.990 (-3.990)	1.5000			
	3	<i>d</i>	-11.000 (-10.000)	5.7500	2.0000	0.5681	0.6293
Pt (Set 1)	6	<i>s</i>	-10.000 (-9.000)	2.5500			
	6	<i>p</i>	-5.960 (-4.960)	2.2500			
	5	<i>d</i>	-10.600 (-9.600)	6.0130	2.3960	0.6562	0.5711
Pt (Set 2)	6	<i>s</i>	-9.960 (-8.960)	2.5540			
	6	<i>p</i>	-3.260 (-2.260)	2.5350			
	5	<i>d</i>	-9.850 (-8.850)	6.0130	2.6960	0.6707	0.5844

^a H, C, and Ni parameters from A.B. Anderson, *J. Am. Chem. Soc.* **100** (1978) 1153-1159; Pt (Set 1) values from A.B. Anderson, and A.T. Hubbard, *Surf. Sci.* **99** (1980) 384-391 and D.B. Kang and A.B. Anderson, *Surf. Sci.* **155** (1985) 639-652.

^b Principal quantum number

^c Valence-state ionization potential (unadjusted potentials in parentheses)

^d Slater orbital exponent

^e Linear coefficient

Table 3.2 Structural Parameters of Isolated Hydrocarbons, C_2H_x , $x = 2, 4, 6$

Molecule	x	sp^n	$r(C-C) / \text{Å}$	$r(C-H) / \text{Å}$	$\theta_{\text{HCH}} / \text{deg}$
Experimental					
Acetylene ^a	2	sp	1.203	1.061	($\theta_{\text{CCH}} = 180.0$)
Ethylene ^b	4	sp^2	1.339 ± 0.001	1.085 ± 0.002	117.8 ± 0.3
Ethane ^a	6	sp^3	1.526	1.088	107.4
ASED-MO Method					
Acetylene	2	sp	1.324	1.150	($\theta_{\text{CCH}} = 180.0$)
Ethylene	4	sp^2	1.498	1.185	118.5
Ethane	6	sp^3	1.761	1.201	113.9
DFT					
Acetylene	2	sp	1.212	1.088	($\theta_{\text{CCH}} = 180.0$)
Ethylene	4	sp^2	1.332	1.106	116.8
Ethane	6	sp^3	1.510	1.111	107.1

^a D.J. DeFrees, B.A. Levi, S.K. Pollack, W.J. Hehre, J.S. Binkley, and J.A. Pople, *J. Am. Chem. Soc.* **101** (1979) 4085-4089.

^b J.L. Duncan, I.J. Wright, D. Van Lerberghe, *J. Molec. Spectrosc.* **42** (1972) 463-477.

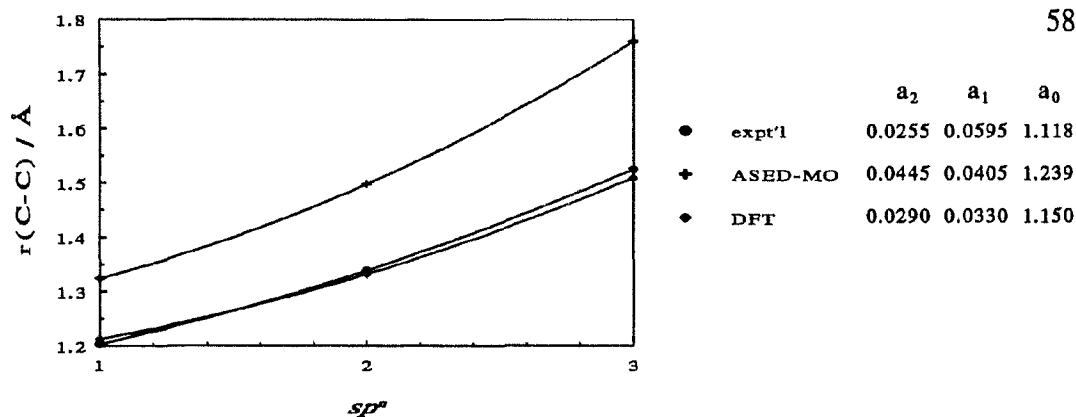


Figure 3.1 Quadratic fits and coefficients, a_2 , a_1 , and a_0 , of the experimental and theoretical, both ASED-MO and DFT, C-C bond lengths, $r(\text{C-C})$'s, of C_2H_2 , C_2H_4 , and C_2H_6 as a function of their states of hybridization, sp^n , $n = 1, 2$, and 3, respectively.

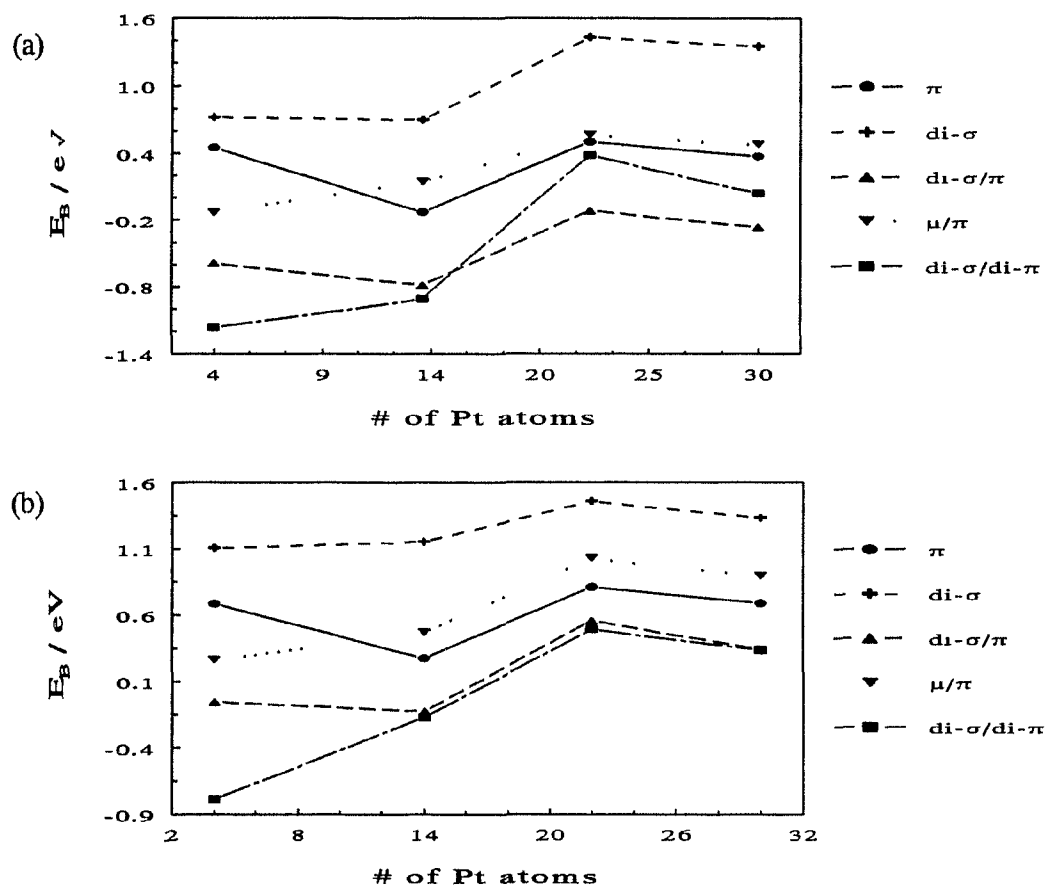


Figure 3.2 Comparison of calculated binding energies, E_B 's, for I_4 in five adsorption sites on Pt(111) using (a) parameter set of Ref. [5] and (b) parameter adjustment of original data set analogous to that used for Ni(111).

b. Symmetry Constraints

Given the manifold degrees of freedom of the system investigated, to render the problem computationally tractable, symmetry constraints had to be imposed: some embodied experimental results, while others prevented abrupt structural transitions symptomatic of the finite-sized cluster model. The experimentally deduced local molecular symmetries, C_2 and C_1 , respectively, for the C_2H_4 [29] and C_2H_2 [38] adsorption complexes, were verified and implemented, where appropriate. In the adsorption study, whereas minimal symmetry assumptions were incorporated in the examination of the dehydrogenation mechanism. On the basis of LEED results [25], commensurate (2×2) ethylene and acetylene overlayers were assumed, with each like molecule treated equivalently. Questions such as the validity of the imposed symmetry constraints are addressed in Chapter 4, with the discussion of results.

c. Error Estimates

The convergence criteria used in the geometry optimizations are listed in Table 3.3, as are the estimated errors in the optimized variables. The higher estimated errors reflect the dependence of the optimized coordinate variables and energies upon the initial configuration, and were inferred by comparison of results obtained from different input values. The tolerance of relative coordinate variable and energy changes are obviously twice these errors. Tabulation of structural parameters and binding energies stemming

Table 3.3 Convergence Criteria and Estimated Errors in the ASED-MO Calculations

Deviation	Convergence Criteria (optimizing procedure)	Estimated Error (precision)	Theoretical Error (accuracy)
$\Delta r / \text{\AA}$	0.001	± 0.005	± 0.01
$\Delta \theta / \text{deg}$	0.057	± 0.5	± 1
$\Delta E / \text{eV}$	0.0001	± 0.0005	± 0.005
norm of gradient	10^{-10}	-	-

from the adsorption study and investigation of the dehydrogenation mechanism adhere to these error estimates, which indicate the precision or reproducibility of the calculated data. These errors, however, are subject also to errors within the method arising from the parameter choice; the particular cluster model and spin-configuration convention employed; the imposed adsorbate symmetry constraints; restriction of the Ni atoms to their ideal bulk lattice positions; as well as the ASED-MO method itself. Hence, estimates of the theoretical error, *i.e.*, the accuracy within the method, are also given in Table 3.3. Given the limited, quantitative accuracy of the ASED-MO method, emphasis will be on the qualitative, structural and energetic trends, considered more reliable, when extracting information from the calculated results to describe the real, physical system.

2. Density-Functional Theory (DFT) Computations

The DFT treatment employed the LCGTO method [123], as incorporated in the "deMon" program developed by St-Amant and Salahub [124,125]. All computations were performed within the LSDA, implementing the Dirac exchange [126], as modified by von Barth and Hedin for the spin-polarized case [127], and the VWN correlation [98] functionals. The four Ni atoms in the diamond-shaped cluster were frozen at their relative positions in the unit cell of the bulk lattice, while the adsorbate geometry was optimized, though some single-point energies were also calculated to compare with the ASED-MO results. The auxiliary and orbital basis sets used in the DFT calculations are listed in Table 3.4, along with the model-core potentials

Table 3.4 Basis Sets Used in the Density-Functional Calculations

Atom	Auxiliary $(n_s^{CD}, n_{spd}^{CD}; n_s^{XC}, n_{spd}^{XC})^a$	Orbital $(n_s^1, \dots, n_s^K / n_p^1, \dots, n_p^L / n_d^1, \dots, n_d^M)^b$	Model-Core-Potential $(n_V^{MCP}; n_s^{MCP}, n_p^{MCP}, n_d^{MCP})^c$
H	(5,1;5,1)	(41/1)	-
C	(5,2;5,2)	(5211/411/1)	-
Ni	(3,4;3,4)	(311/31/311)	(5:7,4)

^a n_s^{CD} (n_s^{XC}) and n_{spd}^{CD} (n_{spd}^{XC}) are the numbers of s -type and sets of same-exponent s -, p - and d -type gaussians, respectively, used to variationally (least-squares) fit the charge density (exchange-correlation potential)

^b K , L , and M contractions of s -, p -, and d -type gaussians with $\{n_s^1, \dots, n_s^K\}$, $\{n_p^1, \dots, n_p^L\}$, and $\{n_d^1, \dots, n_d^M\}$ primitives, respectively

^c n_V^{MCP} is the number of s -type gaussians used to fit the potential seen by the valence electrons and n_s^{MCP} , n_p^{MCP} , and n_d^{MCP} are the numbers of s -, p -, and d -type gaussians, respectively, used to fit the s , p , and d core orbitals

(MCP's) that replaced the Ni $1s$, $2s$, $2p$, and $3s$ core electrons. In each self-consistent-field (SCF) iteration, the charge density (CD) was fitted variationally, *i.e.*, analytically [128], whereas the exchange-correlation (XC) potential was least-squares fitted [129] on a medium grid randomizing the angular points of the radial shells; at the end of each converged SCF procedure, the exchange-correlation contributions to the total energy and the energy gradients were calculated by numerical integration on an augmented grid [130]. In the geometry optimization procedures, the Broyden-Fletcher-Goldfarb-Shanno (BFGS) algorithm was selected to update the approximate Hessian matrix, with a largest average atomic displacement of typically 0.07 bohr permitted at any particular step. The convergence criteria for the SCF iterations and geometry optimizations were 10^{-5} and 10^{-4} hartrees, respectively, corresponding in turn to the values within which consecutive total energies must lie and of the norm of the gradient necessary to terminate the SCF and optimization procedures.

a. Self-Consistent-Field (SCF) Convergence

Oscillatory behaviour in the SCF solutions of the KS orbital equations was frequently encountered, induced by the swapping of nearly degenerate occupied and virtual orbitals close to the Fermi level, ϵ_F , of the Ni clusters. The commonly employed Direct Inversion of the Iterative Subspace (DIIS) algorithm [131] was not invoked to accelerate SCF convergence, its function being impeded when either the gap between the highest occupied and lowest unoccupied molecular orbitals, *i.e.*, the HOMO/LUMO gap,

is small or fractional occupation numbers are permitted. Instead, two other techniques were implemented to enhance SCF convergence: damping plus smearing and level shifting. Damping involves a mixing parameter, dmixing, denoted by α , which defines the fraction of the output density produced by the m^{th} SCF iteration, ρ_{out}^m , that is mixed with the m^{th} -iteration input density, ρ_{in}^m , to yield the input density for the next, $(m+1)^{\text{th}}$, iteration:

$$\rho_{in}^{m+1} = \alpha \rho_{out}^m + (1-\alpha) \rho_{in}^m, \quad 0 < \alpha < 1. \quad (3.1)$$

Presently restricted to be ≤ 0.05 to avoid SCF divergences due to the near-degeneracies at ϵ_F , dmixing was used in conjunction with a smear parameter, denoted by ω , that allows fractional occupation within a chosen energy bandwidth around ϵ_F . Iterative reduction of the smear and dmixing parameters to achieve integral occupation within a converged SCF procedure necessitated a simultaneously increased number of SCF cycles to conform with the slower, but stabler, convergence accompanying the smaller dmixing parameters and consequent reduced iterative step. Alternatively, the level shift procedure [132,133] was activated to artificially increase the HOMO/LUMO gap by $2\epsilon_{SHIFT}$ to decrease the mixing, and hence eliminate the swapping of orbitals between the occupied and virtual shells. Level shifting often led to a destabilization of the occupied orbitals [134] and consequently an electron configuration with an empty orbital lower in energy than an occupied one, a manifestation of the self-interaction error [135] introduced by approximations, such as the LSDA, to the exact density functional for the ground-state energy. Complications plagued both techniques for enhancing SCF convergence, rendering an optimized geometry within a converged SCF

procedure with integral occupation numbers computationally prohibitive and frequently impossible to achieve; the density-functional analysis was thus restricted to isolated molecular adsorption and comparative, single-point energy calculations along relevant, coordinate variable changes on the simple, Ni_4 cluster model.

B. Cluster Model

Electronic structure calculations routinely exploit the spatially localized nature of the surface-adsorbate bond (due to substrate-adsorbate ionic or covalent bond formation or metallic screening of the adsorbate potential) by replacing the substrate by atoms only within the immediate vicinity of the adsorbates, *i.e.*, by employing a cluster model that implicitly assumes that surface hybridization is dominated by the adsorbate, and not neighbouring substrate atoms. In the study of surface properties, both semiempirical [136,137] and *ab initio* [138] MO methods generally show cluster models to adequately simulate the extended system. Attempts to minimize truncation problems include: restoring the correct coordination to the edge atoms with a surrounding, pseudoatomic shell [139,140]; and cluster embedding of the adsorbate and some substrate neighbours, through a unitary, orbital-localization transformation, within a larger cluster whose electronic structure is treated more approximately [141,142].

Appropriate choice of clusters is crucial, however, to minimize artifacts of cluster truncation in computations modelling the extended system by finite atomic arrays. Thus, the dependence of the ASED-MO results on the cluster size (lateral extent and depth),

symmetry, and spin configuration was systematically investigated to ascertain the limitations and utility of the cluster representation of the Ni(111) surface. Cluster dependence of the geometries and energies optimized in the adsorption and reactivity studies was monitored as a function of the total number of atoms, n , the number of layers, ℓ , and the lateral extent, as gauged by the number of atoms in the topmost layer, d , of a variety of cluster models, alternately designated by the number of atoms in each layer, $(n_1/n_2/\dots/n_\ell)$. The cluster configuration, especially its symmetry with respect to the adsorption site, can markedly influence the local symmetry of the optimized adsorbate molecule, as well as its relative binding energy. The qualitative ramifications of the dependence of the calculated results on the cluster will be sketched out in this chapter, while more quantitative considerations will be addressed, and the layer dependence continually explored, in the discussion of the adsorption sites and dehydrogenation mechanism in Chapter 4. Sufficiently converged results, to be demonstrated presently, were achieved with the moderately symmetric, three-layered clusters comprised of a surface layer housing the chemisorption-bonded Ni's and their nearest neighbours.

The cluster models, Ni_n , ($n = 4 \rightarrow 80$), were symmetric about either the centre of a unit cell or an individual atom of the extended lattice, with all atoms fixed at their ideal, bulk lattice positions. Depicted in Figure 3.3, the clusters ranged from four to twenty-four atoms in the topmost layer ($d = 4 \rightarrow 24$) and one to four layers deep ($\ell = 1 \rightarrow 4$): second- and third-layer atoms were placed in the alternate interstices of the top layer, displaced by half a nnn relative to each other, while the fourth layer was a translated replica of the first.

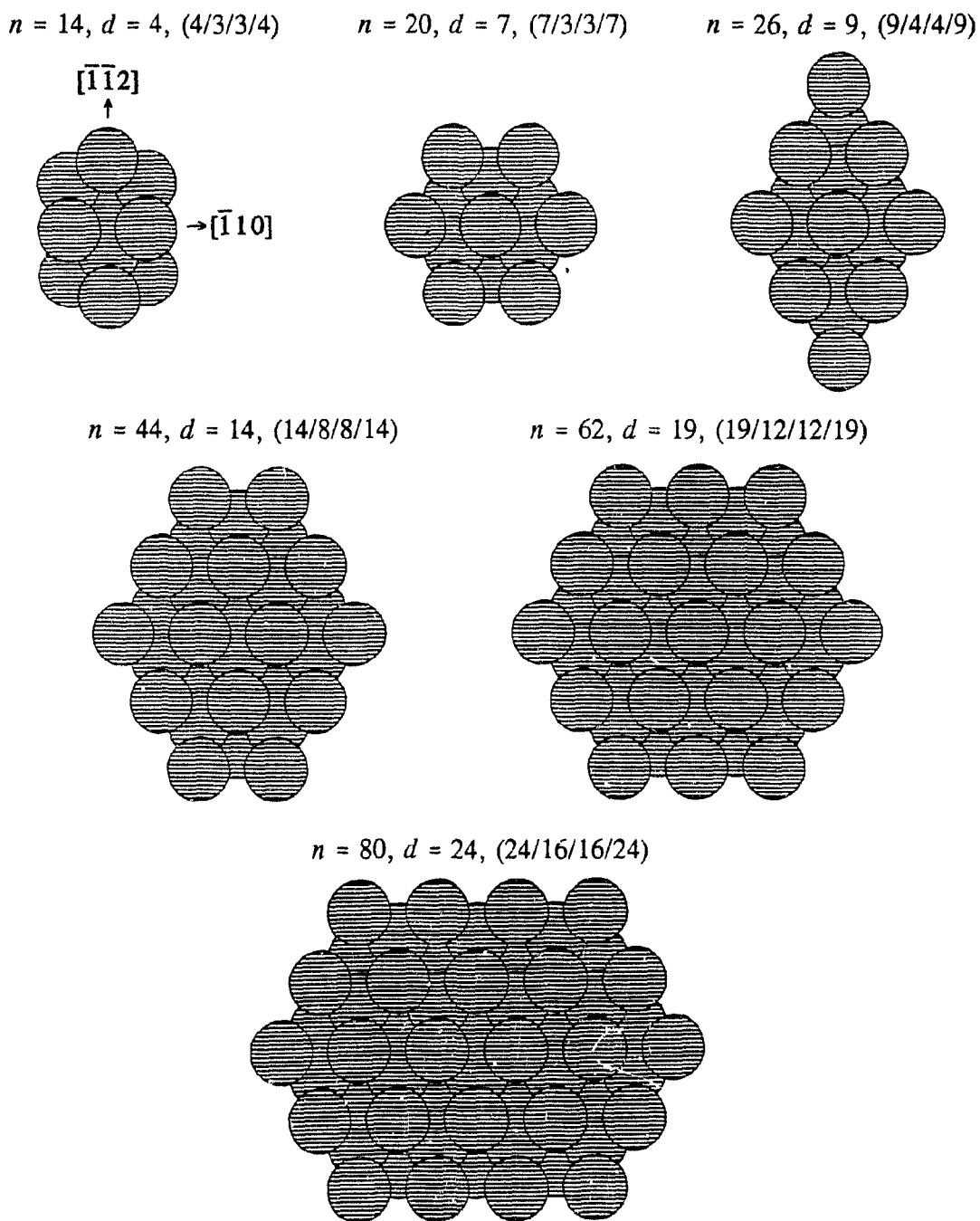


Figure 3.3 Bulk cluster models of the Ni(111) surface, Ni_n , for $n = 14, 20, 26, 44, 62,$ and 80 total number of Ni atoms, corresponding, respectively, to $d = 4, 7, 9, 14, 19,$ and 24 number of atoms in the topmost layer, and ranging from $\ell = 1 \rightarrow 4$ number of layers. The cluster designations, $(n_1/n_2 \dots /n_\ell)$, reflecting the number of atoms in each layer, and the two principal azimuthal directions are indicated.

The two sets of energy level diagrams displayed in Figures 3.4 and 3.5 for $d = 4, 14,$ and 24 and the $d = 14$ cluster series as $\ell = 1 \rightarrow 4$, respectively, indicate the convergence of the cluster electronic structure with both the number of atoms in the top layer and with successive layers. As expected, the density of states increases with increasing n , and hence d and ℓ , to give a well-defined metal d band and broad, overlapped s and p bands. Figures 3.6 and 3.7 show the corresponding Mulliken population analyses (MPA's) [143] for the two cluster series as functions of d and ℓ . The electronic structure of the bare clusters converges adequately for $d = 14, \ell = 3$, with the Ni atomic orbital occupations varying most dramatically for the orbitals in the surface plane, $d_{x^2-y^2}$ and d_{xy} , less active in chemisorption bonding (see Sect. 4.A.1.a).

1. Adsorption Sites

The adsorption studies of C_2H_4 and C_2H_2 focused on five binding sites (and their corresponding bonding configurations): the onefold atop (π); twofold aligned bridging (di- σ); threefold triangular or Δ (di- σ/π); threefold bridging/atop (μ/π); and fourfold bridging or μ (di- σ /di- π). Both types of threefold hollow, *i.e.*, the hexagonal close-packed (hcp) and face-centred cubic (fcc) sites over second-layer atoms (repeat sequence *abab...*) and hollows (repeat sequence *abcabc...*), respectively, were studied. The binding sites are shown in Figure 3.8 for C_2H_4 on the $n = 44, d = 14, \ell = 4$, *i.e.*, (14/8/8/14) cluster of Figure 3.3 (d).

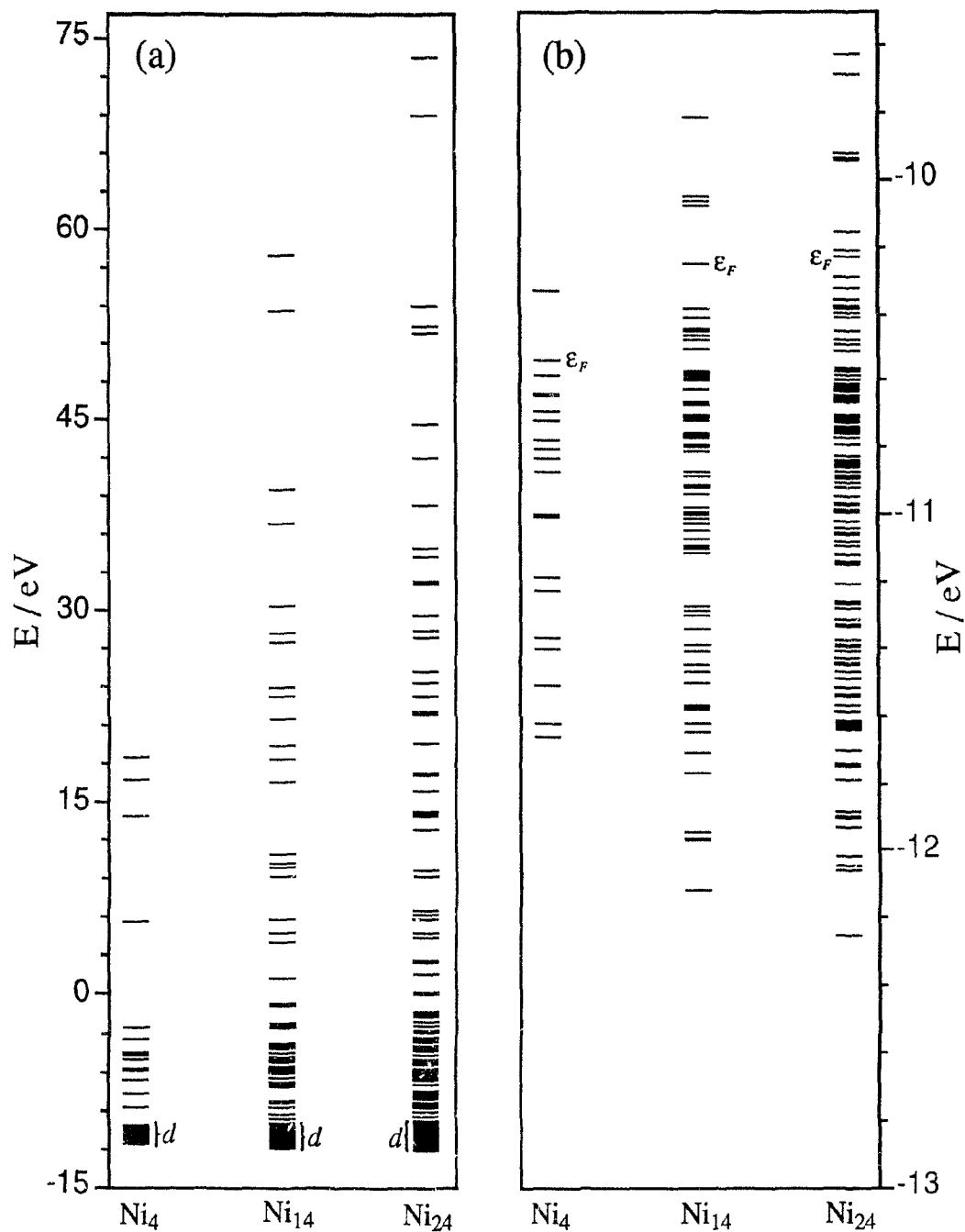


Figure 3.4 Energy level diagrams for the $\ell = 1$; $d = 4, 14$, and 24 series of clusters, Ni_n : (a) full set of $9 \times n$ levels with d bands highlighted (other levels comprise the broad and overlapping s and p bands) and (b) expanded view of the d bands with the cluster Fermi levels, ϵ_F 's, indicated.

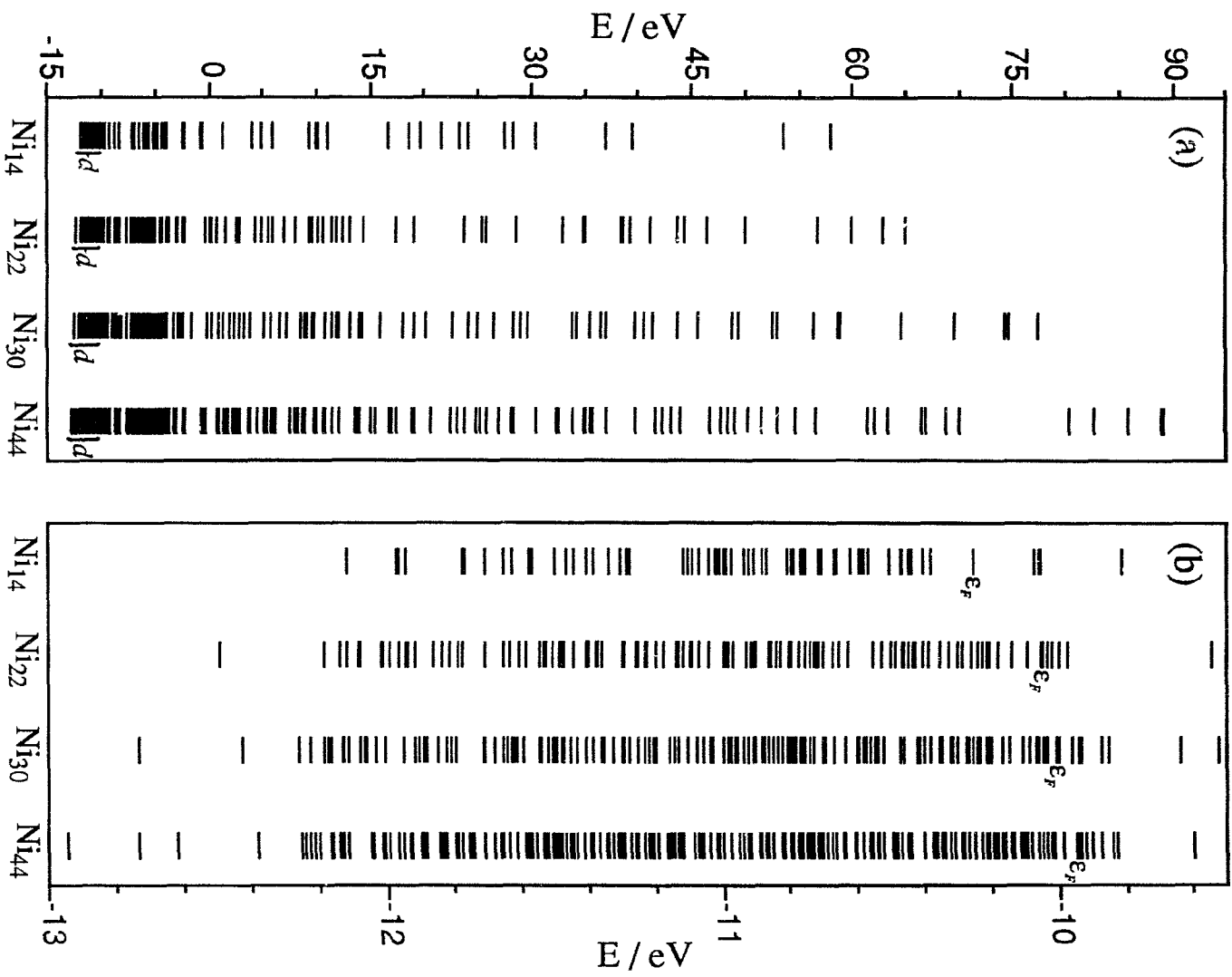


Figure 3.5 Energy level diagrams for the $d = 14$ series of clusters, Ni_n , $n = 14, 22, 30,$ and 44 , as $\ell = 1 \rightarrow 4$: (a) full set of $9 \times n$ levels and (b) expanded view of the cluster d bands.

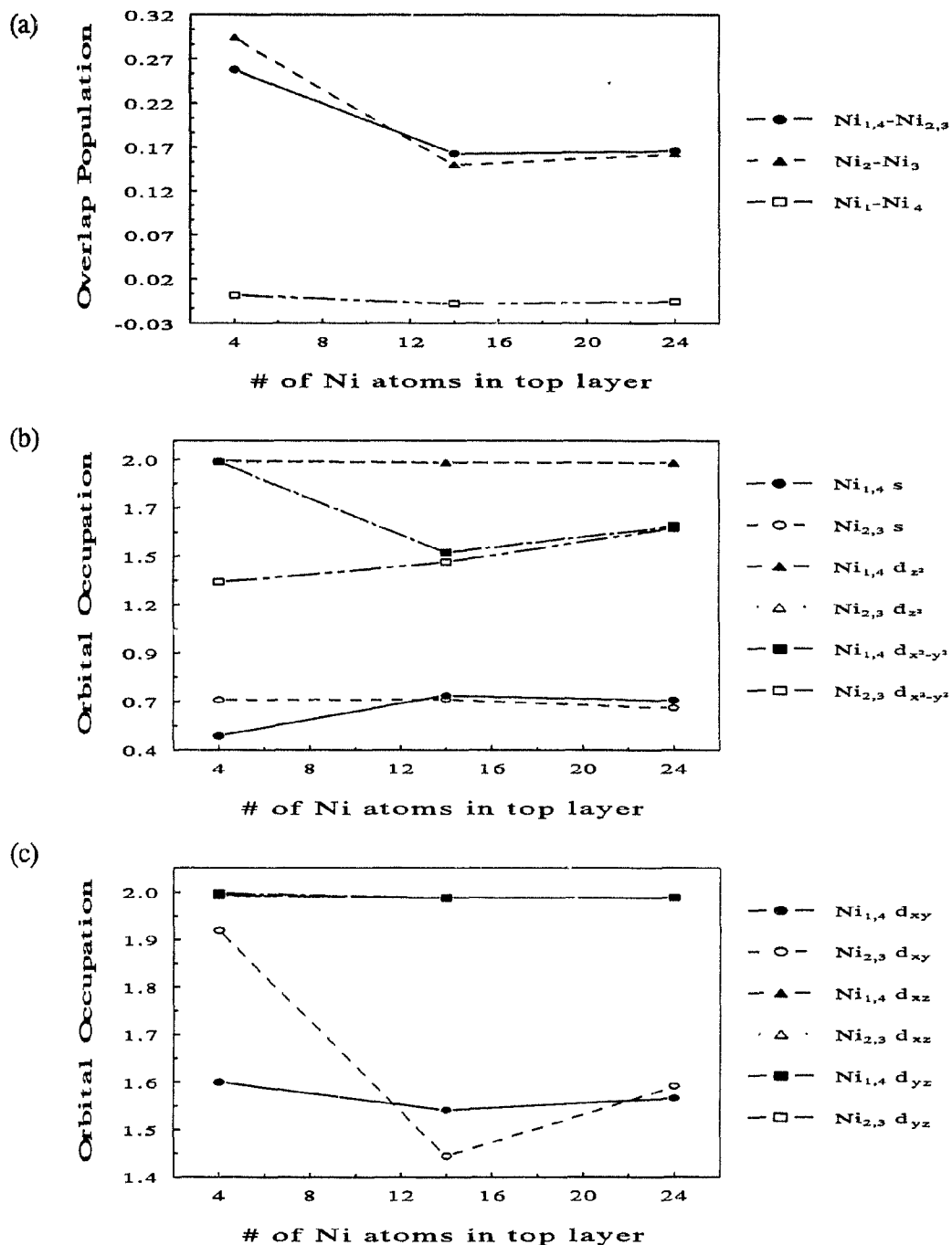


Figure 3.6 Mulliken population analysis (MPA) for the $d = 4, 14,$ and 24 Ni clusters: (a) Ni–Ni overlap populations; and atomic orbital occupations for Ni (b) s , $d_{x^2-y^2}$, and (c) d_{xy} , d_{xz} , d_{yz} .

(a) Ni–Ni Overlap

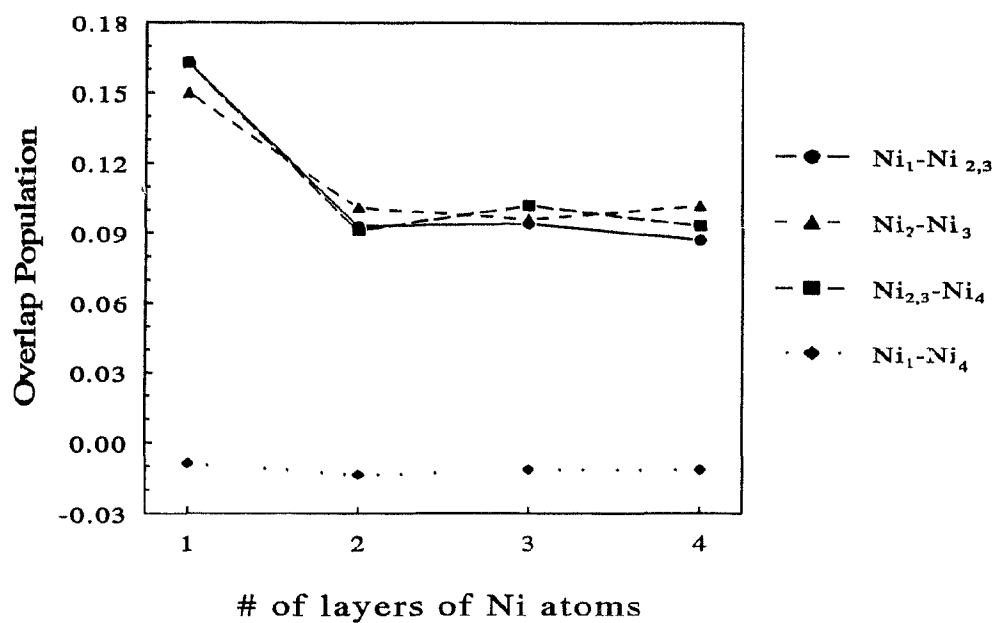
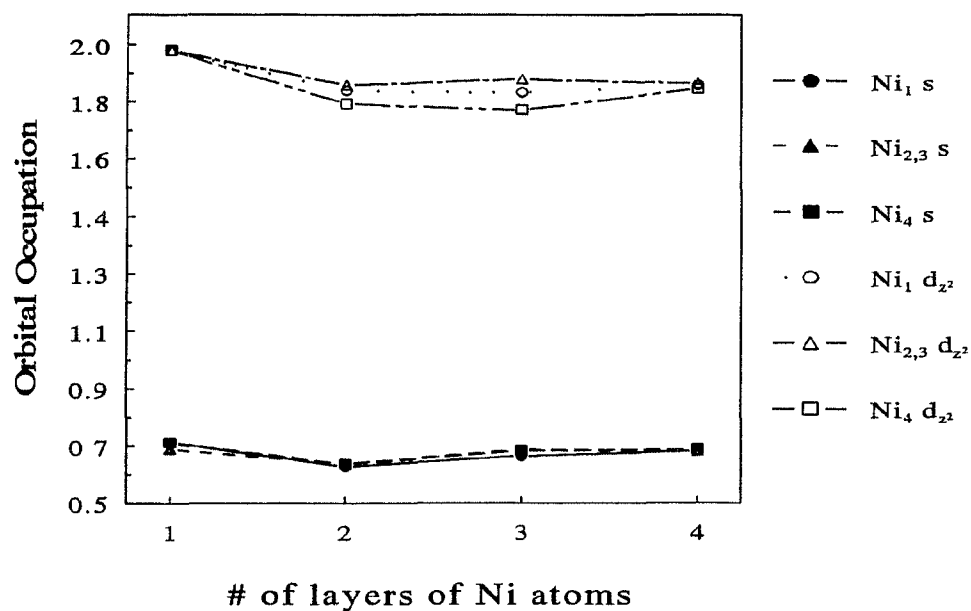
(b) Ni s and d_{z^2} 

Figure 3.7 MPA for the $d = 14$ series of Ni clusters as $\ell = 1 \rightarrow 4$: (a) Ni–Ni overlap populations; and atomic orbital occupations for Ni (b) s and d_{z^2} , (c) $d_{x^2-y^2}$ and d_{xy} , and (d) d_{xz} and d_{yz} .

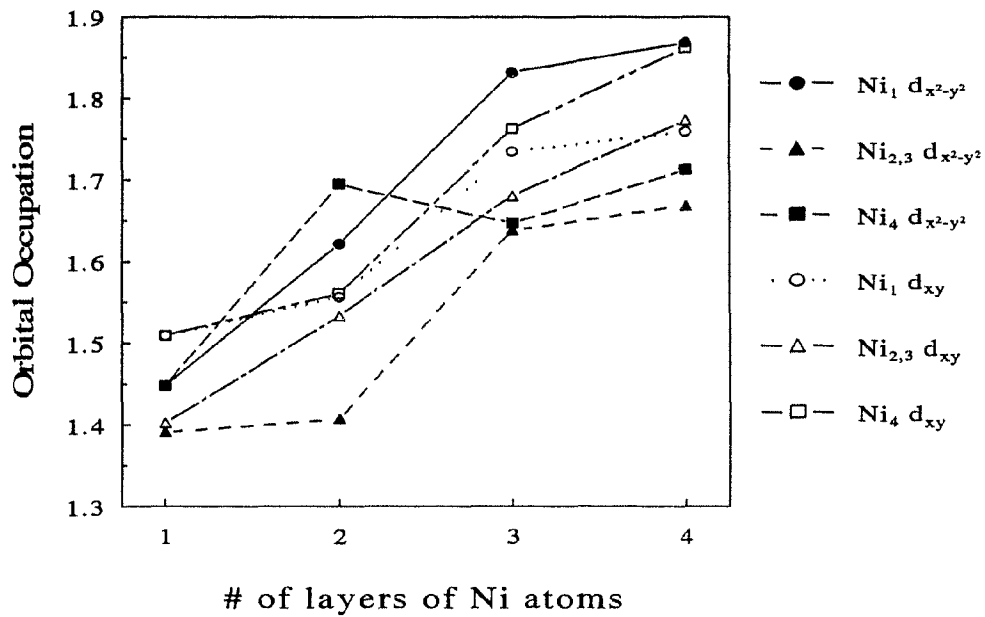
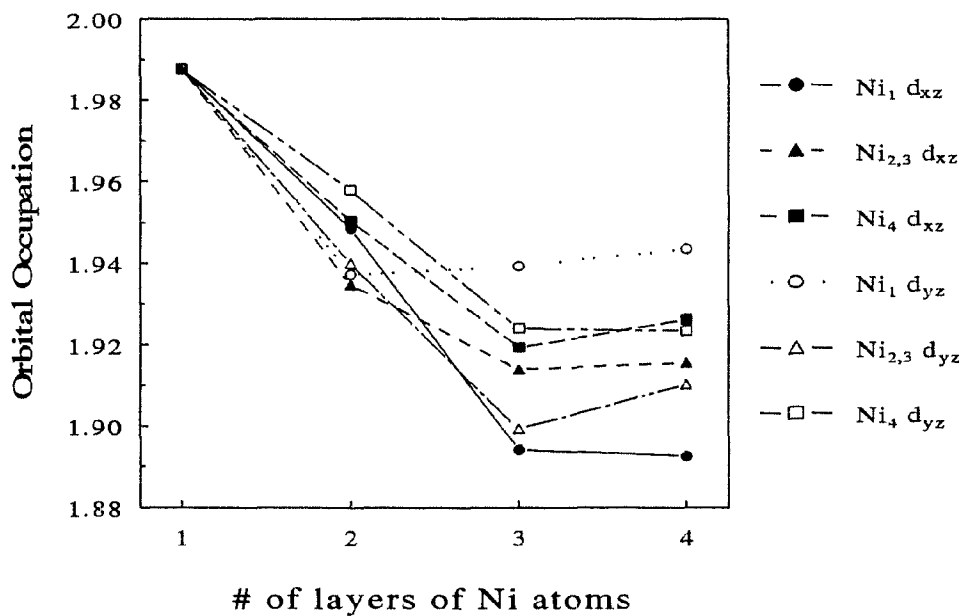
(c) Ni $d_{x^2-y^2}$ and d_{xy} (d) Ni d_{xz} and d_{yz} 

Figure 3.7 Cont'd

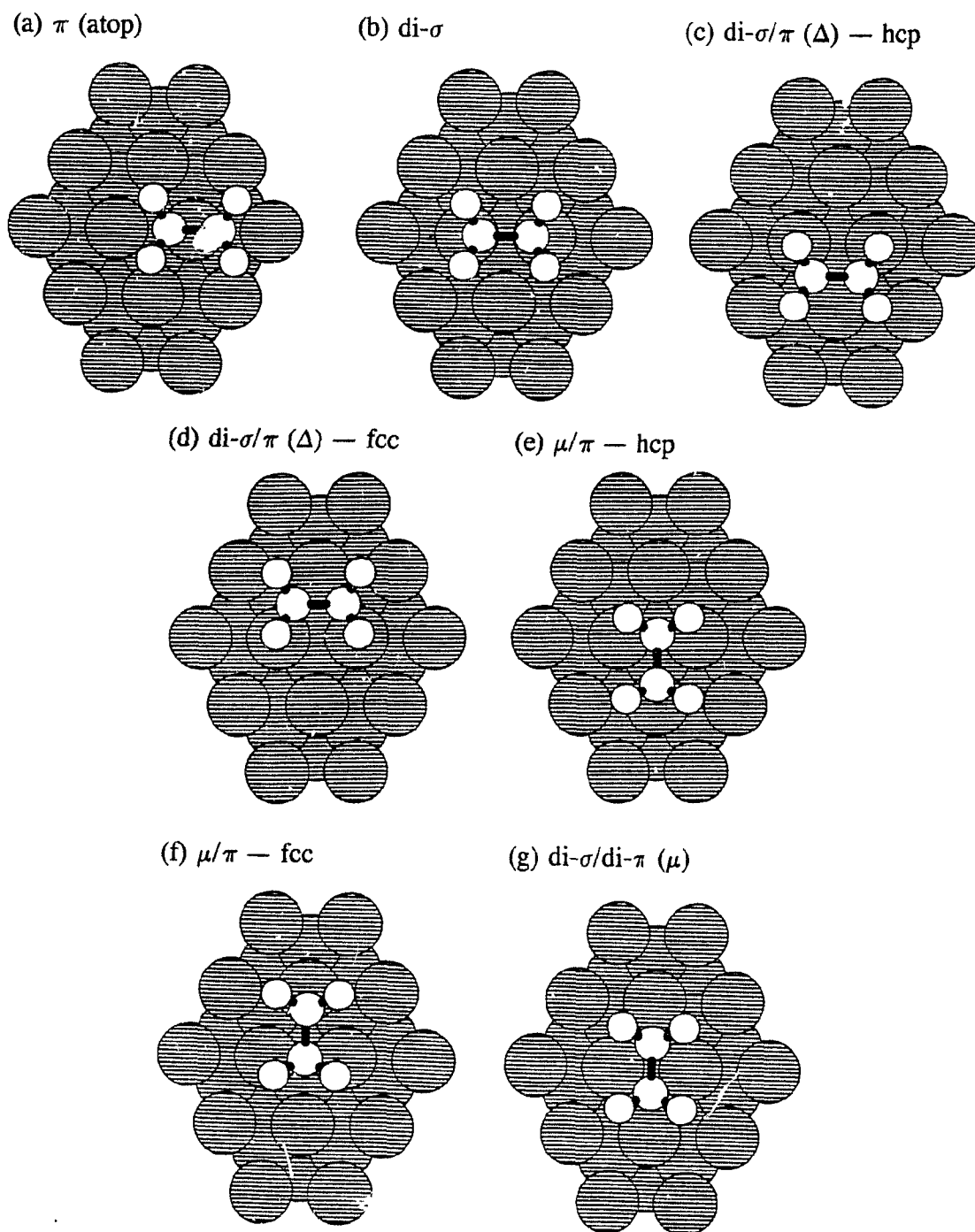


Figure 3.8 Five bonding configurations (and corresponding adsorption sites) investigated, shown for the $n = 44$, $d = 14$, $l = 4$, or (14/8/8/14) cluster model: (a) π (onefold atop); (b) di- σ (twofold aligned bridging); (c) di- σ/π (threefold triangular or Δ) — hcp; (d) di- σ/π (threefold triangular or Δ) — fcc; (e) μ/π (threefold bridging/atop) — hcp; (f) μ/π (threefold bridging/atop) — fcc; and (g) di- $\sigma/\text{di-}\pi$ (fourfold bridging or μ). Hcp and fcc denote threefold sites over second-layer atoms and hollows, respectively.

a. Layer Dependence

The layer dependence of both the stability ordering and optimized geometries of the C_2H_4 and C_2H_2 adsorption sites reveals the relative energies more variable than the adsorbate structures, in the progression from one- to four-layered clusters ($\ell = 1 \rightarrow 4$). While values fluctuate for the smaller clusters, binding energies, E_B 's, generally decrease within each d series with ℓ , and so n , in the cluster model, though less with each successive layer; Figures 3.9 – 3.11 (pp. 78 – 80) show the trend for the $d = 4, 14$, and 24 series. For clusters with equal n but different d and hence ℓ , E_B 's are greater for larger ℓ . The layer dependence of the relative stabilities is most prominent for the high coordination sites, *i.e.*, between the threefold hcp and fcc sites, for which differences are small, and for the μ site. Adequate convergence in the binding energies is observed with the three-layered clusters, as their relative orderings and differences between sites vary little with addition of a fourth layer.

Adsorbate geometries vary marginally with the number of layers, ℓ , in the cluster model. Figures 3.12 – 3.14 (pp. 81 – 83) monitor C_2H_4 and C_2H_2 C–C bond distances, $r(C-C)$, as $\ell = 1 \rightarrow 4$, which typically change by $\leq 0.05 \text{ \AA}$ as successive layers are added, and usually $> 0.01 \text{ \AA}$ for clusters of moderate lateral extent ($d \geq 14$) and depth ($\ell \geq 2$). For C_2H_4 , $r(C-C)$ is routinely overestimated for all sites on the one-layered clusters (when compared with larger cluster values), but stabilizes with additional ℓ . The reduced adsorbate interaction with the chemisorption-bonded Ni's upon successive addition of layers, as implied by the decreased C–C bond stretch, correlates with the

coordination between these surface- and subsurface-layer Ni's, which competes with the chemisorption bond for electron density. In contrast, for the more compact C_2H_2 , which, when adsorbed in the high coordination sites involving the threefold hollow sites of the Ni lattice, can interact to some extent with the second-layer Ni atoms, the $r(C-C)$ values may be underestimated on the smaller, one-layered clusters, but then shows the same trend on clusters of greater lateral extent ($d \geq 9$) as C_2H_4 . The predominant effect in most cases is observed on going from one- to two-layered clusters, as the Ni atoms in the third and fourth layers only interact indirectly with the surface Ni's bonded to the adsorbate molecules. The high coordination (*i.e.*, $di-\sigma/\pi$, μ/π , and μ) sites exhibit the greatest layer dependence, as expected from the diminishing effect of metal-metal bonding on the chemisorption bond. Also, the layer dependence is inverse to the lateral extent of the clusters.

b. Lateral Extent

The cluster lateral dimensions also affected most prominently the high coordination (threefold and fourfold) sites. The progression from $d = 4 \rightarrow 24$, *i.e.*, to clusters of increasing lateral extent, dampens out the oscillations in, and consequently levels out the E_B and $r(C-C)$ layer-dependence curves; see Figures 3.9 - 3.11 and 3.12 - 3.14. The $d = 14$ series, which include the first coordination shell surrounding, thereby fully saturating, the chemisorption-bonded Ni's, appear to satisfy a minimal requirement of the cluster lateral extent. Partial inclusion of the next-nearest-neighbours, or second

coordination shell, in the surface layer (*e.g.*, $d = 14 \rightarrow 24$), does not alter results significantly, though relative orderings between the two series do shuffle slightly with ℓ . The equivalence and inequivalence of like atoms also vary in some instances with the lateral extent of the cluster, due to asymmetrical edge effects for the like atoms on the smaller clusters (*e.g.*, $d = 14 \rightarrow 24$ in Table 4.3 on p. 139 for the C_2H_2 atop site).

c. Configuration and Symmetry

In addition to cluster size, the influence of the cluster configuration was investigated, particularly its symmetry with respect to the adsorption site. The adsorption sites considered demanded two sets of cluster configurations, those symmetric about the π site and those about the di- σ and μ sites (and also roughly about the di- σ/π and μ/π sites); see Figures 3.15 and 3.16 (pp. 84 and 85) and compare with Figures 3.9 - 3.11 and 3.12 - 3.14, respectively. Combining results from both sets sometimes masked trends which could be established within a set. On smaller clusters, the stability ordering of the π and di- σ sites for C_2H_4 depended upon about which site the cluster was symmetric. The cluster size, and where and how symmetrically the adsorbate is placed with respect to the cluster, also influence relative binding energies and structural parameters, as well as the symmetry constraints necessary to be imposed to keep the molecule in the appropriate bonding configuration. Edge effects due to cluster truncation, again most evident with the smaller clusters, could be minimized by selection of a cluster of sufficient lateral extent and symmetry.

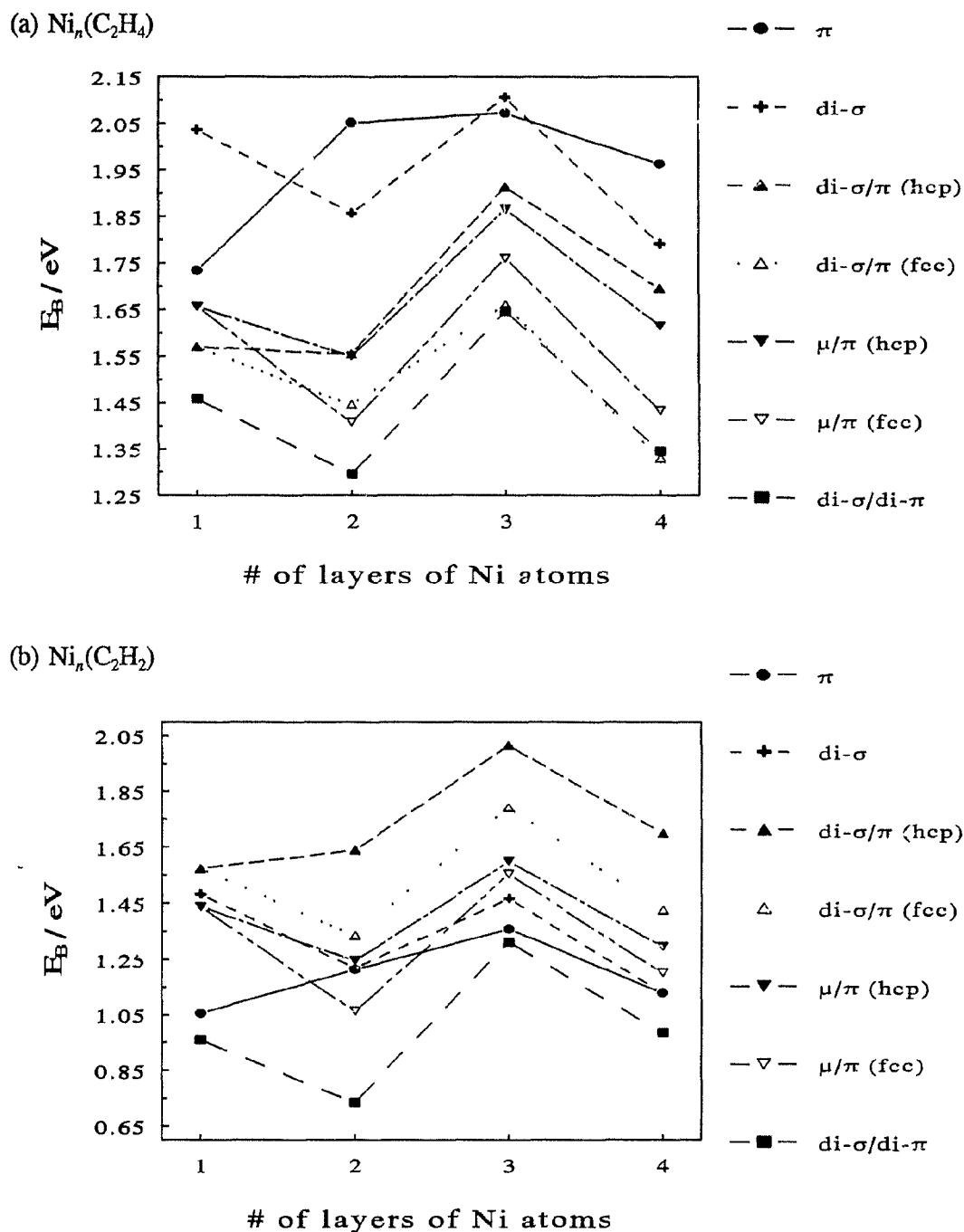


Figure 3.9 Cluster layer dependence of adsorbate relative site stabilities: binding energy, E_B , as a function of the number of layers of Ni atoms, $l = 1 \rightarrow 4$, for five bonding configurations of (a) C_2H_4 and (b) C_2H_2 on the $d = 4$ series of clusters, Ni_n , $n = 4, 7, 10$, and 14 , symmetric about the centre of a unit cell of the extended lattice.

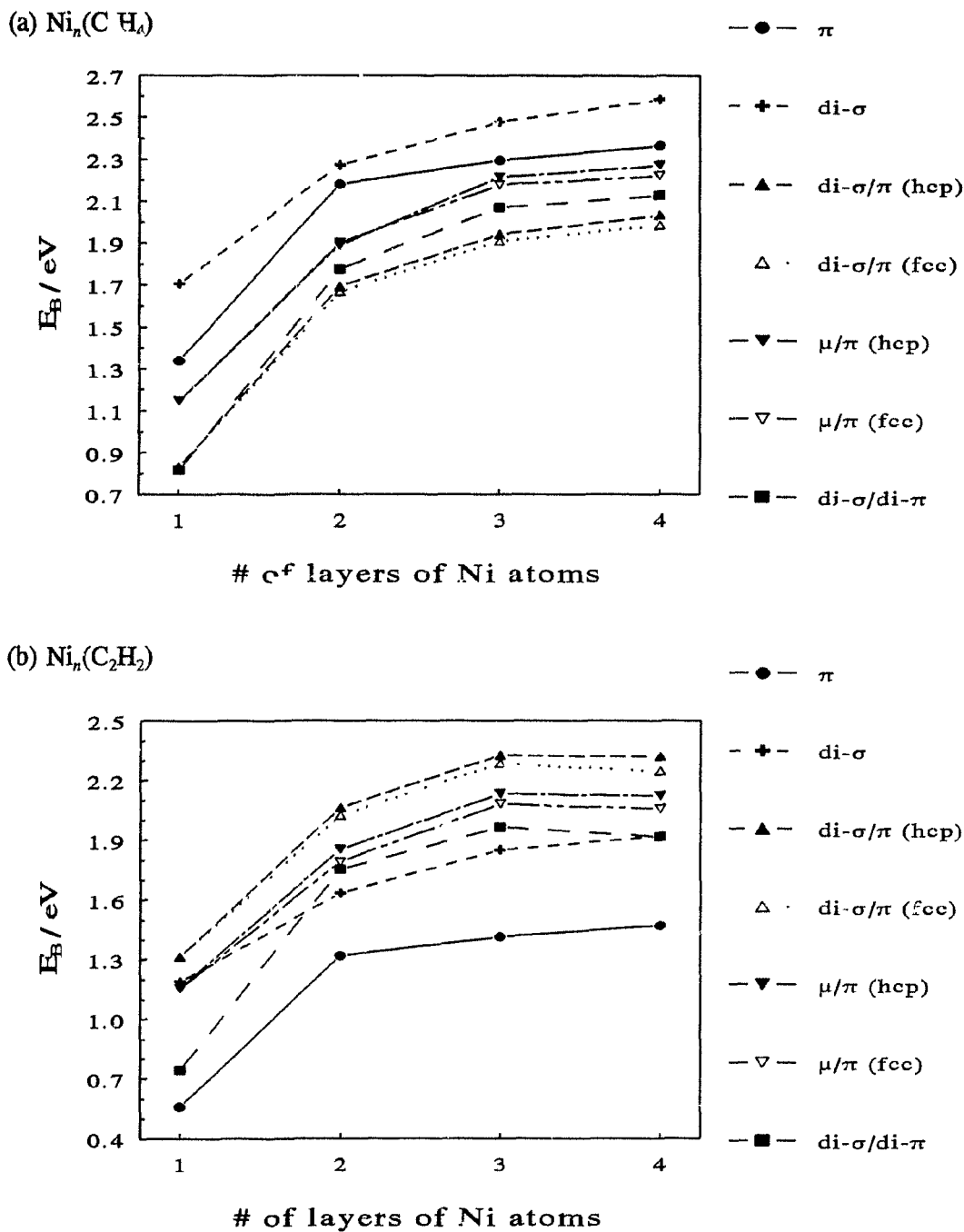


Figure 3.10 E_B as a function of $l = 1 \rightarrow 4$ for (a) C_2H_4 and (b) C_2H_2 on the $d = 14$ series of clusters, Ni_n , $n = 14, 22, 30,$ and 44 , symmetric about the centre of a unit cell of the extended lattice.

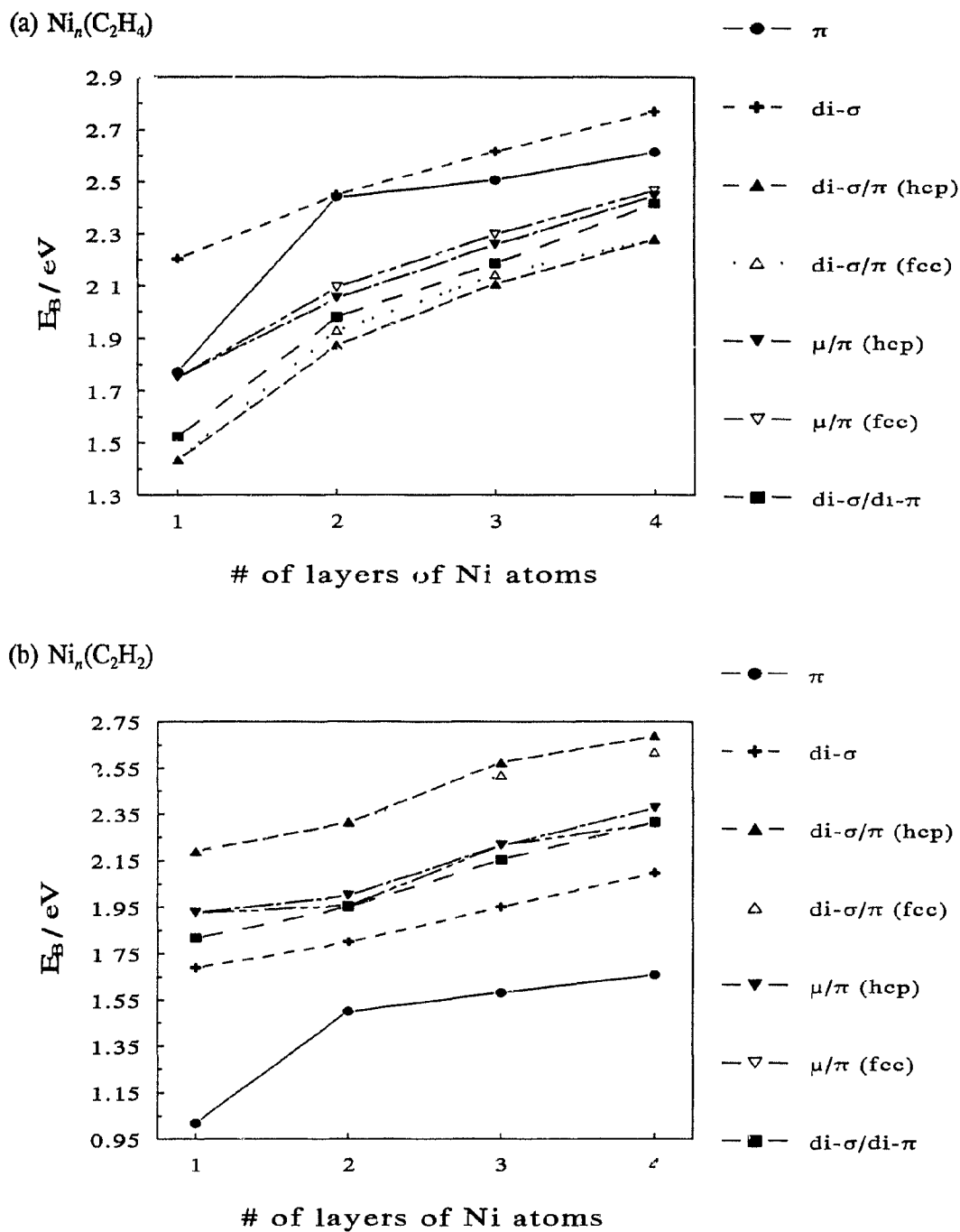


Figure 3.11 E_B as a function of $\ell = 1 \rightarrow 4$ for (a) C_2H_4 and (b) C_2H_2 on the $d = 24$ series of clusters, Ni_n , $n = 24, 40, 56$, and 80 , symmetric about the centre of a unit cell of the extended lattice.

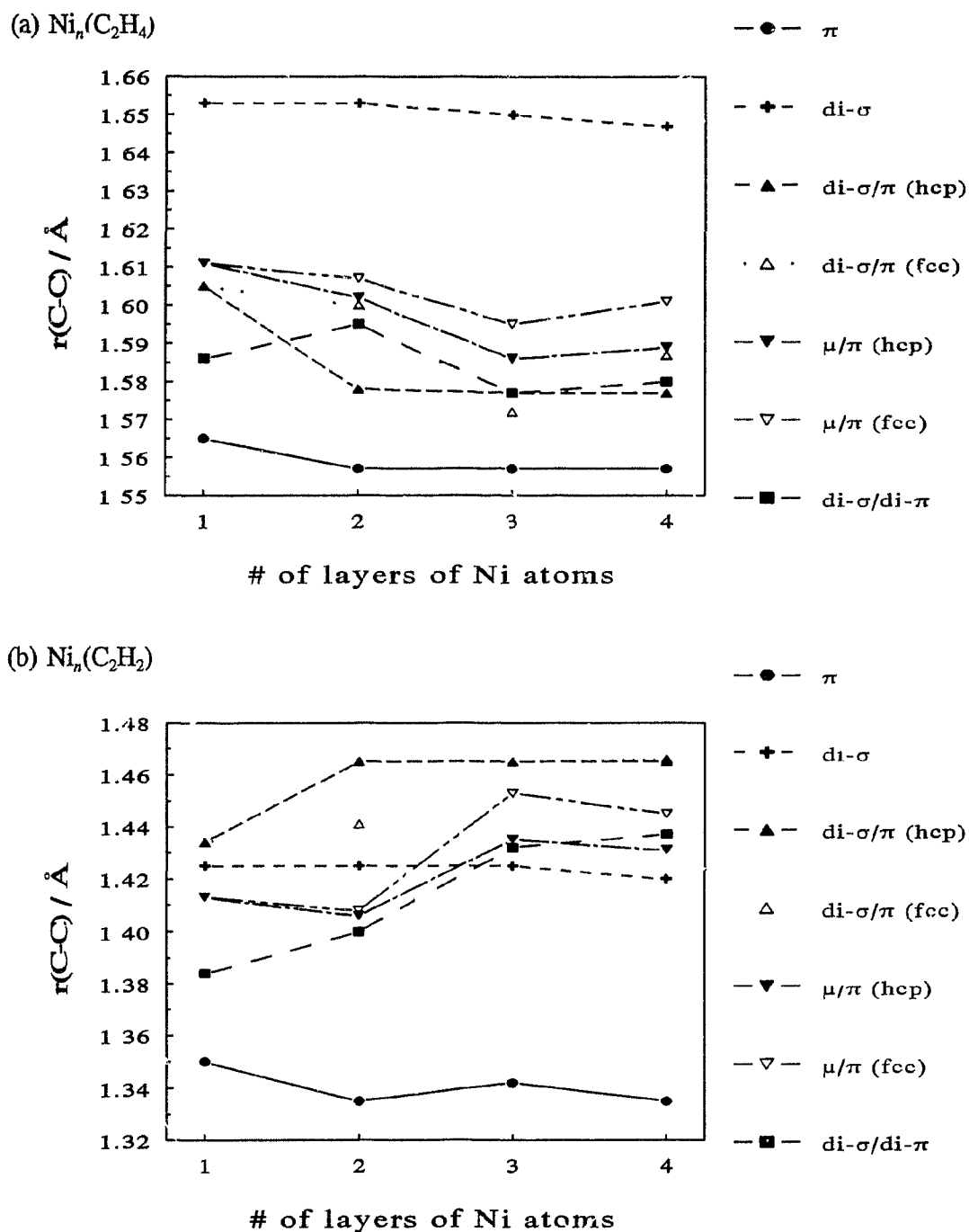


Figure 3.12 Cluster layer dependence of adsorbate structure: C—C bond distance, $r(\text{C}-\text{C})$, as a function of the number of layers of Ni atoms, $l = 1 \rightarrow 4$, for five bonding configurations of (a) C_2H_4 and (b) C_2H_2 on the $d = 4$ series of clusters, Ni_n , $n = 4, 7, 10$, and 14.

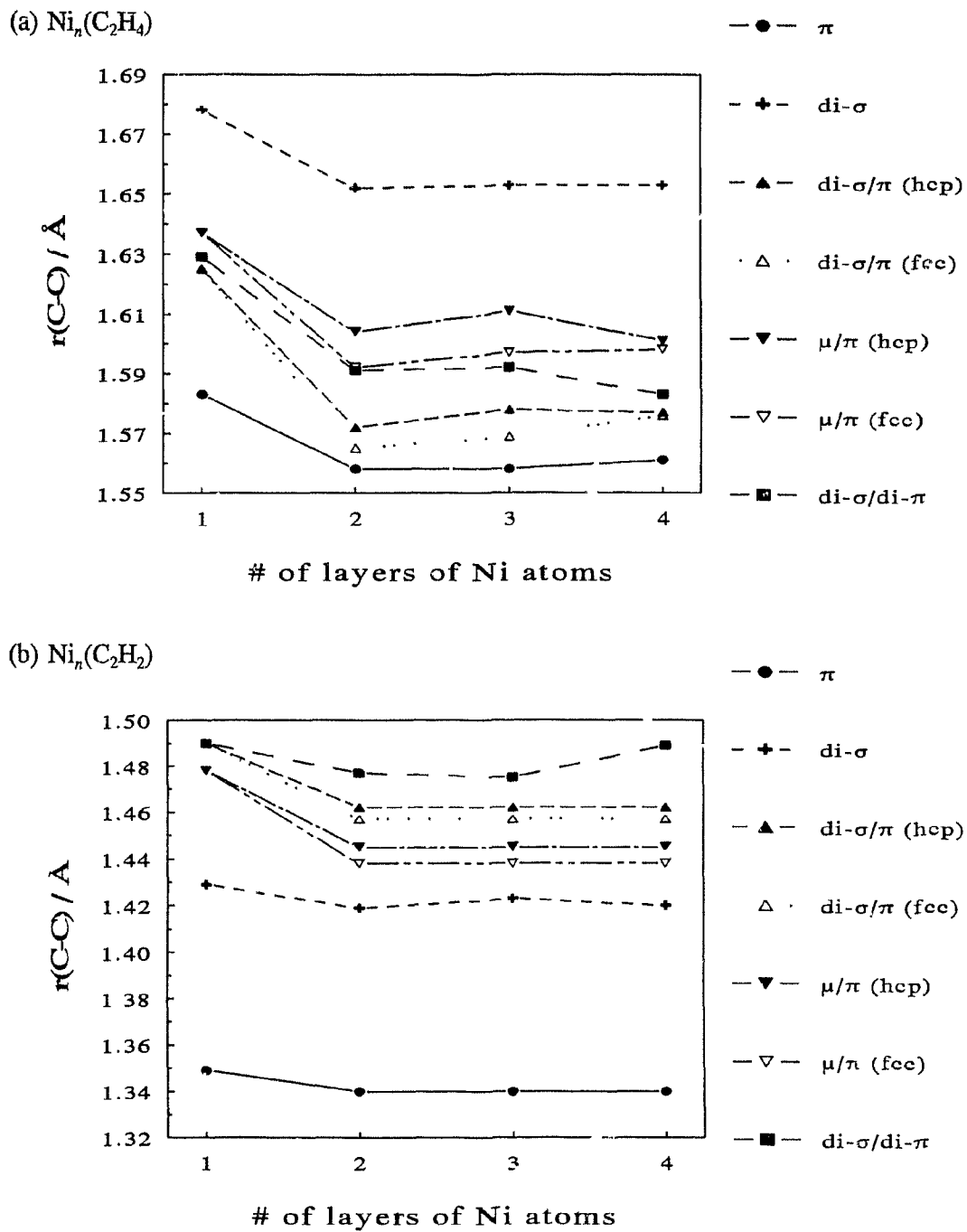


Figure 3.13 $r(\text{C}-\text{C})$ as a function of $\ell = 1 \rightarrow 4$ for (a) C_2H_4 and (b) C_2H_2 on the $d = 14$ series of Ni_n , $n = 14, 22, 30,$ and 44 .

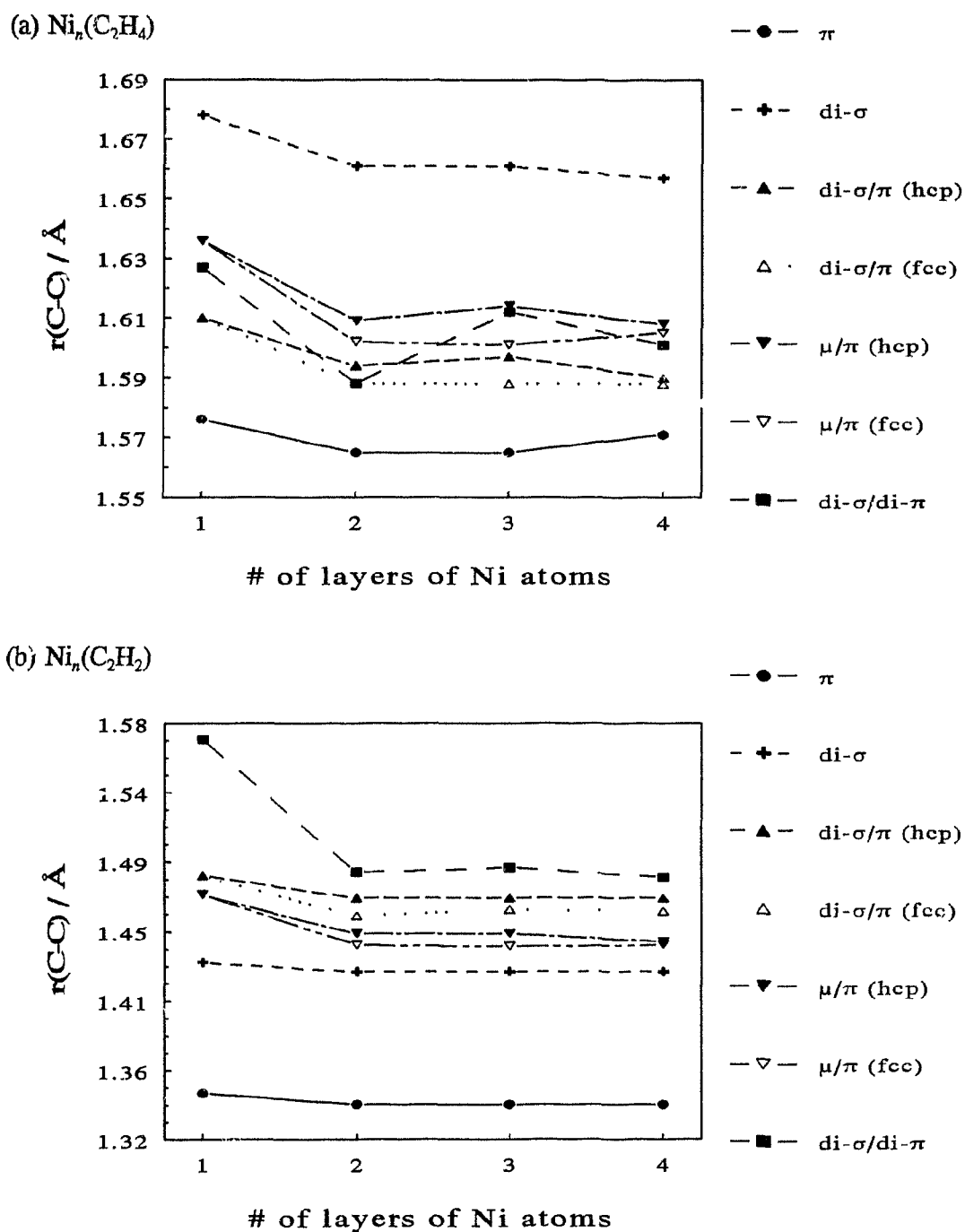


Figure 3.14 $r(\text{C}-\text{C})$ as a function of $\ell = 1 \rightarrow 4$ for (a) C_2H_4 and (b) C_2H_2 on the $d = 24$ series of Ni_n , $n = 24, 40, 56$, and 80 .

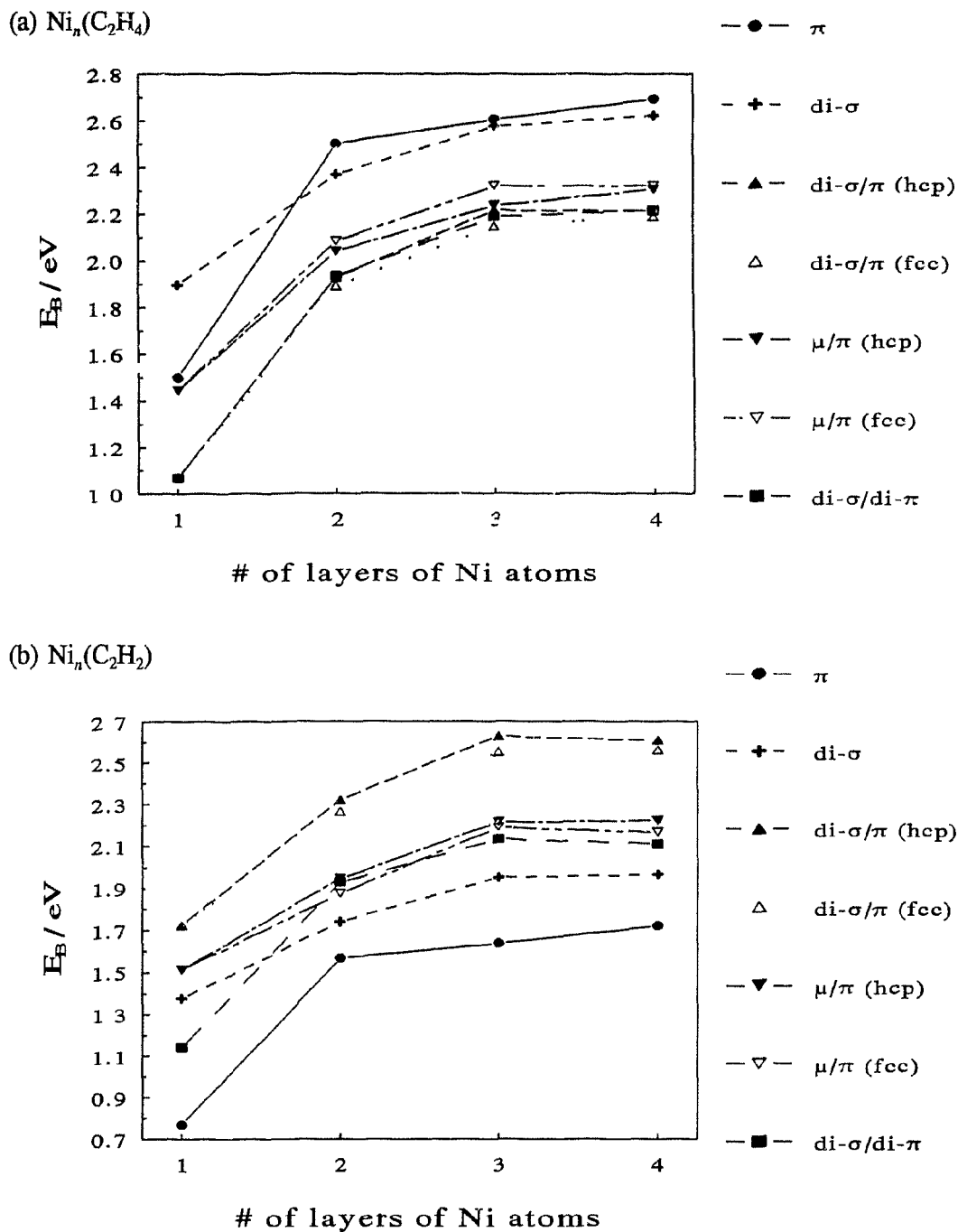


Figure 3.15 Cluster layer dependence of adsorbate relative site stabilities. E_B as a function of $\ell = 1 \rightarrow 4$ for (a) C_2H_4 and (b) C_2H_2 on the $d = 19$ series of clusters, Ni_n , $n = 19, 31, 43$, and 62 , symmetric about an individual atom of the extended lattice.

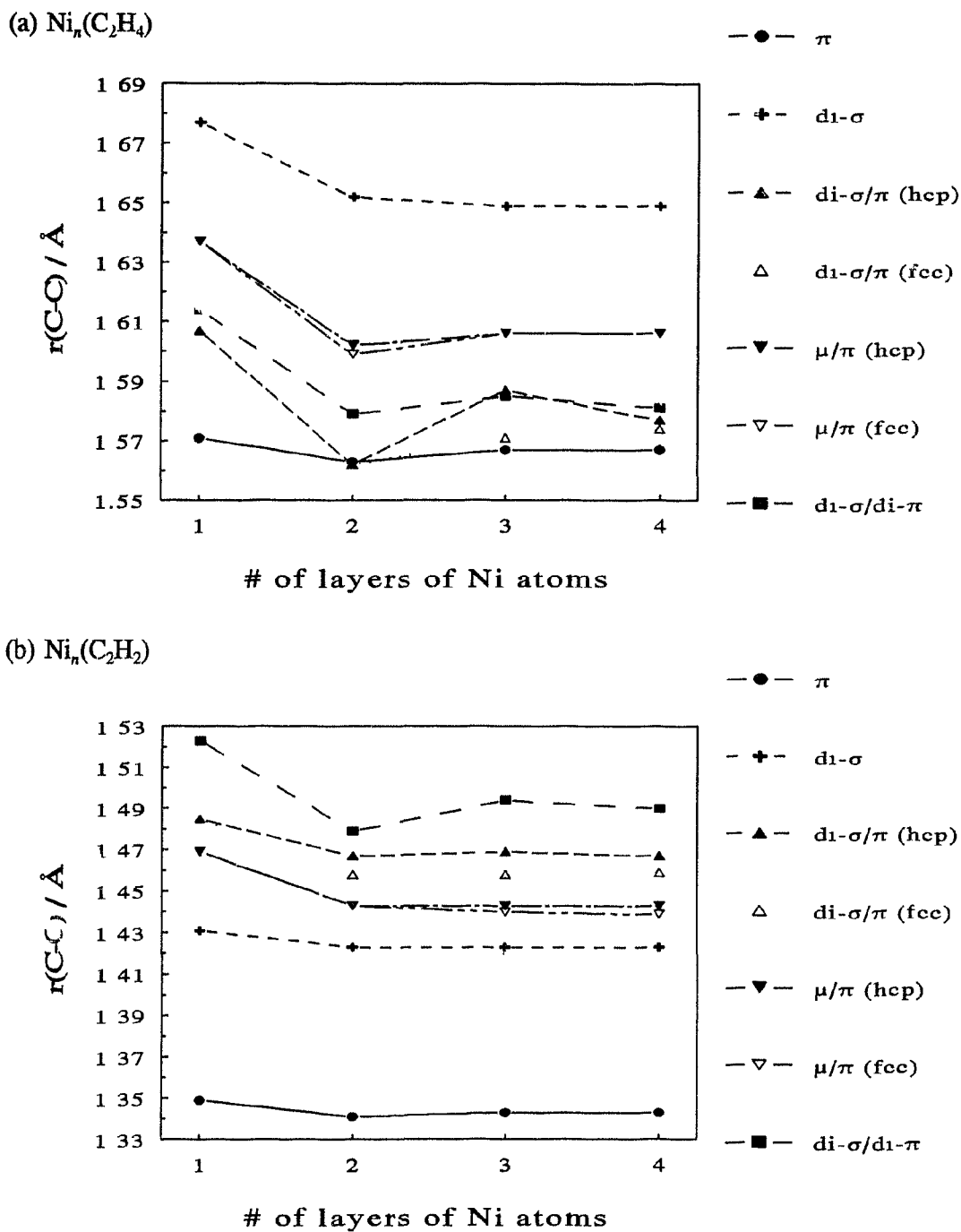


Figure 3.16 Cluster layer dependence of adsorbate structure: $r(\text{C}-\text{C})$ as a function of $\ell = 1 \rightarrow 4$ for (a) C_2H_4 and (b) C_2H_2 on the $d = 19$ series of Ni_n , $n = 19, 31, 43,$ and 62 .

d. Spin Configuration

Bulk nickel, being paramagnetic, has a spin magnetic moment of $\mu = 0.6$ Bohr magnetons/Ni atom, which suggests a high spin configuration. The cluster model of the surface, however, is finite, and hence its spin properties need not necessarily parallel those of the extended system. Artificial imposition of high spin on the cluster populates high lying antibonding orbitals, which in the bulk would be a near-continuum of vacant energy levels above the Fermi level, ϵ_F . As the number of cluster atoms increases, so too does the density of states of the d -band orbitals near ϵ_F (see Figures 3.4 and 3.5), and hence its approximation to the bulk improves. A simple, statistical mechanical assignment of thermal energy of $\sim k_B T$ to each electron makes accessible only those levels within $\sim 2 - 3 k_B T$, and hence it is unrealistic to occupy high lying levels in the cluster model to simulate the bulk magnetic moment. However, the energy levels, calculated within a one-electron theory which leaves out the exchange and correlation interactions, are approximate, as they omit the energy gain accompanying electron pairing. Arguably then, imposing spin unpairing partially counterbalances the neglect of exchange interaction in the theory, but at the cost of introducing the subjective choice of which levels to doubly, and which to singly occupy. Adopting a low-spin configuration throughout at least maintains a degree of internal consistency in the calculations, being subject only to the errors of the theoretical method, rather than a variable, ad hoc imposition of spin unpairing to mimic the exchange interaction.

Whether high- or low-spin clusters are more appropriate is debatable, but conclusions drawn from the adsorption study and the main thread of the argument for the proposed dehydrogenation mechanism should remain unaltered. All clusters in this study were restricted to be of low-spin configuration, which pairs all substrate electrons, contrary to Anderson's convention of assuming a high-spin cluster configuration [5,105], where all d -band orbitals are at least singly occupied. Clusters were kept low-spin to avoid the additional arbitrariness introduced in the calculations by the imposition of high-spin configuration, *e.g.*, when to use high spin, how to determine the number of unpaired electrons, within what energy bandwidth to singly occupy orbitals, etc. The qualitative invariance of the results between low- and high-spin configurations has been explored and corroborated, for reasonably-sized clusters, justifying the more convenient low-spin convention. The sensitivity on the cluster spin unpairing of the adsorption parameters for C_2H_4 and C_2H_2 is documented presently, while that of the proposed dehydrogenation mechanism is postponed until Chapter 4.

Figures 3.17 - 3.22 plot, as a function of the number of unpaired electrons, s , in the Ni cluster, the net energy changes, ΔE_{spin} , upon adsorption for the systems, $Ni_n(C_2H_x)$, $x = 2$ and 4, equal to the difference between the adsorbate binding energy and the cost of spin unpairing in the substrate. *i.e.*,

$$\Delta E_{spin} = E_B - E(\text{spin unpairing}) , \quad (3.2)$$

where

$$E(\text{spin unpairing}) = E[Ni_n(\text{high spin})] - E[Ni_n(\text{low spin})] ; \quad (3.3)$$

while Figures 3.23 - 3.28 show the corresponding C-C bond distances, $r(C-C)$'s.

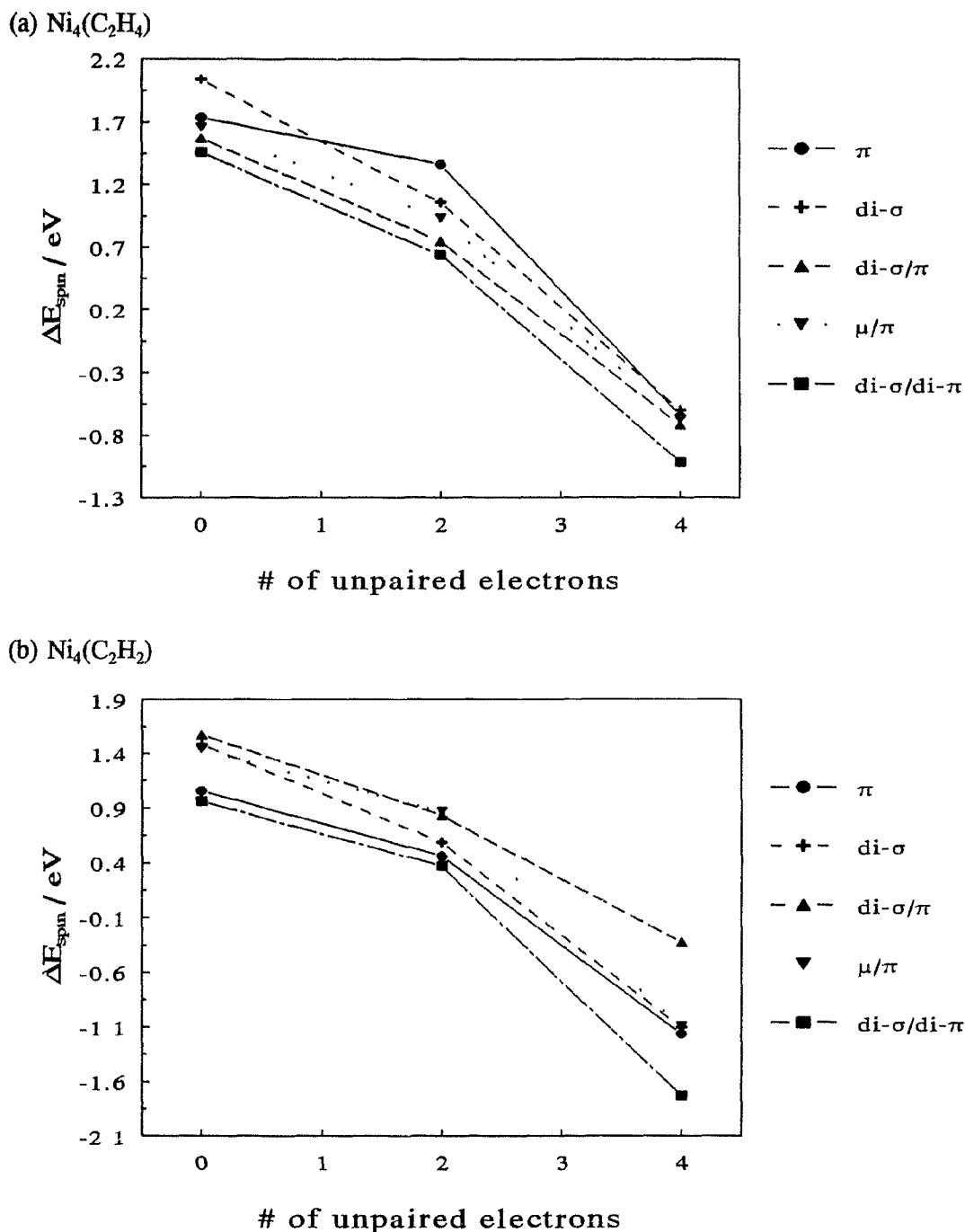


Figure 3.17 Effect of spin unpairing on adsorbate relative site stabilities: net energy change upon adsorption, ΔE_{spin} , as a function of the number of unpaired electrons, s , for five bonding configurations of (a) C_2H_4 and (b) C_2H_2 on the $d = 4$, $\ell = 1$ cluster, Ni_4 .

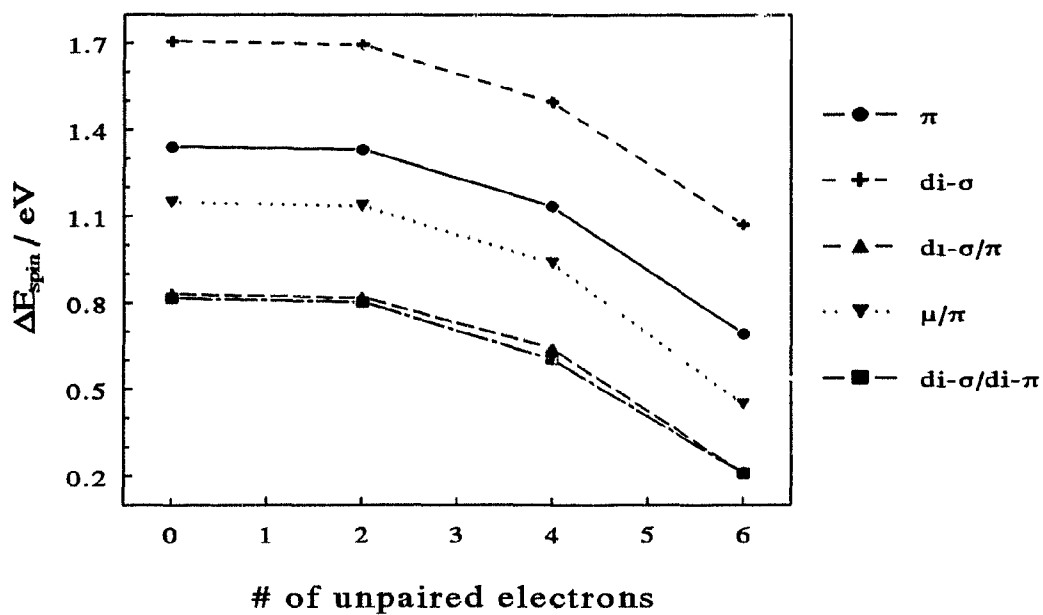
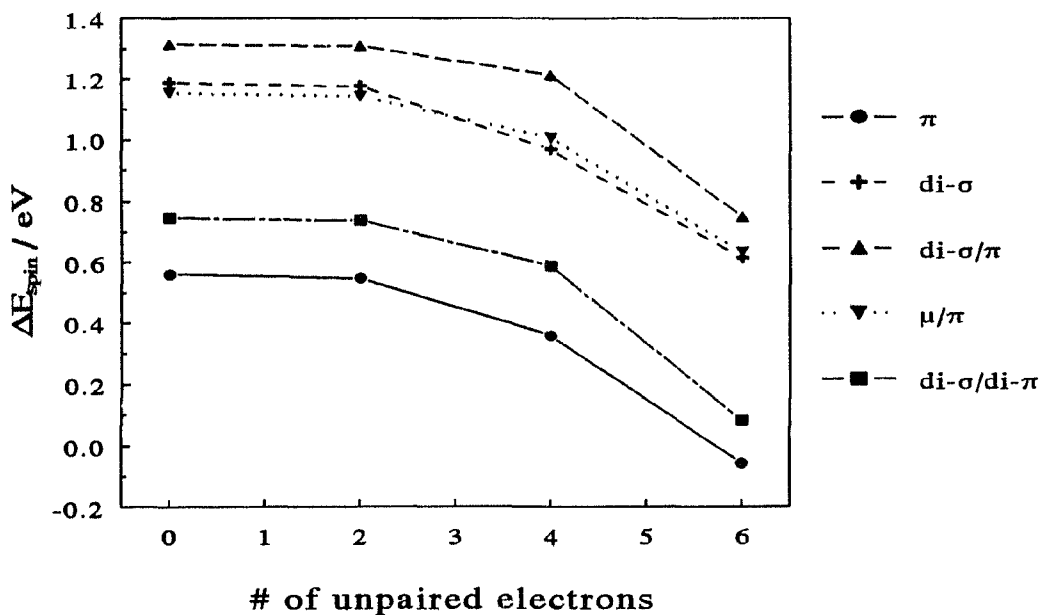
(a) $\text{Ni}_{14}(\text{C}_2\text{H}_4)$ (b) $\text{Ni}_{14}(\text{C}_2\text{H}_2)$ 

Figure 3.18 ΔE_{spin} as a function of s for (a) C_2H_4 and (b) C_2H_2 on the $d = 14$, $\ell = 1$ cluster, Ni_{14} .

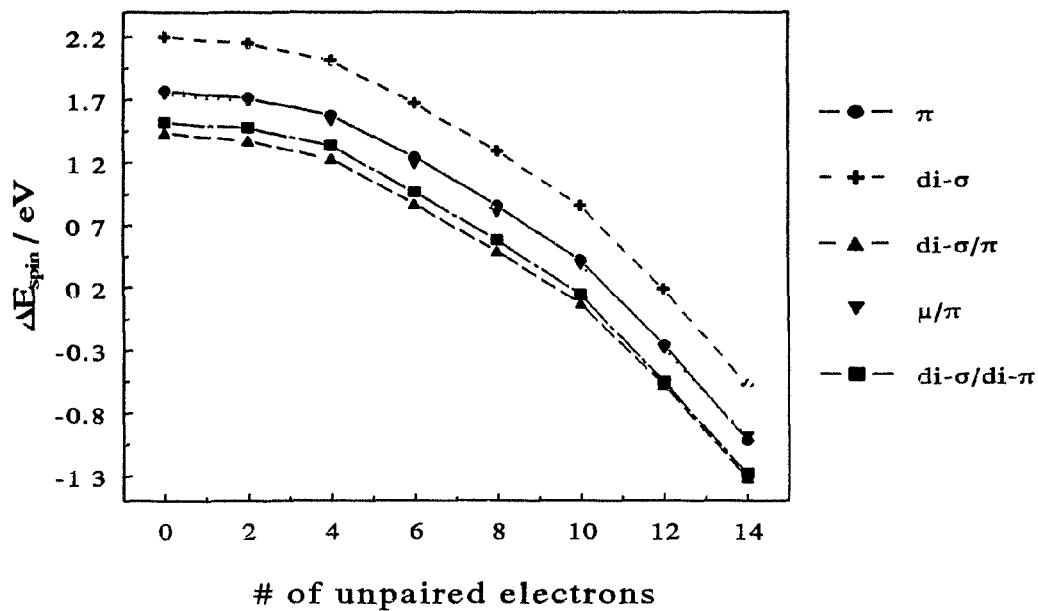
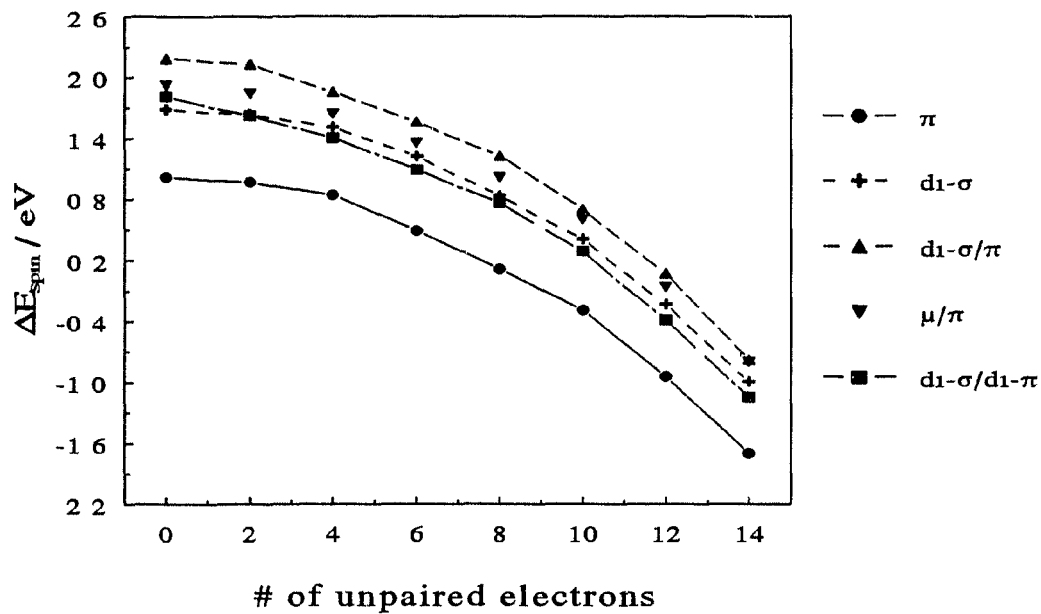
(a) $\text{Ni}_{24}(\text{C}_2\text{H}_4)$ (b) $\text{Ni}_{24}(\text{C}_2\text{H}_2)$ 

Figure 3.19 ΔE_{spin} as a function of s for (a) C_2H_4 and (b) C_2H_2 on the $d = 24$, $\ell = 1$ cluster, Ni_{24} .

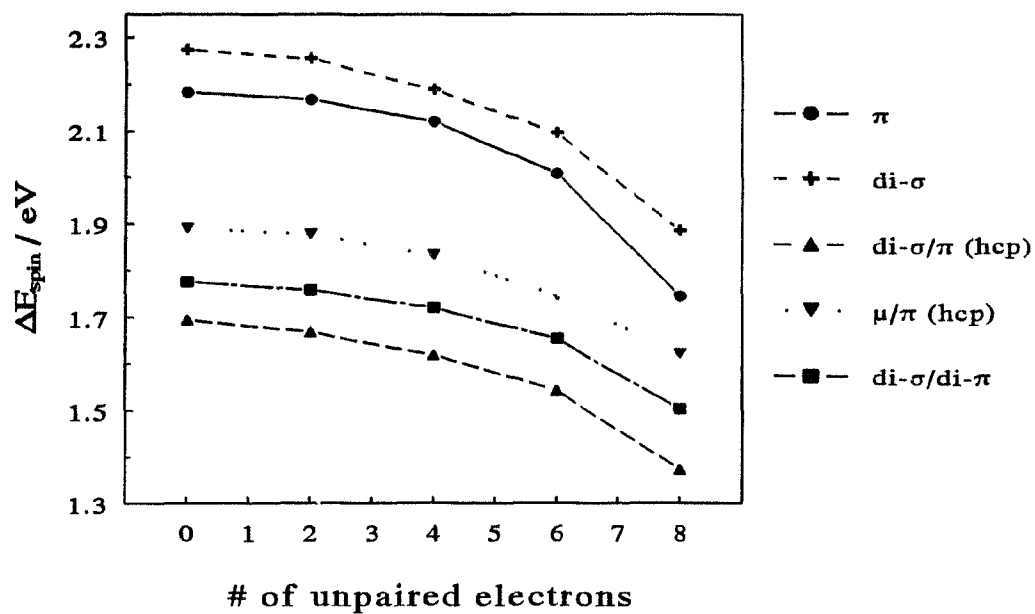
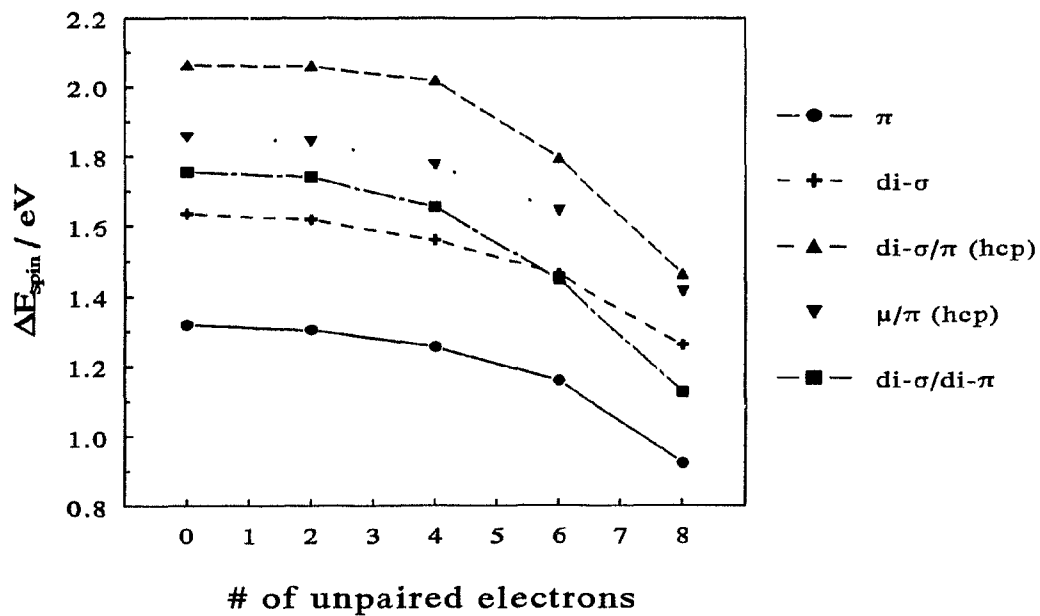
(a) $\text{Ni}_{22}(\text{C}_2\text{H}_4)$ (b) $\text{Ni}_{22}(\text{C}_2\text{H}_2)$ 

Figure 3.20 ΔE_{spin} as a function of s for (a) C_2H_4 and (b) C_2H_2 on the $d = 14$, $\ell = 2$, (14/8) cluster, Ni_{22} .

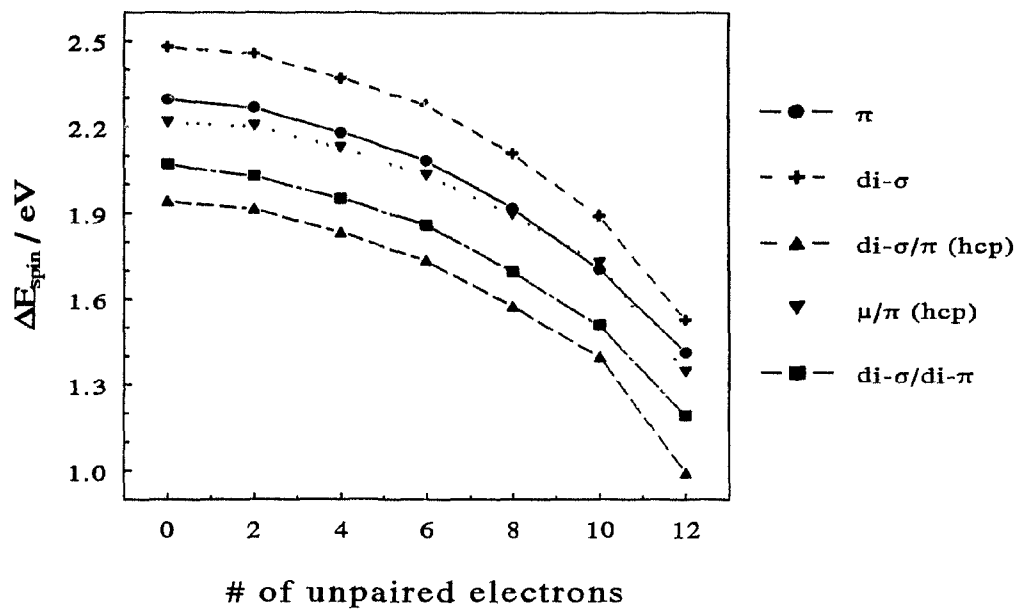
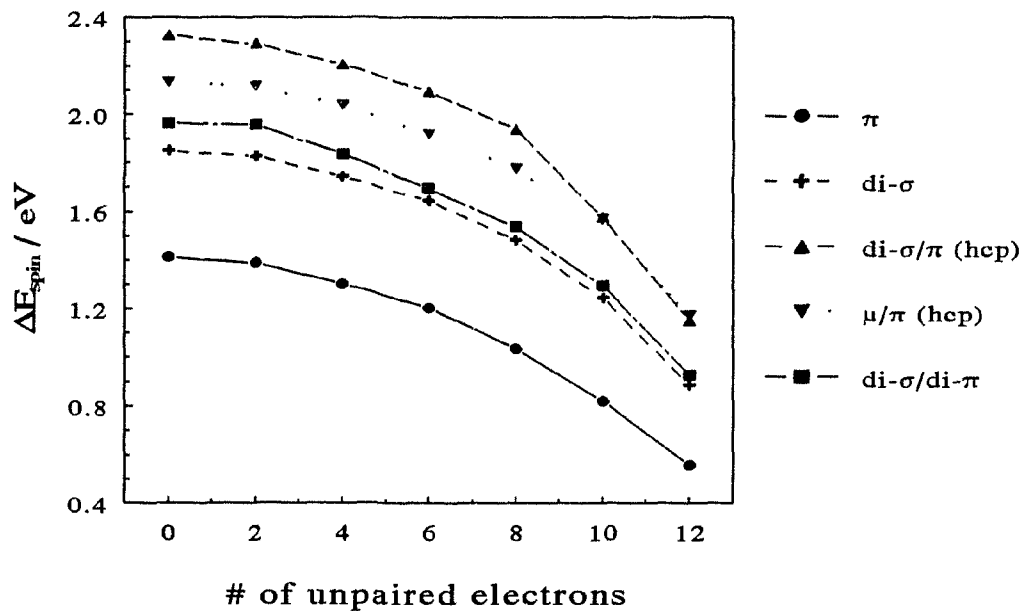
(a) $\text{Ni}_{30}(\text{C}_2\text{H}_4)$ (b) $\text{Ni}_{30}(\text{C}_2\text{H}_2)$ 

Figure 3.21 ΔE_{spin} as a function of s for (a) C_2H_4 and (b) C_2H_2 on the $d = 14$, $l = 3$, $(14/8/8)$ cluster, Ni_{30} .

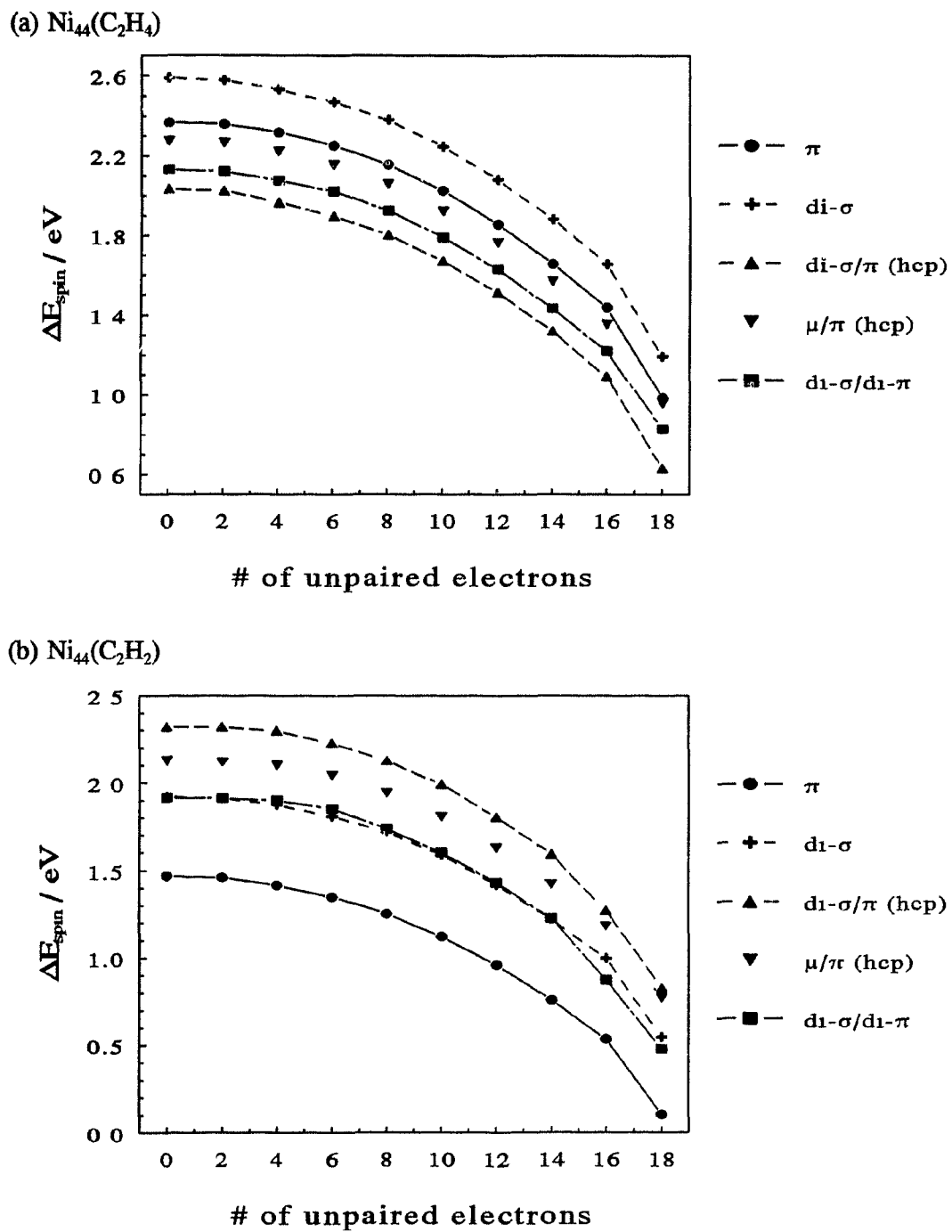


Figure 3.22 ΔE_{spin} as a function of s for (a) C_2H_4 and (b) C_2H_2 on the $d = 14$, $\ell = 4$, (14/8/8/14) cluster, Ni_{44} .

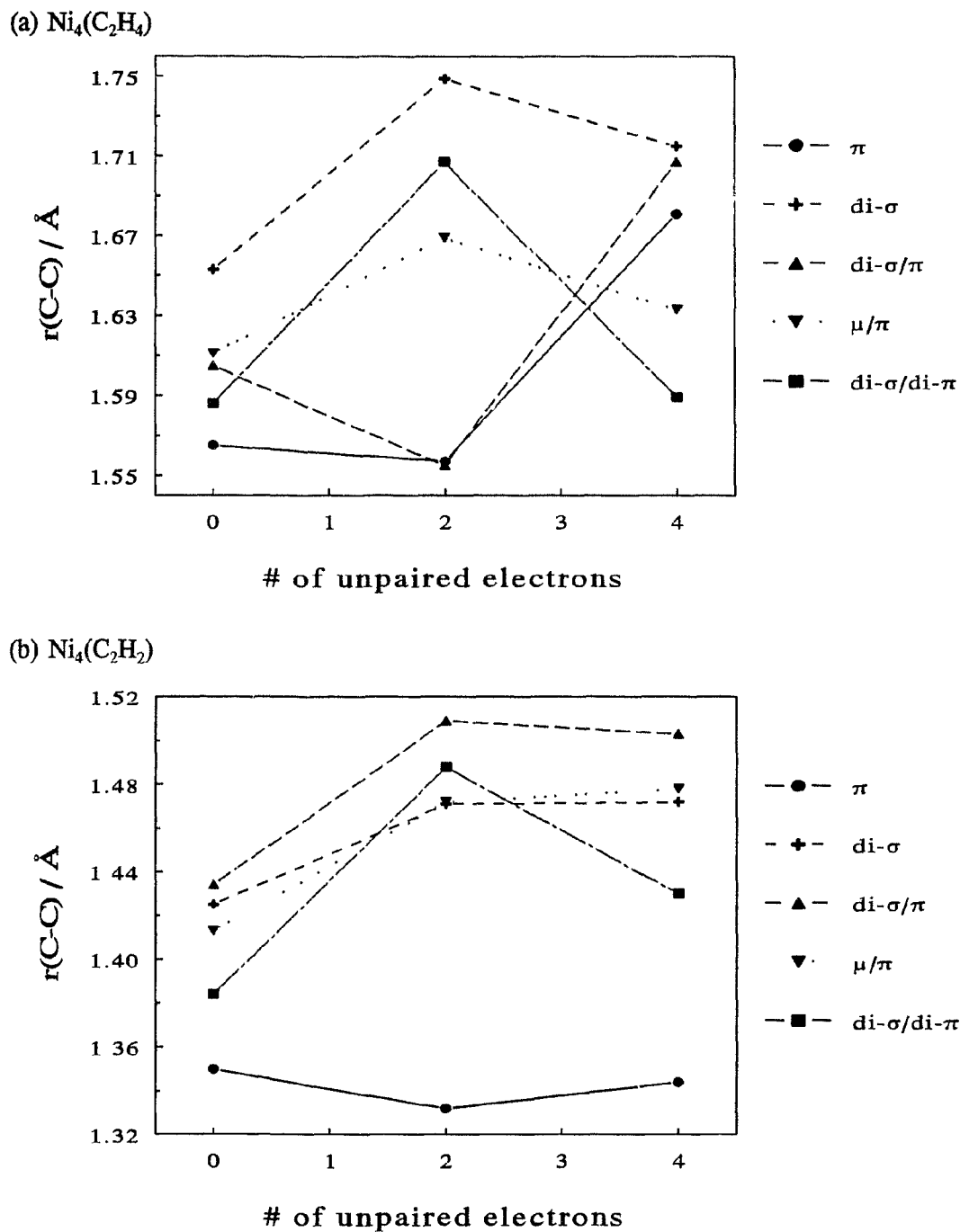


Figure 3.23 Effect of cluster spin unpairing on adsorbate structure: C–C bond distance, $r(\text{C}-\text{C})$, as a function of the number of unpaired electrons, s , for five bonding configurations of (a) C_2H_4 and (b) C_2H_2 on the $d = 4$, $l = 1$ cluster, Ni_4 .

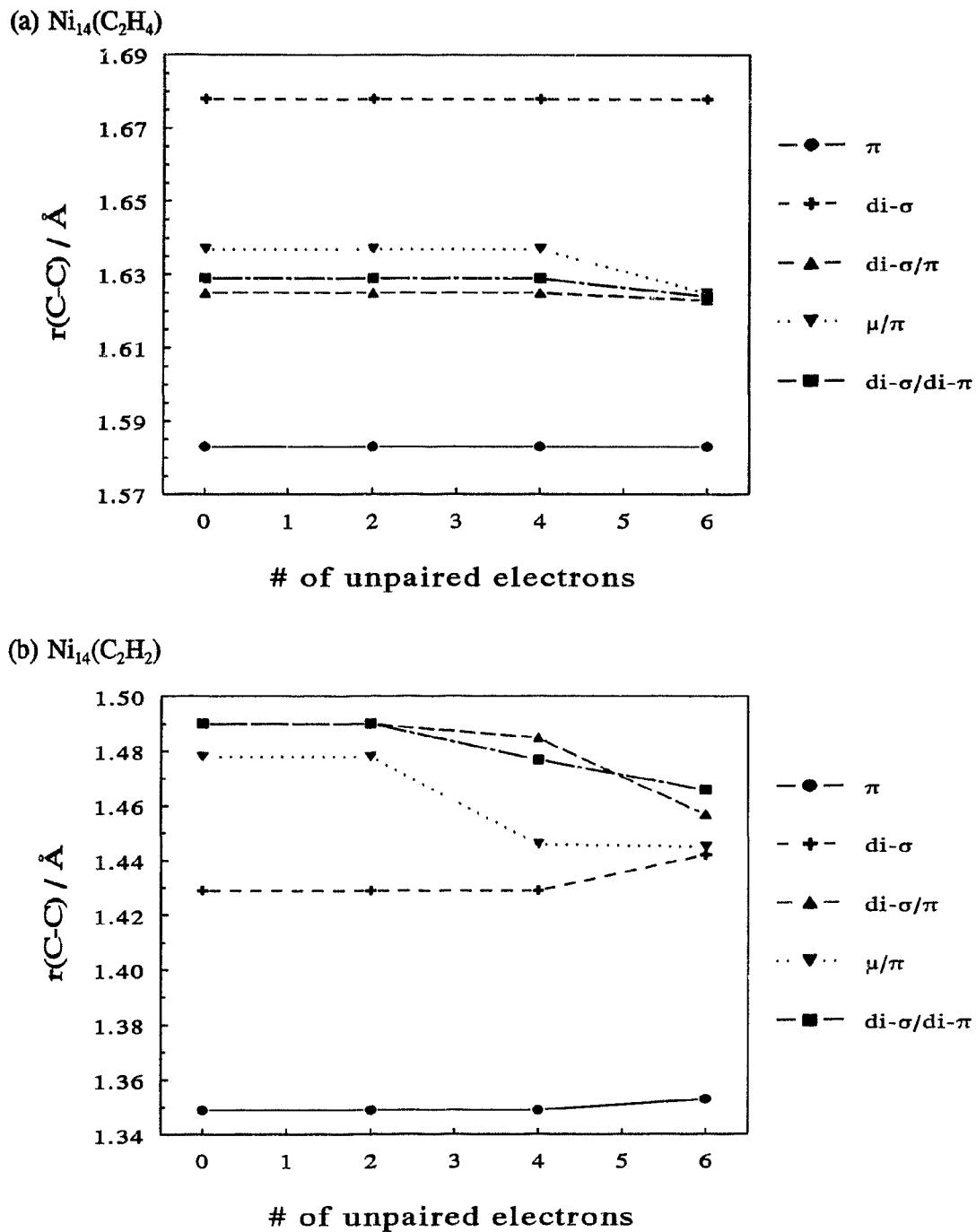


Figure 3.24 $r(\text{C}-\text{C})$ as a function of s for (a) C_2H_4 and (b) C_2H_2 on the $d = 14$, $\ell = 1$ cluster, Ni_{14} .

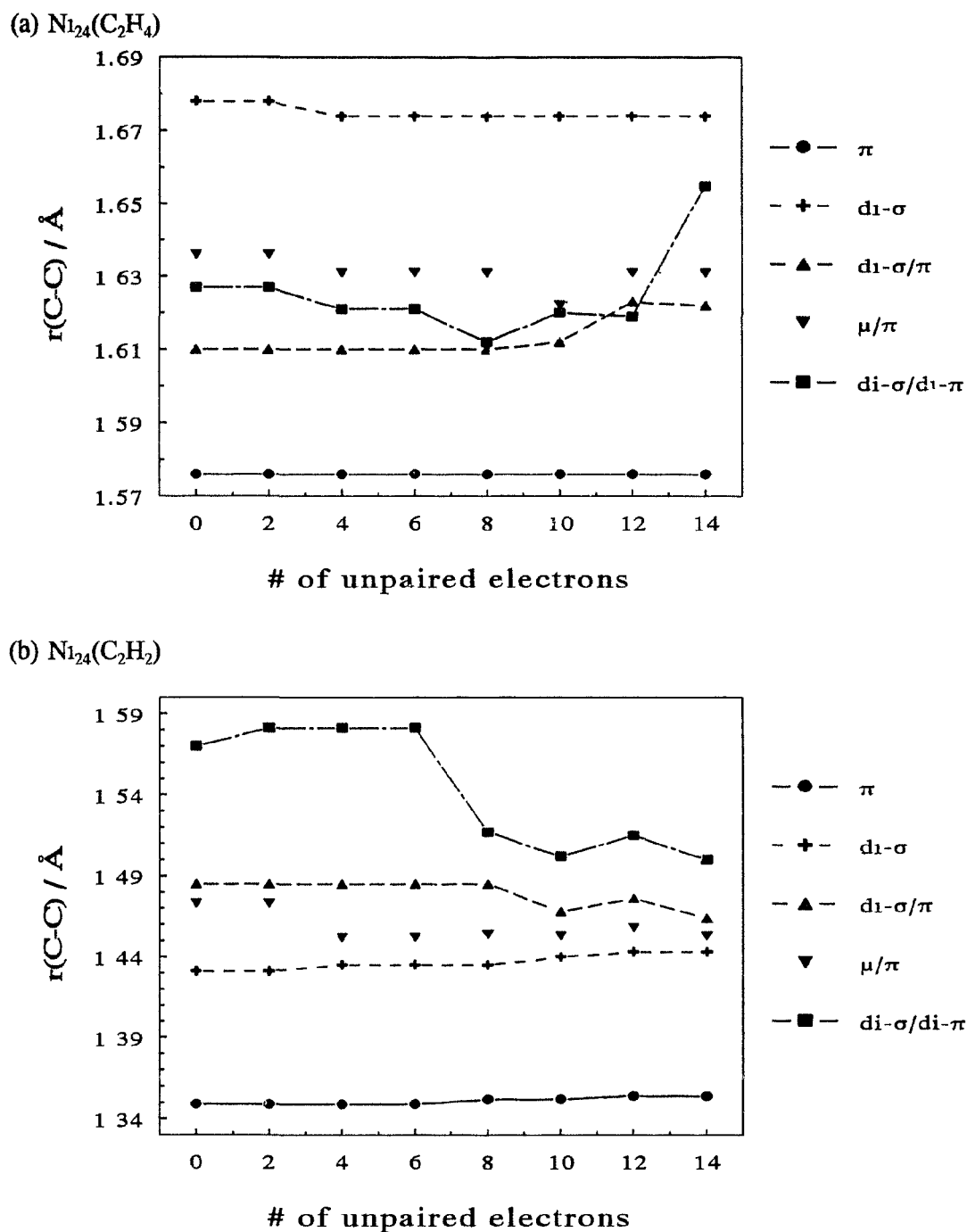


Figure 3.25 $r(\text{C}-\text{C})$ as a function of s for (a) C_2H_4 and (b) C_2H_2 on the $d = 24$, $\ell = 1$ cluster, Ni_{24} .

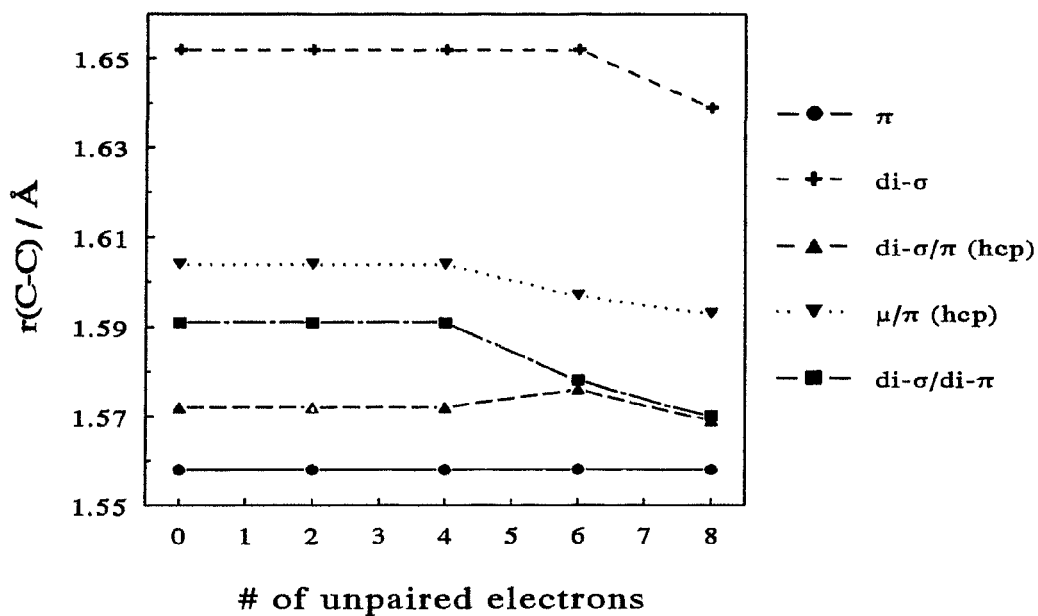
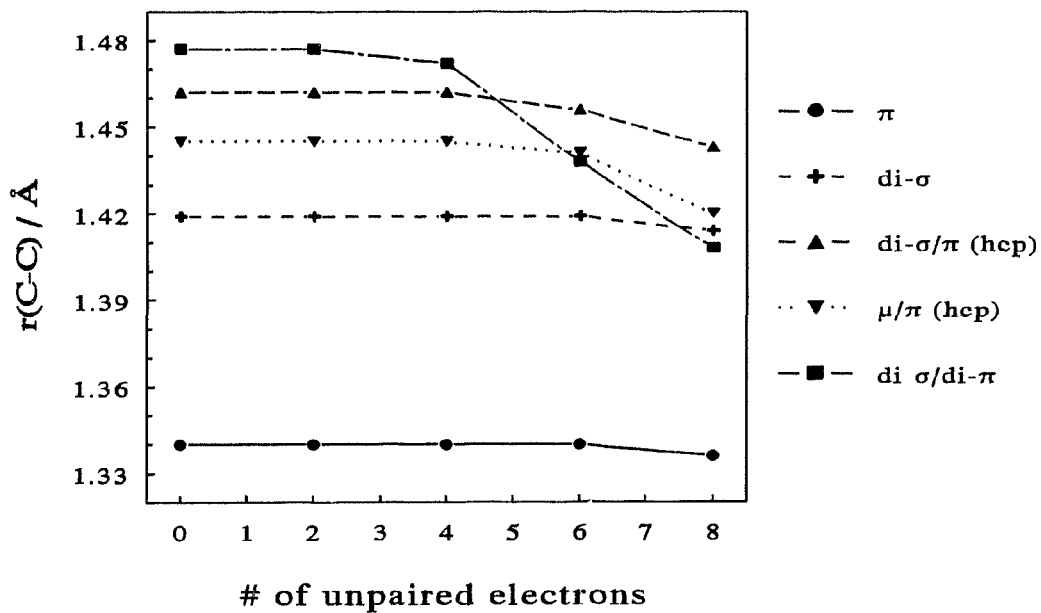
(a) $\text{Ni}_{22}(\text{C}_2\text{H}_4)$ (b) $\text{Ni}_{22}(\text{C}_2\text{H}_2)$ 

Figure 3.26 $r(\text{C}-\text{C})$ as a function of s for (a) C_2H_4 and (b) C_2H_2 on the $d = 14$, $\ell = 2$, (14/8) cluster, Ni_{22} .

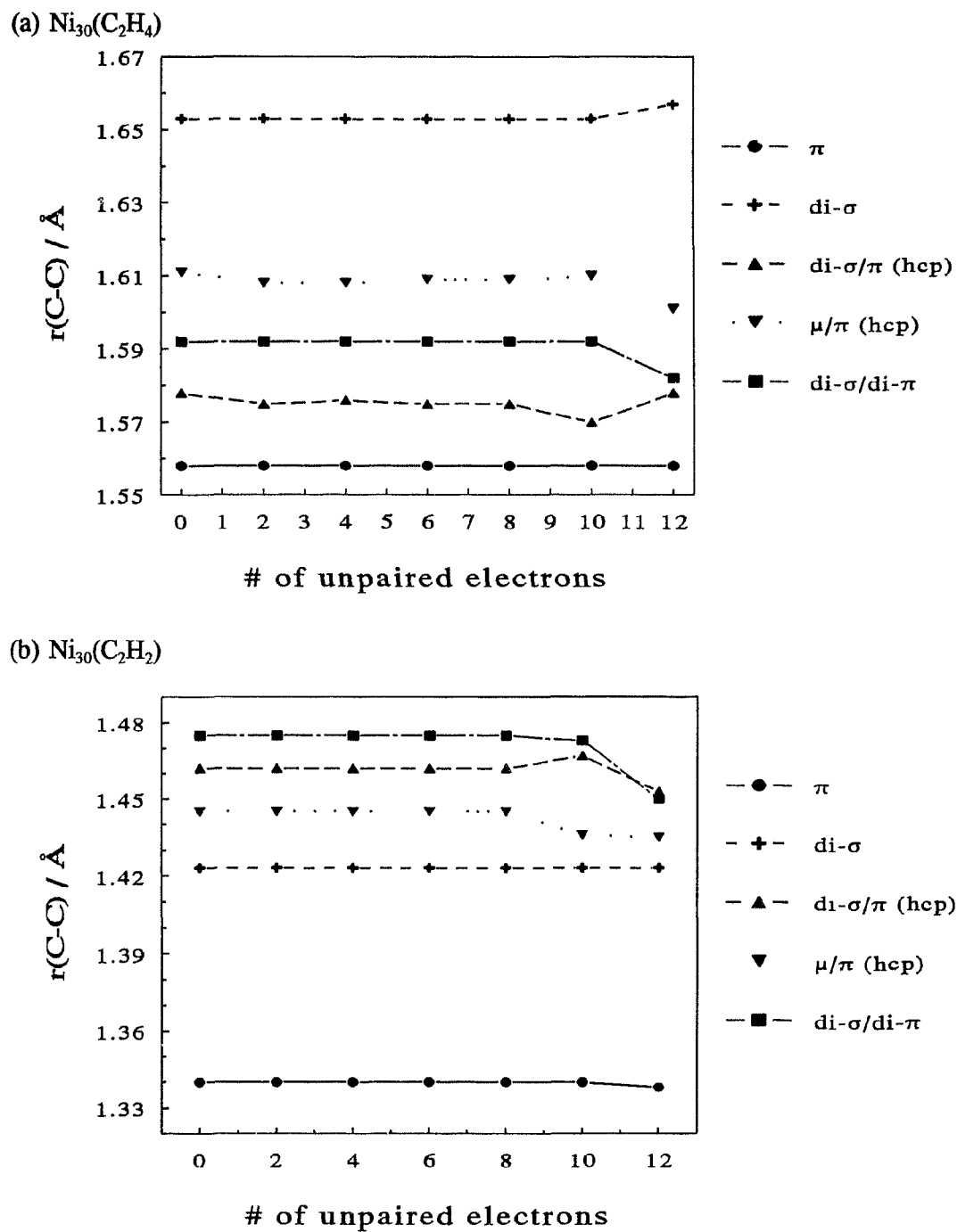


Figure 3.27 $r(\text{C}-\text{C})$ as a function of s for (a) C_2H_4 and (b) C_2H_2 on the $d = 14$, $\ell = 3$, (14/8/8) cluster, Ni_{30} .

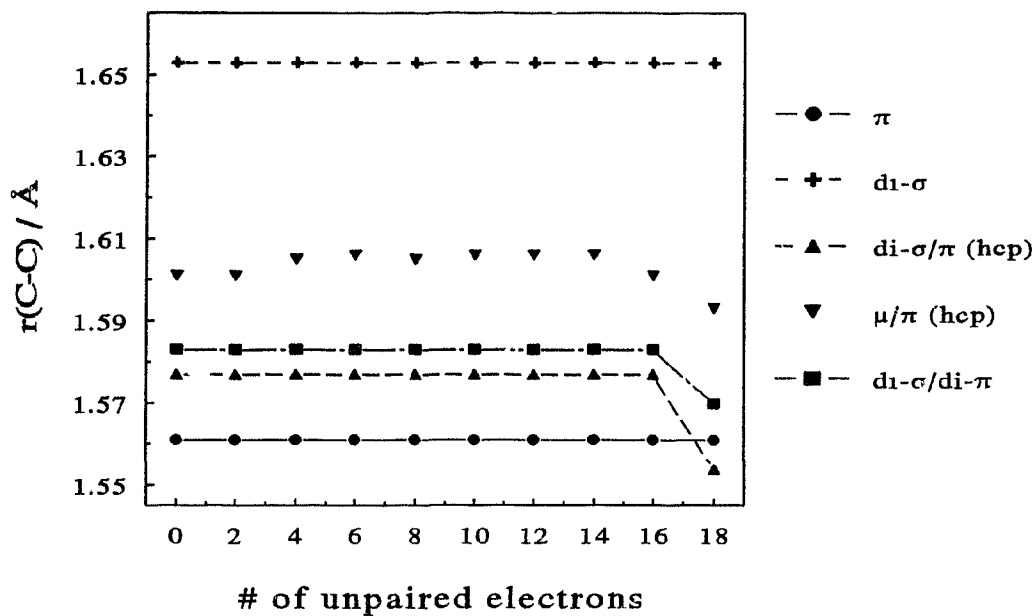
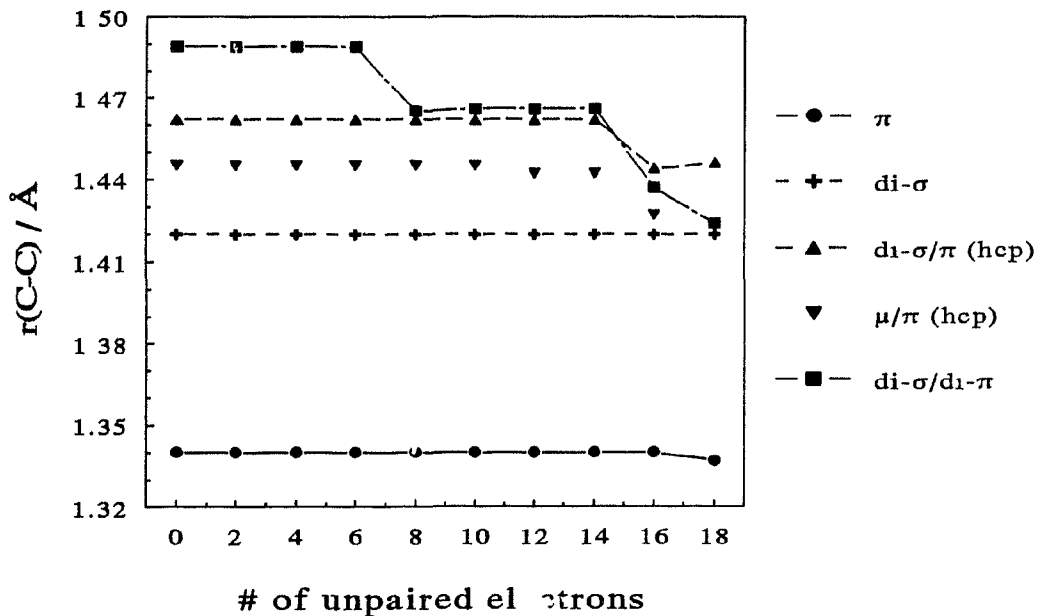
(a) $\text{Ni}_{44}(\text{C}_2\text{H}_4)$ (b) $\text{Ni}_{44}(\text{C}_2\text{H}_2)$ 

Figure 3.28 $r(\text{C}-\text{C})$ as a function of s for (a) C_2H_4 and (b) C_2H_2 on the $d = 14$, $\ell = 4$, (14/8/8/14) cluster, Ni_{44} .

The effects of cluster spin unpairing are examined in Figures 3.17 – 3.19 and 3.23 – 3.25 as the lateral extent of the surface layer is increased, $d = 4, 14,$ and $24,$ while Figures 3.18 plus 3.20 – 3.22 and 3.24 plus 3.26 – 3.28 focus on its layer dependence for the $d = 14$ series, $\ell = 1 \rightarrow 4.$ For $C_2H_4,$ the energetic ordering and differences of the various adsorption sites are maintained for all but the atop and di- σ sites on the smallest $d = 4$ series, as shown in Figures 3.17 – 3.19 (a), while subtle reversals in site stability ordering are observed for C_2H_2 in Figures 3.17 – 3.19 (b). The C–C bond distances, as demonstrated in Figures 3.23 – 3.25, are extremely sensitive to s on the smallest cluster series, but perturbing effects with spin unpairing lessen on the clusters of greater lateral extent for both molecules, with C_2H_2 again affected more; *cf.* (a) and (b). The addition of successive layers improves the stability of both the energetic and structural results, as Figures 3.18 plus 3.20 – 3.22 and 3.24 plus 3.26 – 3.28 attest.

2. Coordinate Variable Changes

The cluster dependence along various coordinate variable changes, relevant to the study of the dehydrogenation mechanism, was also ascertained. Figures 3.29 and 3.30 (pp. 102 and 103) show the relative energy change, $\Delta E,$ and C–C bond distance, $r(C-C),$ respectively, as functions of simultaneous parametric lengthening of two *trans* C–H bonds, $\Delta r(C-H),$ of di- σ -bonded C_2H_4 on two series of one- to four-layered clusters of differing lateral extent, $d = 4$ and $14.$ Little distinguishes the curves, within and across both cluster series, with the exception of the overestimation, as compared with

values on other clusters, of $r(\text{C}-\text{C})$ on the $n = 14$, $\ell = 1$ cluster. Figures 3.31 - 3.34 (pp. 104 - 107) display the results of a similar investigation of ΔE and $r(\text{C}-\text{C})$ as functions of rotation about an axis through the centre of the $\text{C}-\text{C}$ bond and perpendicular to the surface, $\Delta\phi_{\text{C}}$, for di- σ -bonded C_2H_4 and C_2H_2 . Qualitatively, the ΔE and $r(\text{C}-\text{C})$ curves in Figures 3.31 and 3.32 for C_2H_4 are quite similar, though their values can vary with both d and ℓ , as seen most conspicuously for the $n = 14$, $\ell = 1$ cluster; for C_2H_2 , the ΔE and $r(\text{C}-\text{C})$ curves of Figures 3.33 and 3.34 differed even qualitatively with d and ℓ , with a cluster-dependent reversal in the stability ordering of the di- σ and μ sites, corresponding to $\Delta\phi_{\text{C}} = 0.0^\circ$ and 90.0° , respectively.

In summary, the adsorption site stability ordering and optimized structures for acetylene and ethylene, as well as relative energy and geometrical variable changes along some coordinate parameters, were sensitive to the cluster model, the former more than the latter in both cases. While the surface is modelled throughout as a low-spin cluster with zero unpaired electrons, selected calculations repeated on clusters of high spin yielded identical qualitative conclusions. Approximate qualitative and quantitative convergence of results is obtained with symmetric, three-layered clusters comprised of a surface layer which includes the unit cell constituting the adsorption site and its first coordination shell. Clusters obeying these criteria were henceforth adopted as a practical compromise between desired accuracy and computational economy. Addition of a fourth cluster layer did still perceptibly alter the calculated values, however, showing that, despite the local nature of the chemisorption bond, substrate atoms quite distant from the adsorbate exert an indirect influence by affecting the model representation of the surface.

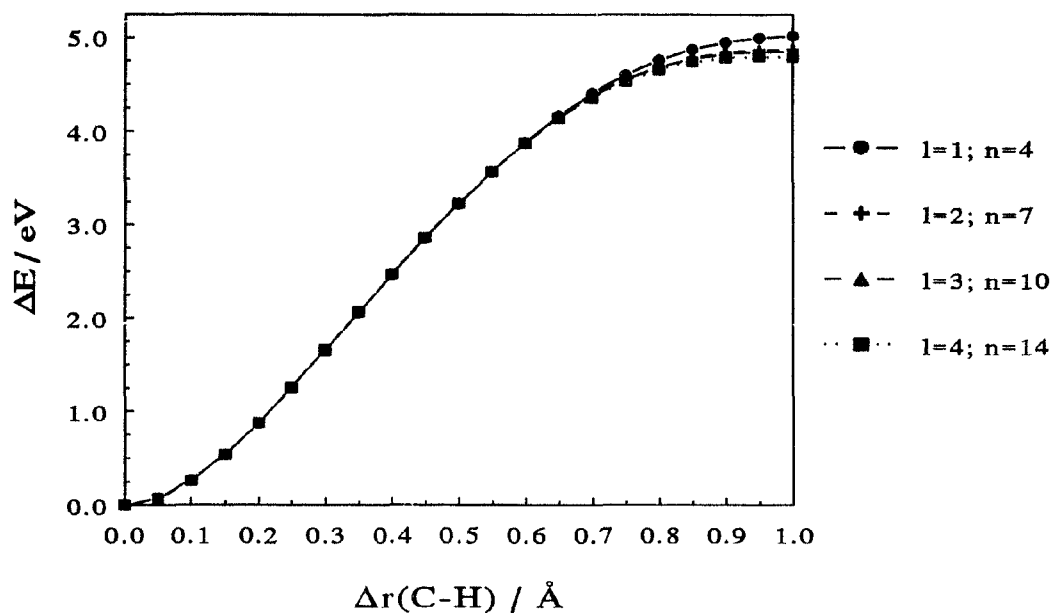
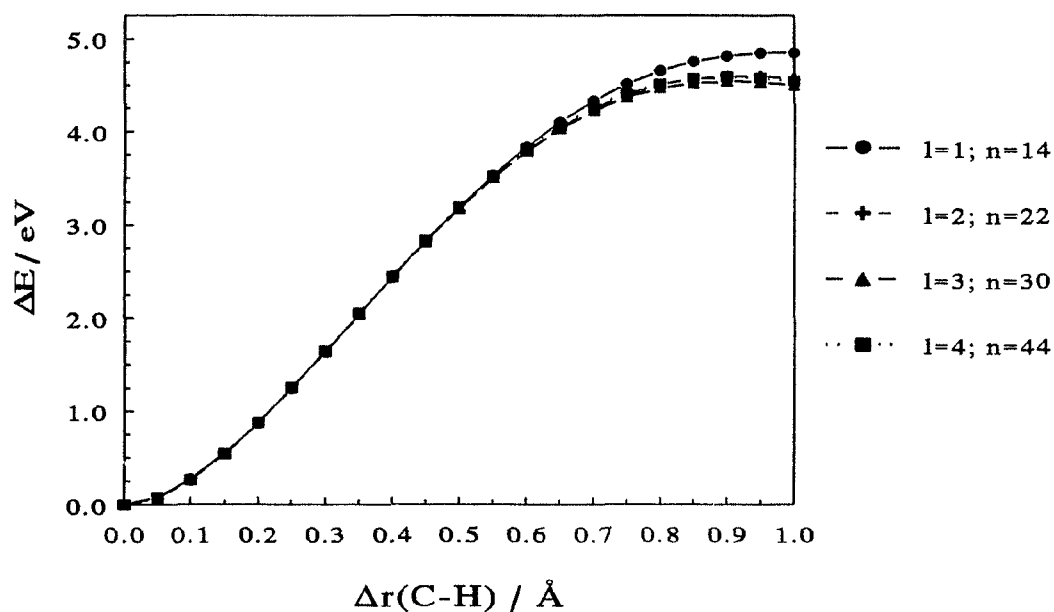
(a) $d = 4$ (b) $d = 14$ 

Figure 3.29 Cluster layer and lateral extent dependence along parametric coordinate variable changes: relative energy change, ΔE , as a function of C-H bond stretch, $\Delta r(\text{C-H})$, for C_2H_4 on two series of Ni clusters, Ni_n , for $l = 1 \rightarrow 4$, (a) $d = 4$; $n = 4, 7, 10$, and 14 , and (b) $d = 14$; $n = 14, 22, 30$, and 44 .

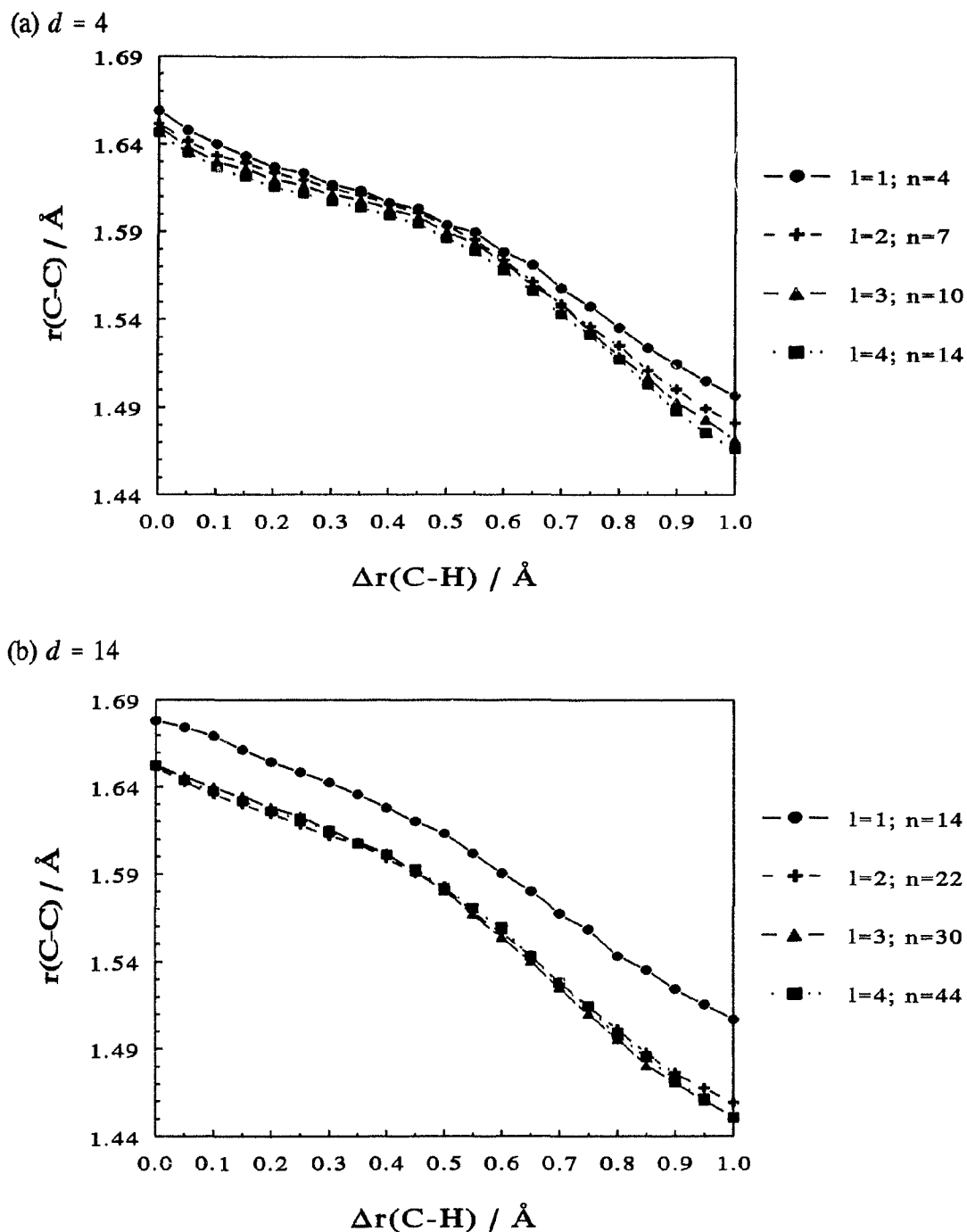


Figure 3.30 $r(\text{C-C})$ as a function of $\Delta r(\text{C-H})$ for C_2H_4 on two series of Ni_n , $l = 1 \rightarrow 4$: (a) $d = 4$; $n = 4, 7, 10$, and 14 , and (b) $d = 14$; $n = 14, 22, 30$, and 44 .

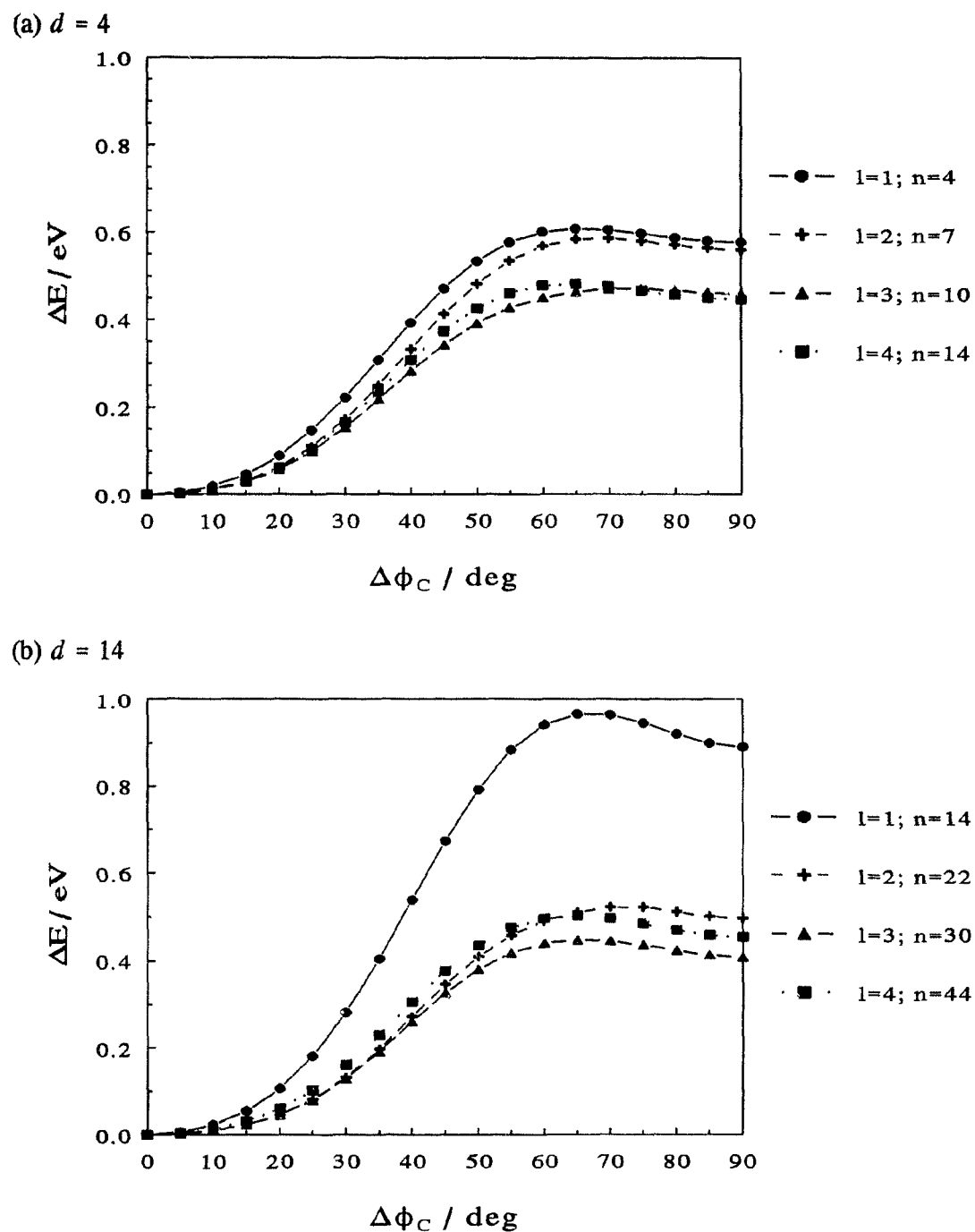


Figure 3.31 ΔE as a function of rotation about an axis through the centre of the C—C bond and perpendicular to the surface, $\Delta\phi_C$, for di- σ -bonded C_2H_4 on two $l = 1 \rightarrow 4$ series of Ni_n : (a) $d = 4$; $n = 4, 7, 10$, and 14 ; and (b) $d = 14$; $n = 14, 22, 30$, and 44 .

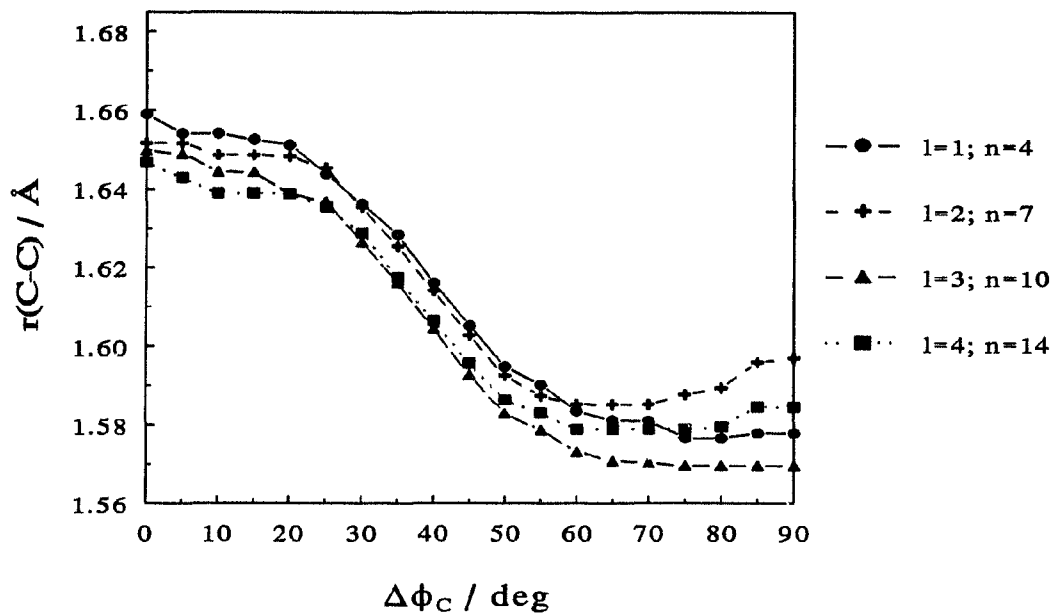
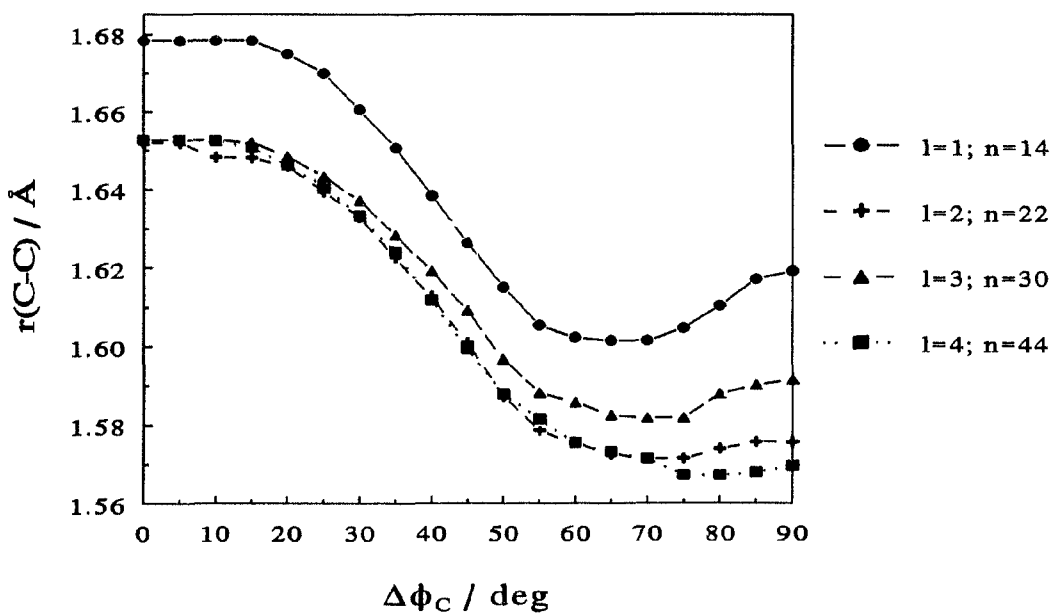
(a) $d = 4$ (b) $d = 14$ 

Figure 3.32 $r(\text{C}-\text{C})$ as a function of $\Delta\phi_C$ for C_2H_4 on two $l = 1 \rightarrow 4$ series of Ni_n : (a) $d = 4$ and (b) $d = 14$.

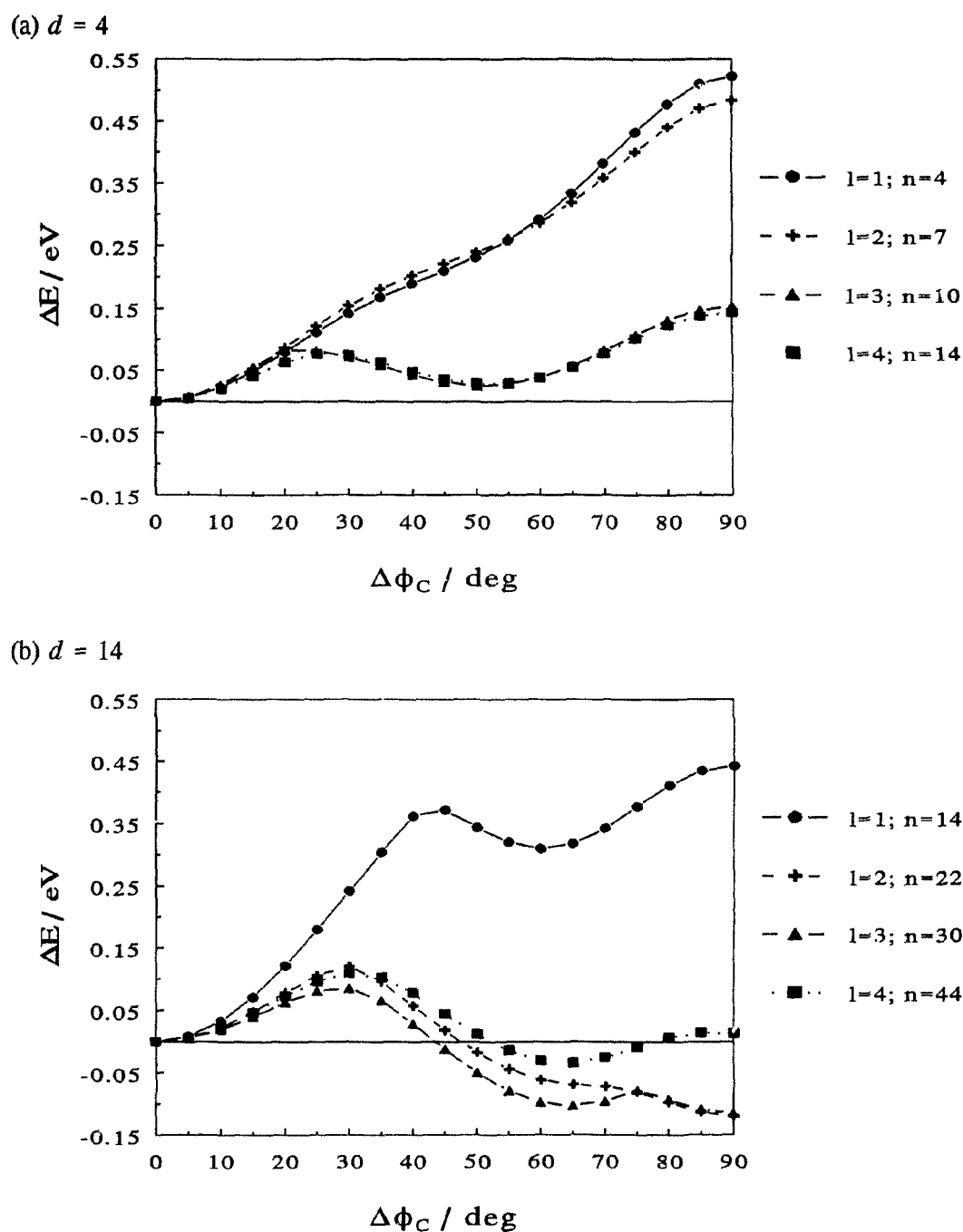


Figure 3.33 ΔE as a function of $\Delta\phi_C$ for di- σ -bonded C_2H_2 on two $l = 1 \rightarrow 4$ series of Ni_n : (a) $d = 4$ and (b) $d = 14$.

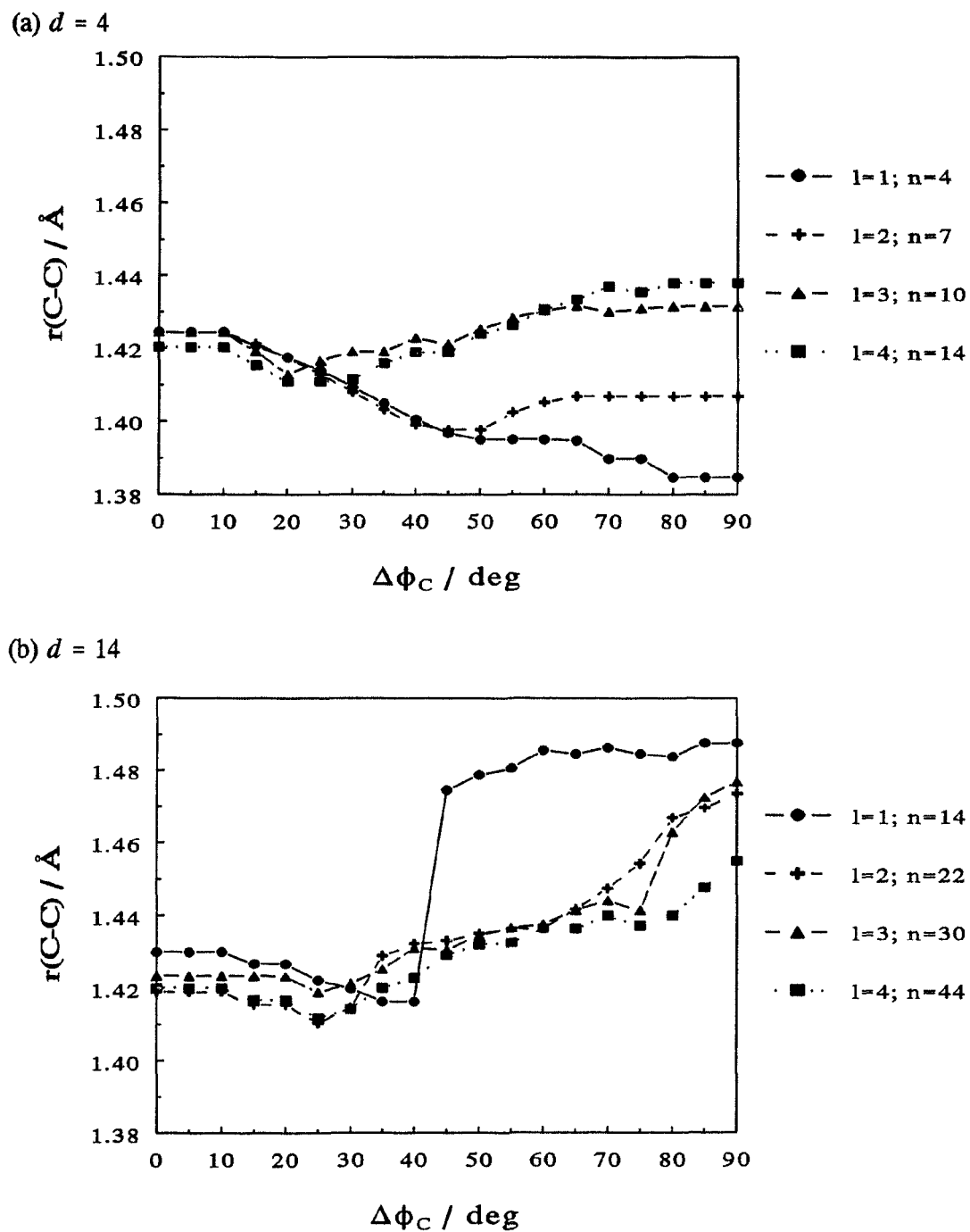


Figure 3.34 $r(\text{C}-\text{C})$ as a function of $\Delta\phi_C$ for C_2H_2 on two $l = 1 \rightarrow 4$ series of Ni_n : (a) $d = 4$ and (b) $d = 14$.

Chapter 4: RESULTS AND DISCUSSION

A. ASED-MO Calculations

1. Adsorption Sites of Ethylene and Acetylene

As mentioned in the previous chapter, the ethylene and acetylene adsorption studies focused on five binding sites, and their associated bonding configurations, as well as both the hexagonal close-packed (hcp) and face-centred cubic (fcc) threefold hollow sites over the second-layer atoms and hollows, respectively, viz.: the onefold atop, twofold aligned bridging, threefold triangular (Δ) and bridging/atop, and fourfold bridging (μ) sites, corresponding, respectively, to the π , di- σ , di- σ/π , μ/π and di- $\sigma/\text{di-}\pi$ configurations (recall Figure 3.8). Both the C_2H_4 and C_2H_2 species distort, upon adsorption in all sites, to structures with the C–H bonds bent away from the surface and C–C bond stretches corresponding to estimated states of hybridization of $sp^{2.3} - sp^{2.6}$ for C_2H_4 and $sp^{1.1} - sp^{2.0}$ for C_2H_2 . In the optimization of a single or pair of C_2H_4 's, the latter in the experimental (2×2) overlayer structure [25], on Ni clusters of comparable size and symmetric about the adsorption site, the di- σ bonding configuration was slightly favoured over the π . On all clusters, C_2H_2 prefers the di- σ/π bonding configuration, or Δ binding site, which was also the case when two molecules were adsorbed in their (2×2) LEED structure [25].

a. Single Adsorbate Molecules

As introduced in Chapter 3, the single molecular adsorption studies employed six series of Ni clusters, ranging from four to twenty-four atoms in the topmost layer, $d = 4, 7, 9, 14, 19,$ and 24 ; one to four layers, $\ell = 1, 2, 3,$ and 4 ; with a total number of Ni atoms of $n = 14, 20, 26, 44, 62,$ and 80 , respectively, for the $\ell = 4$ clusters (see Figure 3.3). Three of the cluster series ($d = 4, 14, 24$) are symmetric about the centre of a unit cell, and hence, the di- σ and μ sites, the other three ($d = 7, 9, 19$), about an individual atom of the extended lattice, and thus, the π site. While the qualitative cluster dependences were explored in the last chapter, more quantitative aspects are examined here, with focus on the three largest cluster series, $d = 14, 19,$ and 24 .

I. Ethylene: $\text{Ni}_n(\text{C}_2\text{H}_4)$

Figure 4.1 (pp. 114 - 115) shows both the optimized geometries and binding energies, E_b 's, for a single C_2H_4 molecule in several possible adsorption sites on the $n = 80, d = 24, \ell = 4,$ or $(24/16/16/24)$ cluster, while Table 4.1 (pp. 116 - 123) compares calculated parameters of C_2H_4 on three series of one- to four-layered Ni clusters, $d = 14, 19,$ and 24 , the first and last being symmetric about the di- σ and μ sites, the other, about the π . At a glance, the tabulated structural parameters, both across and within the three cluster series, appear fairly constant, a testimony to the local nature of the chemisorption bond between the C_2H_4 adsorbate and substrate Ni atoms. But, closer inspection discerns

subtle sensitivities of the computed adsorbate relative stabilities and optimized structures on n , d , ℓ , and adsorption site symmetry of the cluster, as discussed in Chapter 3.

From the collective relative binding energies of a single C_2H_4 molecule adsorbed on all the clusters examined (shown in Figure 3.3), the site stability ordering may be represented as $di-\sigma \geq \pi > \mu/\pi$ (hcp) $\sim \mu/\pi$ (fcc) $> \mu > di-\sigma/\pi$ (hcp) $\sim di-\sigma/\pi$ (fcc). That is, the $di-\sigma$ and π bonding configurations are of comparable stability, the favoured site depending upon the n , d , ℓ , and site symmetry of the cluster. Also, the hcp and fcc sites in both the threefold μ/π and $di-\sigma/\pi$ bonding configurations fluctuate in stability depending upon the cluster model, which implies only slight interaction between the C_2H_4 and the second-layer Ni atoms. The structural changes, however, indicate the greatest (least) adsorbate-surface interaction for the $di-\sigma$ (π) configuration, as detailed below.

Universally upon adsorption, C_2H_4 distorts from its gas-phase planar structure to one with the C–C bond elongated and the C–H bonds bent away from the surface, with individual structural parameters depending upon the binding site and cluster model. The C–C bond distance, $r(C-C)$, lengthens, for all sites, to a value intermediate between those calculated for free C_2H_4 and C_2H_6 , in accord with the experimental bond order between one and two [29] and $r(C-C) = (1.60 \pm 0.18) \text{ \AA}$ [14]. Greatest for the $di-\sigma$ configuration and least for the π , the C–C bond stretch, $\Delta_r(C-C)$, ranges roughly from 0.07 to 0.16 \AA , corresponding to estimated states of hybridization of $sp^{2.3} - sp^{2.6}$ and corrected $r(C-C)$'s of 1.39 – 1.45 \AA , as interpolated from the quadratic fits displayed in Figure 3.1. The C–H bond lengths, $r(C-H)$'s, shorten marginally (between 0.03 and 0.04 \AA) from that of the calculated gas-phase structure. The optimized height of the C

atoms above the surface, $z(\text{C})$, ranges from approximately 1.72 to 1.93 Å, corresponding to the μ and di- σ sites, respectively; *cf.* $z(\text{C}) = (1.90 \pm 0.02)$ Å from the PD analysis [14]. The θ_{CCH} distortion from its gas-phase value of 120.8° , and hence the angle of bend of the C–H bonds from the C–C bond axis ($180^\circ - \theta_{\text{CCH}}$), are greatest for the di- σ -bonded C_2H_4 and the pair of H's bonded to the C situated atop a Ni atom in the μ/π site ($\Delta\theta_{\text{CCH}} = -7^\circ$), and least for the π -bonded species ($\Delta\theta_{\text{CCH}} = -2^\circ$). The angle of C–H bond inclination from the surface, ϕ , related to the θ_{HCH} (and θ_{CCH}) distortions through the equations in the footnote of Table 4.1, is greatest for the pair of H's above Ni atoms in the di- σ/π configuration ($\phi = 21 - 25^\circ$), and least for the other pair bridging two surface Ni's ($\phi = 6 - 10^\circ$), with the C–H bonds of C_2H_4 in the atop site also only moderately elevated from the surface ($\phi \sim 9^\circ$).

Subtleties regarding the molecular symmetry, both internal and with respect to the underlying lattice, such as equivalence of like atoms and relative orientation of the molecular axis, were also ascertained for the various binding sites. Ethylene adsorbed in the atop site orients preferentially such that the geminal H's are above adjacent threefold sites of the Ni lattice, rather than each H bridging two Ni's. All H's are equivalent in the optimized structure, notwithstanding the contrasting environments of each pair of *cis* H's with respect to the underlying Ni's, *i.e.*, one pair is positioned over the hcp sites, the other, the fcc sites; the H's are presumably far enough from the surface ($z(\text{H})$ *ca.* 2.0 Å) to not distinguish the presence or absence of the second-layer Ni atoms below them. The molecule was fixed and centred over top a Ni atom, as it would otherwise deviate on the smaller clusters from the atop site being investigated or even optimize to an alternate binding site. All H's were found to be equivalent in the di- σ

configuration also, again despite the equivalence of only the *cis* H's once the second layer is included. For the di- σ/π configuration, the molecule was fixed in the Δ site, the adsorption site proposed in the LEED study of Hammer *et al.* [25]; otherwise, it would translate to the more stable di- σ configuration. In this site, the equivalence of the H's is broken by Ni's in the first layer, such that only the *cis* H's are equivalent, as one pair of H's sits above Ni atoms, while each in the other pair bridges two Ni's. Only in the μ/π arrangement was the molecular axis tilted with respect to the surface plane with the geminal H's equivalent. This preference is easily rationalized by observing that one C sits over and interacts directly with one Ni atom, while the other C bridges two Ni's. In the μ site, all H's were equivalent in the optimized geometry, thus not detecting the second-layer Ni's, which break the equivalence of the H's on different C's.

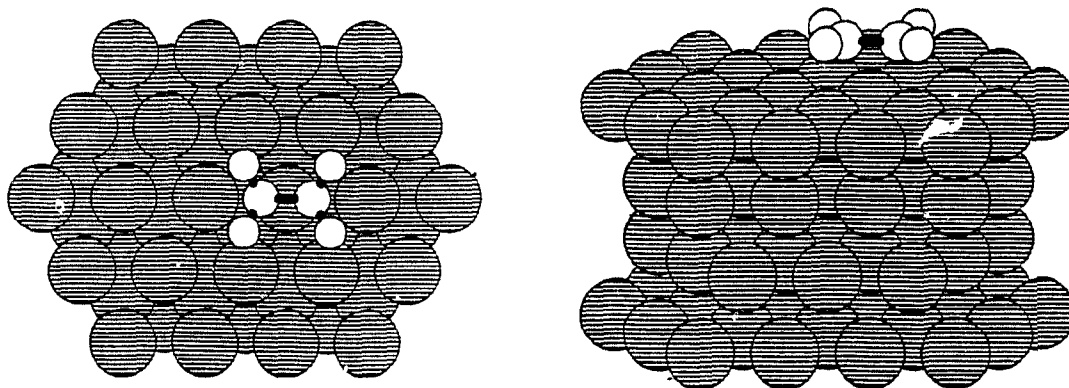
Rough bonding diagnostics, Mulliken population analyses (MPA's) are reported in Table 4.2 (pp. 124 - 126) for C₂H₄ adsorbed in the five binding sites on the largest Ni₈₀, (24/16/16/24) cluster model, focusing on the central Ni₄ unit cell most active in the chemisorption bond. The C-C and Ni-Ni overlap populations decrease from their isolated hydrocarbon and bare cluster values, while the Ni-C populations trace the respective chemisorption bonding (positive) and antibonding (negative) interactions. As detailed by Hoffmann [144], bonding between the adsorbate and substrate is accomplished at the expense of bonding within the individual components, *i.e.*, C-C and Ni-Ni bonding are weakened as Ni-C bonds are formed. The Ni's dominating the chemisorption bond can be deduced from the positive Ni-C overlaps for the various configurations, indicating the origin of their nomenclature: Ni₁-C_{1,2} in the π

configuration; $\text{Ni}_2\text{-C}_2$ and $\text{Ni}_3\text{-C}_1$ in the $\text{di-}\sigma$ and $\text{di-}\sigma/\pi$; $\text{Ni}_1\text{-C}_1$ and $\text{Ni}_{2,3}\text{-C}_2$ in the μ/π ; and $\text{Ni}_1\text{-C}_1$ and $\text{Ni}_4\text{-C}_2$ in the μ .

Indicative of the well-established Dewar-Chatt-Duncanson [145] (organometallic molecules) or Blyholder [146] (surface complexes) model of adsorbate $\pi \rightarrow$ metal d donation and metal $d \rightarrow \pi^*$ backdonation description of transition-metal bonding with unsaturated species, the π MO depopulates while the π^* MO populates, along with the corresponding modifications in the appropriate Ni AO occupations (notably, the d_{z^2} , d_{xz} , and d_{yz}). The degree of change in the π and π^* orbital occupations for the various bonding configurations roughly parallels their relative stabilities, except for the atop site, which interacts most weakly: $\text{di-}\sigma > \mu/\pi > \mu \sim \text{di-}\sigma/\pi > \pi$. The Ni s orbitals, also active in bonding, depopulate in the adsorption complexes. Mixing of metal s and d_{z^2} orbitals yields lobes outwardly directed from the surface, giving a facile σ -type interaction with the π and π^* adsorbate orbitals, as in the $\text{di-}\sigma$ bonding configuration.

The cluster dependences on d and ℓ of the various overlap populations and orbital occupations, shown in Figures 4.2 (pp. 127 - 128) and 4.3 (pp. 129 - 131) for the most stable $\text{di-}\sigma$ configuration, reinforces the conclusion of Chapter 3 (Sect. 3.B.1.a) that the $d = 14$, $\ell = 3$ cluster yields sufficiently convergent adsorption results. A representative adsorbate MO energy level diagram is displayed in Figure 4.4 (p. 132) for the distorted C_2H_4 species when adsorbed in the five binding sites on the $d = 24$, $\ell = 4$, (24/16/16/24) cluster. The corresponding interaction energy level diagrams for the $\text{Ni}_{80}(\text{C}_2\text{H}_4)$ system, depicted in Figure 4.5 (p. 133), show the relative placement of the frontier orbitals of C_2H_4 , viz., the π and π^* MO's, with respect to the well-defined metal d band, which dominate the chemisorption bonding.

(a) π (onfold atop); $E_B = 2.614$ eV



(b) $d_1\text{-}\sigma$ (twofold aligned bridging); $E_B = 2.769$ eV

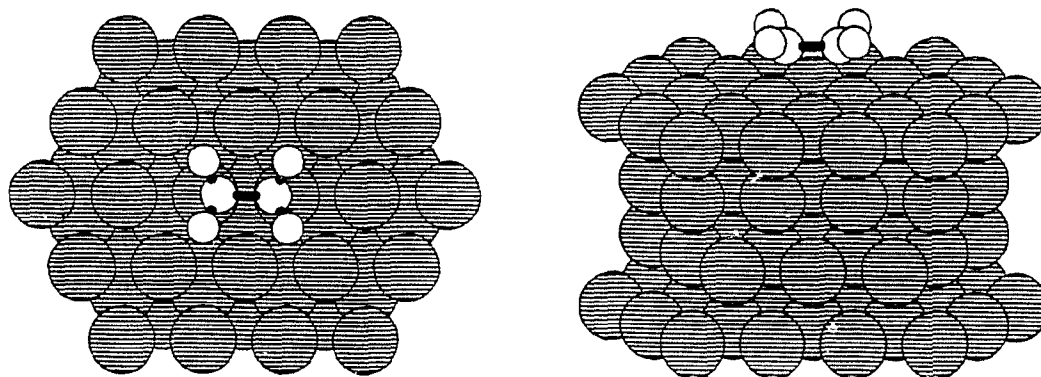


Figure 4.1 $\text{Ni}_{80}(\text{C}_2\text{H}_4)$ adsorption system: optimized geometries and binding energies for (a) - (g) five bonding configurations (and corresponding adsorption sites) of C_2H_4 on the $n = 80$, $l = 4$, $d = 24$ or (24/16/16/24) cluster model. Hcp and fcc denote threefold sites over second-layer atoms and hollows, respectively. Two perspectives are shown for the π and $d_1\text{-}\sigma$ configurations, corresponding to viewing down and slightly rotated from edge-on to the surface plane.

Table 4.1 Optimized Adsorption Parameters for $\text{Ni}_n(\text{C}_2\text{H}_4)$ for Three Series of Clusters: $d = 14, 19, 24^a$; $\ell = 1, 2, 3, 4$

ℓ	E_B^b / eV	$\Delta r(\text{C}-\text{C})^c / \text{Å}$	$\Delta r(\text{C}-\text{H})^c / \text{Å}$	$z(\text{C})^d / \text{Å}$	$\theta_{\text{CCH}}^{e,f} / \text{deg}$	$\phi^{e,f} / \text{deg}$
π (onefold atop site)						
$n = 14, 22, 30, 44:$						
1	1.341	0.09 ($sp^{2.36}$)	-0.03	1.923	117.9	11.3
2	2.183	0.06 ($sp^{2.26}$)	-0.03	1.905	118.8	8.9
3	2.297	0.06 ($sp^{2.26}$)	-0.03	1.896	118.8	8.9
4	2.367	0.06 ($sp^{2.27}$)	-0.03	1.896	118.8	9.2
$n = 19, 31, 43, 62:$						
1	1.498	0.07 ($sp^{2.31}$)	-0.03	1.917	118.5	10.4
2	2.502	0.07 ($sp^{2.28}$)	-0.04	1.877	118.9	8.7
3	2.606	0.07 ($sp^{2.30}$)	-0.04	1.862	118.6	8.6
4	2.695	0.07 ($sp^{2.30}$)	-0.04	1.862	118.6	8.6
$n = 24, 40, 56, 80:$						
1	1.772	0.08 ($sp^{2.33}$)	-0.03	1.913	118.5	10.7
2	2.441	0.07 ($sp^{2.29}$)	-0.04	1.877	118.5	9.1
3	2.507	0.07 ($sp^{2.29}$)	-0.04	1.877	118.5	9.1
4	2.614	0.07 ($sp^{2.31}$)	-0.04	1.865	118.6	9.1

See footnotes at end of Table on p. 123

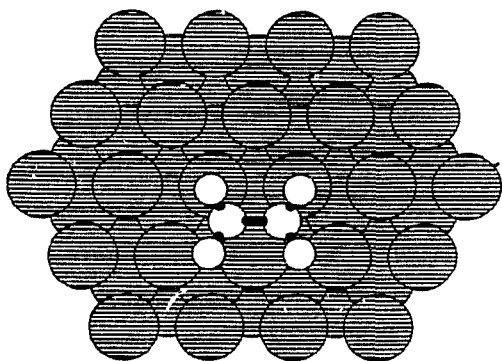
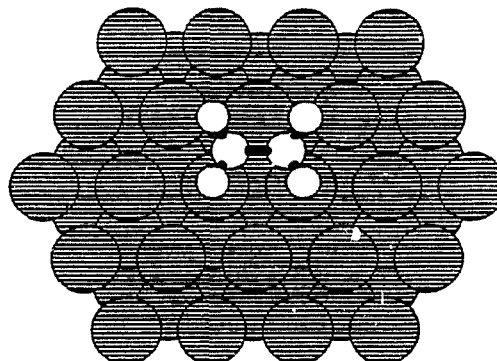
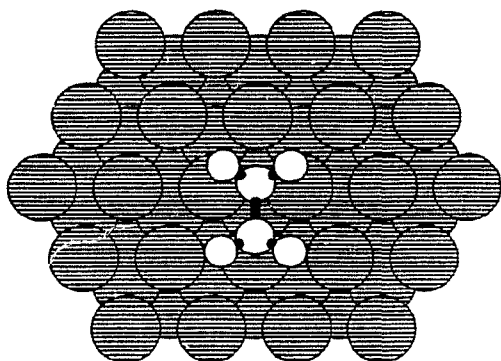
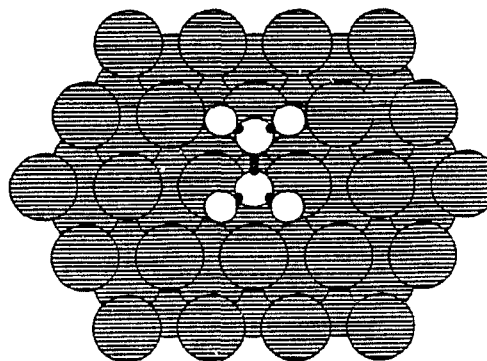
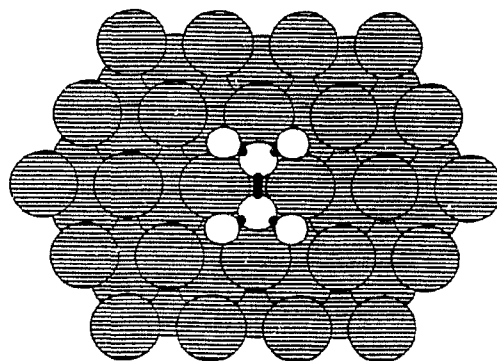
(c) di- σ/π (Δ) — hcp; $E_B = 2.279$ eV(d) di- σ/π (Δ) — fcc; $E_B = 2.280$ eV(e) μ/π — hcp; $E_B = 2.446$ eV(f) μ/π — fcc; $E_B = 2.466$ eV(g) di- $\sigma/\text{di-}\pi$ (μ); $E_B = 2.416$ eV

Figure 4.1 Cont'd

Table 4.1 Cont'd

ℓ	$E_B^b /$ eV	$\Delta r(\text{C}-\text{C})^c /$ Å	$\Delta r(\text{C}-\text{H})^c /$ Å	$z(\text{C})^d /$ Å	$\theta_{\text{CCH}}^{e,f} /$ deg	$\phi^{e,f} /$ deg
di-σ (twofold aligned bridging site)						
$n = 14, 22, 30, 44:$						
1	1.709	0.18 ($sp^{2.72}$)	-0.02	1.947	112.9	21.9
2	2.274	0.15 ($sp^{2.63}$)	-0.03	1.943	113.7	20.4
3	2.481	0.16 ($sp^{2.63}$)	-0.03	1.936	113.7	20.0
4	2.588	0.16 ($sp^{2.63}$)	-0.03	1.940	113.7	20.0
$n = 19, 31, 43, 62:$						
1	1.897	0.18 ($sp^{2.72}$)	-0.02	1.947	113.1	21.3
2	2.370	0.15 ($sp^{2.63}$)	-0.03	1.944	113.8	20.1
3	2.578	0.15 ($sp^{2.61}$)	-0.03	1.937	114.2	19.8
4	2.623	0.15 ($sp^{2.61}$)	-0.03	1.937	114.2	19.8
$n = 24, 40, 56, 80:$						
1	2.204	0.18 ($sp^{2.72}$)	-0.02	1.942	112.9	21.4
2	2.449	0.16 ($sp^{2.66}$)	-0.03	1.936	113.4	20.3
3	2.617	0.16 ($sp^{2.66}$)	-0.03	1.929	113.6	20.3
4	2.769	0.16 ($sp^{2.64}$)	-0.03	1.929	113.6	20.3

See footnotes at end of Table on p. 123

Table 4.1 Cont'd

ℓ	$E_B^b /$ eV	$\Delta r(\text{C}-\text{C})^c /$ Å	$\Delta r(\text{C}-\text{H})^c /$ Å	$z(\text{C})^d /$ Å	$\theta_{\text{CCH}}^{e,f} /$ deg	$\phi^{e,f} /$ deg
di-σ/π (threefold triangular or Δ site)^g – hcp						
$n = 14, 22, 30, 44:$						
1	0.834	0.13 ($sp^{2.53}$)	-0.04, 0.03	1.858	115.9, 115.0	9.7, 28.0
2	1.694	0.07 ($sp^{2.32}$)	-0.04, 0.03	1.838	118.0, 116.9	9.6, 19.9
3	1.943	0.08 ($sp^{2.34}$)	-0.04, 0.03	1.816	118.0, 116.9	9.8, 20.9
4	2.034	0.08 ($sp^{2.34}$)	-0.04, 0.03	1.829	118.0, 116.9	8.9, 21.7
$n = 19, 31, 43, 62:$						
1	1.071	0.11 ($sp^{2.46}$)	-0.03, 0.02	1.846	116.2, 116.9	7.8, 27.5
2	1.927	0.06 ($sp^{2.28}$)	-0.04, 0.03	1.831	118.6, 117.4	8.5, 19.5
3	2.217	0.09 ($sp^{2.38}$)	-0.04, 0.03	1.790	117.8, 116.7	6.8, 25.4
4	2.214	0.08 ($sp^{2.34}$)	-0.04, 0.03	1.810	118.0, 117.1	7.0, 23.6
$n = 24, 40, 56, 80:$						
1	1.436	0.11 ($sp^{2.47}$)	-0.04, 0.02	1.840	116.6, 115.5	9.3, 27.0
2	1.873	0.10 ($sp^{2.41}$)	-0.04, 0.03	1.801	117.7, 116.1	7.3, 26.0
3	2.108	0.10 ($sp^{2.42}$)	-0.04, 0.03	1.785	117.7, 116.1	7.3, 26.2
4	2.279	0.09 ($sp^{2.39}$)	-0.04, 0.03	1.786	117.7, 116.1	8.6, 24.7

See footnotes at end of Table on p. 123

Table 4.1 Cont'd

ℓ	$E_B^b /$ eV	$\Delta r(\text{C}-\text{C})^c /$ Å	$\Delta r(\text{C}-\text{H})^c /$ Å	$z(\text{C})^d /$ Å	$\theta_{\text{CCH}}^{e,f} /$ deg	$\phi^{e,f} /$ deg
di-σ/π (threefold triangular or Δ site)^g --- fcc						
$n = 14, 22, 30, 44:$						
1	0.834	0.13 ($sp^{2.53}$)	-0.03, 0.04	1.858	115.0, 115.9	28.0, 9.7
2	1.670	0.07 ($sp^{2.29}$)	-0.03, 0.04	1.836	117.4, 118.1	20.0, 9.2
3	1.910	0.07 ($sp^{2.34}$)	-0.03, 0.04	1.810	117.4, 118.1	20.7, 9.1
4	1.986	0.08 ($sp^{2.33}$)	-0.03, 0.04	1.819	116.9, 117.8	21.2, 9.8
$n = 19, 31, 43, 62:$						
1	1.071	0.11 ($sp^{2.46}$)	-0.02, 0.03	1.846	116.2, 116.9	27.5, 7.8
2	1.892	0.06 ($sp^{2.28}$)	-0.03, 0.04	1.829	117.4, 118.6	19.5, 7.7
3	2.147	0.07 ($sp^{2.31}$)	-0.03, 0.04	1.800	117.4, 118.6	23.1, 6.2
4	2.198	0.08 ($sp^{2.33}$)	-0.03, 0.04	1.807	117.1, 118.0	24.0, 6.2
$n = 24, 40, 56, 80:$						
1	1.436	0.11 ($sp^{2.47}$)	-0.02, 0.04	1.840	115.5, 116.6	27.0, 9.3
2	1.928	0.09 ($sp^{2.38}$)	-0.03, 0.04	1.799	116.2, 118.1	25.1, 6.9
3	2.144	0.09 ($sp^{2.38}$)	-0.03, 0.04	1.789	116.2, 118.1	24.6, 7.5
4	2.280	0.09 ($sp^{2.38}$)	-0.03, 0.04	1.786	116.1, 117.7	24.7, 7.6

See footnotes at end of Table on p. 123

Table 4.1 Cont'd

l	$E_B^b /$ eV	$\Delta r(\text{C}-\text{C})^c /$ Å	$\Delta r(\text{C}-\text{H})^c /$ Å	$z(\text{C})^d /$ Å	$\theta_{\text{CCH}}^{e,f} /$ deg	$\phi^{e,f} /$ deg
μ/π (threefold bridging/atop site) ^g — hcp						
$n = 14, 22, 30, 44:$						
1	1.149	0.14 ($sp^{2.57}$)	-0.02, -0.03	1.952, 1.868	113.3, 116.4	20.6, 19.2
2	1.890	0.11 ($sp^{2.45}$)	-0.03, -0.03	1.936, 1.781	113.4, 118.3	20.0, 15.8
3	2.217	0.11 ($sp^{2.47}$)	-0.03, -0.03	1.903, 1.770	113.4, 117.8	20.0, 16.2
4	2.273	0.10 ($sp^{2.43}$)	-0.03, -0.03	1.913, 1.787	113.4, 117.8	19.6, 16.2
$n = 19, 31, 43, 62:$						
1	1.443	0.14 ($sp^{2.57}$)	-0.02, -0.02	1.936, 1.843	113.3, 116.7	21.1, 19.0
2	2.040	0.10 ($sp^{2.44}$)	-0.03, -0.03	1.941, 1.815	113.9, 118.0	19.5, 16.2
3	2.237	0.11 ($sp^{2.45}$)	-0.03, -0.03	1.929, 1.803	113.9, 117.5	19.1, 16.4
4	2.308	0.11 ($sp^{2.45}$)	-0.03, -0.03	1.927, 1.808	113.9, 117.5	19.1, 16.9
$n = 24, 40, 56, 80:$						
1	1.751	0.14 ($sp^{2.57}$)	-0.02, -0.03	1.938, 1.823	113.3, 116.4	20.9, 19.4
2	2.053	0.11 ($sp^{2.46}$)	-0.03, -0.03	1.927, 1.785	113.3, 117.8	20.0, 16.6
3	2.259	0.12 ($sp^{2.48}$)	-0.03, -0.04	1.900, 1.758	113.3, 117.8	20.0, 16.6
4	2.446	0.11 ($sp^{2.46}$)	-0.03, -0.04	1.897, 1.745	113.3, 117.9	20.0, 16.3

See footnotes at end of Table on p. 123

Table 4.1 Cont'd

ℓ	$E_B^b /$ eV	$\Delta r(\text{C}-\text{C})^c /$ Å	$\Delta r(\text{C}-\text{H})^c /$ Å	$z(\text{C})^d /$ Å	$\theta_{\text{CCH}}^{e,f} /$ deg	$\phi^{e,f} /$ deg
μ/π (threefold bridging/atop site)^g — fcc						
$n = 14, 22, 30, 44:$						
1	1.149	0.14 ($sp^{2.57}$)	-0.03, -0.02	1.868, 1.952	116.4, 113.3	19.2, 20.6
2	1.903	0.09 ($sp^{2.40}$)	-0.03, -0.03	1.777, 1.943	118.8, 113.6	14.6, 19.8
3	2.181	0.10 ($sp^{2.42}$)	-0.03, -0.03	1.757, 1.927	118.8, 113.4	14.9, 20.0
4	2.223	0.10 ($sp^{2.42}$)	-0.03, -0.03	1.791, 1.929	118.2, 114.0	15.7, 19.2
$n = 19, 31, 43, 62:$						
1	1.443	0.14 ($sp^{2.57}$)	-0.02, -0.02	1.843, 1.936	116.7, 113.3	19.0, 21.1
2	2.084	0.10 ($sp^{2.43}$)	-0.03, -0.03	1.806, 1.949	118.0, 113.9	15.6, 19.5
3	2.321	0.11 ($sp^{2.45}$)	-0.03, -0.03	1.803, 1.929	117.5, 113.9	16.9, 19.1
4	2.324	0.11 ($sp^{2.45}$)	-0.03, -0.03	1.816, 1.936	117.5, 113.9	16.9, 19.1
$n = 24, 40, 56, 80:$						
1	1.751	0.14 ($sp^{2.57}$)	-0.03, -0.02	1.823, 1.938	116.4, 113.3	19.4, 20.9
2	2.093	0.10 ($sp^{2.44}$)	-0.03, -0.03	1.777, 1.928	118.5, 113.3	15.5, 20.0
3	2.298	0.10 ($sp^{2.43}$)	-0.03, -0.03	1.743, 1.916	118.5, 113.3	15.4, 20.0
4	2.466	0.11 ($sp^{2.45}$)	-0.03, -0.03	1.750, 1.897	117.9, 113.3	16.3, 20.0

See footnotes at end of Table on p. 123

Table 4.1 Cont'd

l	$E_B^b /$ eV	$\Delta r(\text{C}-\text{C})^c /$ Å	$\Delta r(\text{C}-\text{H})^c /$ Å	$z(\text{C})^d /$ Å	$\theta_{\text{CCH}}^{e,f} /$ deg	$\phi^{e,f} /$ deg
di-σ/di-π (fourfold bridging or μ site)						
$n = 14, 22, 30, 44$						
1	0.818	0.13 ($sp^{2.54}$)	-0.03	1.813	114.8	18.5
2	1.776	0.09 ($sp^{2.39}$)	-0.04	1.783	116.0	15.9
3	2.072	0.09 ($sp^{2.40}$)	-0.04	1.753	116.3	16.1
4	2.132	0.09 ($sp^{2.36}$)	-0.04	1.779	116.3	15.3
$n = 19, 31, 43, 62$						
1	1.069	0.12 ($sp^{2.48}$)	-0.03	1.803	115.3	17.5
2	1.935	0.08 ($sp^{2.35}$)	-0.04	1.775	116.4	15.1
3	2.189	0.09 ($sp^{2.37}$)	-0.04	1.750	116.4	15.1
4	2.217	0.08 ($sp^{2.35}$)	-0.04	1.762	116.4	15.1
$n = 24, 40, 56, 80$						
1	1.523	0.13 ($sp^{2.53}$)	-0.03	1.784	114.8	18.6
2	1.979	0.09 ($sp^{2.38}$)	-0.04	1.739	116.1	15.6
3	2.186	0.11 ($sp^{2.48}$)	-0.04	1.704	115.5	17.4
4	2.416	0.10 ($sp^{2.43}$)	-0.04	1.715	115.5	16.7

Footnotes to Table 4.1:

- ^a Four-layered Ni clusters corresponding to $d = 14$, 19, and 24 are shown in Figure 3.3, where the $d = 14$ and 24 series are symmetric about the di- σ and μ adsorption sites and the $d = 19$ series is symmetric about the atop site; Figure 4.1 displays the structures for the $\text{Ni}_{90}(\text{C}_2\text{H}_4)$ adsorption system.
- ^b $E_B = [E(\text{Ni}_n) + E(\text{C}_2\text{H}_4)] - E(\text{Ni}_n(\text{C}_2\text{H}_4))$
- ^c C–C bond stretch and C–H bond contraction from optimized values of 1.498 and 1.185 Å, respectively, for isolated C_2H_4 (estimated states of hybridization, sp^n , interpolated from the quadratic fits of Figure 3.1, in parentheses)
- ^d Perpendicular height(s) of C atoms above the surface plane
- ^e Compare with the bond angles, $\theta_{\text{CCH}} = 120.8^\circ$ (from $\theta_{\text{HCH}} = 118.5^\circ$) optimized for the undistorted planar C_2H_4 molecule and $\phi = 0.0^\circ$ for a planar molecule parallel to the surface. More precisely, ϕ represents the angle of inclination of the C–H bond from the surface plane, *i.e.*, the angle the projection of the C–H bond into a plane perpendicular to the C–C axis makes with an axis both perpendicular to the bond axis and parallel to the surface.
- ^f The following transformation equations:

$$\cos(180^\circ - \theta_{\text{CCH}}) = \cos \frac{1}{2} \theta_{\text{HCH}} \cos \gamma$$

$$\sin \theta_{\text{CCH}} \cos \phi = \sin \frac{1}{2} \theta_{\text{HCH}}$$

$$\sin \theta_{\text{CCH}} \sin \phi = \cos \frac{1}{2} \theta_{\text{HCH}} \sin \gamma ;$$

relate θ_{CCH} and ϕ to θ_{HCH} and γ , the angle of tilt between the bisector of the HCH bond angle and the C–C bond.

- ^g Shift of the centre of the C–C bond from the $[\bar{1}10]$ direction fixed at ± 1.07 Å for di- σ/π configuration and optimized to between $\pm (0.67 - 0.89)$ Å for the μ/π configuration in the hcp and fcc sites
-

Table 4.2 Ni₃₀(C₂H₄) Chemisorption Bonding Indices (Mulliken Population Analyses or MPA's) for Five Binding Sites of Central Ni₄ Unit Cell

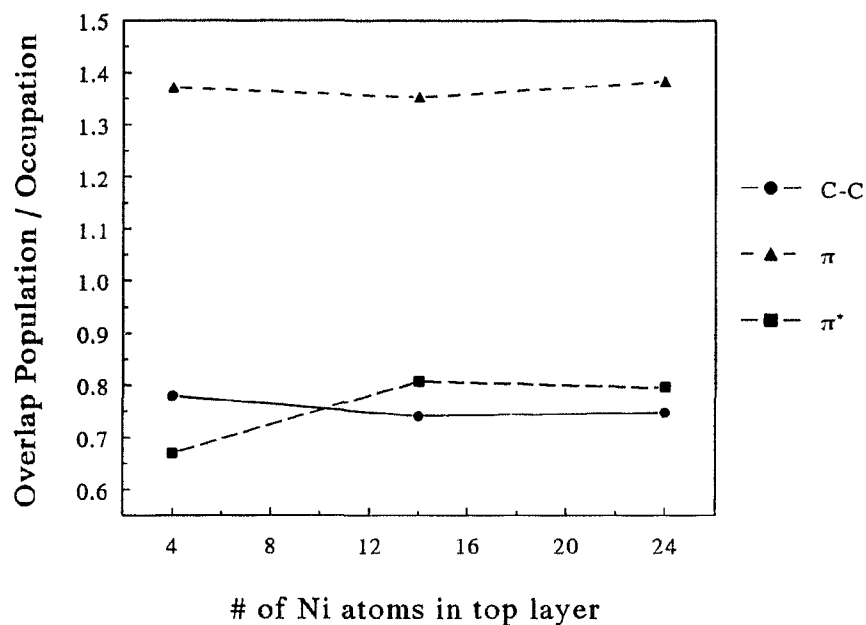
	C ₂ H ₄	Ni ₄	π	d ₁ - σ	d ₂ - σ/π	μ/π	μ
E_B / eV			2.614	2.769	2.279	2.446	2.416
$r(\text{C}-\text{C}) / \text{\AA}$	1.498		1.571	1.657	1.590	1.608	1.601
Overlap Population							
C-C	1.12		0.96	0.79	0.93	0.88	0.91
Ni ₁ -Ni _{2,3}		0.13	0.11, 0.10	0.11	0.10	0.10	0.10
Ni ₂ -Ni ₃		0.15	0.11	0.09	0.11	0.11	0.08
Ni _{2,3} -Ni ₄		0.13	0.11, 0.10	0.11	0.12	0.10	0.09
Ni ₁ -Ni ₄		-0.01	-0.01	-0.01	-0.01	-0.01	-0.01
Ni ₁ -C ₁			-0.02	-0.04	-0.05	0.22	0.05
Ni ₁ -C ₂			-0.06	-0.04	-0.05	-0.08	-0.03
Ni ₂ -C ₁			-0.01	-0.08	-0.07	-0.09	-0.04
Ni ₂ -C ₂			-0.06	0.28	0.10	0.05	-0.05
Ni ₃ -C ₁			0.08	0.28	0.10	-0.09	-0.04
Ni ₃ -C ₂			0.08	-0.08	-0.07	0.05	-0.05
Ni ₄ -C ₁			-0.02	-0.04	-0.01	0.00	-0.03
Ni ₄ -C ₂			-0.05	-0.04	-0.01	-0.05	0.05

Table 4.2 Cont'd

	C_2H_4	Ni_4	π	di- σ	di- σ/π	μ/π	μ
Occupations							
π^*	0		0.44	0.84	0.57	0.69	0.55
π	2		1.63	1.49	1.53	1.50	1.51
$Ni_1 s$		0.73	0.70	0.70	0.64	0.73	0.69
$Ni_{2,3} s$		0.77	0.68, 0.69	0.75	0.70	0.68	0.65
$Ni_4 s$		0.71	0.67	0.67	0.69	0.67	0.67
$Ni_1 d_{z^2}$		1.90	1.88	1.90	1.76	1.52	1.78
$Ni_{2,3} d_{z^2}$		1.91	1.85, 1.39	1.42	1.78	1.72	1.83
$Ni_4 d_{z^2}$		1.90	1.88	1.90	1.89	1.90	1.77
$Ni_1 d_{x^2-y^2}$		1.76	1.76	1.73	1.80	1.72	1.79
$Ni_{2,3} d_{x^2-y^2}$		1.69	1.67, 1.68	1.69	1.69	1.66	1.69
$Ni_4 d_{x^2-y^2}$		1.69	1.70	1.69	1.71	1.68	1.70
$Ni_1 d_{xy}$		1.68	1.66	1.66	1.60	1.67	1.68
$Ni_{2,3} d_{xy}$		1.66	1.66, 1.69	1.66	1.67	1.67	1.60
$Ni_4 d_{xy}$		1.69	1.67	1.66	1.69	1.67	1.70

Table 4.2 Cont'd

	C_2H_4	Ni_4	π	di- σ	di- σ/π	μ/π	μ
$Ni_1 d_{xz}$		1.92	1.91	1.91	1.82	1.80	1.77
$Ni_{2,3} d_{xz}$		1.89	1.92, 1.89	1.88	1.77	1.90	1.84
$Ni_4 d_{xz}$		1.94	1.93	1.93	1.93	1.92	1.78
$Ni_1 d_{yz}$		1.93	1.93	1.93	1.84	1.91	1.93
$Ni_{2,3} d_{yz}$		1.90	1.86, 1.62	1.84	1.88	1.75	1.79
$Ni_4 d_{yz}$		1.89	1.90	1.89	1.89	1.90	1.90

(a) C-C Overlap; π and π^* Occupations

(b) Ni-C and Ni-Ni Overlap

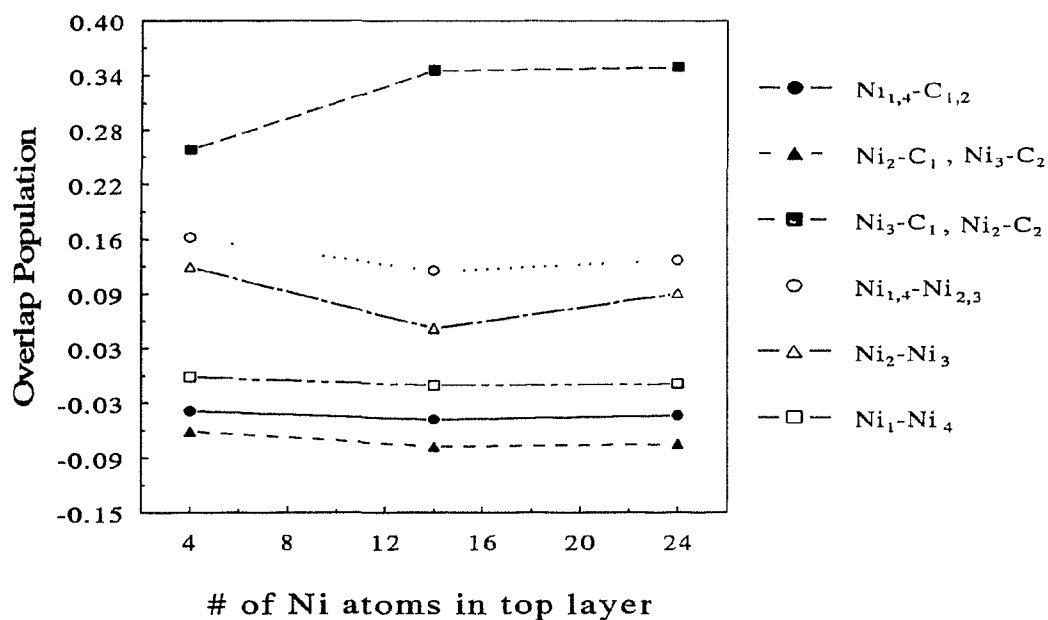


Figure 4.2 Mulliken population analysis (MPA) of di- σ -bonded C_2H_4 on Ni_n for the $d = 4, 14,$ and 24 series of clusters: (a) C-C overlap populations and π and π^* molecular orbital (MO) occupations; (b) Ni-C and Ni-Ni overlap populations; and atomic orbital (AO) occupations for Ni (c) s , d_{z^2} , and $d_{x^2-y^2}$; and (d) d_{xy} , d_{xz} and d_{yz} .

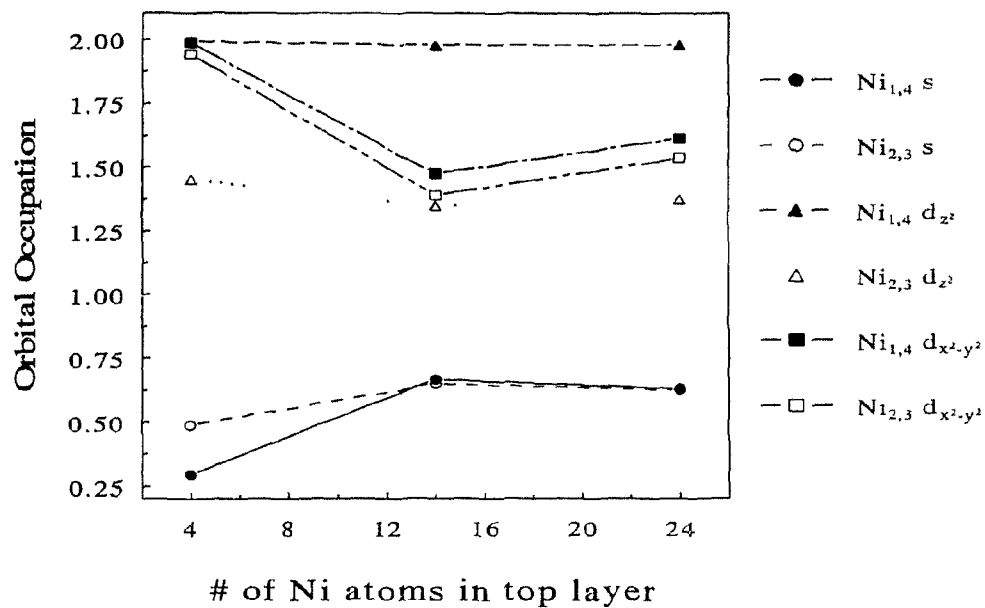
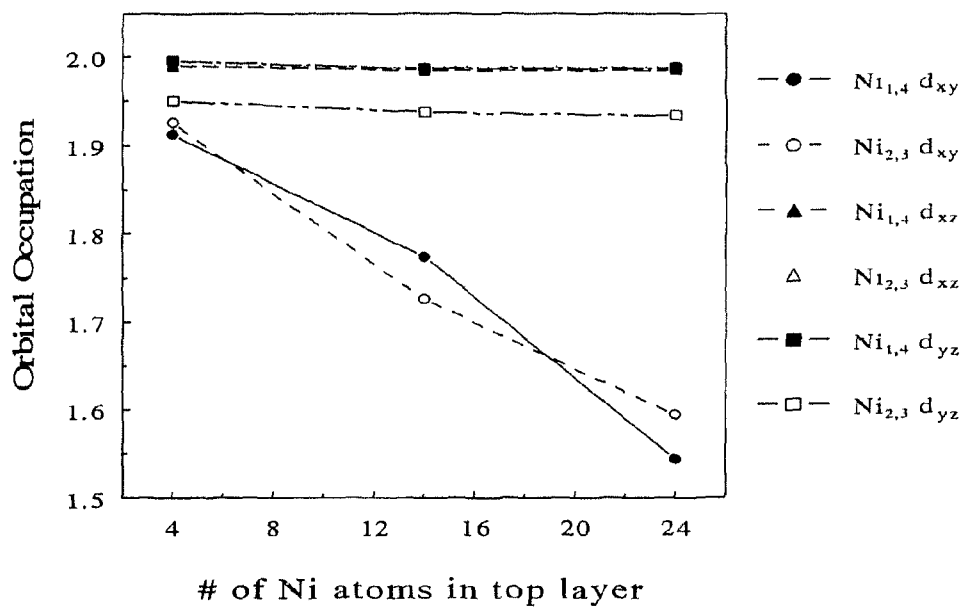
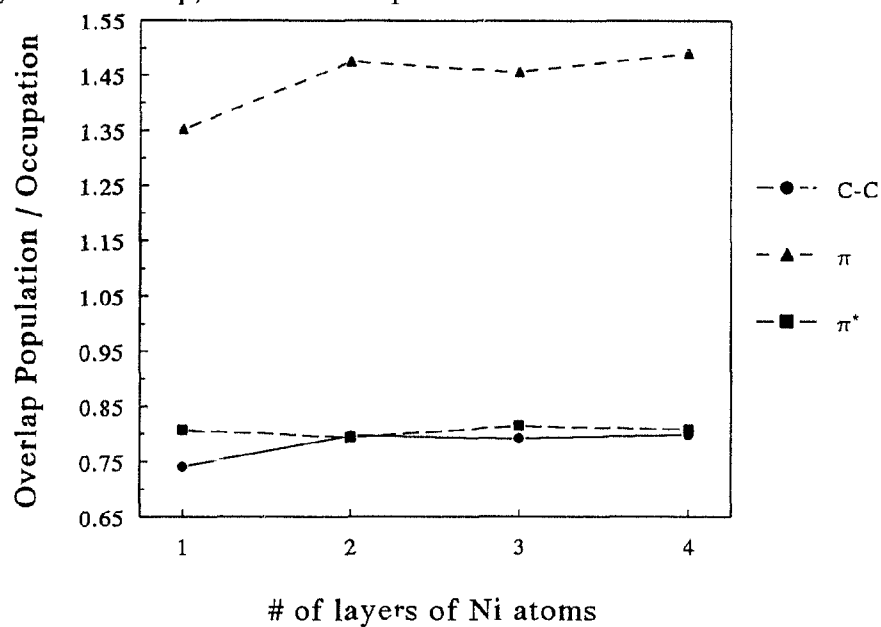
(c) Ni s , d_{z^2} , and $d_{x^2-y^2}$ (d) Ni d_{xy} , d_{xz} and d_{yz} 

Figure 4.2 Cont'd

(a) C-C Overlap; π and π^* Occupations

(b) Ni-C Overlap

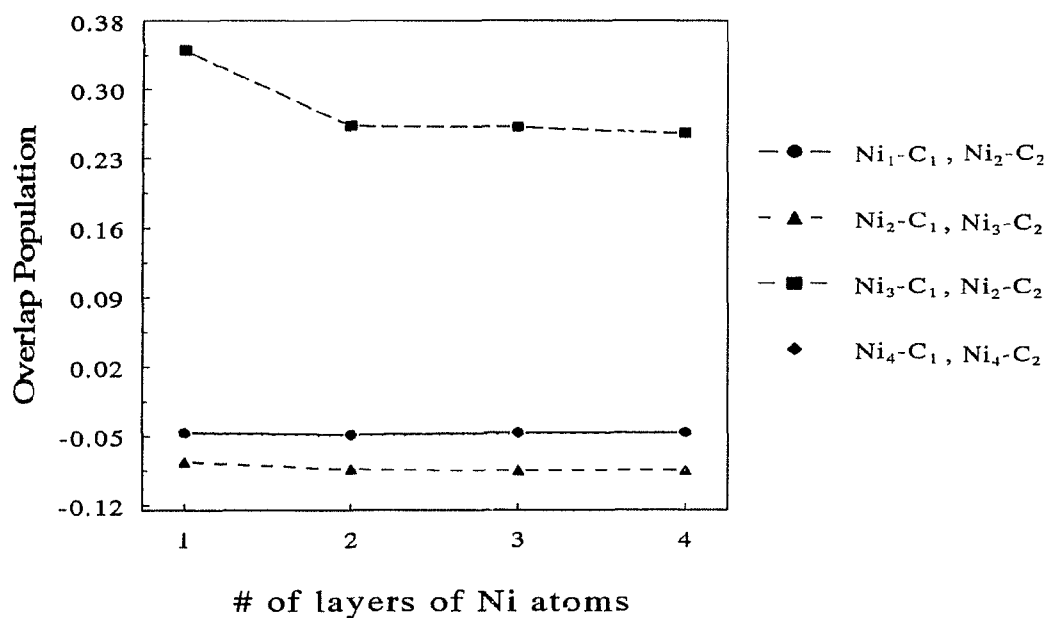


Figure 4.3 MPA of di- σ -bonded C_2H_4 on Ni_n for the $d = 14$ series of clusters as $\ell = 1 \rightarrow 4$: (a) C-C overlap populations and π and π^* MO occupations; (b) Ni-C and (c) Ni-Ni overlap populations; and AO occupations for Ni (d) s , d_{z^2} , (e) $d_{x^2-y^2}$, d_{xy} , (f) d_{xz} and d_{yz} .

(c) Ni–Ni Overlap

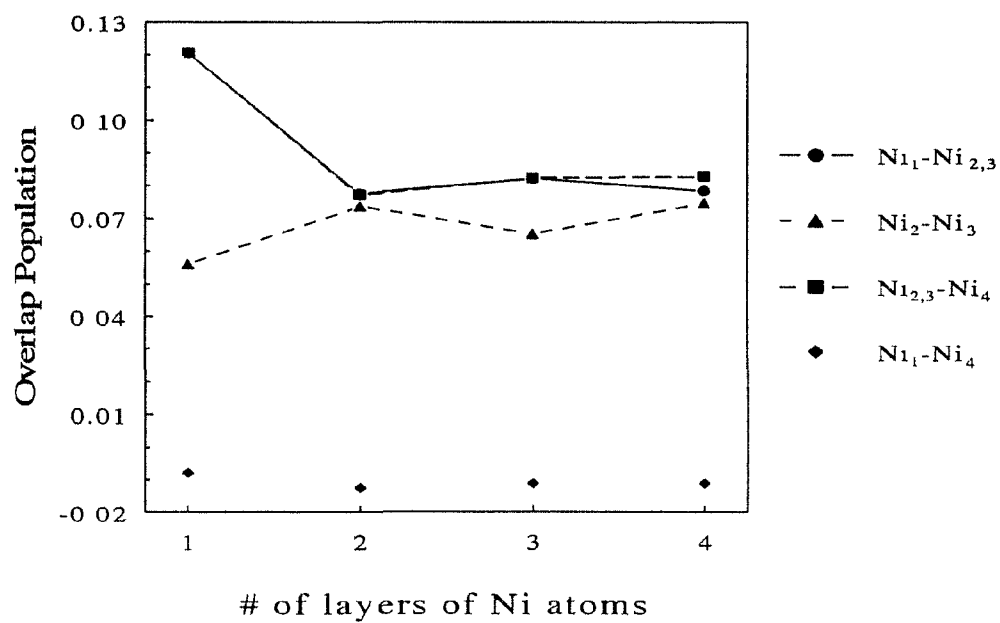
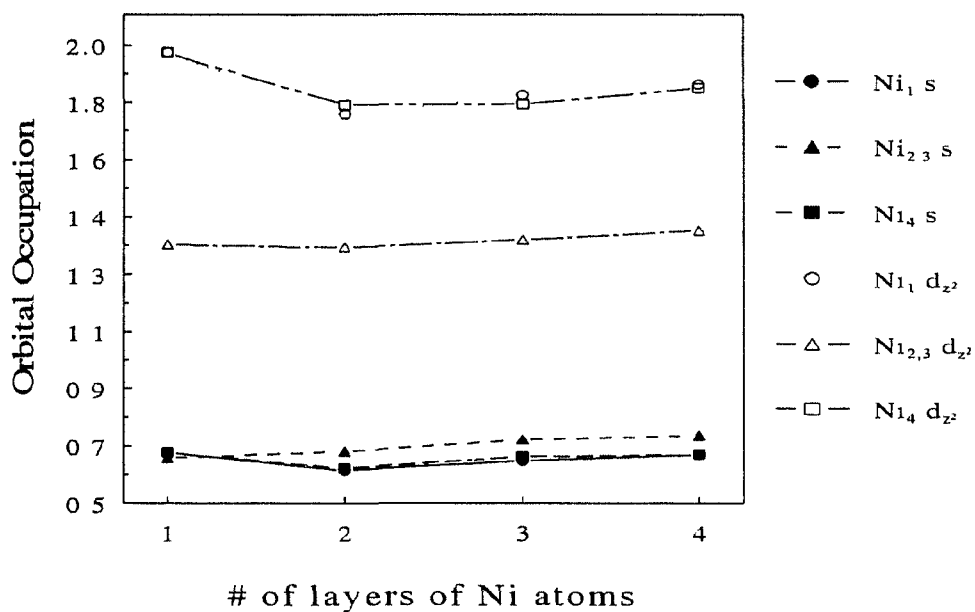
(d) Ni s and d_{z^2} 

Figure 4.3 Cont'd

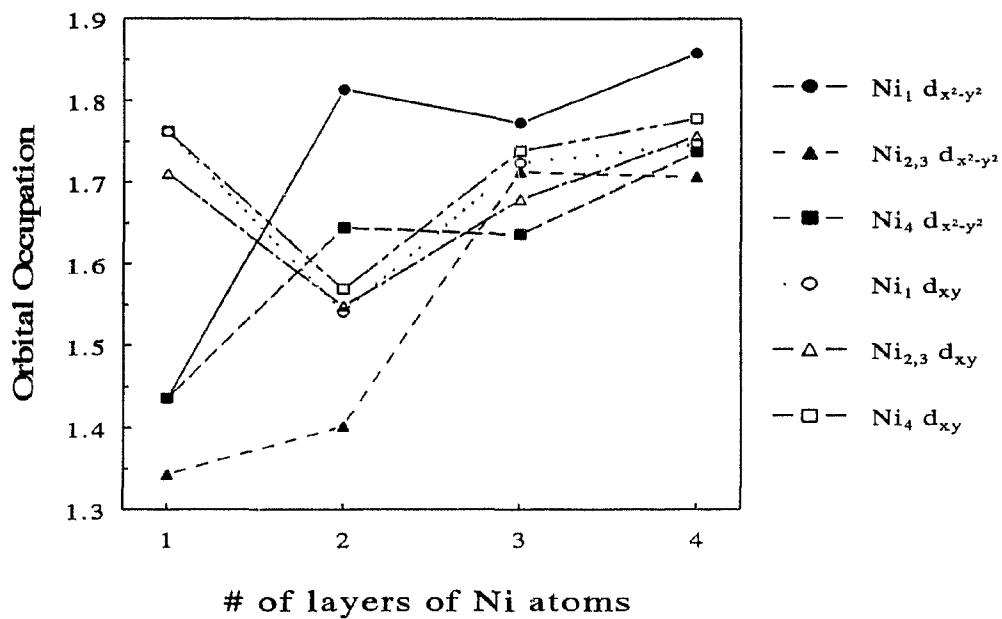
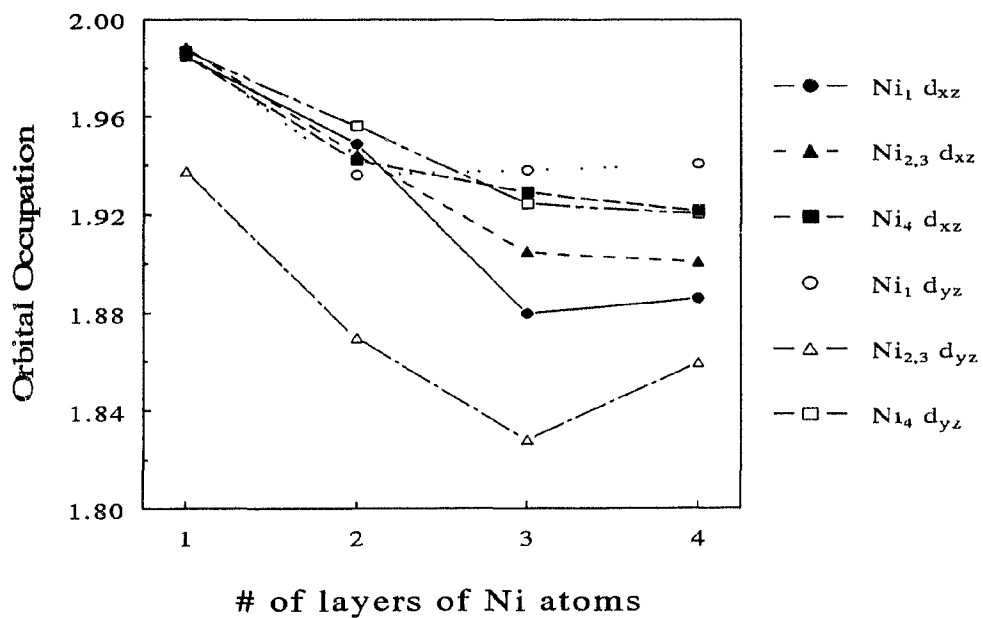
(e) Ni $d_{x^2-y^2}$ and d_{xy} (f) Ni d_{xz} and d_{yz} 

Figure 4.3 Cont'd

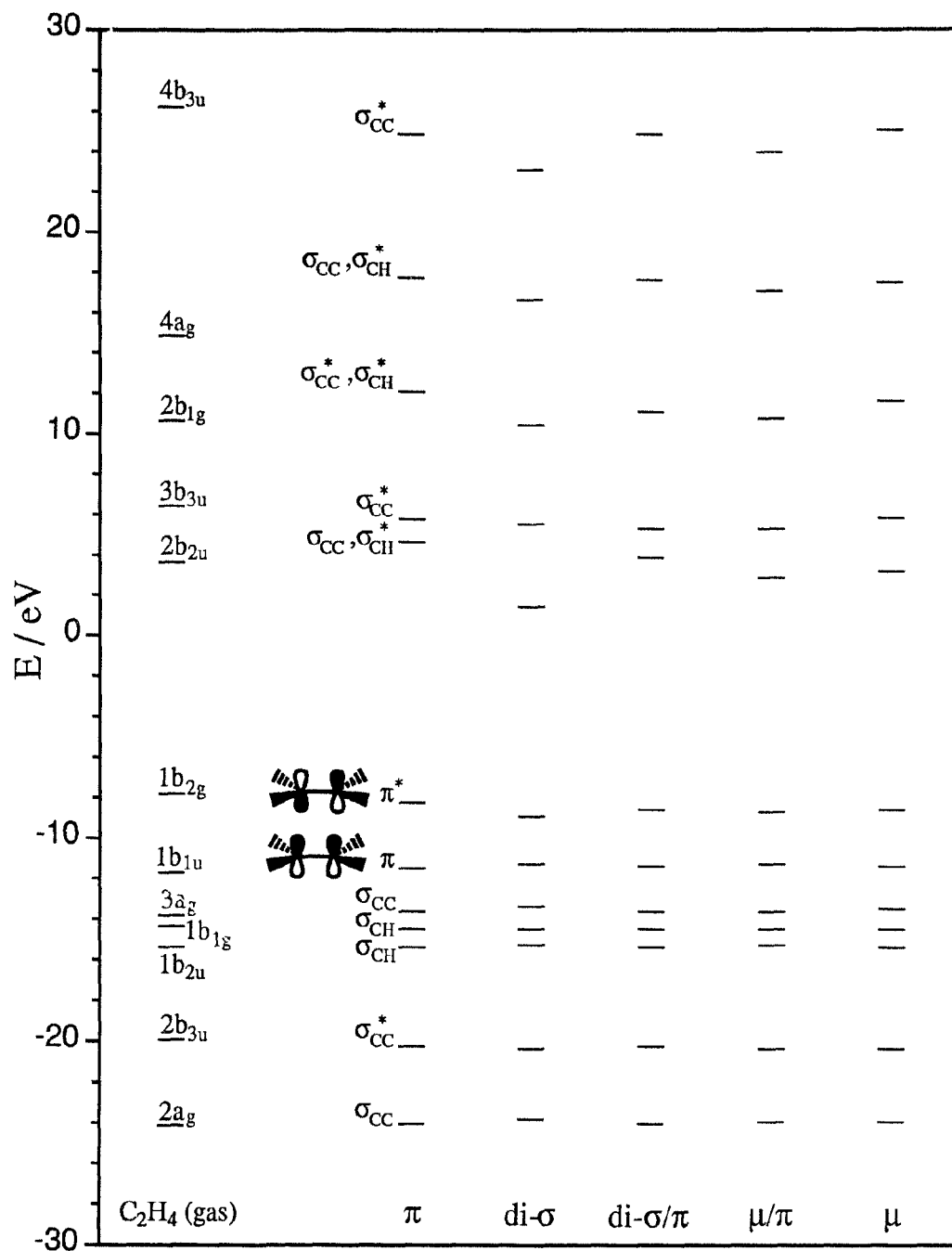


Figure 4.4 Adsorbate MO energy level diagram for C_2H_4 adsorbed on Ni_{80} : C_2H_4 MO energies compared for the gaseous and the distorted molecule when adsorbed in five binding sites. The highest occupied (HOMO) and lowest unoccupied (LUMO) molecular orbitals, π and π^* , are drawn, while the lowest energy levels, $1a_g$ and $1b_{3u}$, corresponding to overlap of the neglected inner-shell C $1s$ AO's, are omitted.

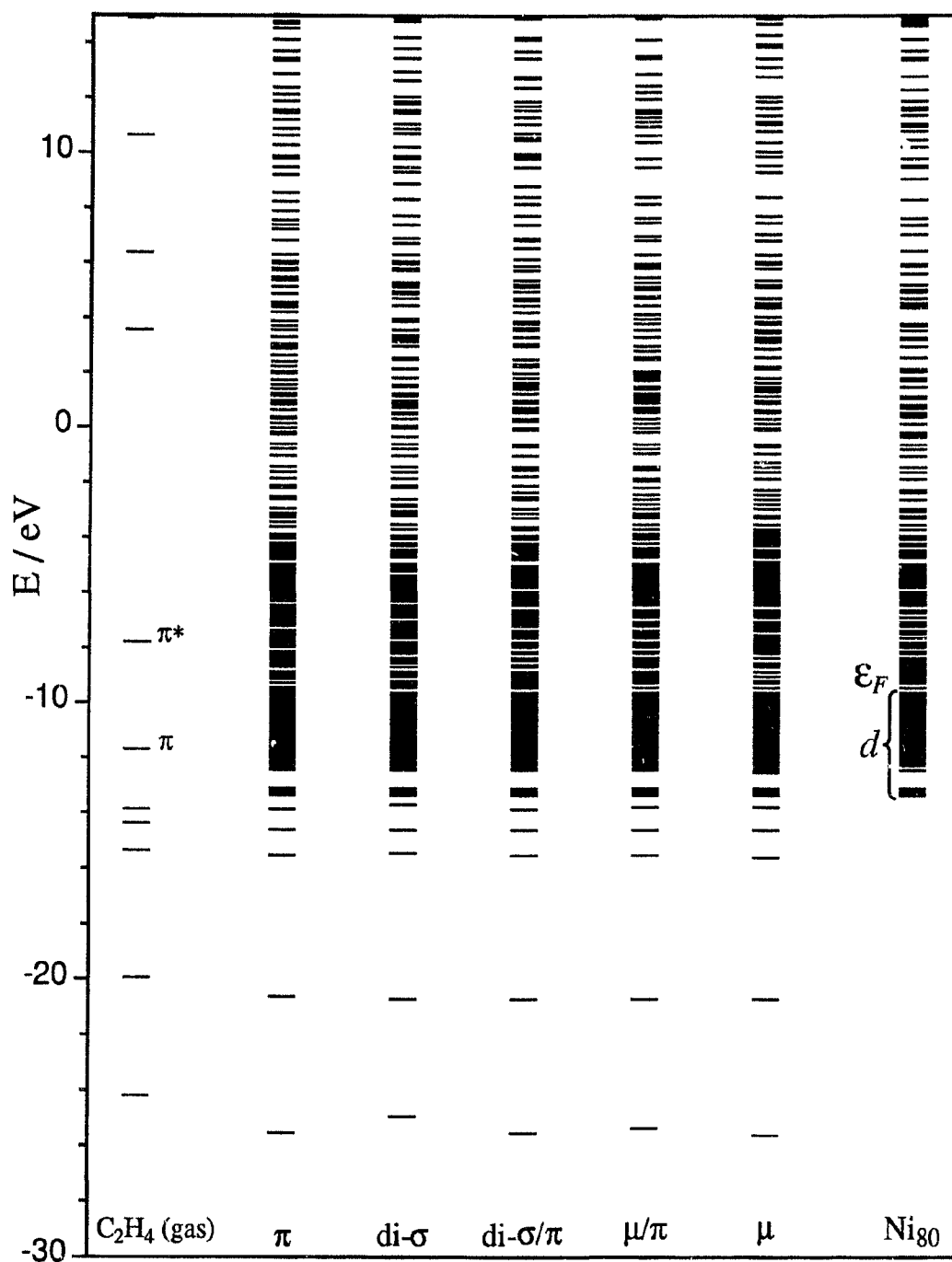


Figure 4.5 MO energy level diagram for $Ni_{80}(C_2H_4)$: chemisorption bonding interaction for C_2H_4 in five adsorption sites. The relative placement of the π and π^* frontier orbitals of gaseous C_2H_4 with respect to the Fermi level, ϵ_F , and d band of the Ni_{80} cluster is indicated.

2. Acetylene: $\text{Ni}_n(\text{C}_2\text{H}_2)$

The corresponding binding energies, optimized structures, and calculated parameters of a single acetylene molecule are given in Figure 4.6 (pp. 137 - 138) and Table 4.3 (pp. 139 - 146). The stability ordering of C_2H_2 adsorbed on the various cluster models is summarized by $\text{di-}\sigma/\pi$ (hcp) \geq $\text{di-}\sigma/\pi$ (fcc) $>$ μ/π (hcp) \geq μ/π (fcc) \geq μ $>$ $\text{di-}\sigma$ $>$ π . On all clusters, C_2H_2 favours the $\text{di-}\sigma/\pi$ bonding configuration, or Δ binding site, in contrast to the preferred $\text{di-}\sigma/\text{di-}\pi$ configuration or μ site deduced from vibrational spectroscopic [33] and PD [39] studies. This apparent contradiction may possibly be attributed to the presence of hydrogen contaminants in the experimental conditions, a conjecture stemming from the analysis of the adsorption sites of C_2H_2 and coadsorbed H in Sect. 4.A.3. In addition to this energetic criterion, however, comparison between the calculated and observed geometries does favour the μ site, as the subsequent discussion reveals.

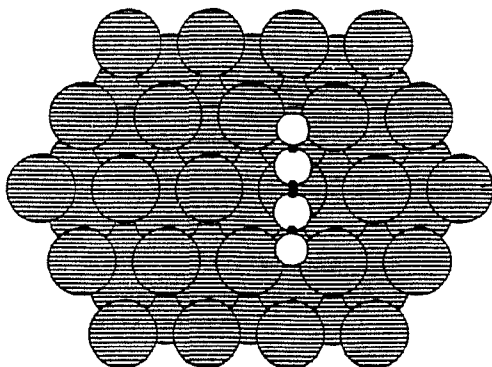
Upon adsorption, the C_2H_2 species distorts from linearity to a planar structure, with expanded C–C bond distances and the C–H bonds bent away from the surface. The lengthened $r(\text{C}–\text{C})$'s are intermediate between those calculated for isolated molecules of C_2H_2 and C_2H_4 , indicative of a bond order between two and three, with estimated states of hybridization of $sp^{1.1} - sp^{2.0}$ and corrected $r(\text{C}–\text{C})$'s of 1.22 - 1.33 Å compared with the PD measurement of $r(\text{C}–\text{C}) = 1.44$ Å [39] and HREELS deduced $\sim sp^{2.5} - sp^3$ hybridization state and estimated $r(\text{C}–\text{C})$ of 1.45 - 1.49 Å [33]. The $\Delta r(\text{C}–\text{C})$ ranges from $\sim (0.02 - 0.16)$ Å, being the least in the atop site and greatest in the μ and Δ

binding sites. In all cases, $r(\text{C-H})$ shortens by $\leq 0.03 \text{ \AA}$. The height of the molecule above the surface ranges from $z(\text{C}) \sim (1.45 - 1.93) \text{ \AA}$, corresponding to the μ and atop sites, respectively, which compares with the PD result of $z(\text{C}) = (1.36/1.37 \pm 0.04) \text{ \AA}$ (fcc/hcp site) [39]. As for C_2H_4 , only in the μ/π binding site is the molecular axis inclined with respect to the surface, which breaks the equivalence of the two H's. The θ_{CCH} distortion ranges from $\sim 10^\circ$ in the atop site to $\sim (40 - 50)^\circ$ in the other bonding configurations. The molecular plane is normal to the surface for all but the di- σ/π -bonded species, for which the C-H bonds are inclined by $\phi \sim 60^\circ$ from the surface plane, corresponding to a tilt of the molecule from the surface normal of $\alpha \sim 20^\circ$, employing the transformation equations in the footnote of Table 4.3.

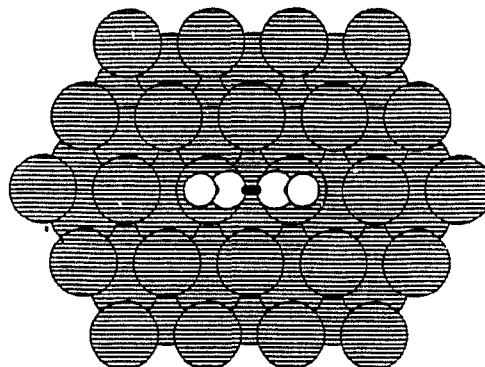
In the atop site, the C_2H_2 C-C bond axis is preferentially oriented along the $[\bar{1}\bar{1}2]$ direction, such that the H's are above threefold sites, as opposed to along the $[\bar{1}10]$ direction, which would place the H's bridging two Ni's. As with C_2H_4 , the C_2H_2 was fixed in this binding site, else it would translate off the smaller clusters or to a more stable site. The equivalence of the H atoms varies as $d = 14 \rightarrow 24$, *i.e.*, with the lateral extent of the cluster, due to asymmetrical edge effects on the clusters of less extent. Both the hcp and fcc sites are about equally favoured for the threefold di- σ/π and μ/π sites, with perhaps a very slight preference for the hcp sites. The two H's were found to be symmetrically equivalent in the optimized structures in all but the μ/π binding sites, the deviation due to the tilting of the molecular axis from the surface, placing the two H's in different environments with respect to the topmost layer of the Ni lattice.

The $\text{Ni}_{80}(\text{C}_2\text{H}_2)$ chemisorption bonding characteristics for the five adsorption sites are examined in Table 4.4 (pp. 147 - 149), which collects the MPA results. Analogous to the $\text{Ni}_{80}(\text{C}_2\text{H}_4)$ system (*cf.* Table 4.2), C-C and Ni-Ni bonding weakens, with respect to the isolated components, as Ni-C bonds form. The doubly degenerate π and π^* orbitals of the gas phase split upon adsorption, with one set of bonding and antibonding orbitals parallel to the surface plane (π_y and π_y^* or π and π^*) and another perpendicular to it (π_z and π_z^* or π_σ and π_σ^*). As might be intuitively clear, the π_z and π_z^* participate more in the chemisorption bond, as the respective orbitals of the incoming molecule rehybridize to a greater extent from the enhanced overlap upon interaction with the orbital lobes arising from mixing of the s and d_{z^2} of the surface Ni atoms, as discussed for C_2H_4 . An additionally strong frontier orbital interaction, however, occurs between the π_y and π_y^* MO's with the metal d_{xz} and d_{yz} . Otherwise, the trends follow those for C_2H_4 : depletion of the Ni s and some of the d_{z^2} orbitals and population of the $d_{x^2-y^2}$ and d_{xy} orbitals of the Ni atoms active in the chemisorption bond. The relative changes in the π_y , π_z , π_z^* , and π_y^* occupations for the five sites decrease in order of their coordination, which closely parallels their stability ordering: $\mu \sim \text{di-}\sigma/\pi > \mu/\pi > \text{di-}\sigma > \pi$. Figures 4.7 (pp. 150 - 152) and 4.8 (pp. 153 - 155) display the MPA dependences on d and ℓ , whereas Figures 4.9 (p. 156) and 4.10 (p. 157), the adsorbate and interaction level diagrams for the $\text{Ni}_{80}(\text{C}_2\text{H}_2)$ system.

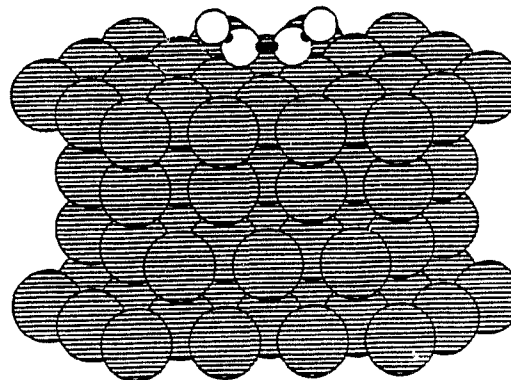
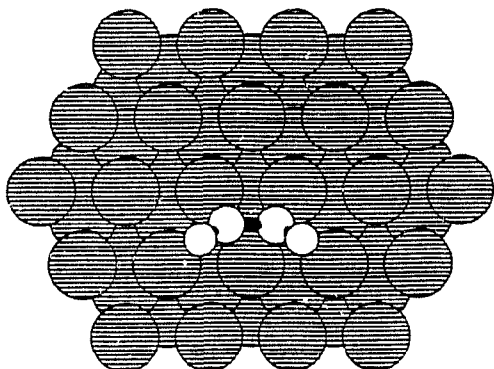
(a) π (onefold atop); $E_B = 1.659$ eV



(b) di- σ (twofold bridging); $E_B = 2.096$ eV



(c) di- σ/π (Δ) — hcp; $E_B = 2.688$ eV



(d) di- σ/π (Δ) — fcc; $E_B = 2.619$ eV

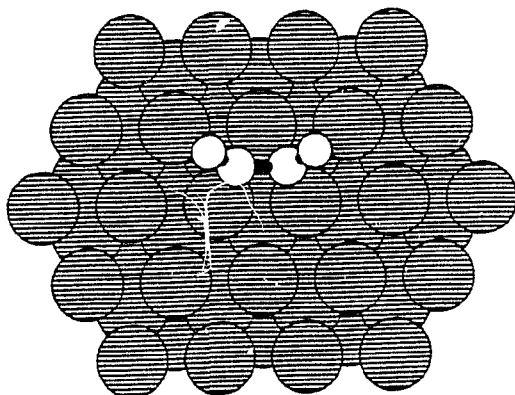
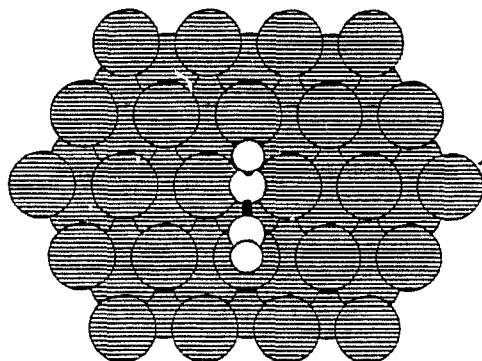
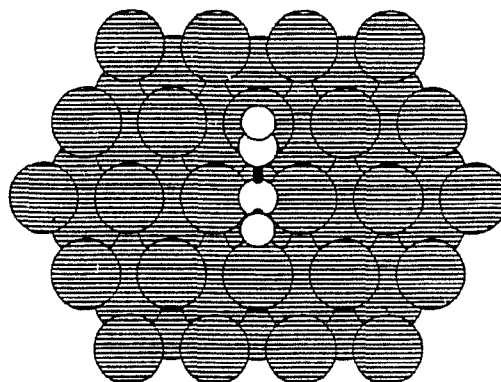


Figure 4.6 $\text{Ni}_{80}(\text{C}_2\text{H}_2)$ adsorption system: optimized geometries and binding energies for (a) - (g) five bonding configurations of C_2H_2 , with two perspectives shown for the di- σ/π and di- $\sigma/\text{di-}\pi$ (μ), on the (24/16/16/24) cluster.

(e) μ/π — hcp; $E_B = 2.375$ eV



(f) μ/π — fcc; $E_B = 2.309$ eV



(g) di- σ /di- π (fourfold bridging or μ); $E_B = 2.315$ eV

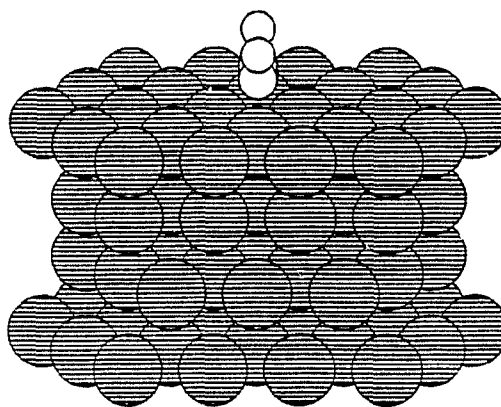
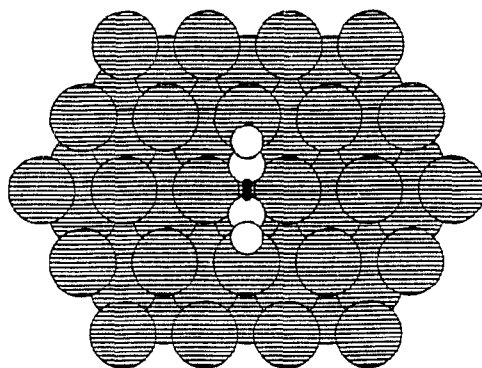


Figure 4.6 Cont'd

Table 4.3 Optimized Adsorption Parameters for $\text{Ni}_n(\text{C}_2\text{H}_2)$ for Three Series of Clusters: $d = 14, 19, 24^a$; $\ell = 1, 2, 3, 4$

ℓ	E_B^b / eV	$\Delta r(\text{C}-\text{C})^c / \text{Å}$	$\Delta r(\text{C}-\text{H})^c / \text{Å}$	$z(\text{C})^d / \text{Å}$	$\theta_{\text{CCH}}^{e,f} / \text{deg}$	$\phi^{e,f} / \text{deg}$
π (onfold atop site)						
$n = 14, 22, 30, 44:$						
1	0.561	0.03 ($sp^{1.18}$)	-0.02	1.980	166.7	90.0
2	1.318	0.02 ($sp^{1.12}$)	-0.03	1.980	170.6, 169.8	89.1, 85.7
3	1.414	0.02 ($sp^{1.12}$)	-0.03	1.967	170.0, 170.3	86.4, 80.5
4	1.470	0.02 ($sp^{1.12}$)	-0.03	1.963	170.0, 169.3	84.7, 83.0
$n = 19, 31, 43, 62:$						
1	0.770	0.03 ($sp^{1.18}$)	-0.02	1.961	167.0	90.0
2	1.599	0.02 ($sp^{1.13}$)	-0.03	1.950	170.3, 170.5	90.0
3	1.637	0.02 ($sp^{1.14}$)	-0.03	1.931	170.2, 170.8	90.0
4	1.721	0.02 ($sp^{1.14}$)	-0.03	1.931	169.7, 170.1	90.0
$n = 24, 40, 56, 80:$						
1	1.019	0.03 ($sp^{1.18}$)	-0.02	1.961	167.0	90.0
2	1.500	0.02 ($sp^{1.13}$)	-0.03	1.953	170.6	90.0
3	1.582	0.02 ($sp^{1.13}$)	-0.03	1.945	170.6	90.0
4	1.659	0.02 ($sp^{1.13}$)	-0.03	1.934	169.5	90.0

See footnotes at end of Table on p. 146

Table 4.3 Cont'd

l	$E_B^b /$ eV	$\Delta r(\text{C}-\text{C})^c /$ Å	$\Delta r(\text{C}-\text{H})^c /$ Å	$z(\text{C})^d /$ Å	$\theta_{\text{CCH}}^{e,f} /$ deg	$\phi^{e,f} /$ deg
di-σ (twofold aligned bridging site)						
$n = 14, 22, 30, 44$						
1	1.189	0.11 ($sp^{1.66}$)	0.00	1.877	135.9	90.0
2	1.635	0.10 ($sp^{1.61}$)	0.00	1.874	137.4	90.0
3	1.850	0.10 ($sp^{1.63}$)	0.00	1.863	136.7	90.0
4	1.922	0.0 ($sp^{1.61}$)	0.00	1.871	136.7	90.0
$n = 19, 31, 43, 62$						
1	1.377	0.11 ($sp^{1.67}$)	0.00	1.869	135.7	90.0
2	1.739	0.10 ($sp^{1.63}$)	0.00	1.869	136.8	90.0
3	1.951	0.10 ($sp^{1.63}$)	0.00	1.859	136.7	90.0
4	1.966	0.10 ($sp^{1.63}$)	0.00	1.866	136.7	90.0
$n = 24, 40, 56, 80$						
1	1.689	0.11 ($sp^{1.67}$)	0.00	1.869	135.7	90.0
2	1.801	0.10 ($sp^{1.64}$)	0.00	1.868	136.4	90.0
3	1.952	0.10 ($sp^{1.64}$)	0.00	1.858	136.4	90.0
4	2.096	0.10 ($sp^{1.64}$)	0.00	1.857	136.0	90.0

See footnotes at end of Table on p. 146

Table 4.3 Cont'd

ℓ	$E_B^b /$ eV	$\Delta r(\text{C}-\text{C})^c /$ Å	$\Delta r(\text{C}-\text{H})^c /$ Å	$z(\text{C})^d /$ Å	$\theta_{\text{CCH}}^{e,f} /$ deg	$\phi^{e,f} /$ deg
di-σ/π (threefold triangular or Δ site)^g — hcp						
$n = 14, 22, 30, 44:$						
1	1.315	0.17 ($sp^{1.96}$)	-0.01	1.578	131.2	64.1
2	2.064	0.14 ($sp^{1.83}$)	-0.02	1.589	134.4	60.3
3	2.328	0.14 ($sp^{1.83}$)	-0.02	1.583	134.3	60.3
4	2.322	0.14 ($sp^{1.83}$)	-0.02	1.583	134.3	60.3
$n = 19, 31, 43, 62:$						
1	1.725	0.16 ($sp^{1.94}$)	-0.01	1.567	131.8	62.1
2	2.320	0.14 ($sp^{1.85}$)	-0.02	1.569	134.7	59.3
3	2.630	0.15 ($sp^{1.86}$)	-0.02	1.564	133.7	58.2
4	2.611	0.14 ($sp^{1.85}$)	-0.02	1.567	134.1	58.8
$n = 24, 40, 56, 80:$						
1	2.190	0.16 ($sp^{1.94}$)	-0.01	1.562	132.0	62.4
2	2.315	0.15 ($sp^{1.87}$)	-0.02	1.567	133.8	59.3
3	2.575	0.15 ($sp^{1.87}$)	-0.02	1.563	133.8	58.6
4	2.688	0.15 ($sp^{1.87}$)	-0.02	1.566	133.6	59.0

See footnotes at end of Table on p. 146

Table 4.3 Cont'd

ℓ	$E_B^b /$ eV	$\Delta r(\text{C}-\text{C})^c /$ Å	$\Delta r(\text{C}-\text{H})^c /$ Å	$z(\text{C})^d /$ Å	$\theta_{\text{CCH}}^{e,f} /$ deg	$\phi^{e,f} /$ deg
di-σ/π (threefold triangular or Δ site)^g — fcc						
$n = 14, 22, 30, 44:$						
1	1.315	0.17 ($sp^{1.86}$)	-0.01	1.578	131.2	64.1
2	2.026	0.13 ($sp^{1.80}$)	-0.02	1.591	134.4	59.2
3	2.286	0.13 ($sp^{1.80}$)	-0.02	1.591	134.7	59.3
4	2.249	0.13 ($sp^{1.80}$)	-0.02	1.592	133.5	60.4
$n = 19, 31, 43, 62:$						
1	1.725	0.16 ($sp^{1.94}$)	-0.01	1.567	131.8	62.1
2	2.263	0.13 ($sp^{1.81}$)	-0.02	1.569	135.4	58.4
3	2.552	0.13 ($sp^{1.81}$)	-0.02	1.567	135.4	57.6
4	2.564	0.14 ($sp^{1.81}$)	-0.02	1.569	135.1	58.3
$n = 24, 40, 56, 80:$						
1	2.190	0.16 ($sp^{1.94}$)	-0.01	1.562	132.0	62.4
2	2.316	0.14 ($sp^{1.82}$)	-0.02	1.572	135.2	56.6
3	2.520	0.14 ($sp^{1.84}$)	-0.02	1.570	133.9	58.3
4	2.619	0.14 ($sp^{1.83}$)	-0.02	1.568	134.0	57.7

See footnotes at end of Table on p. 146

Table 4.3 Cont'd

ℓ	$E_B^b /$ eV	$\Delta r(\text{C}-\text{C})^c /$ Å	$\Delta r(\text{C}-\text{H})^c /$ Å	$z(\text{C})^d /$ Å	$\theta_{\text{CCH}}^{e,f} /$ deg	$\phi^{e,f} /$ deg
μ/π (threefold bridging/atop site) ^g — hcp						
n = 14, 22, 30, 44:						
1	1.155	0.15 ($sp^{1.91}$)	0.00, -0.01	1.762, 1.565	126.2, 139.4	90.0, 90.0
2	1.854	0.12 ($sp^{1.74}$)	-0.01, -0.02	1.770, 1.577	127.6, 143.7	90.0, 90.0
3	2.133	0.12 ($sp^{1.74}$)	-0.01, -0.02	1.757, 1.577	127.6, 143.2	90.0, 90.0
4	2.125	0.12 ($sp^{1.74}$)	-0.01, -0.02	1.762, 1.583	128.2, 142.5	90.0, 90.0
n = 19, 31, 43, 62:						
1	1.512	0.15 ($sp^{1.86}$)	0.00, -0.01	1.774, 1.574	126.1, 139.5	90.0, 90.0
2	1.945	0.12 ($sp^{1.73}$)	-0.01, -0.02	1.764, 1.579	128.1, 143.4	90.0, 90.0
3	2.215	0.12 ($sp^{1.73}$)	-0.01, -0.02	1.757, 1.575	128.1, 142.5	90.0, 90.0
4	2.222	0.12 ($sp^{1.73}$)	-0.01, -0.02	1.760, 1.575	128.1, 142.5	90.0, 90.0
n = 24, 40, 56, 80:						
1	1.927	0.15 ($sp^{1.88}$)	0.00, -0.01	1.752, 1.558	126.3, 139.5	90.0, 90.0
2	2.001	0.13 ($sp^{1.76}$)	-0.01, -0.02	1.764, 1.575	126.6, 142.6	90.0, 90.0
3	2.215	0.13 ($sp^{1.76}$)	-0.01, -0.02	1.758, 1.558	126.8, 142.6	90.0, 90.0
4	2.375	0.12 ($sp^{1.76}$)	-0.01, -0.02	1.758, 1.572	127.4, 142.6	90.0, 90.0

See footnotes at end of Table on p. 146

Table 4.3 Cont'd

ℓ	$E_B^b /$ eV	$\Delta r(\text{C}-\text{C})^c /$ Å	$\Delta r(\text{C}-\text{H})^c /$ Å	$z(\text{C})^d /$ Å	$\theta_{\text{CCH}}^{e,f} /$ deg	$\phi^{e,f} /$ deg
μ/π (threefold bridging/atop site) ^g — fcc						
$n = 14, 22, 30, 44:$						
1	1.155	0.15 ($sp^{1.91}$)	-0.01, 0.00	1.565, 1.762	139.4, 126.2	90.0, 90.0
2	1.792	0.11 ($sp^{1.71}$)	-0.02, -0.01	1.581, 1.773	145.2, 128.8	90.0, 90.0
3	2.082	0.11 ($sp^{1.71}$)	-0.02, -0.01	1.581, 1.776	144.1, 128.8	90.0, 90.0
4	2.059	0.11 ($sp^{1.71}$)	-0.02, -0.01	1.588, 1.779	144.1, 128.8	90.0, 90.0
$n = 19, 31, 43, 62:$						
1	1.512	0.15 ($sp^{1.86}$)	-0.01, 0.00	1.574, 1.774	139.5, 126.1	90.0, 90.0
2	1.874	0.12 ($sp^{1.73}$)	-0.02, -0.01	1.576, 1.767	144.0, 128.1	90.0, 89.0
3	2.190	0.12 ($sp^{1.72}$)	-0.02, -0.01	1.579, 1.773	144.2, 128.1	90.0, 90.0
4	2.166	0.12 ($sp^{1.71}$)	-0.02, -0.01	1.579, 1.773	143.1, 128.1	90.0, 90.0
$n = 24, 40, 56, 80:$						
1	1.927	0.15 ($sp^{1.88}$)	-0.01, 0.00	1.558, 1.752	139.5, 126.3	90.0, 90.0
2	1.957	0.12 ($sp^{1.73}$)	-0.02, -0.01	1.572, 1.769	144.3, 127.2	90.0, 90.0
3	2.218	0.12 ($sp^{1.74}$)	-0.02, -0.01	1.571, 1.766	143.6, 127.8	90.0, 90.0
4	2.309	0.12 ($sp^{1.73}$)	-0.02, -0.01	1.572, 1.761	142.6, 127.4	90.0, 90.0

See footnotes at end of Table on p. 146

Table 4.3 Cont'd

ℓ	$E_B^b /$ eV	$\Delta r(\text{C}-\text{C})^c /$ Å	$\Delta r(\text{C}-\text{H})^c /$ Å	$z(\text{C})^d /$ Å	$\theta_{\text{CCH}}^{e,f} /$ deg	$\phi^{e,f} /$ deg
di-σ/di-π (fourfold bridging or μ site)						
$n = 14, 22, 30, 44:$						
1	0.746	0.17 ($sp^{1.96}$)	-0.01	1.490	128.0	90.0
2	1.755	0.15 ($sp^{1.90}$)	-0.02, -0.02	1.467, 1.461	128.7, 129.1	90.0
3	1.966	0.15 ($sp^{1.89}$)	-0.02, -0.02	1.467, 1.458	129.0, 129.3	90.0
4	1.916	0.17 ($sp^{1.96}$)	-0.02, -0.02	1.456, 1.447	126.3, 127.2	90.0
$n = 19, 31, 43, 62:$						
1	1.141	0.20 ($sp^{2.11}$)	-0.01	1.455	123.4	90.0
2	1.929	0.16 ($sp^{1.91}$)	-0.02	1.454	128.6	88.6
3	2.134	0.17 ($sp^{1.98}$)	-0.02	1.444	125.6	90.0
4	2.111	0.17 ($sp^{1.96}$)	-0.02	1.447	126.3	90.0
$n = 24, 40, 56, 80:$						
1	1.818	0.25 ($sp^{2.31}$)	-0.01	1.398	117.0	90.0
2	1.951	0.16 ($sp^{1.95}$)	-0.02	1.440	127.6	90.0
3	2.155	0.17 ($sp^{1.96}$)	-0.02	1.437	126.9	90.0
4	2.315	0.16 ($sp^{1.94}$)	-0.02	1.448	127.6	90.0

Footnotes to Table 4.3:

- ^a Four-layered Ni clusters corresponding to $d = 14, 19,$ and 24 are shown in Figure 3.3, where the $d = 14$ and 24 series are symmetric about the di- σ and μ adsorption sites and the $d = 19$ series is symmetric about the atop site; Figure 4.6 displays the structures for the $\text{Ni}_{80}(\text{C}_2\text{H}_2)$ adsorption system
- ^b $E_B = [E(\text{Ni}_n) + E(\text{C}_2\text{H}_2)] - E(\text{Ni}_n(\text{C}_2\text{H}_2))$
- ^c C–C bond stretch and C–H bond contraction from optimized values of 1.324 and 1.150 Å, respectively, for isolated C_2H_2 (estimated states of hybridization, sp^n , interpolated from the quadratic fits of Figure 3.1, in parentheses)
- ^d Perpendicular height(s) of C atoms above the surface
- ^e Compare with the bond angles of $\theta_{\text{CCH}} = 180.0^\circ$ for the undistorted linear C_2H_2 molecule and $\phi = 90.0^\circ$ for a planar molecule oriented perpendicular to the surface plane, where ϕ is the angle of inclination of the C–H bonds from the surface
- ^f The following transformation equations:

$$\cos(180^\circ - \theta_{\text{CCH}}) = \cos\alpha \cos\gamma$$

$$\sin\theta_{\text{CCH}} \cos\phi = \sin\alpha$$

$$\sin\theta_{\text{CCH}} \sin\phi = \cos\alpha \sin\gamma ;$$

relate θ_{CCH} and ϕ to α , the angle of bend of the C–H bonds out of the plane normal to the surface, and γ , the angle of tilt between the projection of the C–H bond into the plane normal to the surface and the C–C bond axis.

- ^g Shift of the centre of the C–C bond from the $[\bar{1}10]$ direction optimized to roughly ± 1.00 Å and ± 0.75 Å for the di- σ/π and μ/π configurations, respectively, in the hcp and fcc sites
-

Table 4.4 Ni₈₀(C₂H₂) Chemisorption Bonding Indices (MPA's) for Five Binding Sites of the Central Ni₄ Unit Cell

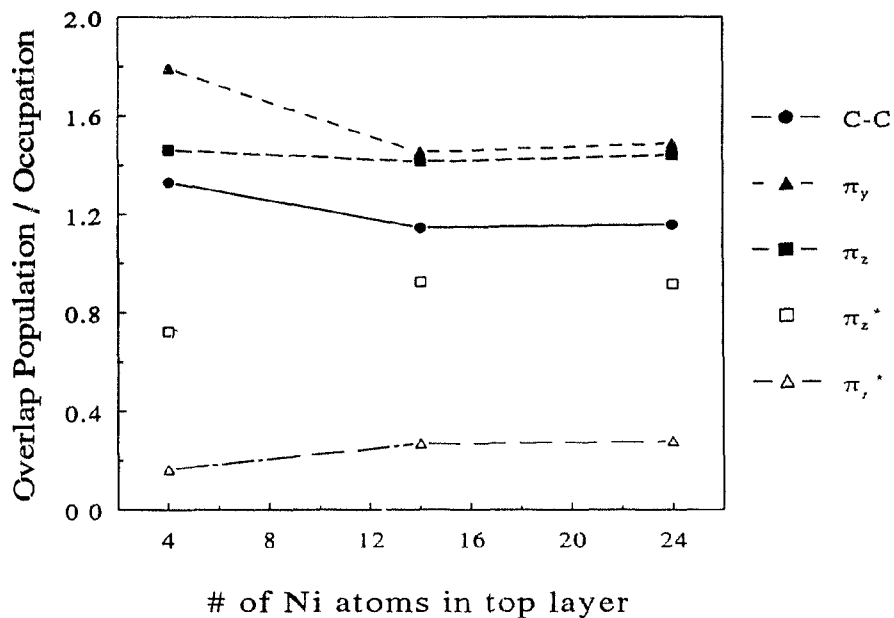
	C ₂ H ₂	Ni ₄	π	di- σ	di- σ/π	μ/π	μ
E_B / eV			1.659	2.096	2.688	2.375	2.315
$r(\text{C}-\text{C}) / \text{\AA}$	1.324		1.342	1.425	1.471	1.444	1.484
Overlap Population							
C-C	1.74		1.71	1.40	1.24	1.29	1.19
Ni ₁ -Ni _{2,3}		0.13	0.12, 0.10	0.11	0.08	0.05	0.09
Ni ₂ -Ni ₃		0.15	0.12	0.06	0.06	0.10	0.04
Ni _{2,3} -Ni ₄		0.13	0.12, 0.10	0.10	0.12	0.10	0.09
Ni ₁ -Ni ₄		-0.01	-0.01	-0.01	-0.01	-0.01	-0.01
Ni ₁ -C ₁			-0.05	-0.04	0.10	0.50	0.27
Ni ₁ -C ₂			-0.01	-0.04	0.10	-0.14	-0.05
Ni ₂ -C ₁			-0.03	-0.14	-0.13	-0.10	0.13
Ni ₂ -C ₂			-0.02	0.42	0.44	0.27	0.13
Ni ₃ -C ₁			0.04	0.42	0.44	-0.10	0.13
Ni ₃ -C ₂			0.04	-0.14	-0.13	0.27	0.13
Ni ₄ -C ₁			-0.01	-0.04	-0.01	0.00	-0.05
Ni ₄ -C ₂			-0.05	-0.04	-0.01	-0.05	0.27

Table 4.4 Cont'd

	C ₂ H ₂	Ni ₄	π	di- σ	di- σ/π	μ/π	μ
Occupations							
π_y^* (π^*)	0		0.04	0.13	0.30	0.23	0.29
π_z^* (π_σ^*)	0		0.24	0.91	0.94	0.91	0.91
π_z (π_σ)	2		1.73	1.54	1.50	1.53	1.47
π_y (π)	2		1.98	1.96	1.62	1.67	1.54
Ni ₁ s		0.73	0.70	0.70	0.68	0.69	0.73
Ni _{2,3} s		0.77	0.72, 0.68	0.76	0.75	0.72	0.68
Ni ₄ s		0.71	0.67	0.67	0.69	0.67	0.71
Ni ₁ d _{z²}		1.90	1.89	1.89	1.50	1.88	1.74
Ni _{2,3} d _{z²}		1.91	1.91, 1.40	1.40	1.53	1.63	1.50
Ni ₄ d _{z²}		1.90	1.89	1.89	1.88	1.89	1.74
Ni ₁ d _{x²-y²}		1.76	1.77	1.72	1.71	1.76	1.77
Ni _{2,3} d _{x²-y²}		1.69	1.69, 1.67	1.67	1.64	1.64	1.65
Ni ₄ d _{x²-y²}		1.69	1.70	1.69	1.70	1.68	1.68
Ni ₁ d _{xy}		1.68	1.66	1.64	1.54	1.73	1.60
Ni _{2,3} d _{xy}		1.66	1.67, 1.66	1.66	1.65	1.67	1.53
Ni ₄ d _{xy}		1.69	1.67	1.65	1.67	1.64	1.58

Table 4.4 Cont'd

	C_2H_2	Ni_4	π	di- σ	di- σ/π	μ/π	μ
$Ni_1 d_{xz}$		1.92	1.91	1.91	1.72	1.91	1.69
$Ni_{2,3} d_{xz}$		1.89	1.91, 1.75	1.82	1.70	1.87	1.74
$Ni_4 d_{xz}$		1.94	1.93	1.93	1.92	1.93	1.70
$Ni_1 d_{yz}$		1.93	1.93	1.93	1.79	1.92	1.88
$Ni_{2,3} d_{yz}$		1.90	1.90, 1.82	1.82	1.87	1.69	1.69
$Ni_4 d_{yz}$		1.89	1.89	1.89	1.89	1.90	1.86

(a) C-C Overlap; π_y , π_z , π_z^* , and π_y^* Occupations

(b) Ni-C Overlap

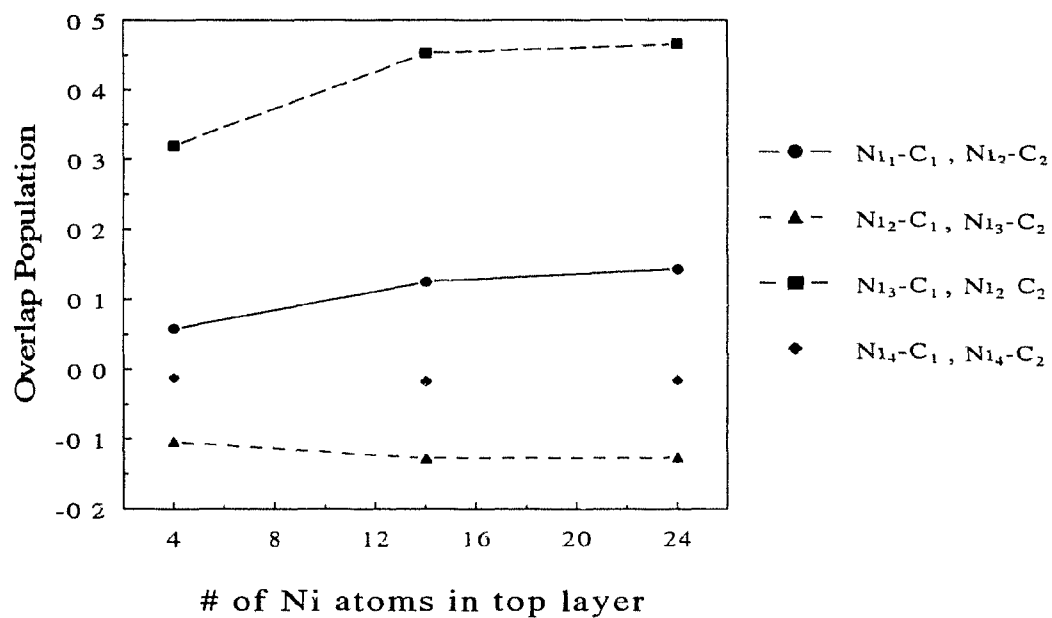


Figure 4.7 MPA of di- σ/π -bonded C_2H_2 on Ni_n for the $d = 4, 14,$ and 24 series of clusters: (a) C-C overlap populations and $\pi_y, \pi_z, \pi_z^*,$ and π_y^* MO occupations; (b) Ni-C and (c) Ni-Ni overlap populations; and AO occupations for Ni (d) $s, d_{z^2},$ (e) $d_{x^2-y^2}, d_{xy},$ (f) d_{xz} and d_{yz}

(c) Ni–Ni Overlap

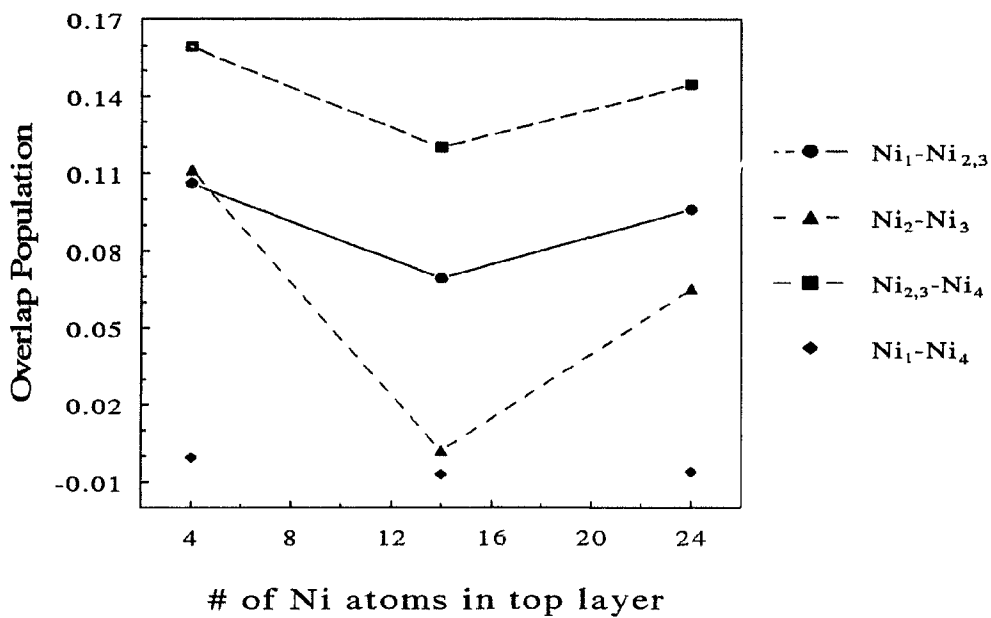
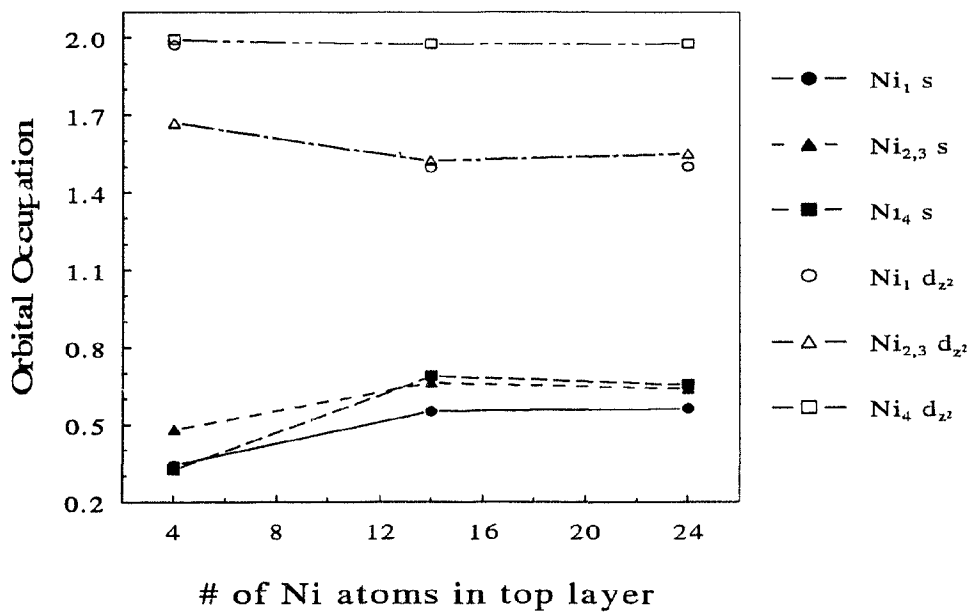
(d) Ni s and d_{z^2} 

Figure 4.7 Cont'd

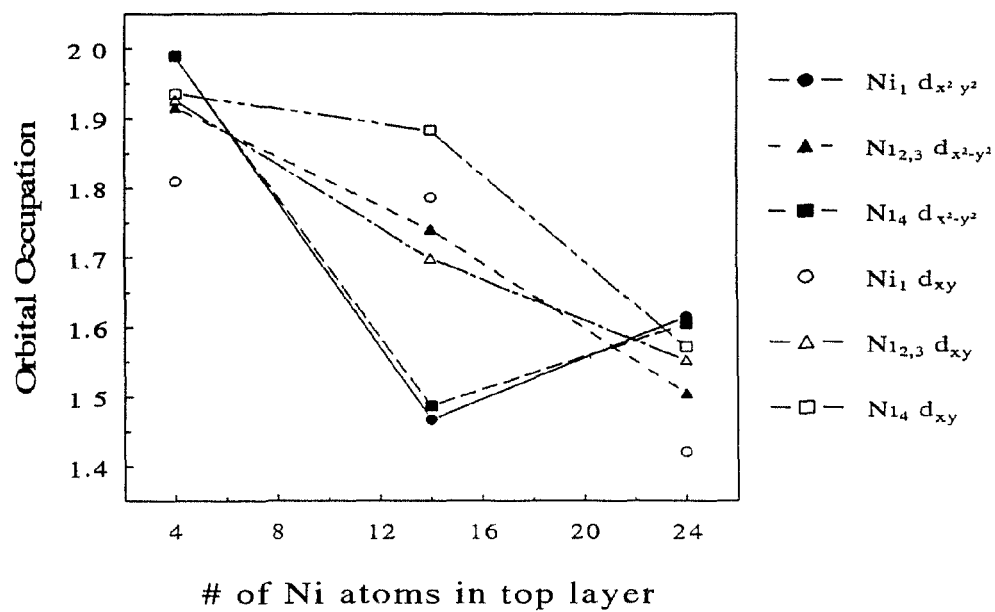
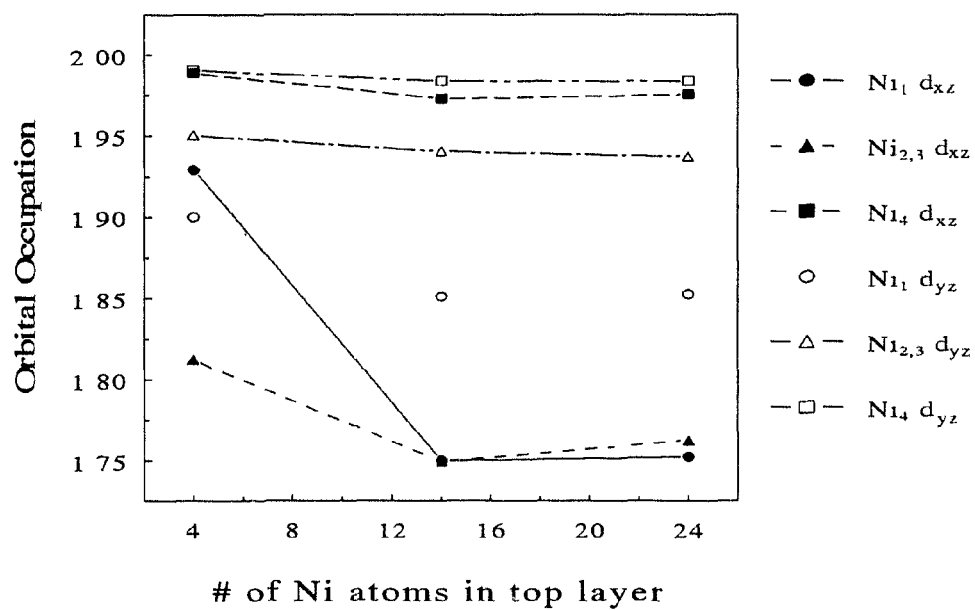
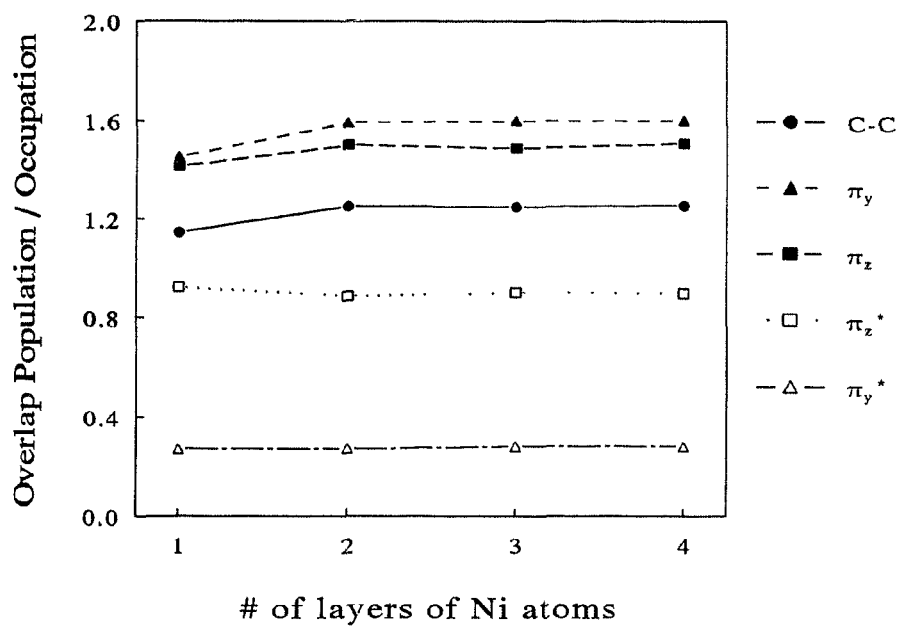
(e) Ni $d_{x^2-y^2}$ and d_{xy} (f) Ni d_{xz} and d_{yz} 

Figure 4.7 Cont'd

(a) C–C Overlap; π_y , π_z , π_z^* , and π_y^* Occupations

(b) Ni–C Overlap

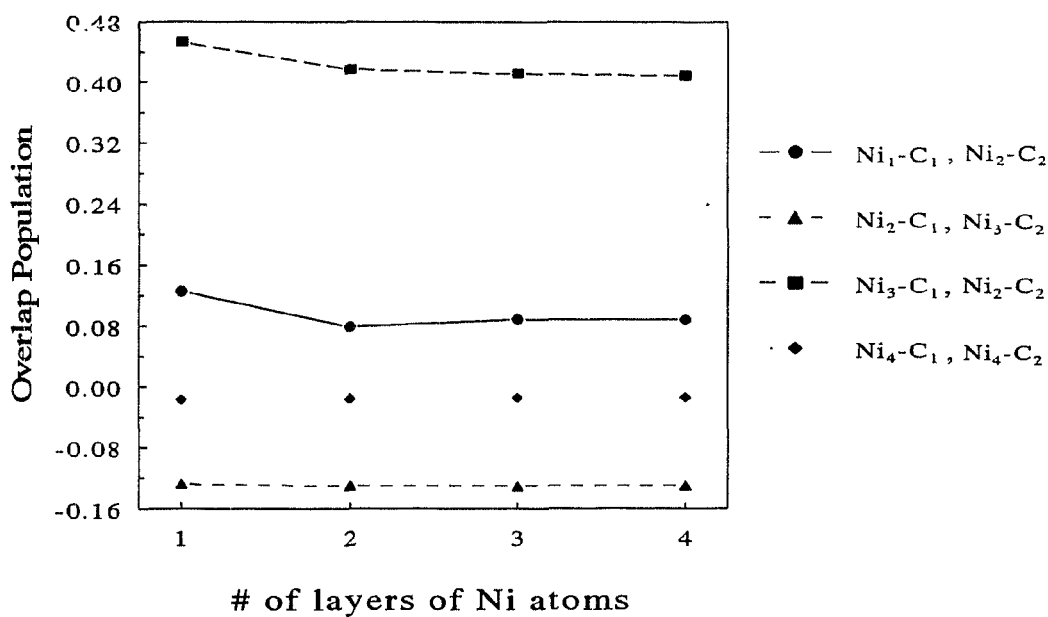


Figure 4.8 MPA of di- σ/π -bonded C_2H_2 on Ni_n for the $d = 14$ series of clusters as $\ell = 1 \rightarrow 4$: (a) C–C overlap populations and π_y , π_z , π_z^* , and π_y^* MO occupations; (b) Ni–C and (c) Ni–Ni overlap populations; and AO occupations for Ni (d) s , d_{z^2} , (e) $d_{x^2-y^2}$, d_{xy} , (f) d_{xz} and d_{yz} .

(c) Ni-Ni Overlap

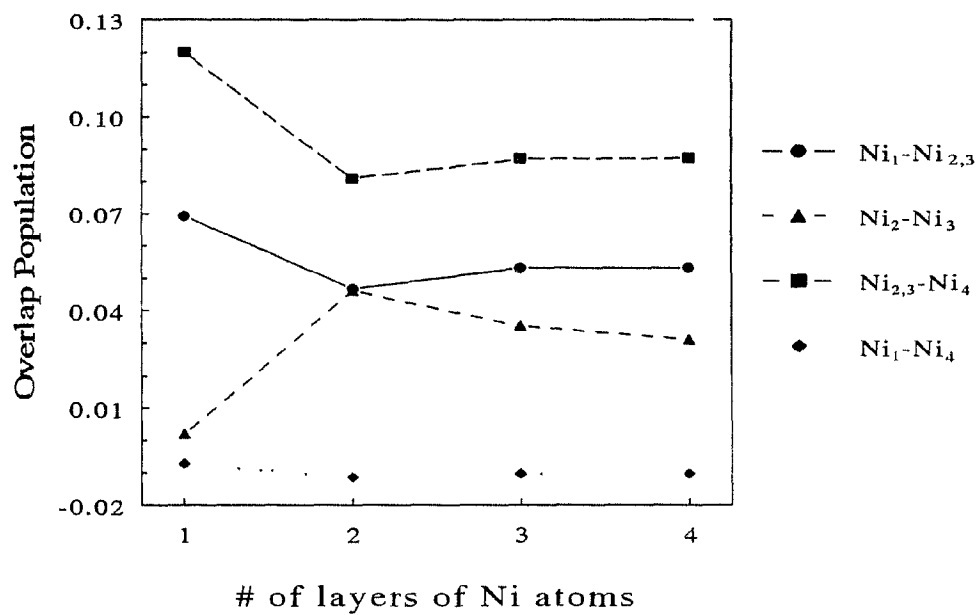
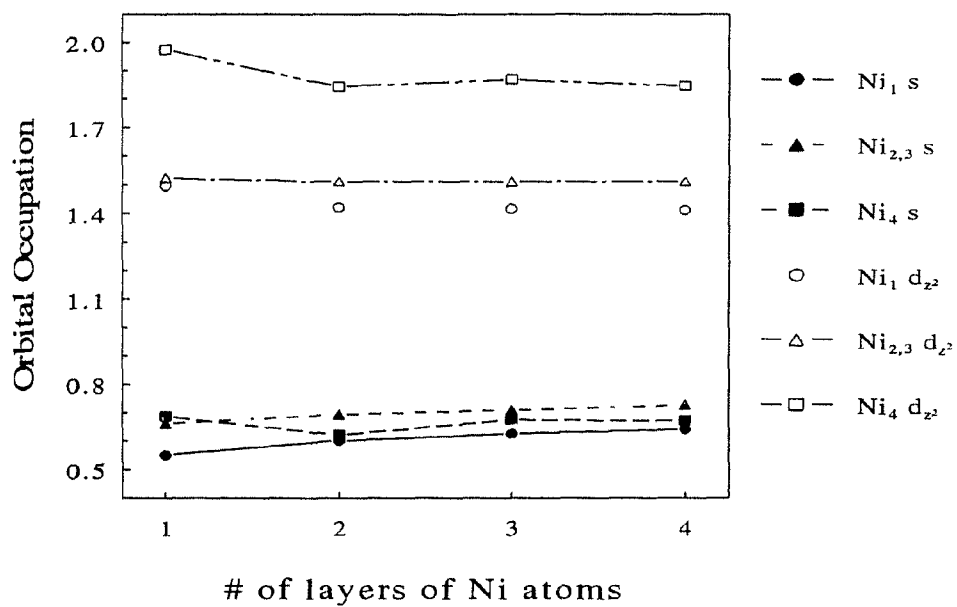
(d) Ni s and d_{z^2} 

Figure 4.8 Cont'd

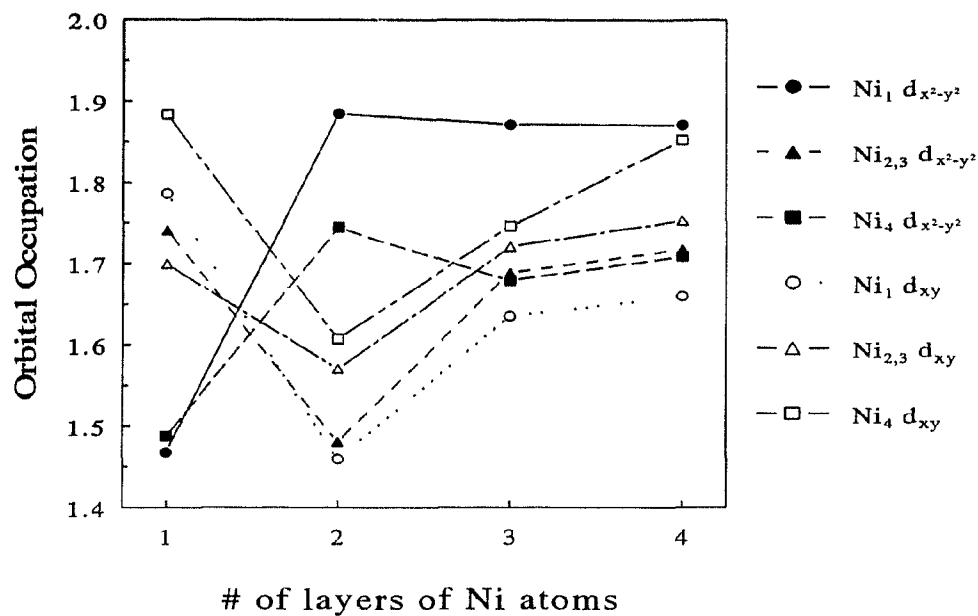
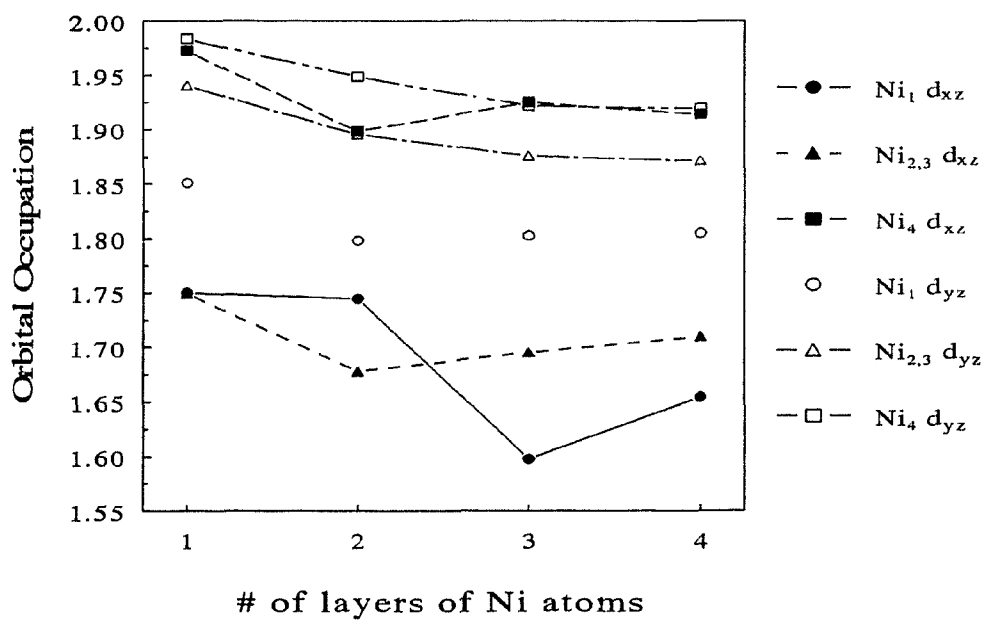
(e) Ni $d_{x^2-y^2}$ and d_{xy} (f) Ni d_{xz} and d_{yz} 

Figure 4.8 Cont'd

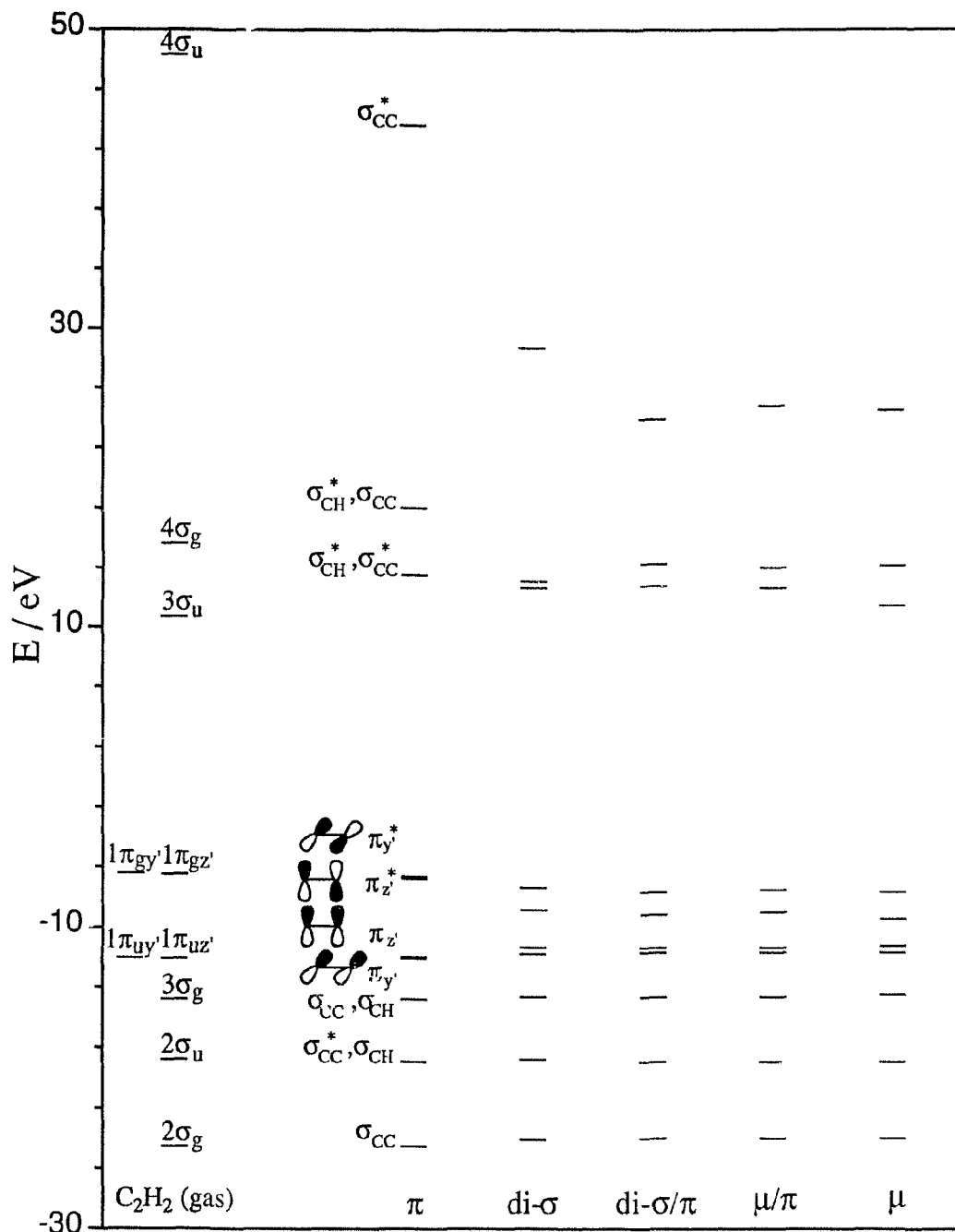


Figure 4.9 Adsorbate MO energy level diagram for C_2H_2 adsorbed on Ni_{80} : C_2H_2 MO energies compared for the gaseous and the distorted molecule when adsorbed in five adsorption sites. The HOMO's, π_y and π_z , and LUMO's, π_z^* and π_y^* , are drawn, while the lowest energy levels, $1\sigma_g$ and $1\sigma_u$, corresponding to overlap of the neglected C $1s$ AO's, are omitted, as for C_2H_4 .

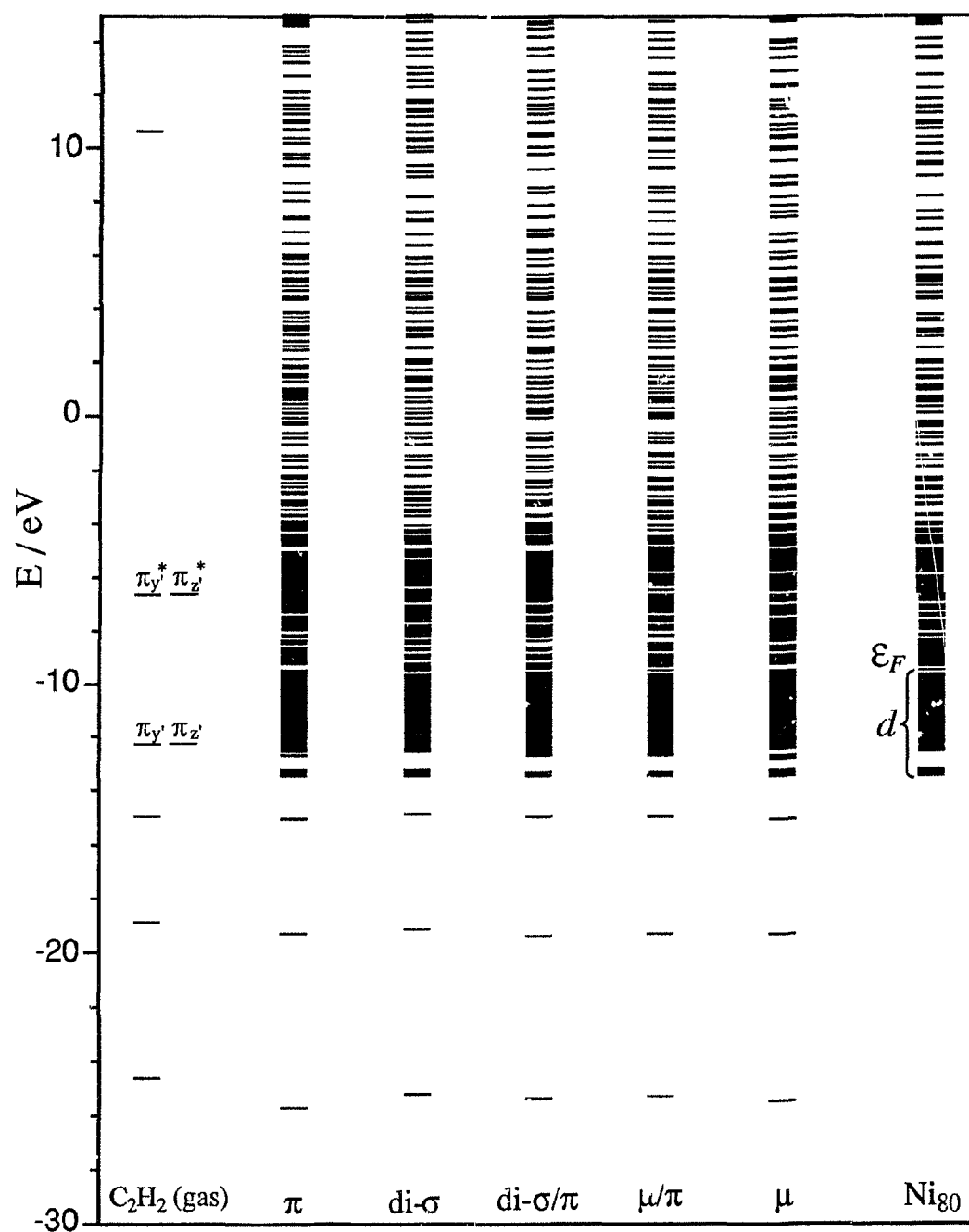


Figure 4.10 MO energy level diagram for $Ni_{80}(C_2H_2)$: chemisorption bonding interaction for C_2H_2 in five adsorption sites. The relative placement of the π_y, π_z, π_y^* and π_z^* frontier orbitals of gaseous C_2H_2 with respect to ϵ_F and the d band of the Ni_{80} cluster is indicated.

b. Two Adsorbate Molecules in (2×2) Overlayer Structure

Both the optimization of two adsorbate molecules and the ensuing study of the dehydrogenation mechanism required enlarged cluster models. Motivated by the cluster dependence analysis of Chapter 3, one-, two-, and three-layered Ni_n clusters, corresponding to $n = 30, 51, \text{ and } 72$, were adopted, with the surface layer consisting of a pair of unit cells and their first coordination shells, so as to surround the chemisorption-bonded Ni's by their nearest neighbours, and additional Ni's to impart a moderate degree of rotational and reflection symmetry. Two cluster series symmetric about two adsorbates in atop sites, $d = 19$ and 37 , were also examined to probe the effect of cluster site symmetry.

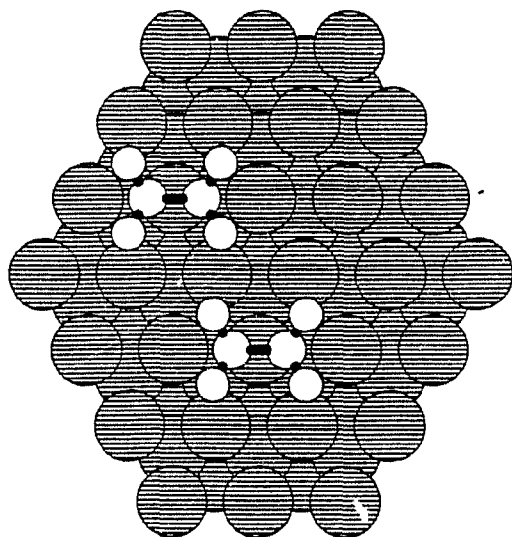
1. Ethylene: $\text{Ni}_n(\text{C}_2\text{H}_4)_2$

As displayed in Figure 4.11 (pp. 160 - 161) for the $\text{Ni}_{72}(\text{C}_2\text{H}_4)_2$ system and documented in Table 4.5 (pp. 162 - 164), the optimization of two symmetrically equivalent C_2H_4 molecules in the experimental (2×2) overlayer structure [25] in the various adsorption sites on enlarged cluster models, $n = 30, 51, \text{ and } 72$, maintained the stability ordering deduced for a single molecule: $\text{di-}\sigma \sim \pi > \mu/\pi > \mu \sim \text{di-}\sigma/\pi$. The similarity of the optimized geometries and relative binding site preferences for one and two molecules indicates insignificant lateral interactions between the adsorbates in the (2×2) overlayer structure; compare Tables 4.1 and 4.5.

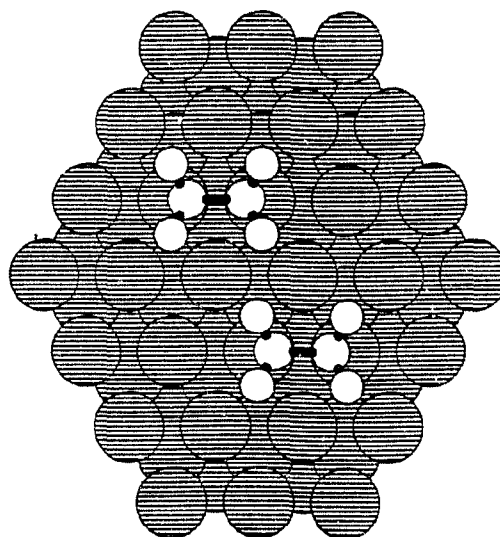
As shown in the cluster dependence analysis, the relative stabilities may depend on the cluster lateral extent, number of layers, and configuration, *i.e.*, its symmetry with respect to the adsorption site. Hence, the adsorption of two C_2H_4 's was studied with three series of clusters: the $d = 19$ and 37 series, both symmetric about the π site, with the latter of greater lateral extent so as to diminish the influence of cluster site symmetry; and the $d = 30$ series symmetric about the di- σ site. Though the two adsorption sites are comparable in stability, the di- σ configuration was slightly preferred and, being also the experimentally deduced one, was adopted in subsequent calculations probing the decomposition, discussed in the next section.

The equivalency constraint of the two C_2H_4 's was verified by alternatively optimizing two di- σ -bonded molecules independently, which yielded identical results, as expected from the symmetry of the cluster and also the extended lattice. This is true also for the di- σ /di- π -bonded molecules, but for the other three adsorption sites, the two molecules are located asymmetrically on the cluster. This, however, is an artifact of the finite cluster and so symmetric equivalence of the two adsorbates was imposed in all calculations probing the adsorption sites. During the decomposition reaction, the two molecules may behave independently, which will be addressed in the investigation of the dehydrogenation mechanism.

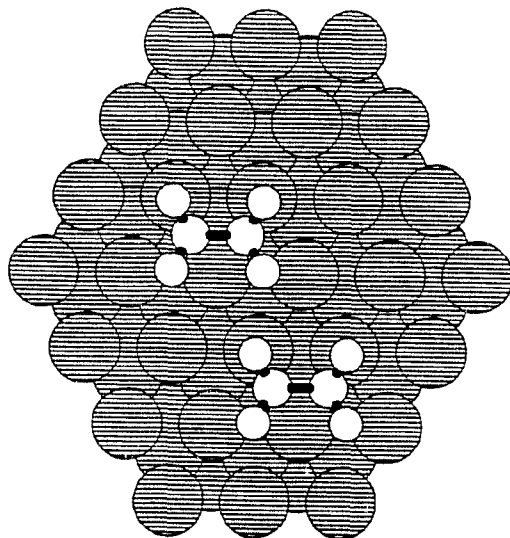
(a) π (onefold atop); $E_B = 2.402$ eV



(b) di- σ (twofold bridging); $E_B = 2.512$ eV



(c) di- σ/π (Δ) — hcp; $E_B = 2.015$ eV



(d) μ/π — hcp; $E_B = 2.184$ eV

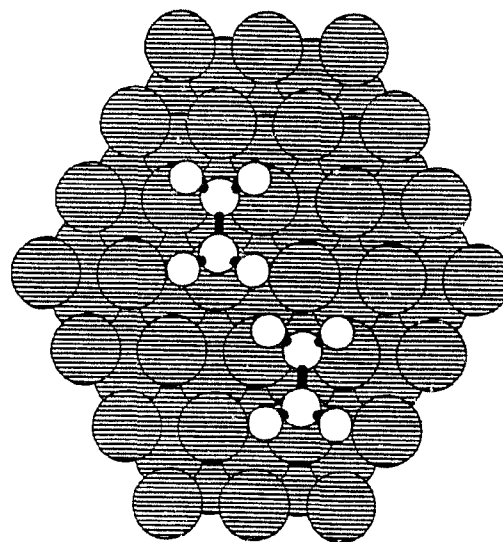


Figure 4.11 $\text{Ni}_{72}(\text{C}_2\text{H}_4)_2$ adsorption system: optimized geometries and binding energies for (a) - (e) five bonding configurations of two C_2H_4 's in (2×2) overlayer structure on the (30/21/21) cluster.

(e) di- σ /di- π (fourfold bridging or μ); $E_B = 2.090$ eV

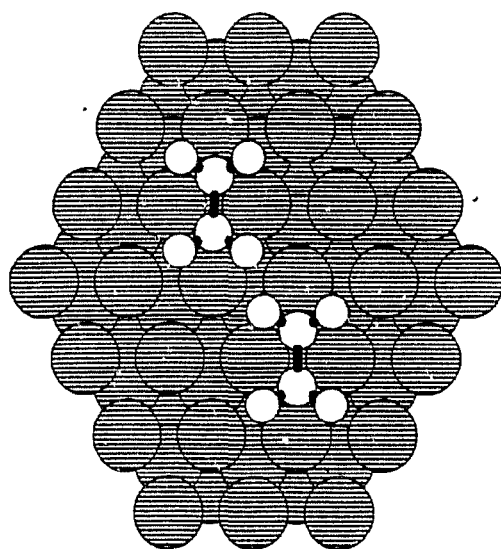


Figure 4.11 Cont'd

Table 4.5 Optimized Adsorption Parameters for $\text{Ni}_n(\text{C}_2\text{H}_4)_2$ for Three Series of Clusters: $d = 19, 30, 37^a$; $\ell = 1, 2, 3$

ℓ	E_B^b / eV	$\Delta r(\text{C}-\text{C})^c / \text{\AA}$	$\Delta r(\text{C}-\text{H})^c / \text{\AA}$	$z(\text{C})^d / \text{\AA}$	$\theta_{\text{CCH}}^{e,f} / \text{deg}$	$\phi^{e,f} / \text{deg}$
π (onefold atop)						
$n = 30, 51, 72$						
1	1.606	0.08 ($sp^{2.34}$)	-0.03	1.919	118.5	10.9
2	2.392	0.06 ($sp^{2.28}$)	-0.04	1.886	118.5	9.1
3	2.402	0.06 ($sp^{2.28}$)	-0.04	1.878	118.5	8.8
$n = 19, 31, 43$						
1	1.599	0.08 ($sp^{2.34}$)	-0.03	1.928	118.4	11.3
2	2.089	0.06 ($sp^{2.26}$)	-0.04	1.907	118.7	8.9
3	2.259	0.06 ($sp^{2.27}$)	-0.04	1.898	118.7	8.9
$n = 37, 64$						
1	1.717	0.08 ($sp^{2.34}$)	-0.03	1.912	118.5	10.8
2	2.527	0.07 ($sp^{2.30}$)	-0.04	1.875	118.5	9.3

See footnotes at end of Table on p. 164

Table 4.5 Cont'd

l	$E_B^b /$ eV	$\Delta r(\text{C}-\text{C})^c /$ Å	$\Delta r(\text{C}-\text{H})^c /$ Å	$z(\text{C})^d /$ Å	$\theta_{\text{CCH}}^{e,f} /$ deg	$\phi^{e,f} /$ deg
di-σ (twofold aligned bridging)						
$n = 30, 51, 72:$						
1	2.031	0.18 ($sp^{2.72}$)	-0.02	1.943	112.9	21.5
2	2.443	0.16 ($sp^{2.64}$)	-0.03	1.938	113.6	20.1
3	2.512	0.15 ($sp^{2.63}$)	-0.03	1.932	114.0	19.8
$n = 37, 64:$						
1	2.105	0.18 ($sp^{2.70}$)	-0.02	1.943	113.3	21.3
2	2.452	0.16 ($sp^{2.71}$)	-0.03	1.939	113.7	20.3
di-σ/π (threefold triangular or Δ)^e — hcp						
$n = 30, 51, 72:$						
1	1.243	0.11 ($sp^{2.48}$)	-0.04, -0.02	1.841	117.0, 115.7	8.3, 27.6
2	1.929	0.09 ($sp^{2.37}$)	-0.04, -0.03	1.815	117.7, 116.5	8.1, 23.8
3	2.015	0.09 ($sp^{2.37}$)	-0.04, -0.03	1.800	117.7, 116.5	8.8, 22.7

See footnotes at end of Table on p. 164

Table 4.5 Cont'd

l	E_B^b / eV	$\Delta r(\text{C}-\text{C})^c / \text{Å}$	$\Delta r(\text{C}-\text{H})^c / \text{Å}$	$z(\text{C})^d / \text{Å}$	$\theta_{\text{CCH}}^{e,f} / \text{deg}$	$\phi^{e,f} / \text{deg}$
μ/π (threefold bridging/atop) ^g — hep						
$n = 30, 51, 72:$						
1	1.523	0.13 ($sp^{2.55}$)	-0.02, -0.03	1.933, 1.823	112.8, 116.5	21.4, 19.6
2	2.077	0.10 ($sp^{2.43}$)	-0.03, -0.03	1.923, 1.773	112.9, 118.1	20.4, 15.9
3	2.184	0.11 ($sp^{2.44}$)	-0.03, -0.03	1.910, 1.759	112.9, 118.1	20.4, 16.0
$\text{di-}\sigma/\text{di-}\pi$ (fourfold bridging or μ)						
$n = 30, 51, 72:$						
1	1.266	0.12 ($sp^{2.48}$)	-0.03	1.792	115.0	18.2
2	1.965	0.08 ($sp^{2.36}$)	-0.04	1.758	116.3	15.4
3	2.090	0.08 ($sp^{2.34}$)	-0.04	1.748	116.6	15.2

^a $d = 19$ and 37 series of Ni clusters symmetric about the atop site ($d = 19$ series shown in Figure 3.3, while $d = 37$ series has an additional surrounding shell of Ni atoms); $d = 30$ series symmetric about the $\text{di-}\sigma$ and μ sites, with $\text{Ni}_{72}(\text{C}_2\text{H}_4)_2$ structures shown in Figure 4.11

^b $E_B = \frac{1}{2}\{E(\text{Ni}_n) + 2E(\text{C}_2\text{H}_4)\} - E(\text{Ni}_n(\text{C}_2\text{H}_4)_2)$, *i.e.*, the binding energy per C_2H_4

^{c-f} As in Table 4.1

^g Shift of the centre of the C-C bond from the $[\bar{1}10]$ direction fixed at 1.074 Å for the $\text{di-}\sigma/\pi$ configuration and optimized to 0.831, 0.754, and 0.744 Å on the $n = 30, 51$ and 72 clusters, respectively, for the μ/π configuration

2. Acetylene: $\text{Ni}_n(\text{C}_2\text{H}_2)_2$

With two acetylene molecules adsorbed in the (2×2) overlayer LEED structure [25] on the Ni_n series of clusters, $n = 30, 51,$ and 72 , the di- σ/π configuration is again the most stable; see Figure 4.12 (pp. 166 - 167) and Table 4.6 (pp. 168 - 169). The stability ordering of the adsorption sites, layer-dependent as for a single molecule, may be summarized as $\text{di-}\sigma/\pi > \mu/\pi > \mu > \text{di-}\sigma > \pi$. Only the hcp site was investigated for the di- σ/π and μ/π sites, as little difference was observed between it and the fcc site in the adsorption analysis of a single C_2H_2 molecule. Adsorption on the $d = 19$ series of clusters symmetric about the atop site does not favour it any more than on the $d = 30$ cluster series symmetric about the di- σ and μ sites. Weak lateral interactions between adjacent C_2H_2 molecules is indicated by the close similarity between the optimized geometries calculated for one and two molecules on comparable clusters; *cf.* Tables 4.3 and 4.6. The structural parameters calculated for two C_2H_2 's will form the basis for comparison when the dehydrogenation mechanism is investigated to establish whether or not acetylene has been formed as a product of the various reaction schemes studied.

2. Dehydrogenation Mechanism

With the adsorption sites of the reactant and product hydrocarbons established, the dehydrogenation mechanism was scrutinized. Initially, the geometries of two C_2H_4 molecules adsorbed on several Ni clusters, $\text{Ni}_n(\text{C}_2\text{H}_4)_2$, were optimized along various

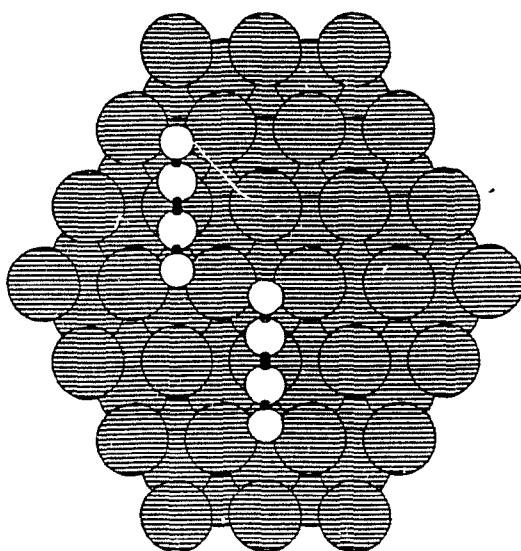
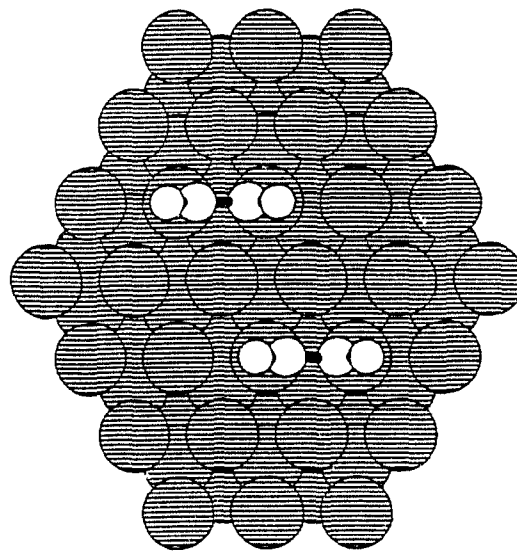
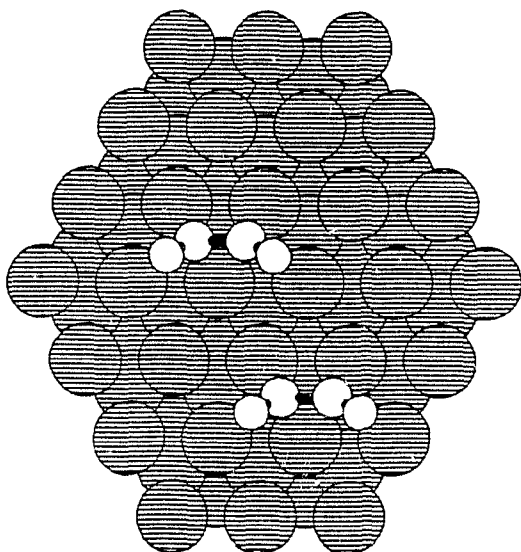
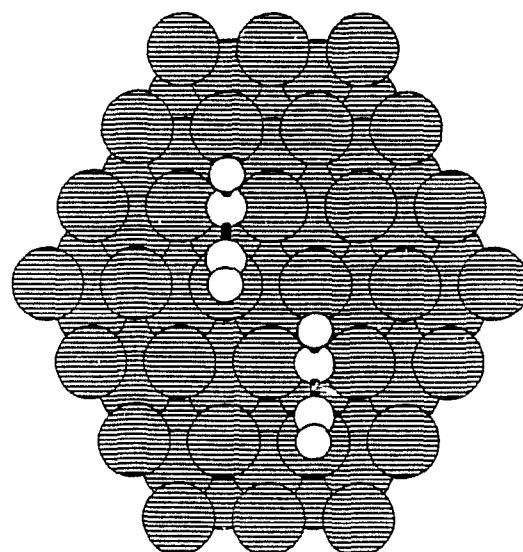
(a) π (c..efold atop); $E_B = 1.472$ eV(b) di- σ (twofold bridging); $E_B = 1.862$ eV(c) di- σ/π (Δ) — hcp; $E_B = 2.373$ eV(d) μ/π — hcp; $E_B = 2.068$ eV

Figure 4.12 $\text{Ni}_{72}(\text{C}_2\text{H}_2)_2$ adsorption system: optimized geometries and binding energies for (a) – (e) five bonding configurations of two C_2H_2 's in (2×2) overlayer structure on the (30/21/21) cluster.

(e) $\text{di-}\sigma/\text{di-}\pi$ (fourfold bridging or μ); $E_B = 1.961 \text{ eV}$

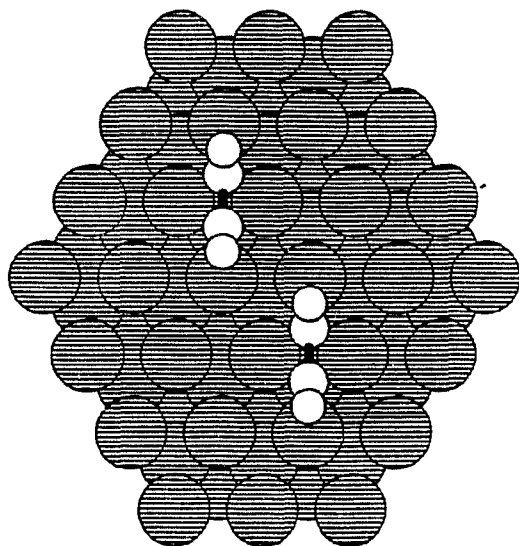


Figure 4.12 Cont'd

Table 4.6 Optimized Adsorption Parameters for $\text{Ni}_n(\text{C}_2\text{H}_2)_2$ for Two Series of Clusters: $d = 19, 30^a$; $\ell = 1, 2, 3$

ℓ	E_B^b / eV	$\Delta r(\text{C}-\text{C})^c / \text{\AA}$	$\Delta r(\text{C}-\text{H})^c / \text{\AA}$	$z(\text{C})^d / \text{\AA}$	$\theta_{\text{CCH}}^{e,f} / \text{deg}$	$\phi^{e,f} / \text{deg}$
$n = 19, 31:$						
π (onefold atop)						
1	0.748	0.03 ($sp^{1.19}$)	-0.02	1.974	166.7	85.1
2	1.266	0.02 ($sp^{1.13}$)	-0.03	1.982, 1.980	170.1, 170.6	86.9, 85.5
$n = 30, 51, 72:$						
π (onefold atop)						
1	0.868	0.03 ($sp^{1.18}$)	-0.02	1.962, 1.971	167.5, 166.1	92.5, 91.8
2	1.494	0.02 ($sp^{1.13}$)	-0.03	1.956, 1.965	170.7, 169.4	90.7, 93.2
3	1.472	0.02 ($sp^{1.13}$)	-0.03	1.945, 1.950	170.4, 169.7	93.6, 96.0
$di-\sigma$ (twofold aligned bridging)						
1	1.516	0.10 ($sp^{1.66}$)	0.00	1.868	135.9	90.0
2	1.803	0.10 ($sp^{1.62}$)	0.00	1.868	136.8	90.0
3	1.862	0.10 ($sp^{1.62}$)	0.00	1.862	136.8	90.0

Table 4.6 Cont'd

ℓ	$E_B^b /$ eV	$\Delta r(\text{C}-\text{C})^c /$ Å	$\Delta r(\text{C}-\text{H})^c /$ Å	$z(\text{C})^d /$ Å	$\theta_{\text{CCH}}^{e,f} /$ deg	$\phi^{e,f} /$ deg
di-σ/π (threefold triangular or Δ)^g — hcp						
1	1.927	0.16 ($sp^{1.95}$)	-0.01	1.565	131.5	63.0
2	2.285	0.14 ($sp^{1.84}$)	-0.02	1.577	134.1	60.0
3	2.373	0.14 ($sp^{1.85}$)	-0.02	1.570	133.9	59.8
μ/π (threefold bridging/atop)^g — hcp						
1	1.670	0.15 ($sp^{1.86}$)	-0.00, -0.01	1.762, 1.565	126.2, 139.0	90.0, 90.0
2	2.015	0.12 ($sp^{1.73}$)	-0.01, -0.02	1.769, 1.586	127.5, 143.1	90.0, 90.0
3	2.068	0.12 ($sp^{1.73}$)	-0.01, -0.02	1.766, 1.579	127.5, 143.1	90.0, 90.0
di-$\sigma/\text{di-}\pi$ (fourfold bridging or μ)						
1	1.326	0.15 ($sp^{1.90}$)	-0.01	1.494	129.4	90.0
2	1.877	0.16 ($sp^{1.91}$)	-0.02	1.463	128.5	90.0
3	1.961	0.16 ($sp^{1.93}$)	-0.02	1.453	127.7	90.0

^a $d = 19$ cluster series symmetric about the atop site, while the $d = 30$ series is symmetric about the di- σ and μ sites; $\text{Ni}_{72}(\text{C}_2\text{H}_2)_2$ structures shown in Figure 4.12

^b $E_B = \frac{1}{2}\{[E(\text{Ni}_n) + 2E(\text{C}_2\text{H}_2)] - E(\text{Ni}_n(\text{C}_2\text{H}_2)_2)\}$, *i.e.*, the binding energy per C_2H_2

^{c-f} As in Table 4.3

^g Shift of the centre of the C-C bond from $[\bar{1}10]$ direction on the $n = 30, 51,$ and 72 clusters optimized to 1.005, 1.011, and 1.005 Å and 0.791, 0.752, and 0.752 Å for the di- σ/π and μ/π configurations, respectively

proposed reaction coordinates, but the calculated energy barriers exceeded the experimental activation energy, E_a^{exp} , by more than an order of magnitude. Model $Ni_n(C_2H_4)_2H_2$ systems were subsequently introduced, where the two extra H's simulate those of neighbouring C_2H_4 's in the extended overlayer, constrained to be symmetrically equivalent to appropriate H's on the two C_2H_4 's considered. In the mechanism being advanced, each di- σ -bonded C_2H_4 rotates, at elevated temperatures, relative to the Ni lattice about an axis through the centre of the C-C bond and perpendicular to the surface. The concomitant, effective molecular twist brings the two interior H's on adjacent molecules closer to each other and a corresponding surface Ni atom; the resultant H-H and metal-H interactions weaken the respective C-H bonds, which lengthen and eventually rupture. The intermolecular H's tunnel, in a process fast compared with the thermally activated rotation, through the potential barrier arising along the shortening of their internuclear distance to form the decoupled, dehydrogenation products: C_2H_2 fragments, which rotate to the μ site, and an intermediate, chemisorption precursor, physisorbed H_2 . The subsequent dissociation of molecular H_2 to H atoms chemisorbed in the Ni threefold sites slightly perturbs the C_2H_2 's from alignment with the $[\bar{1}\bar{1}2]$ direction. In this and the next section, the calculations investigating and corroborating this proposed decomposition mechanism are documented and interpreted.

a. $\text{Ni}_n(\text{C}_2\text{H}_4)_2$: $n = 30, 51, 72$

Initial investigations of the dehydrogenation mechanism employed model $\text{Ni}_n(\text{C}_2\text{H}_4)_2$ systems, where $n = 30, 51,$ and 72 , corresponding respectively to $\ell = 1, 2,$ and 3 , as in the adsorption studies of two adsorbate molecules. Of the various alternative decomposition routes probed on these model systems, none yielded satisfactory correlation with the experimental findings. Some of the computed results, however, are included here, as they form the groundwork and impetus for the subsequent, model $\text{Ni}_n(\text{C}_2\text{H}_4)_2\text{H}_2$ calculations, by addressing questions regarding symmetry constraints, cluster dependences, reaction coordinates, etc.

1. Concerted Parametric Stretch of *trans* C–H Bonds

A natural starting point to delve into the dehydrogenation mechanism and second-order reaction kinetics is the concerted elimination of *trans* H's from the reactant ethylenes, to form a bimolecular, transient complex which decomposes to the proposed intermediate products, acetylene and molecular hydrogen. As Figure 4.13 (a) (p. 174) reveals, concerted parametric lengthening of *trans* C–H bonds, $\Delta r(\text{C–H})$, from a pair of C_2H_4 's for the $\text{Ni}_{30}(\text{C}_2\text{H}_4)_2$ system occurs at a prohibitively high energetic cost. Additional layers are expected, based on the cluster dependence analysis, to lower the energetics somewhat, but not by the more than order of magnitude required to approach the experimental E_a of ~ 0.30 eV [44]. Also, even after $\Delta r(\text{C–H}) = 1.000$ Å, which

requires ~ 10 eV, the fragment C–C bond distance, $r(\text{C–C})$, of 1.495 Å, down from 1.677 Å for the reactant molecules, is still not at the $r(\text{C–C})$ of 1.428 Å calculated for each di- σ -bonded acetylene molecule on the Ni₃₀ cluster (see Table 4.6 for $\Delta r(\text{C–C})$ and sp^n). The separation distance between the two interior intermolecular H's, postulated to come together to form the intermediate decomposition product, H₂, increases, due to the counterclockwise rotation of the two ethylene molecules as the C–H bonds lengthen.

Hence, the C–C bond axis was aligned along the $[\bar{1}10]$ direction of the Ni lattice or the di- σ site, *i.e.*, the rotation angle, ϕ_C , was fixed at 0.0°, and the preceding calculation repeated, producing an energy barrier of $\Delta E_{max} = 5.949$ eV at $\Delta r(\text{C–H}) = 0.550$ Å, corresponding to $r(\text{C–H}) = 1.714$ Å, as shown in Figure 4.13 (b). Acetylene and H₂ are formed, as well as two exterior H atoms, as evidenced by the C–C bond length, $r(\text{C–C}) = 1.430$ Å, and intermolecular H–H distance, $r(\text{H–H}) = 0.742$ Å, at $\Delta r(\text{C–H}) = 0.900$ Å. The reaction scheme for this calculation can be written as $2\text{C}_2\text{H}_4 \rightarrow 2\text{C}_2\text{H}_2 + \text{H}_2 + 2\text{H}$. While the potential energy curve exhibits the qualitative behaviour expected along a reaction coordinate, the predicted E_a is again too high.

2. Constrained Coupled Rotation of the C₂H₄'s about ϕ_C and ϕ_{CH}

Another reaction coordinate, the concerted rotation in the surface plane of each of the two C₂H₄'s with simultaneous lowering, and concomitant rise of a pair of *trans* H's towards, and away from the surface, was probed for its proposed role in activating the

C–H bonds, either by weakening the lowered pair through interaction with surface metal atoms or by allowing the elevated H's to react unhindered by the substrate. Figure 4.14 (p. 175) examines the four possibilities of this constrained rotation, about an axis through the centre of the C–C bond and perpendicular to the surface, by the angle $\Delta\phi_C$, coupled to a counter-rotation of the methylene ($-\text{CH}_2$) groups about the angle $\Delta\phi_{\text{CH}_2}$. The energetically favoured pathway leading to a decreased intermolecular H–H separation, $r(\text{H}-\text{H})$, is revealed by the relative energy change, ΔE , curves in Figure 4.14 (a), to be clockwise rotation of the two C_2H_4 's relative to the surface accompanied by a counterclockwise counter-rotation, when viewed along the C–C bond axis, of the $-\text{CH}_2$ groups, which brings a pair of *trans* H's on each molecule closer to the surface and a neighbouring H on an adjacent C_2H_4 . This motion can be envisioned as a molecular twist about the centre of the internal C–C bond axis, with the remaining bond of the $\sim sp^3$ -hybridized C anchored to a Ni atom, keeping the C–Ni chemisorption bonds intact. Clockwise rotation about both ϕ_C and ϕ_{CH_2} , which lowers the opposite pair of *trans* H's towards the surface, also decreases the $r(\text{H}-\text{H})$ as the H's lift off the surface, but costs double the energy to achieve the same $r(\text{H}-\text{H})$ as the opposite $-\text{CH}_2$ rotation, as this motion disrupts the C–Ni bonds. The other two situations move the intermolecular H's further apart, as Figure 4.14 (b) reveals.

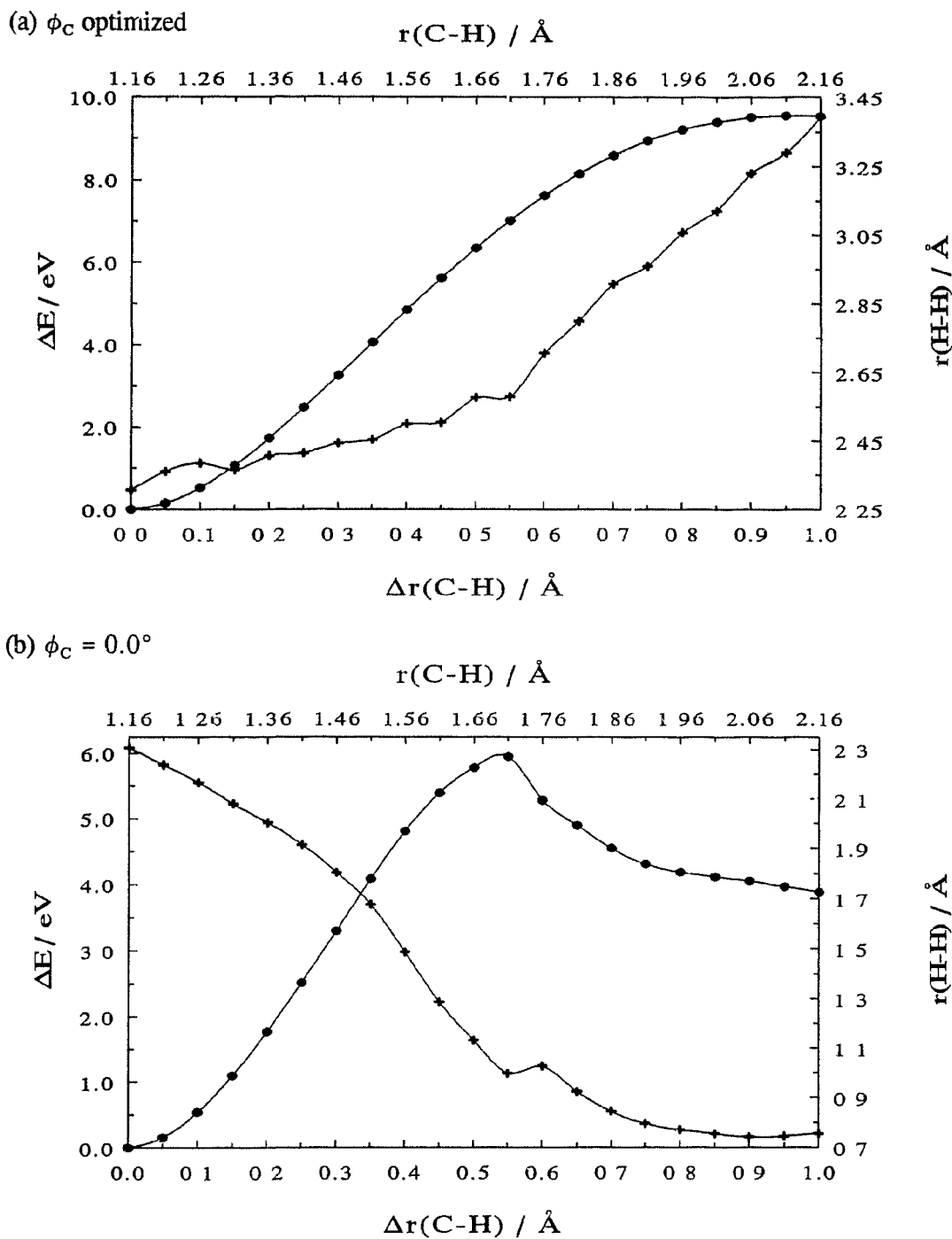


Figure 4.13 Concerted cleavage of *trans* C–H bonds from each C_2H_4 of the $Ni_{30}(C_2H_4)_2$ system: relative energy change, ΔE , and intermolecular H–H distance, $r(H-H)$, as functions of C–H bond stretch, $\Delta r(C-H)$, for (a) unrestricted ϕ_C rotation relative to the Ni lattice and (b) $\phi_C = 0.0^\circ$, *i.e.*, C–C bond axis fixed along $[\bar{1}10]$ direction (di- σ site).

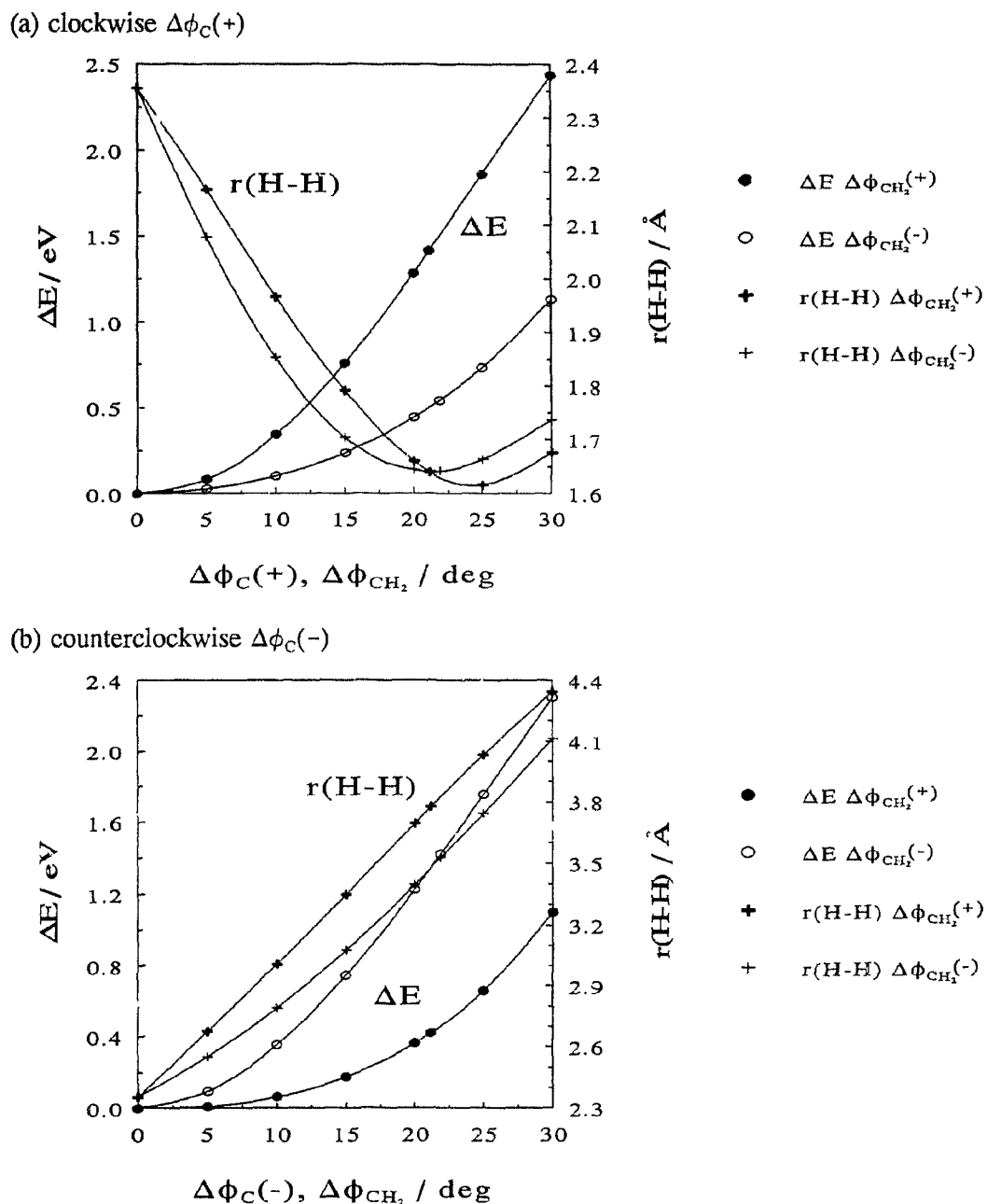


Figure 4.14 Constrained coupled rotation of adjacent C_2H_4 's about an axis through the centre of each C-C bond and perpendicular to the surface, $\Delta\phi_C$, and counter-rotation of the $-\text{CH}_2$ groups, $\Delta\phi_{\text{CH}_2}$, for $\text{Ni}_{30}(\text{C}_2\text{H}_4)_2$: (a) clockwise (+) and (b) counterclockwise (-) rotation about $\Delta\phi_C$ for both clockwise (+) and counterclockwise (-) rotation about $\Delta\phi_{\text{CH}_2}$ (viewing down the C-C axis).

3. Rotation of the C_2H_4 's about ϕ_C

The constraint of maintaining the same C–C bond rotation and $-CH_2$ counter-rotation angle was subsequently removed, the results for clockwise ϕ_C rotation are shown in Figure 4.15 (a). Evidently, this halves the energy cost of the rotation by allowing the $-CH_2$ groups to distort as the molecule rotates relative to the Ni lattice. In this instance, the molecules were allowed to translate along the surface and the symmetries of the two molecules, both internally and with respect to each other, were relaxed, to probe the imposed local symmetry constraints. In the case of counterclockwise ϕ_C rotation, Figure 4.15 (b) compares ΔE for two situations: C_2 symmetry and no translational degrees of freedom for the adsorbed C_2H_4 's, and C_1 symmetry with ΔX and ΔY translations permitted along the surface. Clearly, the results validate the imposed constraints on this one-layered cluster, as expected from its symmetry and the rotational invariance of the atomic environments in *trans* positions of the molecule. Despite breaking the cluster rotational symmetry, the addition of a second layer of atoms leaves the symmetry of the motion undisturbed, as the $n = 52$, $\ell = 2$ cluster results of Figure 4.16 (a) reveals. The cluster layer dependence of this rotation, under a C_2 local symmetry constraint, is displayed in Figure 4.16 (b), where ΔE and $r(H-H)$ are shown as functions of $\Delta\phi_C$ for the $n = 30$, 51, and 72 series of $\ell = 1$, 2, and 3 clusters.

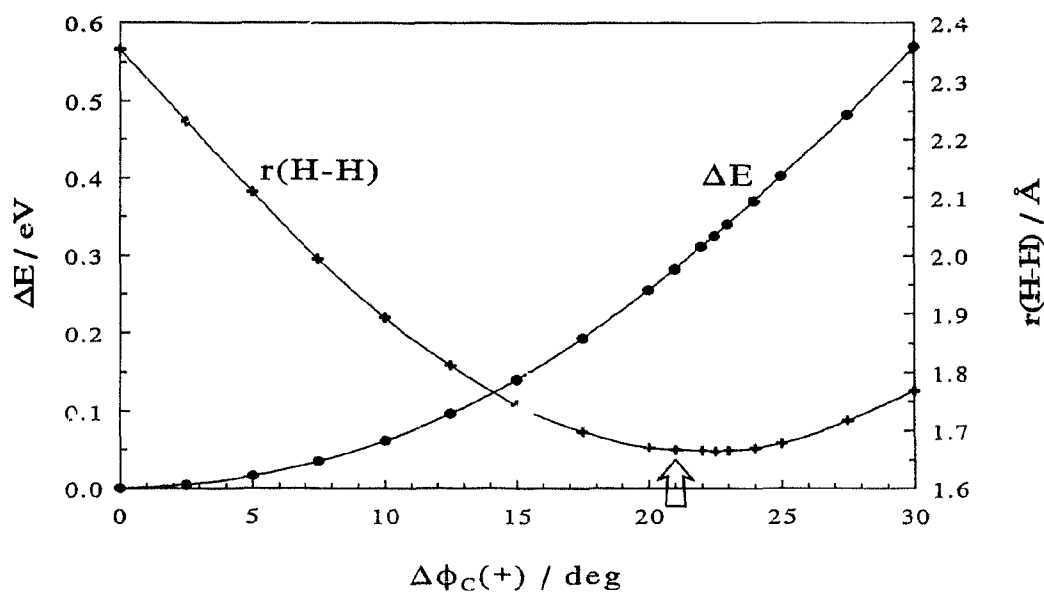
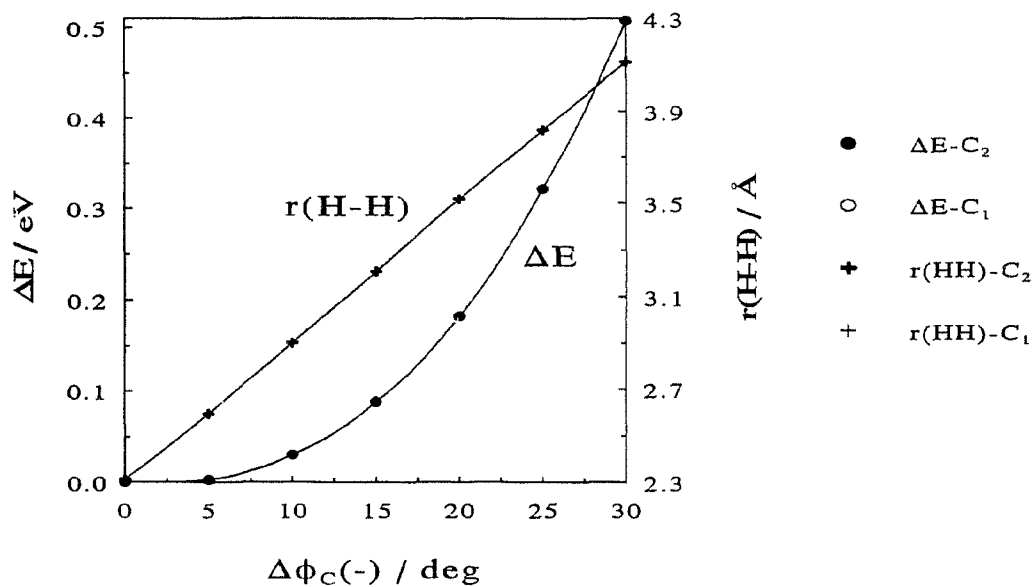
(a) $\Delta\phi_C(+)$; C_2 (b) $\Delta\phi_C(-)$; C_2 and C_1 

Figure 4.15 Concerted rotation of C_2H_4 's about $\Delta\phi_C$ for $\text{Ni}_{30}(\text{C}_2\text{H}_4)_2$: (a) clockwise (+) rotation under C_2 local molecular symmetry constraint and (b) counterclockwise (-) rotation under C_2 and C_1 symmetry constraints.

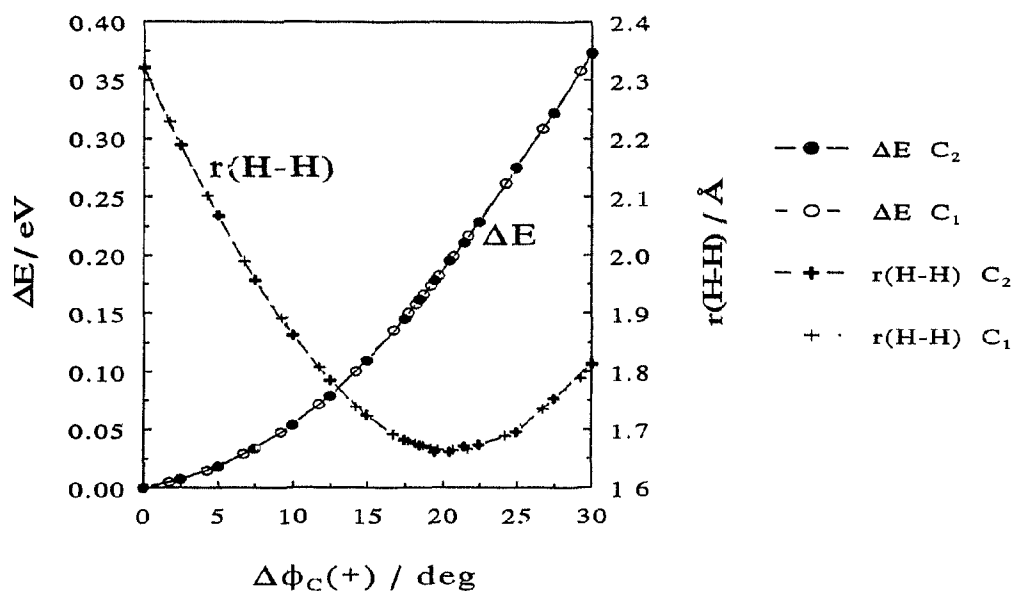
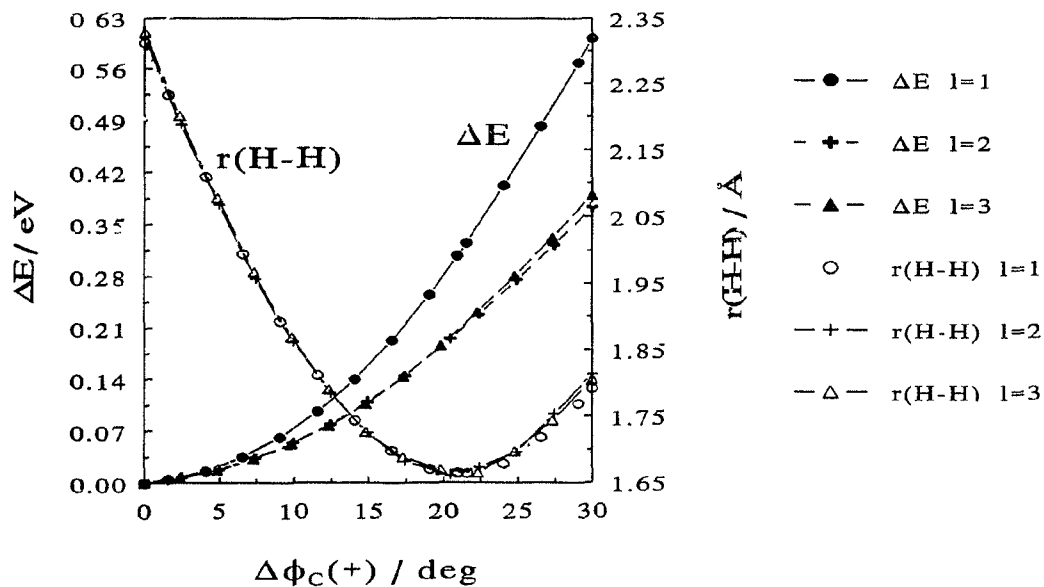
(a) $n = 51$, C_2 and C_1 (b) $n = 30, 51, \text{ and } 72$; $\ell = 1 \rightarrow 3$; C_2 

Figure 4.16 Molecular symmetry constraint and cluster layer dependences for $\text{Ni}_n(\text{C}_2\text{H}_4)_2$ of ΔE and $r(\text{H-H})$ as functions of $\Delta\phi_{C(+)}$: (a) $n = 51$, $\ell = 2$, C_2 and C_1 symmetries; and (b) $n = 30, 51, \text{ and } 72$, corresponding to $\ell = 1, 2, \text{ and } 3$, under C_2 symmetry.

Three scenarios for ϕ_C rotation of the two ethylene molecules were delineated: concerted rotation, in which both rotate in unison; coupled rotation, where the rotation of one influences the other; and independent rotation, where it does not. The concerted, coupled, and independent rotations were investigated by parametrically rotating (and optimizing) both molecules together, rotating one and relaxing the other, and rotating one while holding the other fixed, respectively, and their results compared in Figure 4.17; to facilitate the comparison, the displayed energy curve for the concerted rotation of two molecules is halved. In each case, $\Delta E \sim 0.28$ eV per molecule achieves a minimum H–H separation distance, $r_{min}(H-H)$, but which varies from 1.661, 1.945, to 1.871 Å. For the concerted rotation, $r_{min}(H-H)$ occurs at $\Delta\phi_C = 20.0^\circ$, whereas the other two cases require $\Delta\phi_C = 30.0^\circ$. Comparison with the energetic requirement of 0.28 eV to rotate a single C_2H_4 by $\Delta\phi_C = 30.0^\circ$ on the comparable $n = 14$, $\ell = 1$ cluster (*cf.* Figure 3.31) strongly implies that the C_2H_4 's rotate independently. However, a concerted rotation, which minimizes $r(H-H)$ while requiring only a marginal increase in energy, can be viewed as a random event of two independent C_2H_4 rotations most conducive to their decomposition and was hence adopted in the subsequent examination of the dehydrogenation mechanism for the $Ni_n(C_2H_4)_2H_2$ model systems, as discussed in Sect. 4.A.2.c.1.

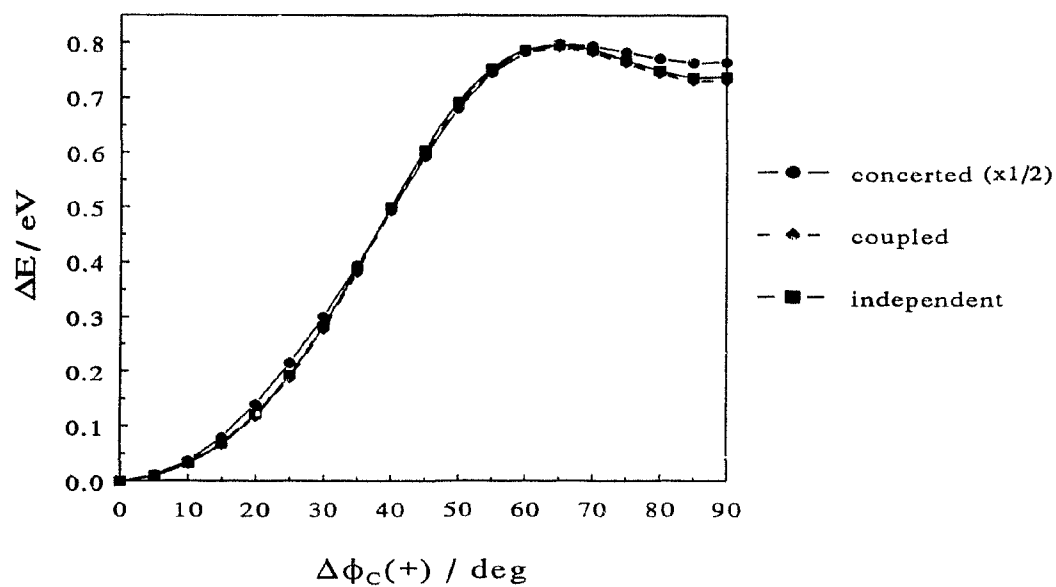
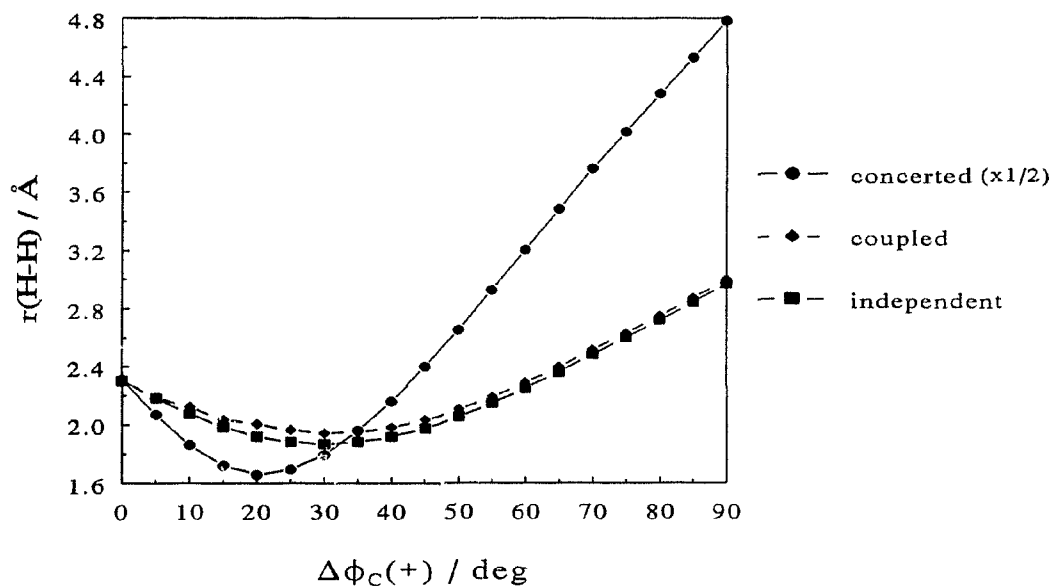
(a) ΔE (b) $r(\text{H-H})$ 

Figure 4.17 Concerted, coupled and independent rotations of two C_2H_4 's about $\Delta\phi_C(+)$ for $\text{Ni}_{30}(\text{C}_2\text{H}_4)_2$: (a) ΔE and (b) $r(\text{H-H})$.

4. Concerted Stretch of *trans* C–H Bonds after Rotation about ϕ_C

For the structure in Figure 4.15 (a) yielding $r_{min}(\text{H-H})$ after rotation by $\Delta\phi_C = 21.0^\circ$, the *trans* C–H bonds of each C_2H_4 were parametrically lengthened while optimizing all other coordinate variables except ϕ_C , producing the ΔE and $r(\text{H-H})$ curves shown in Figure 4.18. Again, the energy cost to rupture the two C–H bonds exceeds E_a^{exp} by more than an order of magnitude, though $r(\text{H-H})$ does drop to ~ 0.75 Å. The artificial constraint of fixing ϕ_C obviously contributes to the high barrier, but relaxing this angle simply leads to the original geometry before rotation.

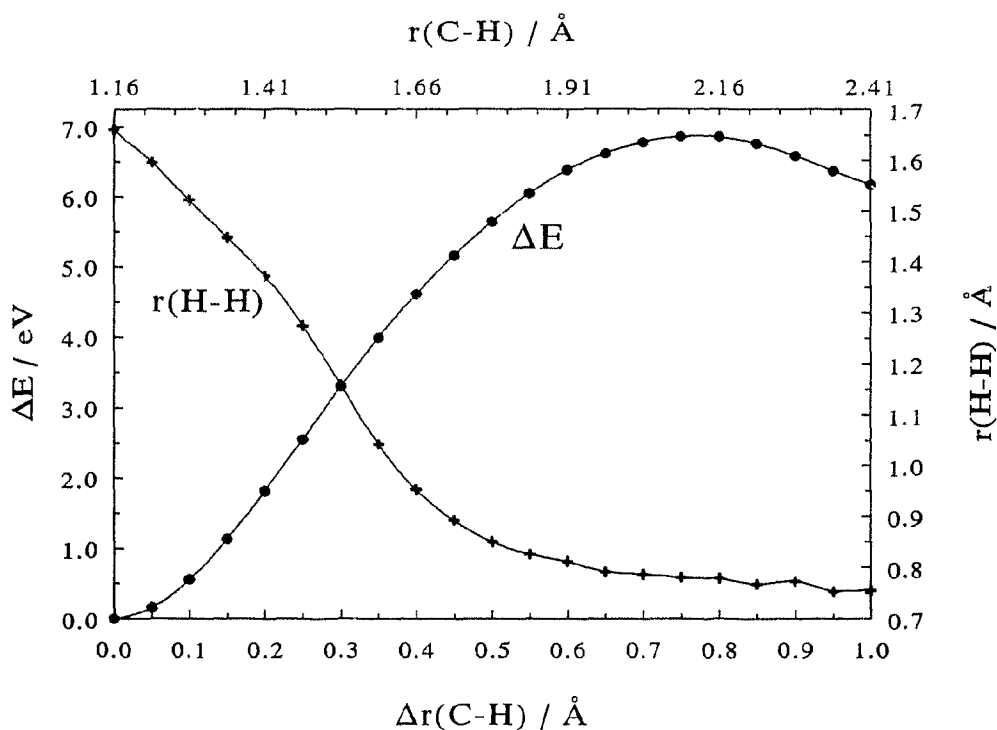


Figure 4.18 Parametric lengthening of *trans* C–H bonds after rotation about $\Delta\phi_C$ for $\text{Ni}_{30}(\text{C}_2\text{H}_4)_2$: $\Delta\phi_C$ fixed at 21.0° , corresponding to the structure of Figure 4.15 (a) which yielded a minimum in the intermolecular H–H separation distance, $r_{min}(\text{H-H})$.

5. Incremental Shortening of $r(\text{H}-\text{H})$ along Line Connecting their Centres

The next set of calculations treats each C_2H_4 as composed of C_2H_2 and two H units, anticipating the dehydrogenation products. The $r(\text{H}-\text{H})$ between the pair of *trans* H's on adjacent C_2H_4 's was parametrically shortened along the line connecting their centres in equal increments of Δx and Δy along the surface, while their height above the surface was held fixed. The C_2H_2 coordinates were optimized under C_2 symmetry while maintaining the molecular axis parallel to the surface but permitting centre-of-mass translations of the molecule, ΔX and ΔY , along the surface. The results for the $n = 30$, $\ell = 1$ and $n = 51$, $\ell = 2$ clusters are shown in Figure 4.19. The energetic requirement is still too great, but a dip in the ΔE curve at a $r(\text{H}-\text{H})$ close to that of isolated H_2 gives a positive indication of the hypothesized formation of H_2 on the surface as an intermediate of the decomposition reaction.

6. Shortening of $r(\text{H}-\text{H})$ while Optimizing H's

Subsequently, the H_2 , in addition to the C_2H_2 , coordinates were separately optimized, allowing for both rotations and translations of the anticipated decomposition products. The acetylene was optimized under C_1 symmetry constraint while the intermolecular H's were treated as an H_2 entity. As Figure 4.20 attests, a drop in the energy curve is again observed at $r(\text{H}-\text{H}) \sim 0.7 \text{ \AA}$, but this time on the order of 2 - 3 eV. The acetylene optimizes to a configuration possessing essentially C_2 symmetry, as the comparison curve

in Figure 4.20 shows. Despite this, subsequent calculations continue to optimize the C_2H_2 fragment under C_1 symmetry, the experimentally deduced symmetry of C_2H_2 on the Ni(111) surface.

b. $Ni_{30}(C_2H_4)_2H_2$: Preliminary Calculations

1. Elimination of *trans* H's

The $Ni_{30}(C_2H_4)_2$ calculations probing the elimination of *trans* H's were repeated for a model $Ni_{30}(C_2H_4)_2H_2$ system, the additional H's mimicking those on neighbouring C_2H_4 's to simulate possible interaction between these intermolecular H's. The results of concerted parametric lengthening of a pair of *trans* C-H bonds, $\Delta r(C-H)$, from each molecule, shown in Figure 4.21 (a), differ little from the $Ni_{30}(C_2H_4)_2$ results in Figure 4.13 (a), as the counterclockwise rotation of the ethylenes again increases $r(H-H)$, making the presence of the additional H's inconsequential. Fixing the ϕ_c rotation angle along the $[\bar{1}10]_1$ direction, however, changes the potential energy curve along $\Delta r(C-H)$ dramatically, as shown in Figure 4.21 (b), as the ΔE_{max} is reduced to two thirds its value without the extra H's, and the now early transition state leads to an exothermic reaction, in contrast to the late transition state and endothermicity of Figure 4.13 (b). The intermolecular H-H interaction presumably lowers the activation barrier for the reaction, which leads to the formation of H_2 molecules.

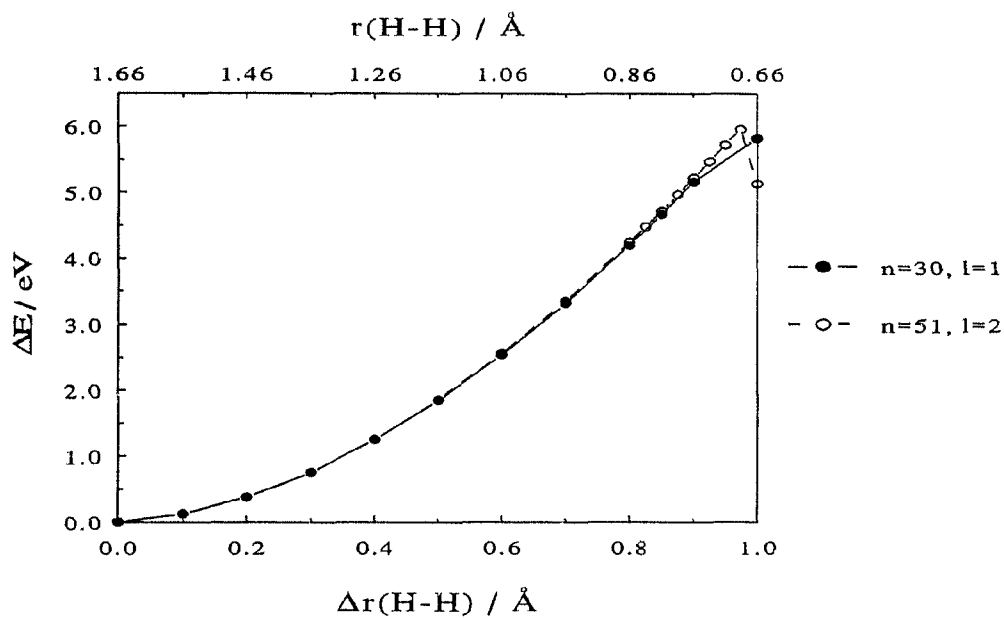


Figure 4.19 Incremental shortening of $r(\text{H-H})$, $\Delta r(\text{H-H})$, along line connecting nuclear centres, otherwise fixing H positions while optimizing C_2H_2 components of $\text{Ni}_n(\text{C}_2\text{H}_4)_2$: $n = 30, l = 1$ and $n = 51, l = 2$.

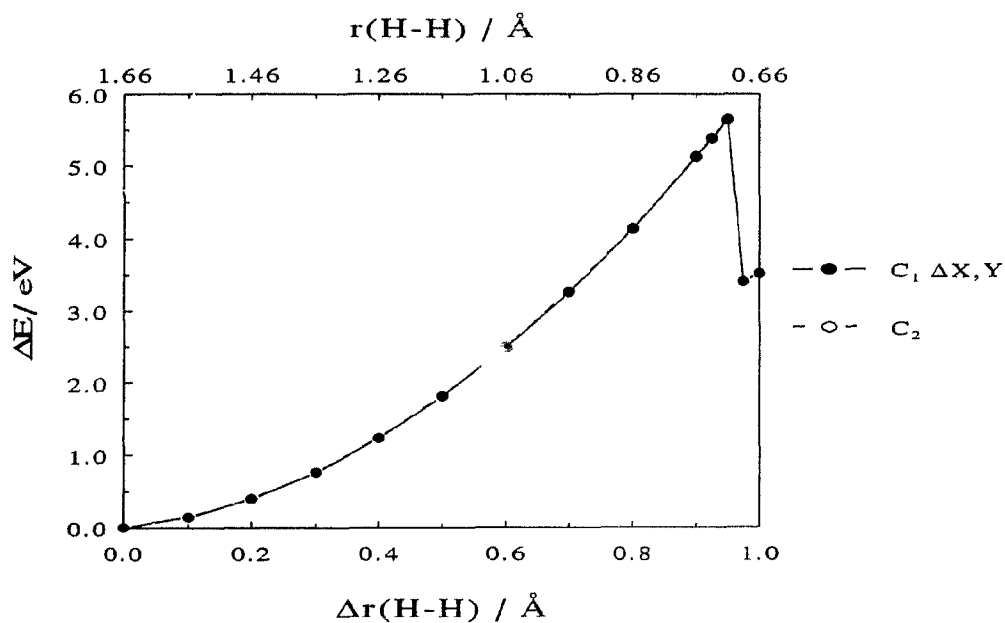


Figure 4.20 Parametric shortening of $r(\text{H-H})$ optimizing coordinates of both anticipated dehydrogenation products, H_2 and C_2H_2 , for $\text{Ni}_{30}(\text{C}_2\text{H}_4)_2$: C_2H_2 's optimized under C_1 and C_2 symmetry with and without translations, ΔX and ΔY , along the surface, respectively.

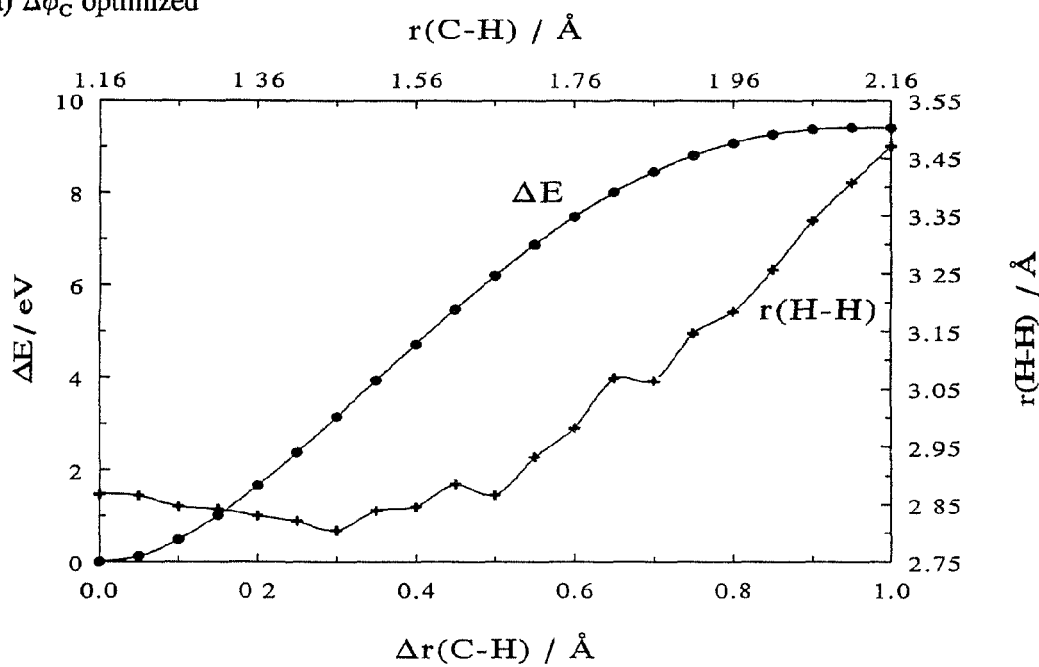
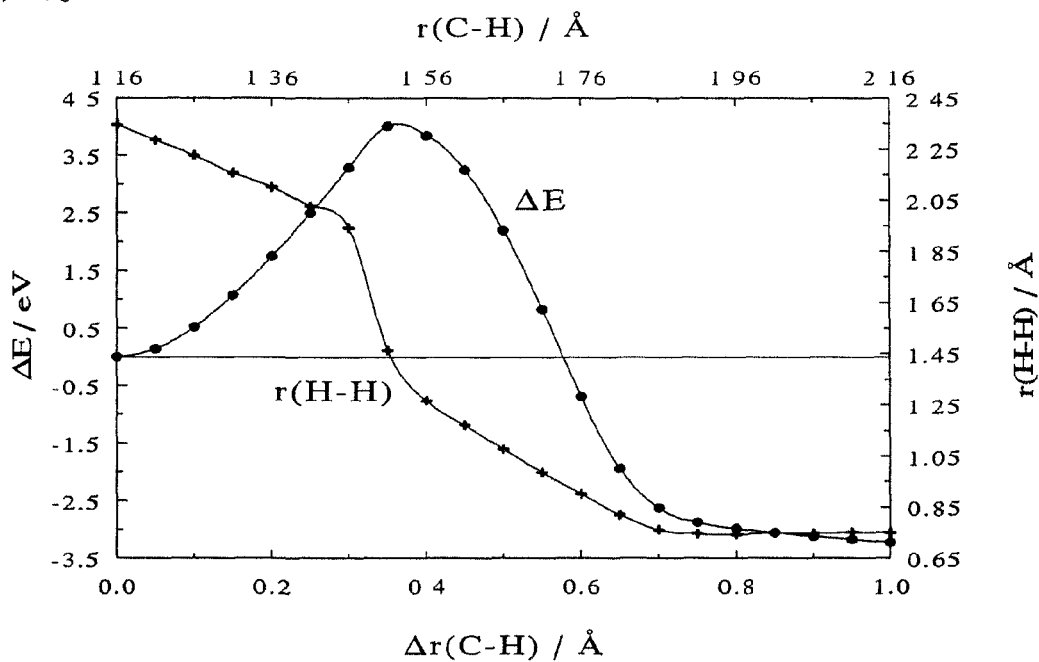
(a) $\Delta\phi_C$ optimized(b) $\Delta\phi_C = 0.0^\circ$ 

Figure 4.21 Concerted stretch of *trans* C-H bonds of each C_2H_4 of the $\text{Ni}_{30}(\text{C}_2\text{H}_4)_2\text{H}_2$ model system, with $\Delta\phi_C$ (a) optimized and (b) fixed at 0.0° .

c. $\text{Ni}_n(\text{C}_2\text{H}_4)_2\text{H}_2$: $n = 30, 51, 72$

1. Rotation of C_2H_4 's about ϕ_C

All subsequent discussion on ethylene decomposition focuses on the $\text{Ni}_n(\text{C}_2\text{H}_4)_2\text{H}_2$ model systems, where $n = 30, 51,$ and 72 , corresponding to $\ell = 1, 2,$ and 3 , as in the foregoing $\text{Ni}_n(\text{C}_2\text{H}_4)_2$ studies, with specific commentary on the Ni_{72} results. As depicted in Figure 4.22 (p. 188), ethylene rotation from the di- σ site about an axis through the centre of the C–C bond and perpendicular to the surface, $\Delta\phi_C$, yields a barrier of $\Delta E_{max}^{rot} = 0.382$ eV, comparable to the experimental E_a of $(0.30/0.31 \pm 0.02)$ eV [44]. (The two experimental values, derived from different losses in the time-resolved HREELS experiments, reflect independent measurements of the same observable.) All other geometrical variables were optimized, subject to the constraints of equivalent C_2H_4 molecules and local C_2 symmetry, along this initial reaction coordinate. As the C_2H_4 's rotate, the methylene ($-\text{CH}_2$) groups counter-rotate, the coupled motion corresponding effectively to a twist of the molecule about the C–C bond axis, as occurs in the first excited electronic state of gas-phase C_2H_4 [147]. This torsion of the $-\text{CH}_2$ groups, invoked also to explain the dehydrogenation of C_2H_4 on the Pt(111) surface [5], brings a pair of *trans* H's on each C_2H_4 towards both the surface [8] and another H atom on an adjacent molecule. The latter effect is manifested in a decreased intermolecular H–H separation, $r(\text{H}–\text{H})$, from ~ 2.352 Å to 1.736 Å, with a minimum, $r_{min}(\text{H}–\text{H})$, at the same rotation angle, $\Delta\phi_C = 16.0^\circ$, yielding ΔE_{max}^{rot} . While rotated in unison to reduce

the number of degrees of freedom to be optimized, the C_2H_4 's likely rotate independently rather than simultaneously (see Section 4.A.2.a.3); however, the system configuration minimizes $r(H-H)$ has both C_2H_4 's rotated by the same angle (see Figure 4.17 on p. 180), and can occur as a random event of independent rotations with some finite statistical probability. A cluster layer dependence analysis along this reaction coordinate, as in Figure 4.23 (p. 189) and Table 4.7 (p. 190), which also documents results along a second reaction coordinate discussed below, reveals convergence of both the relative energetics and structural parameters on going from one- to three-layered clusters.

2. Parameter: Shortening (and Lengthening) of $r(H-H)$

The internuclear distance between *trans* H's on adjacent C_2H_4 's, $r(H-H)$, was chosen as a second reaction coordinate and iteratively shortened. All other geometrical variables, including the ϕ_C angle, were optimized, subject to the constraints of equivalent C_2H_4 molecules and local C_1 symmetry, from the structure, depicted in Figure 4.22 (b), which yielded $r_{min}(H-H)$ and ΔE_{max}^{rot} as a function of $\Delta\phi_C$. The relative energy curve as a function of (negative) $\Delta r(H-H)$, illustrated in Figure 4.24 (p. 191), exhibits a maximum in ΔE of 2.003 eV at $\Delta r(H-H) = 0.640 \text{ \AA}$, signalling the rupture of two *trans* C-H bonds per molecule. A minimum in ΔE occurs at $\Delta r(H-H) = 1.000 \text{ \AA}$, equivalent to $r(H-H) = 0.736 \text{ \AA}$, which is essentially that of isolated H_2 ; see Figure 4.24 (b). Examination of the cluster layer dependence of this concerted dehydrogenation step in Figure 4.25 (p. 192) and Table 4.7 shows the convergence of results as $\ell = 1 \rightarrow 3$.

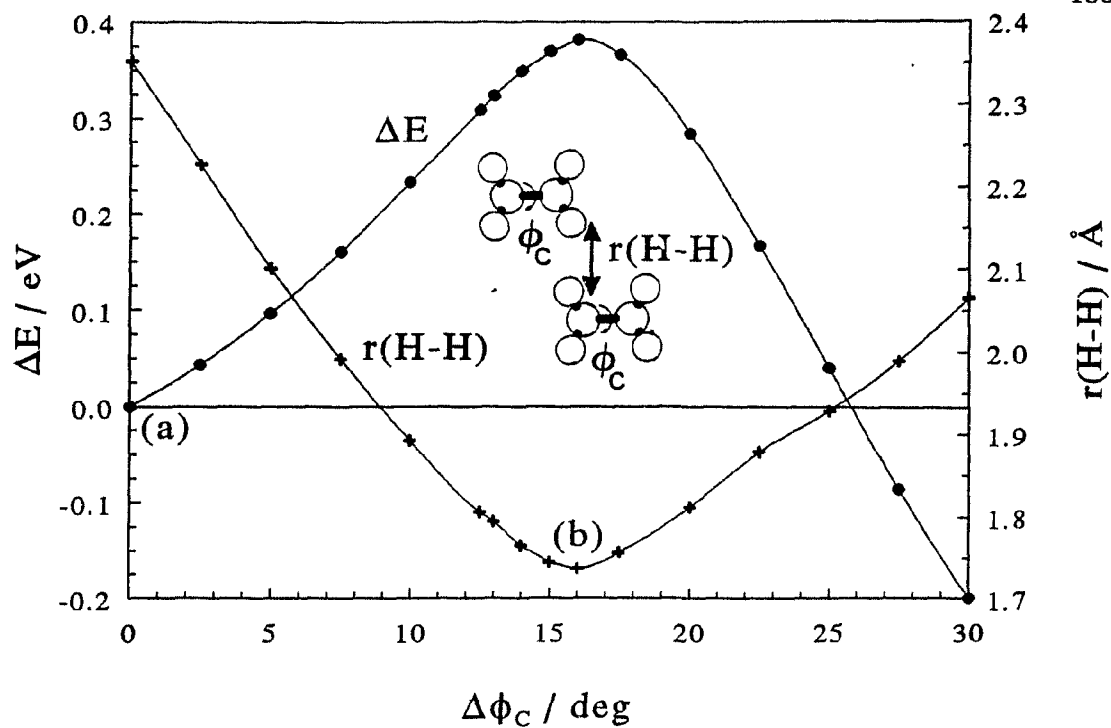
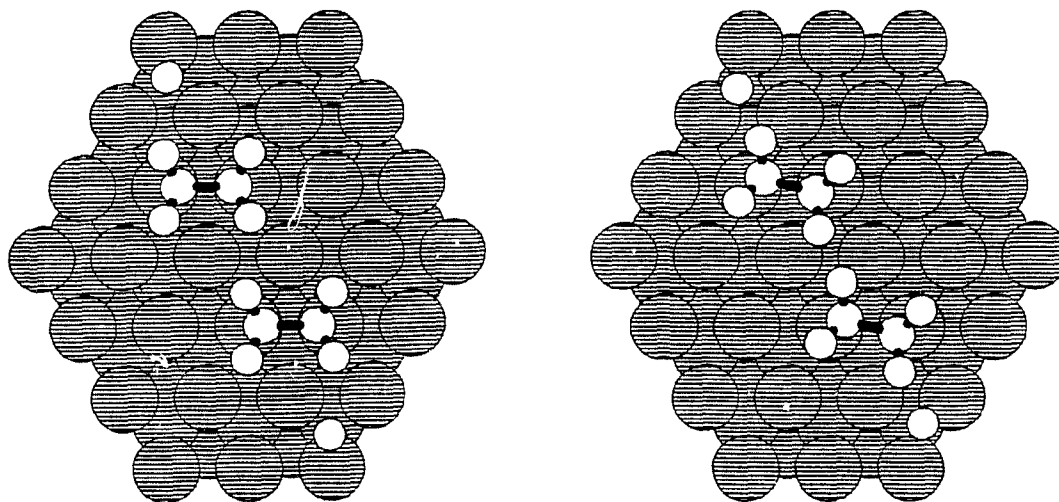
(a) $\Delta\phi_C = 0.0^\circ$ (b) $\Delta\phi_C = 16.0^\circ$ 

Figure 4.22 Initial rotation in the dehydrogenation mechanism of di- σ -bonded C₂H₄ for the Ni₇₂(C₂H₄)₂H₂ model system: relative energy change, ΔE , and intermolecular H-H distance, $r(\text{H-H})$, as functions of clockwise rotation about an axis through the centre of each C-C bond and perpendicular to the surface, $\Delta\phi_C$, with optimized structures shown for (a) $\Delta\phi_C = 0.0^\circ$ and (b) $\Delta\phi_C = 16.0^\circ$.

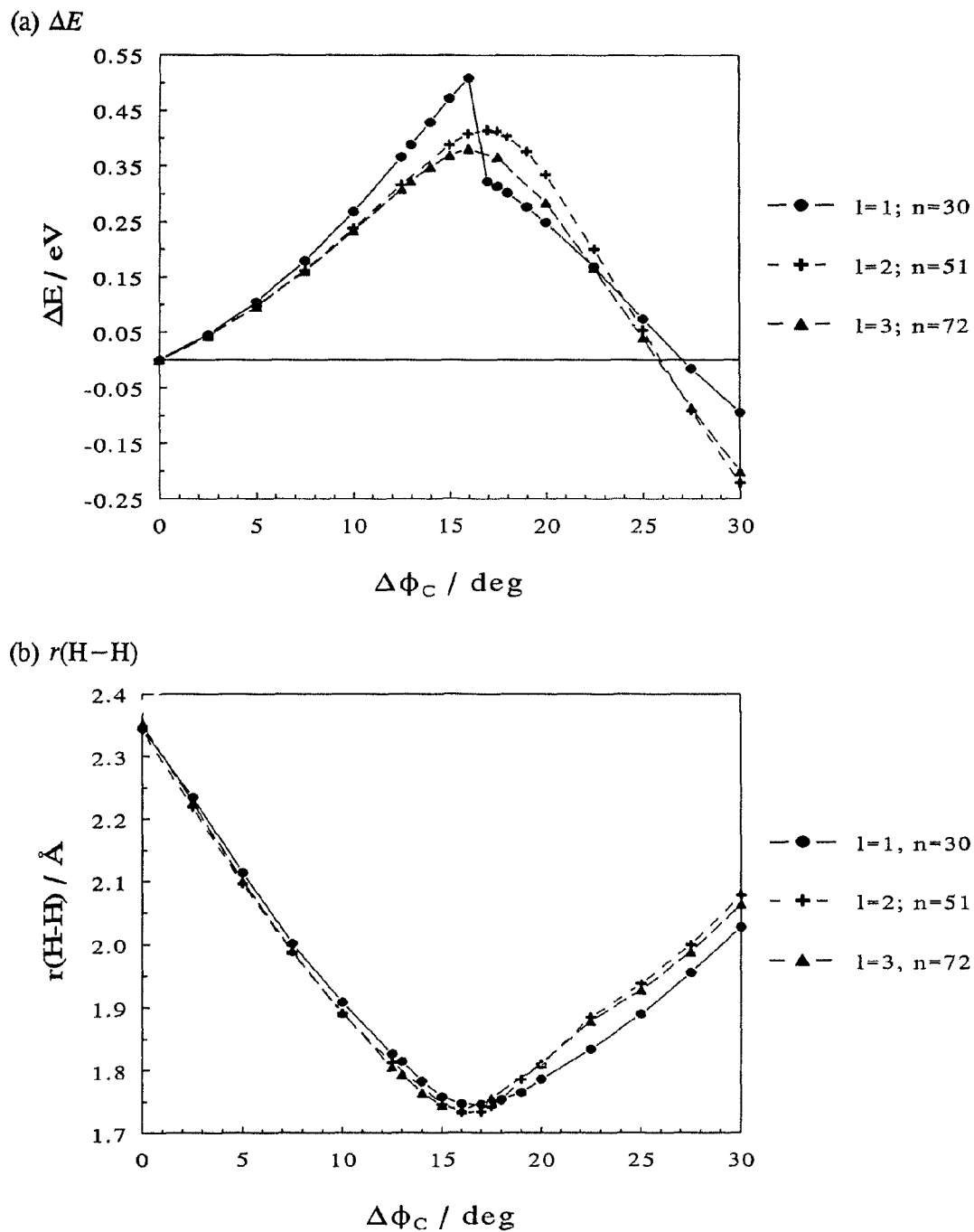


Figure 4.23 Cluster layer dependence of initial C_2H_4 rotation illustrated in Figure 4.22 for $\text{Ni}_n(\text{C}_2\text{H}_4)_2\text{H}_2$, $n = 30, 51$, and 72 , corresponding to $l = 1, 2$, and 3 : (a) ΔE and (b) $r(\text{H-H})$ as functions of $\Delta\phi_C$.

Table 4.7 Cluster Layer Dependence of Dehydrogenation Mechanism Parameters for the $\text{Ni}_n(\text{C}_2\text{H}_4)_2\text{H}_2$ Model Systems: $n = 30, 51, 72$; $\ell = 1, 2, 3^a$

ℓ	$\Delta\phi_c$ / deg	$\Delta r(\text{H-H})$ / Å	ΔE / eV	$r(\text{H-H})$ / Å	$z(\text{H})$ / Å	$z_{\text{CM}}(\text{H}_2)$ / Å	$z(\text{C})$ / Å	$r(\text{C-H})$ / Å	sp^n
$\Delta\phi_c$:									
1	0.0	-	-	2.345	2.370 2.316	-	1.942	1.160	$sp^{2.72}$
2	0.0	-	-	2.343	2.331 2.287	-	1.938	1.156	$sp^{2.64}$
3	0.0	-	-	2.352	2.265 2.323	-	1.932	1.155	$sp^{2.63}$
1	16.0	-	0.509	1.747	2.184 2.438	-	1.920	1.165	$sp^{2.65}$
2	17.0	-	0.415	1.734	2.006 2.466	-	1.907	1.143	$sp^{2.56}$
3	16.0	-	0.382	1.736	2.022 2.448	-	1.903	1.144	$sp^{2.57}$
$\Delta r(\text{H-H})$:									
1	-	0.640	1.674	-	-	1.801	1.877	1.386	$sp^{2.61}$
2	-	0.625	2.000	-	-	1.762	1.866	1.386	$sp^{2.48}$
3	-	0.640	2.003	-	-	1.785	1.867	1.399	$sp^{2.46}$
1	-	1.000	-4.182	-	-	5.994	1.871	5.143	$sp^{1.65}$
2	-	1.000	-3.733	-	-	2.468	1.843	2.631	$sp^{1.60}$
3	-	1.000	-3.581	-	-	2.459	1.822	2.667	$sp^{1.62}$

^a See footnotes to Tables 4.1 and 4.3 and Figures 4.22 - 4.26 for definitions of terms and corresponding structures and curves.

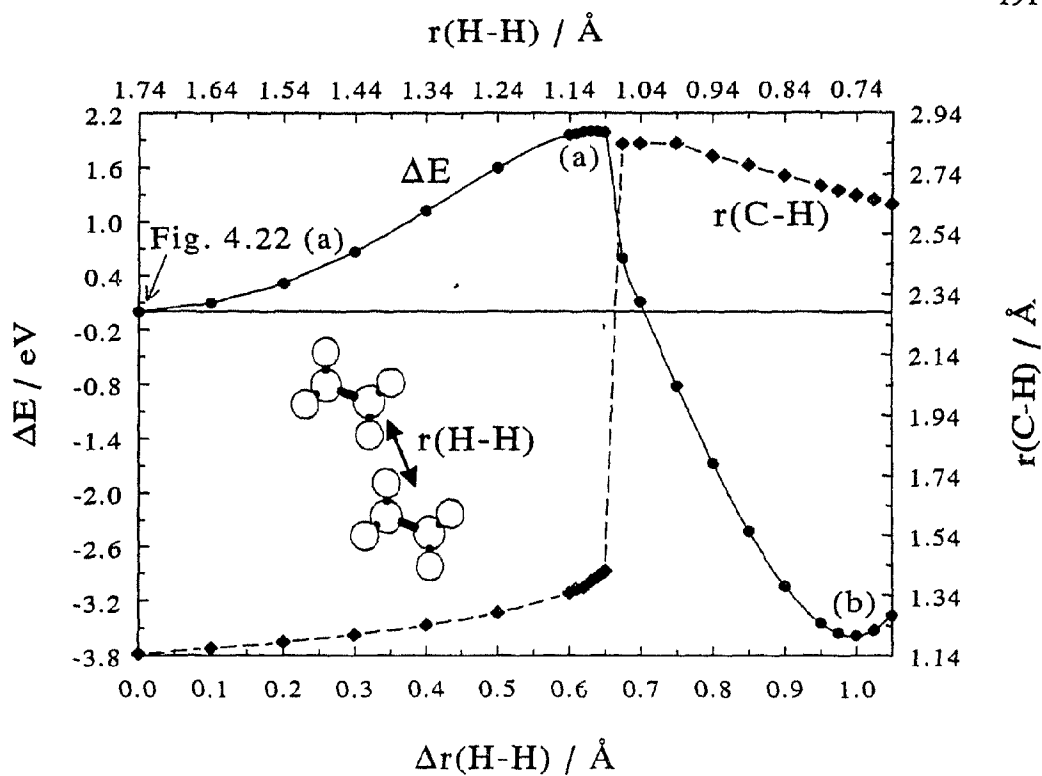
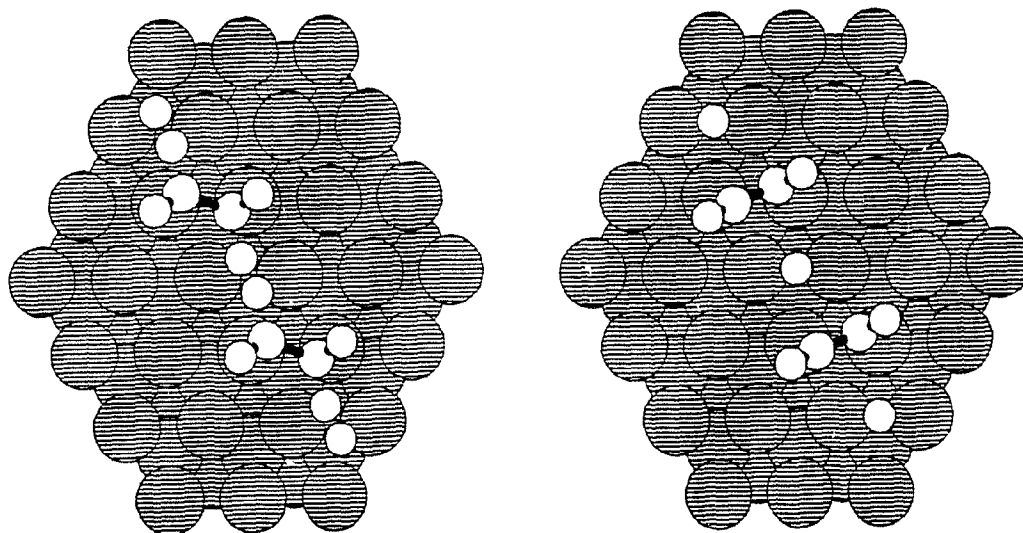
(a) $\Delta r(\text{H-H}) = 0.640 \text{ \AA}$ (b) $\Delta r(\text{H-H}) = 1.000 \text{ \AA}$ 

Figure 4.24 Concerted dehydrogenation step for rotated, di- σ -bonded C_2H_4 's of $\text{Ni}_{72}(\text{C}_2\text{H}_4)_2\text{H}_2$: ΔE and *trans* C-H bond lengths, $r(\text{C-H})$, as functions of decreasing intermolecular H-H distance, $\Delta r(\text{H-H})$, with optimized structures shown for (a) $\Delta r(\text{H-H}) = 0.640 \text{ \AA}$ and (b) $\Delta r(\text{H-H}) = 1.000 \text{ \AA}$.

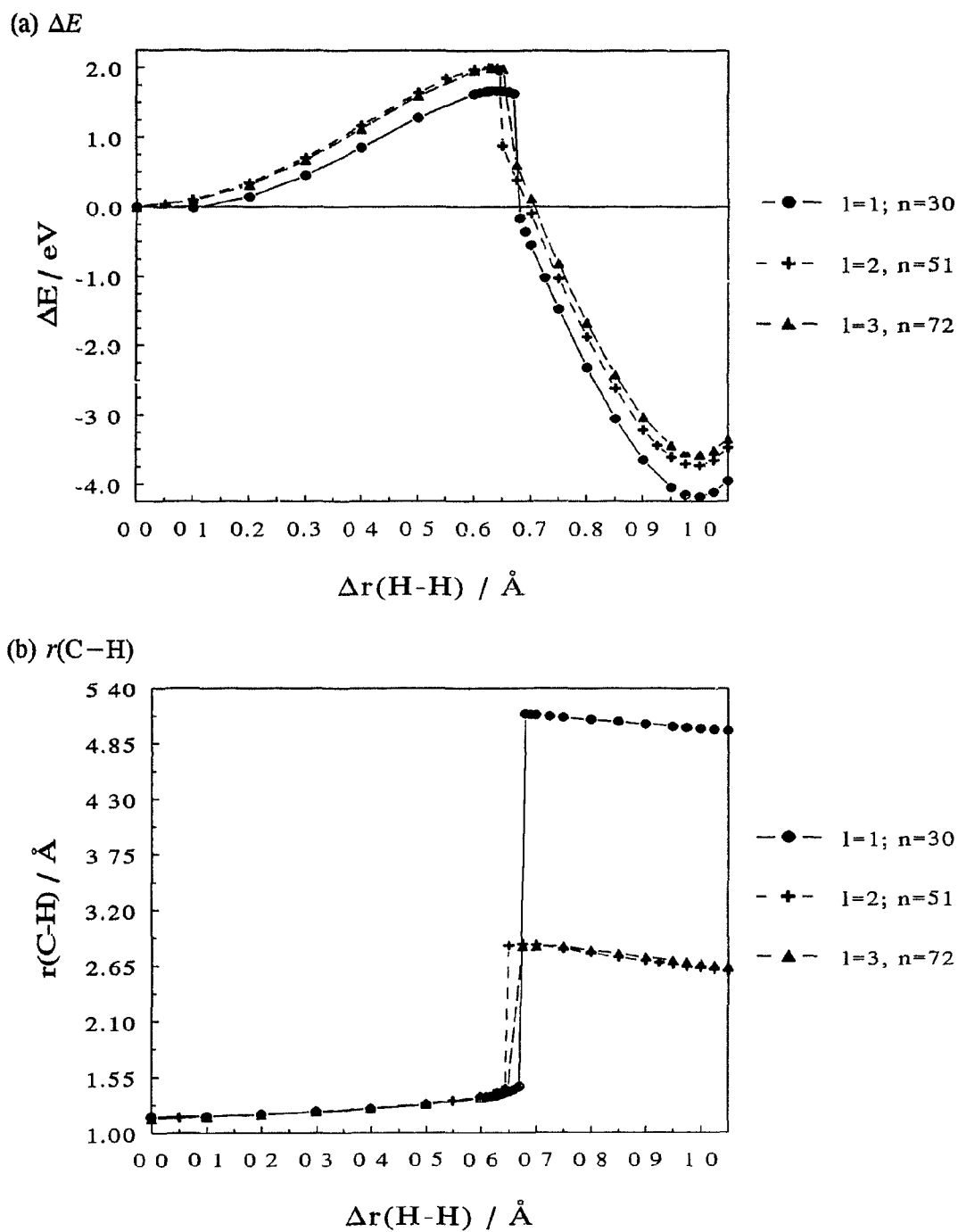


Figure 4.25 Cluster layer dependence of the dehydrogenation step illustrated in Figure 4.24 for $\text{Ni}_n(\text{C}_2\text{H}_4)_2\text{H}_2$, $n = 30, 51,$ and 72 , corresponding to $l = 1, 2,$ and 3 : (a) ΔE and (b) $r(\text{C-H})$ as functions of $\Delta r(\text{H-H})$.

As revealed in Figure 4.26, the intermediate decomposition products correspond to acetylene and molecular hydrogen: (a) planar C_2H_2 fragments, as deduced from their $r(C-C)$ of 1.421 Å (*cf.* $r(C-C) = 1.422$ Å for two di- σ -bonded C_2H_2 's optimized on the same cluster and also $\Delta r(C-C)$'s and sp^n 's in Tables 4.6 and 4.7), are left at an angle of -21.1° from the di- σ site, or $[\bar{1}10]$ direction; while (b) physisorbed H_2 , oriented with its bond axis perpendicular to the surface at a centre-of-mass height of $z_{CM}(H_2) = 2.459$ Å, interacts only weakly with the surface in a chemisorption precursor state. Again for computational economy, a pair of *trans* H's on each C_2H_4 were eliminated in concert, while the elementary step in the dehydrogenation mechanism is thought (though has yet to be conclusively verified) to involve only the two interior intermolecular H's in a concerted tunnelling process.

The nature of the apparent discontinuity just beyond ΔE_{max} in Figure 4.24, and the postulated dissociation of the intermediate decomposition product, H_2 , (in Sect. 4.A.3), were investigated by parametrically lengthening the H_2 separation distance, $\Delta r(H-H)^+$, following the dehydrogenation of C_2H_4 , with the results depicted in Figure 4.27. Of the two physical alternatives, dissociation to atomic H or reformation of the transition state, parametric lengthening of $r(H-H)$ yields the latter, deviated slightly. A manifestation of the abrupt structural changes accompanying the formation of C_2H_2 and H_2 , the discontinuous break in the potential energy curve prevented a complete return to the transition state, due to the artificial parametrization of the system configuration along a single geometrical coordinate, and consequent confinement to a local rather than a global minimum. Optimization of all coordinate variables, *i.e.*, relaxation of all degrees of freedom, to permit sampling of the entirety of configuration space, thereby mapping out

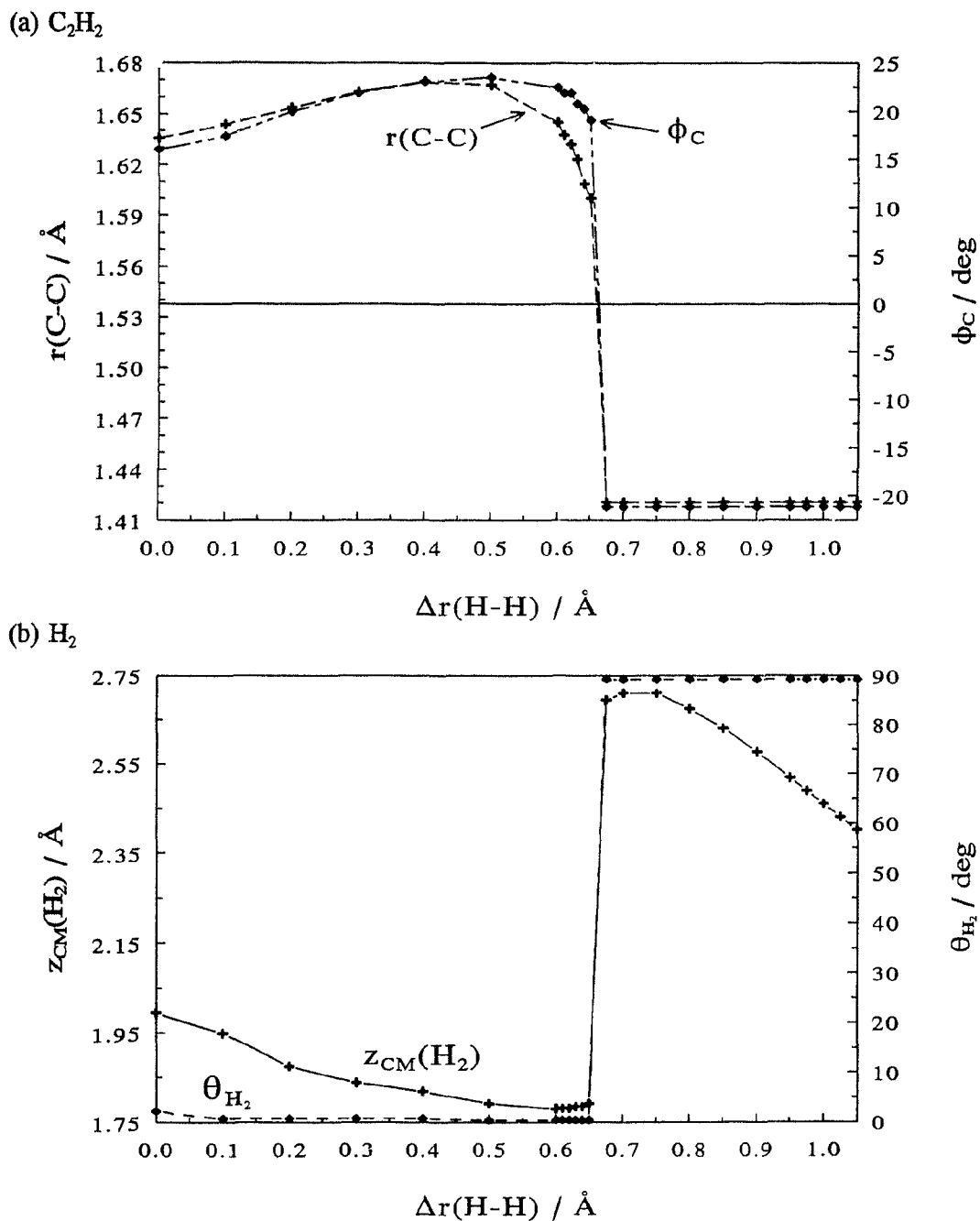


Figure 4.26 Structural changes as functions of $\Delta r(H-H)$ induced by the dehydrogenation step to form the intermediate decomposition products, $2C_2H_2 + 3H_2$, from $Ni_{72}(C_2H_4)_2H_2$: (a) C-C bond distance, $r(C-C)$, and rotation angle from the $[\bar{1}10]$ lattice direction, ϕ_C , of C_2H_2 ; and (b) centre-of-mass height, $z_{CM}(H_2)$, and inclination angle, θ_{H_2} , of physisorbed H_2 relative to the cluster surface.

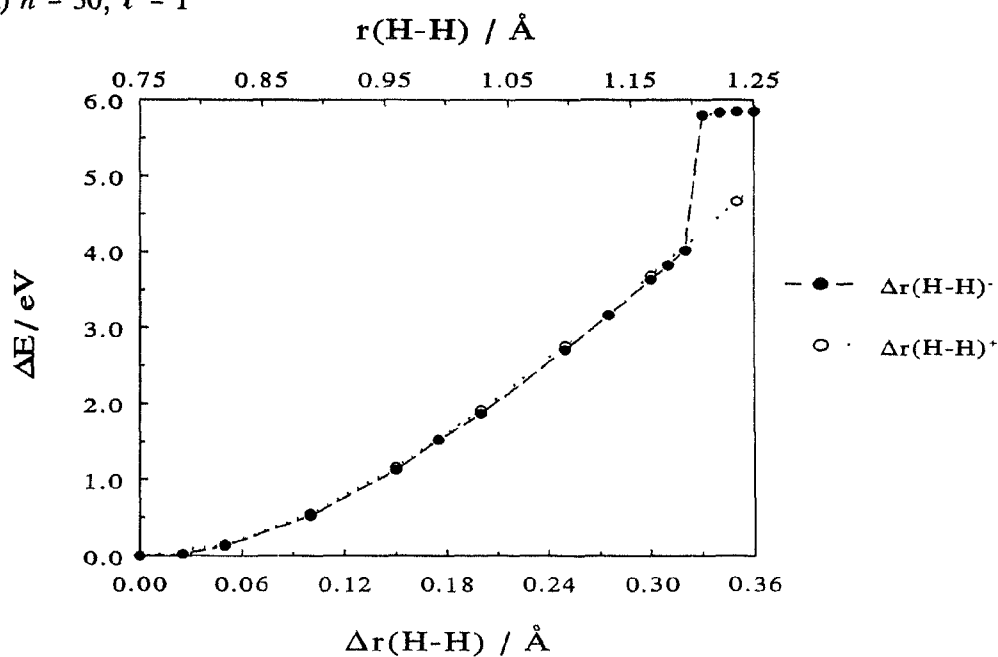
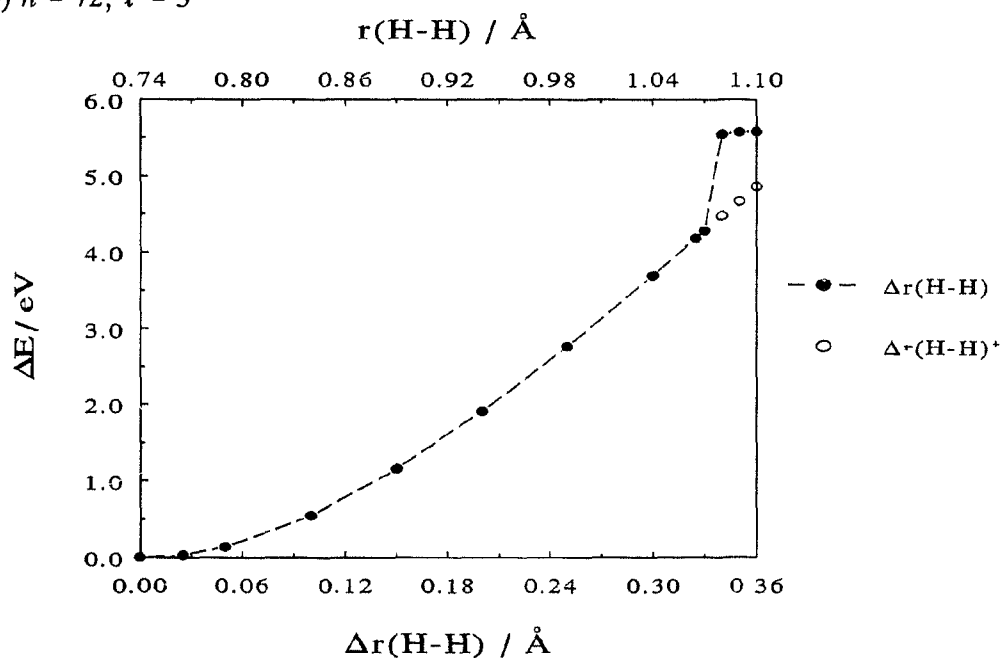
(a) $n = 30, \ell = 1$ (b) $n = 72, \ell = 3$ 

Figure 4.27 Cluster layer dependence of constrained sampling of configuration space for $\text{Ni}_n(\text{C}_2\text{H}_4)_2\text{H}_2$: ΔE as a function of the parametric decrease, $\Delta r(\text{H-H})^-$, and increase, $\Delta r(\text{H-H})^+$, of $r(\text{H-H})$ for (a) $n = 30, \ell = 1$ and (b) $n = 72, \ell = 3$.

the minimum energy path for the reaction, presumably would yield a continuous curve along the generalized reaction coordinate, which would be a combination of the various geometrical coordinates of the system. As Figure 4.27 exhibits, the abrupt break in the curve lessens with successive layers in the Ni cluster, the additional degrees of freedom introduced by the increased number of substrate atoms dampening out drastic fluctuations in the potential energy surface along any particular coordinate. Though constructive in picturing the microscopic, molecular motions involved in the fragmentation process, the use of two "reaction coordinates", $\Delta\phi_C$ and $\Delta r(\text{H-H})$, stretches the formalism of transition-state theory (TST); Figure 4.28 displays the composite relative energy curve (from Figures 4.22 and 4.24 on pp. 188 and 191) along the single reaction coordinate, $r(\text{H-H})$, or generalized reaction coordinate of TST.

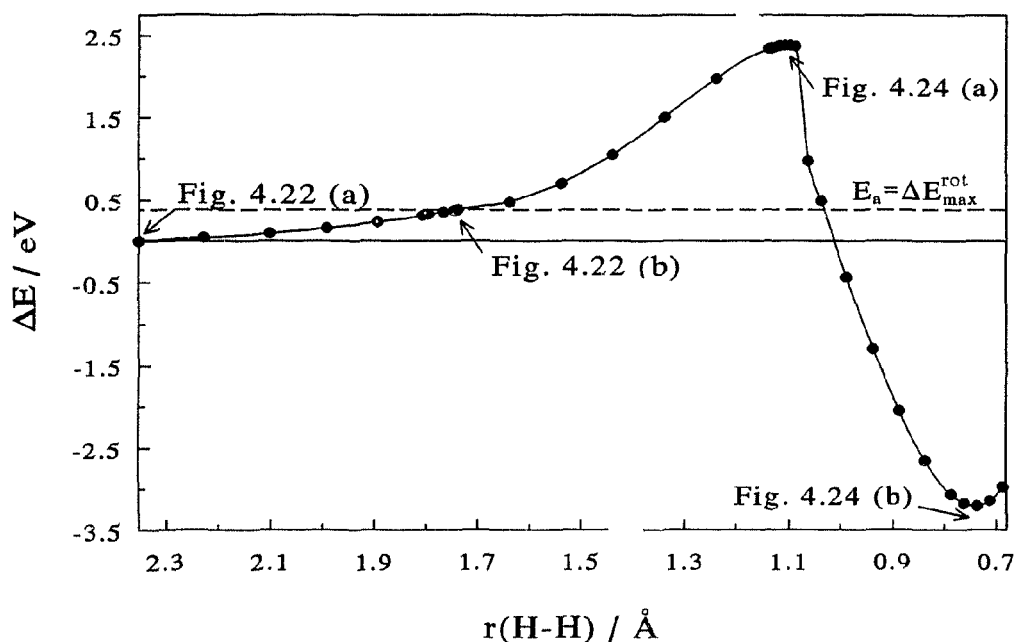


Figure 4.28 Dehydrogenation mechanism for $\text{Ni}_{72}(\text{C}_2\text{H}_4)_2\text{H}_2$ parametrized by the single reaction coordinate, $r(\text{H-H})$, specifying critical configurations and $E_a = \Delta E_{\text{max}}^{\text{rot}}$.

3. Tunnelling of Intermolecular H's

Rather than surmounting the potential barrier along the parametric decrease of $r(\text{H}-\text{H})$, the intermolecular H's on adjacent C_2H_4 's are proposed to tunnel through it. The barrier permeability or tunnelling probability is calculated within the Wentzel-Kramers-Brillouin (WKB) or semi-classical approximation [148] and compared with the computed Boltzmann probability of thermal activation for the decomposition reaction of two ethylene molecules. Acquiring the requisite rotational energy, which brings the intermolecular H's in critical contact, is deduced to be the slow step in the ethylene decomposition, consistent with the experimentally observed thermal-induced reaction. To establish the validity of the tunnelling mechanism, both the activation energy for the decomposition of deuterated ethylene and an upper bound on the normal ethylene decomposition temperature for thermal activation to be the slow step were predicted and compared with the observed values. The effective pre-exponential factor was then deduced, both within a steady-state approximation and by explicit solution of master equations [149] describing the reaction, as derived within a non-equilibrium, statistical mechanical formalism, and found consistent with the experimental value.

The probability for the intermolecular H's to tunnel through the potential energy barrier along $r(\text{H}-\text{H})$ was calculated from the expression for the WKB transmission coefficient:

$$P^{WKB} = \exp \left\{ -\frac{2\sqrt{2\mu}}{\hbar} \int_{x_1}^{x_2} \sqrt{V(x) - E} dx \right\}, \quad (4.1)$$

where μ is the reduced mass for the process; \hbar is Planck's constant; E is the energy of the system, corresponding in this case to the activation energy, E_a , of the decomposition reaction; and the integration extends through the one-dimensional barrier, $V(x)$, along the reaction coordinate, x , from one classical turning point, x_1 , to another, x_2 . For normal or protonated ethylene, the reduced mass is given by

$$\mu_H = \frac{m_H m_H}{m_H + m_H} = \frac{m_H}{2}, \quad (4.2)$$

while for the deuterated species, the mass of deuterium replaces that of hydrogen in the above expression. Numerical integration, via the trapezoidal rule, of $\int_{x_1}^{x_2} \sqrt{V(x) - E_a(C_2H_4)} dx$, where the potential energy curve of Figure 4.28 (p. 196) has been used with $E_a = \Delta E_{max}^{rot}$, yields, upon substitution into eqn. (4.1), for the WKB hydrogen tunnelling probability:

$$P^{WKB} \approx 1.3 \times 10^{-8} \quad (4.3)$$

Table 4.8 examines the cluster layer dependence and convergence of this result, along with other calculated tunnelling parameters, to be discussed presently.

The Boltzmann probability of thermal activation for the decomposition of two ethylene molecules, computed by inserting the calculated activation energy and experimental temperature of reaction, $T \sim 200$ K:

$$P_{ta} = e^{-E_a/k_B T} \approx 2.4 \times 10^{-10}, \quad (4.4)$$

is two orders of magnitude less than the calculated WKB tunnelling probability. Clearly, for not too disparate prefactors, the tunnelling process is fast compared with the rate of

Table 4.8 Cluster Layer Dependence of Tunnelling Parameters for Di- σ - and π -bonded C_2H_4 for the $Ni_n(C_2H_4)_2H_2$ Model^a Systems: $n = 30, 51, 72$ and $n = 37$

ℓ	$\int \sqrt{V(x) - E_a(C_2H_4)} dx$ / $eV^{1/2}\text{\AA}$	P^{WKB} ^c	$P_{i.a.} = e^{-E_a/k_bT}$ ^d	$E_a(C_2D_4)$ ^e / eV	T_c^f / K
di-σ (twofold aligned bridging)					
1	0.495	2.15×10^{-7}	1.49×10^{-13}	0.80	385
2	0.577	1.65×10^{-8}	3.49×10^{-11}	0.75	269
3	0.585	1.28×10^{-8}	2.37×10^{-10}	0.72	244
π (onfold atop)					
1	0.603	7.30×10^{-9}	4.32×10^{-12}	0.91	279

^a For di- σ -bonded C_2H_4 , $n = 30, 51,$ and 72 , corresponding to $\ell = 1, 2,$ and 3 clusters symmetric about the twofold aligned bridging site; for the π -bonded species, $n = 37$, corresponding to a $\ell = 1$ cluster symmetric about the atop site

^b Numerically integrated, via trapezoidal rule, from the ΔE vs. $\Delta r(H-H)$ curves in Figures 4.25 (a) and 4.39 for the di- σ - and π -bonded species, respectively, or alternatively, by truncation of the composite ΔE vs. $r(H-H)$ curves, as in Figure 4.28, with $E_a = \Delta E_{max}^{rot}$

^c WKB tunnelling probability calculated using eqn. (4.1) of text

^d Boltzmann probability for thermal activation computed using $T_{expt} \sim 200$ K

^e Estimated activation energy for deuterated ethylene obtained by equating tunnelling probabilities for normal and deuterated species and using same potential energy curves as in footnote b; cf. $E_a^{expt}(C_2D_4) = (0.53/0.57 \pm 0.02)$ eV

^f Predicted upper bound on ethylene decomposition temperature for thermal activation to be slow compared with tunnelling; cf. $T_{expt} \sim 200$ K

thermal activation requisite for the reactant ethylenes to rotate relative to the Ni substrate, *i.e.*, $r_t = \nu_t P^{WKB} > r_{t.a.} = \nu_{t.a.} P_{t.a.}$ for $\nu_t \sim \nu_{t.a.}$, in accord with the observed thermal-induced reaction. The configuration of critical proximity of the intermolecular H's prior to the tunnelling step and H₂ formation, corresponding to the structure at the height of the potential barrier along $\Delta\phi_C$, is proffered as the transient, bimolecular complex demanded by the measured second-order kinetics [11].

A rough numerical estimate of the activation energy for deuterated ethylene, $E_a(C_2D_4)$, is obtained by equating the hydrogen and deuterium WKB tunnelling probabilities, on the rationale that P^{WKB} for the two isotopic species must exceed some threshold, taken as P_H^{WKB} , for the effective rates of reaction to be appreciable:

$$P_H^{WKB} \sim P_D^{WKB} = \exp \left\{ -\frac{2\sqrt{2\mu_D}}{\hbar} \int_{x_1}^{x_2} \sqrt{V(x) - E_a(C_2D_4)} dx \right\}. \quad (4.5)$$

From the above equality, a value for the integral is extracted and $E_a(C_2D_4)$ numerically estimated using the computed potential energy curve along $r(H-H)$ for the normal reaction. The predicted $E_a(C_2D_4)$ of 0.72 eV (see Table 4.8 for its cluster layer dependence) is of the same order of magnitude as $E_a^{expl}(C_2D_4) = (0.53/0.57 \pm 0.02)$ eV [44], which is encouraging agreement given the error inherent in the initial equality.

The temperature independence of the tunnelling process was exploited to predict an upper bound on the ethylene decomposition temperature, T_c , for thermal activation to be the slow step. The rates of tunnelling and thermal activation, *viz.*,

$$r_t = \nu_t P^{WKB} \quad (4.6)$$

and

$$r_{t.a.} = v_{t.a.} e^{-E_a/k_B T}, \quad (4.7)$$

were equated, and assuming $v_t = v_{t.a.}$, the resulting expression,

$$r_t = r_{t.a.} \quad \Rightarrow \quad P^{WKB} = e^{-E_a/k_B T_c} \quad (4.8)$$

was solved for T_c :

$$T_c = -\frac{E_a}{k_B \ln P^{WKB}} \approx 244 K > T_{expt} \sim 200 K; \quad (4.9)$$

see Table 4.8. The applicability of the second of the following inequalities:

$$T_c < T_{expt} \Rightarrow r_t < r_{t.a.}; \quad T_c > T_{expt} \Rightarrow r_t > r_{t.a.}, \quad (4.10)$$

corroborates the earlier prediction that the tunnelling rate is fast compared with the rate of thermal activation.

Expressions for the effective rate and prefactor were then derived adopting a master-equation formalism [149], which assumes a linear, Markovian (*i.e.*, local in time) rate equation for the time-dependent probability distribution of the system:

$$\frac{dn_v}{dt} = \sum_{v'} [r_{v'v} n_{v'} - r_{vv'} n_v], \quad (4.11)$$

where $r_{v'v}$ ($r_{vv'}$) is the transition probability per unit time or transition rate from microstate v' (v) to microstate v (v') and $n_v(t)$ ($n_{v'}(t)$) the occupation probability at time t for a given microstate v (v'). Within this approach, the time rate of change in the occupation probability of the ground (configurational) state of the reactant ethylene molecules, dn_0/dt , may be written as minus the sum of terms due to transitions from the

ground state (with excitation rate $r_1(E)$ and occupation probability n_0) into higher lying states of energy E plus the sum of terms due to transitions to the ground state from states of energy E (with decay rate $r_1(E)$ and probability n_E):

$$\frac{dn_0}{dt} = - \sum_E r_1(E) n_0 + \sum_E r_1(E) n_E . \quad (4.12)$$

Similarly, the time rate of change in the occupation probability of an excited state of energy E is expressible as

$$\frac{dn_E}{dt} = r_1(E) n_0 - r_1(E) n_E - r_t(E) n_E , \quad r_1(E) \gg r_t(E) , \quad (4.13)$$

where $r_t(E)$ is the rate of tunnelling from the state of energy E , with its decay rate assumed much greater than its excitation rate, *i.e.*, the sum of terms, $-\sum_{E'} r_1(E') n_E$, has

been omitted. Within the steady- or stationary-state approximation (SSA):

$$\frac{dn_E}{dt} = 0 , \quad (4.14)$$

valid if the deactivation rate greatly exceeds the tunnelling rate, *i.e.*, $r_1(E) \gg r_t(E)$, such that the ground- and excited-state molecules are in quasi-equilibrium and hence the condition of detailed balance prevails, then solution of eqn. (4.13) for n_E yields

$$n_E = \frac{r_1(E)}{r_1(E) + r_t(E)} n_0 , \quad (4.15)$$

which when substituted into eqn. (4.12) gives

$$\begin{aligned} \frac{dn_0}{dt} &= \sum_E \left[\frac{r_1(E)r_t(E)}{r_1(E) + r_t(E)} - r_1(E) \right] n_0 \\ &= - \sum_E \frac{r_1(E)r_t(E)}{r_1(E) + r_t(E)} n_0 . \end{aligned} \quad (4.16)$$

Under the assumptions that $r_1 \gg r_t$ and r_1 is roughly independent of E (which lets it be brought outside the summation), as thermal deactivation occurs via spontaneous phonon emission, the following expression is obtained:

$$\begin{aligned} \frac{dn_0}{dt} &= - \frac{1}{r_1} \sum_E r_1(E)r_t(E)n_0 \\ &= - r_{eff} n_0 , \end{aligned} \quad (4.17)$$

where the summation over E can be dropped since the product $r_1(E)r_t(E)$ is a function of E sharply peaked at E_a , the (observable) activation energy, the effective reaction rate being written as

$$r_{eff} = \frac{r_1 r_t}{r_1} = v_{eff} e^{-E_a/k_B T} . \quad (4.18)$$

Setting the pre-exponential factors for thermal activation and tunnelling equal and approximating $v \approx 10^{12} \text{ s}^{-1}$ (\sim vibrational frequency) yields for the corresponding rates:

$$r_1 = v P_{ta} \approx 10^{12} \times e^{-E_a/k_B T} \text{ s}^{-1} , \quad (4.19)$$

and

$$r_t = v P^{WKB} \approx 10^{12} \text{ s}^{-1} \times 10^{-8} = 10^4 \text{ s}^{-1} ; \quad (4.20)$$

with the decay rate estimated at

$$r_l \approx 10^{10} \text{ s}^{-1} . \quad (4.21)$$

The following expression for the effective pre-exponential factor is thus obtained from eqn. (4.18):

$$v_{\text{eff}} = \frac{r_l r_t}{r_l} e^{E_d/k_B T} \approx \frac{v^2 P^{WKB}}{r_l} \approx 10^6 \text{ s}^{-1} , \quad (4.22)$$

consistent with the experimental prefactor of $v_{\text{expt}} = 10^6 \pm 2 \text{ s}^{-1}$ [44].

Beyond the steady-state approximation, explicit solution of the time-dependent master equations for a (simplified) two-state system derives the effective reaction rate as the product of the tunnelling rate and a Boltzmann factor. Analogous to eqns. (4.12) and (4.13), a pair of coupled, first-order, linear differential equations for the time rates of change in the occupation probabilities of the lower (denoted by l) and upper (denoted by u) states may be written as

$$\frac{dn_l}{dt} = -r_l n_l + r_l n_u , \quad (4.23)$$

and

$$\frac{dn_u}{dt} = r_l n_l - r_l n_u - r_t n_u , \quad (4.24)$$

where r_l (r_l) represents the transition probability per unit time from the lower (upper) to the upper (lower) states, n_l (n_u) is the (time-dependent) occupation probability of the lower (upper) state, and r_t is the tunnelling rate out of the upper state. Assuming an exponential time dependence of the occupation probabilities, *i.e.*,

$$\mathbf{n}(t) = \begin{pmatrix} n_i(t) \\ n_u(t) \end{pmatrix} = \begin{pmatrix} n_i(t=0) \\ n_u(t=0) \end{pmatrix} e^{-rt} = \xi e^{-rt}, \quad (4.25)$$

results in the following system of algebraic equations:

$$\begin{pmatrix} -r_1 + r & r_1 \\ r_1 & -(r_1 + r_t) + r \end{pmatrix} \begin{pmatrix} n_i \\ n_u \end{pmatrix} = \begin{pmatrix} 0 \\ 0 \end{pmatrix}, \quad (4.26)$$

which has nontrivial solutions if and only if the determinant of coefficients is zero, *i.e.*,

$$\begin{vmatrix} -(r_1 - r) & r_1 \\ r_1 & -(r_1 + r_t - r) \end{vmatrix} = 0. \quad (4.27)$$

Solving the ensuing quadratic,

$$r^2 - r(r_1 + r_1 + r_t) + r_t r_1 = 0, \quad (4.28)$$

for its two roots, r_+ and r_- :

$$r_{\pm} = \frac{r_1 + r_1 + r_t}{2} \left[1 \pm \sqrt{1 - \frac{4r_t r_1}{(r_1 + r_1 + r_t)^2}} \right], \quad (4.29)$$

by invoking the binomial approximation with $r_1 > r_1, r_t$ such that

$\left[\frac{4r_t r_1}{(r_1 + r_1 + r_t)^2} \right]^2 \ll 1$, yields for the determinantal roots or eigenvalues,

$$r_+ = (r_1 + r_1 + r_t) - \frac{r_t r_1}{r_1 + r_1 + r_t}, \quad r_- = \frac{r_t r_1}{r_1 + r_1 + r_t} \ll r_+, \quad (4.30)$$

which can be shown as a result of detailed balance to be positive semidefinite or nonnegative, *i.e.*, $r_{\pm} \geq 0$ [149]. The smaller root, r_- , corresponds to a slower rate and hence to the experimentally observable rate of reaction to products, while the larger

eigenvalue, r_+ , establishes the initial, transient rate of evolution of the relative populations of the upper and lower states before significant depletion of reactants to products, *i.e.*, before significant tunnelling occurs.

The general solution of the master equations for the occupation probabilities of the two-level system, eqns. (4.23) and (4.24) may be written as

$$n_l(t) = n_{l_1} e^{-r_1 t} + n_{l_2} e^{-r_2 t} \quad (4.31)$$

and

$$n_u(t) = n_{u_1} e^{-r_1 t} + n_{u_2} e^{-r_2 t}, \quad (4.32)$$

where the $n_{l_{1,2}}$ and $n_{u_{1,2}}$ denote constants to be determined. Applying the (arbitrary) initial conditions on the occupation probabilities:

$$n_l(t=0) = n_{l_1} + n_{l_2} = 1 \quad \text{and} \quad n_u(t=0) = n_{u_1} + n_{u_2} = 0, \quad (4.33)$$

which corresponds to the microstate configuration having the lower level fully populated and the upper level empty, gives, upon differentiating the general solution, eqns. (4.31) and (4.32), equating to the appropriate master equation, eqn. (4.23) or (4.24), and evaluating at $t = 0$, the time-dependent distribution functions for the two-state system:

$$n_l(t) = \frac{1}{r_2 - r_1} \left[(r_2 - r_1) e^{-r_1 t} + (r_1 - r_1) e^{-r_2 t} \right] \quad (4.34)$$

and

$$n_u(t) = \frac{r_1}{r_2 - r_1} \left[e^{-r_1 t} - e^{-r_2 t} \right]. \quad (4.35)$$

Alternatively, the occupation probabilities, eqns. (4.34) and (4.35), can be derived by substituting the eigenvalues of eqn. (4.30), r_{\pm} , into the matrix equation, eqn. (4.26), solving for the corresponding eigenvectors, ξ_{\pm} , to yield two independent solutions of the form as in eqn. (4.25), and applying the initial conditions in eqn. (4.33) to determine the two arbitrary constants, c_{\pm} , of the general solution:

$$\begin{pmatrix} n_l(t) \\ n_u(t) \end{pmatrix} = c_+ \xi_+ e^{-r_+ t} + c_- \xi_- e^{-r_- t}, \quad (4.36)$$

which reveals the correspondence $r_+ \rightarrow r_2$ and $r_- \rightarrow r_1$.

The qualitative time dependences of the occupation probabilities of the lower and upper states, plotted representatively in Figure 4.29 (a), can be ascertained by differentiation of eqns. (4.34) and (4.35). The nonvanishing first derivative of eqn. (4.34) for all t reflects the absence of extrema, while its positive second derivative for all t indicates that its slope is always increasing, *i.e.*, $n_l(t)$ is a monotonically decreasing function of time which decays, with initial (negative) slope, $-r_1$, from unity to zero, as the upper level is populated at the expense of the lower level occupation. As the sum of two exponentially decaying functions with significantly different time constants, *i.e.*, $r_2 > r_1$, $n_l(t)$ is initially depopulated in accordance with the fast rate, r_2 , as the upper level populates, but drops off for large times much more slowly following the exponential tail governed by the slow rate, r_1 , as tunnelling to products depletes the supply of reactant molecules. Conversely, the initial (positive) slope of $n_u(t)$, r_1 , reflects the initial injection of species from the lower level, the transient response being dominated by the fast rate, while at large times, tunnelling to products also depopulates

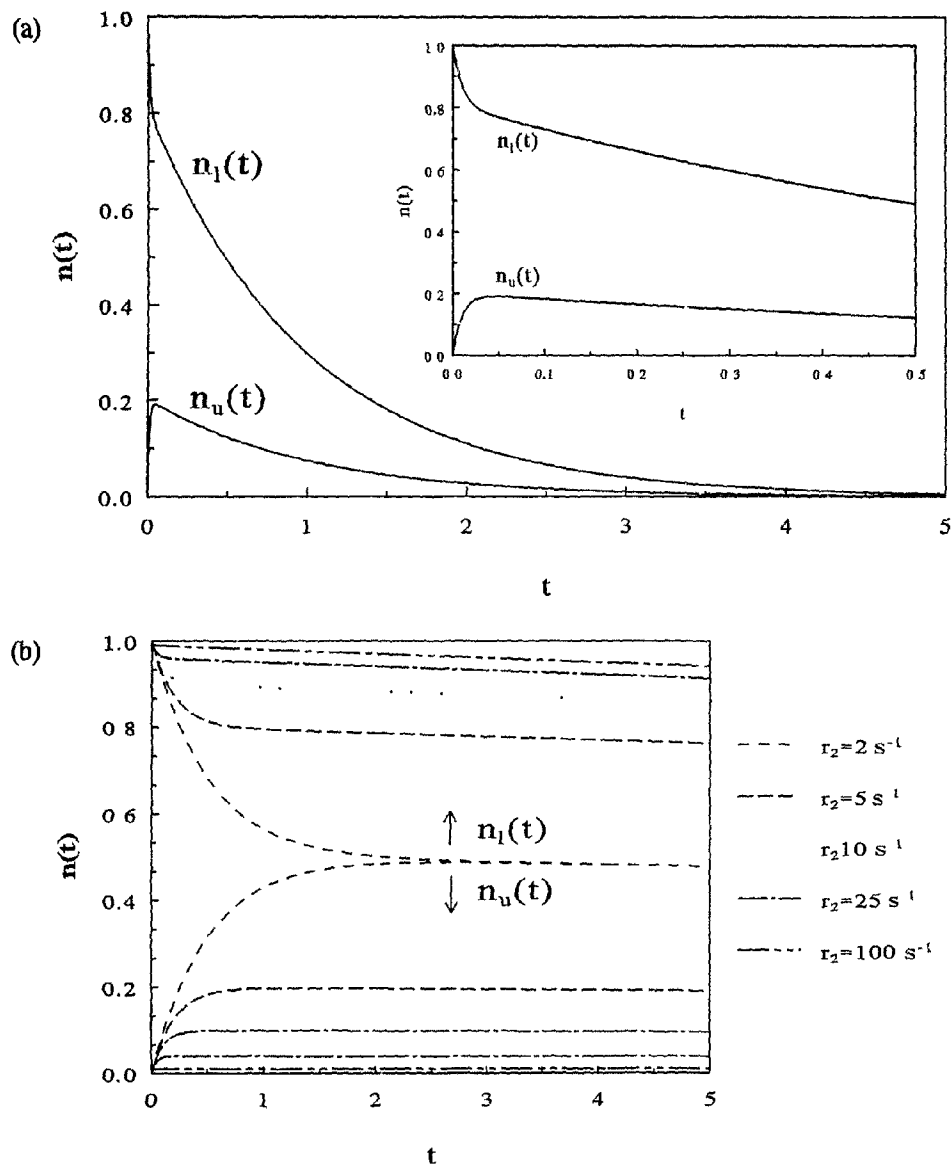


Figure 4.29 (a) Qualitative behaviour of time-dependent occupation probabilities for the lower, $n_l(t)$, and upper, $n_u(t)$, states of eqns. (4.34) and (4.35), shown for $r_1 = 0.05r_2 = 0.01r_2 = 1\text{ s}^{-1}$, with expanded time scale in inset validating SSA. Estimated values of $r_1 = 10^{-6}r_2 = 10^{-14}r_2 = 10^{-4}\text{ s}^{-1}$ yield indiscernible features: $n_l(t)$ exhibits a steep initial decline followed by a gradual decay, while $n_u(t)$ rises sharply, quickly peaks, and then decays slowly, under approximate steady-state conditions. (b) Progression of $n_l(t)$ and $n_u(t)$ with increasing r_2 , for $r_1 = 100r_1 = 0.01\text{ s}^{-1}$, in the approach towards the predicted curves of eqns. (4.38) and (4.39).

the upper state according to the slow rate, *i.e.*, $n_u(t)$ is zero both at initial and long times. Setting the first time derivative of eqn. (4.35) to zero reveals a single extremum in the upper level occupation at $t_{max} = \frac{1}{r_2 - r_1} \ln \frac{r_2}{r_1} > 0$; the negative second derivative of eqn. (4.35) verifies its downward concavity, *i.e.*, that the extremum is a maximum, ensuring the nonnegativity of $n_u(t)$, a physical requirement of an occupation probability. The maximum corresponds to the time when the initial population from the lower state is just offset by the depopulation to products.

Estimating the rates of thermal activation, tunnelling, and decay as in eqns. (4.19) – (4.21), which employ eqns. (4.3) and (4.4) for the WKB and Boltzmann probabilities, *viz.*, $r_t \approx 10^2 \text{ s}^{-1}$, $r_f \approx 10^4 \text{ s}^{-1}$, and $r_1 \approx 10^{10} \text{ s}^{-1}$, shows the following inequalities to hold: $r_1 \gg r_f \gg r_t$, validating approximations used throughout the analysis, including the earlier SSA (see Figure 4.29). Explicit evaluation of the eigenvalues of eqn. (4.30):

$$r_2 = r_+ = (r_t + r_1 + r_f) - \frac{r_t r_1}{r_t + r_1 + r_f} \approx 10^{10} \text{ s}^{-1} \quad \text{fast rate ,} \quad (4.37)$$

$$r_1 = r_- = \frac{r_t r_1}{r_t + r_1 + r_f} \approx 10^{-4} \text{ s}^{-1} \quad \text{slow rate ;}$$

confirms that the fast rate is much greater than the slow rate. The time dependences of the occupation probabilities of eqns. (4.34) and (4.35) can now be quantified:

$$n_l(t) = \frac{1}{r_2 - r_1} \left[(r_2 - r_1) e^{-r_1 t} + (r_1 - r_2) e^{-r_2 t} \right] \approx e^{-r_1 t} \approx e^{-10^{10} t} \quad (4.38)$$

and

$$n_u(t) = \frac{r_1}{r_2 - r_1} \left[e^{-r_1 t} - e^{-r_2 t} \right] \approx \frac{r_1}{r_2} \left[e^{-r_1 t} - e^{-r_2 t} \right] \approx 10^{-8} \left[e^{-10^4 t} - e^{-10^{10} t} \right] . \quad (4.39)$$

The steep initial rise of $n_u(t)$ and concomitant decline of $n_l(t)$, followed by the slow exponential decay of both, attributable to the fast, $r_2 \approx 10^{10} \text{ s}^{-1}$, and slow, $r_1 \approx 10^{-4} \text{ s}^{-1}$, rates, respectively, are indiscernible when plotted, so instead, these curves were displayed in Figure 4.29 (a) for the indicated, representative values. Its inset reveals, on an expanded time scale, the validity of the SSA of eqn. (4.14), invoked in the earlier analysis, for times just beyond the initial, transient rise and fall of $n_u(t)$ and $n_l(t)$, respectively. Its validity is corroborated in Figure 4.29 (b), which depicts the progression of $n_l(t)$ and $n_u(t)$ with increasing r_2 , for fixed $r_1 = 10^{-2} \text{ s}^{-1}$ and $r_1 = 1 \text{ s}^{-1}$, as the predicted numerical values of eqns. (4.38) and (4.39) are approached.

Applying the condition of detailed balance,

$$r_1 n_l = r_1 n_u, \quad (4.40)$$

and the equilibrium Boltzmann or canonical distribution law,

$$\frac{n_u}{n_l} = e^{-\Delta E/k_B T}, \quad (4.41)$$

yields for the rate of thermal activation:

$$r_1 = r_l e^{-\Delta E/k_B T}. \quad (4.42)$$

Substituting this expression into that for the slow rate, r_1 or r_- of eqn. (4.30), gives the effective rate as the product of a Boltzmann factor containing the activation energy and the tunnelling rate as the effective prefactor:

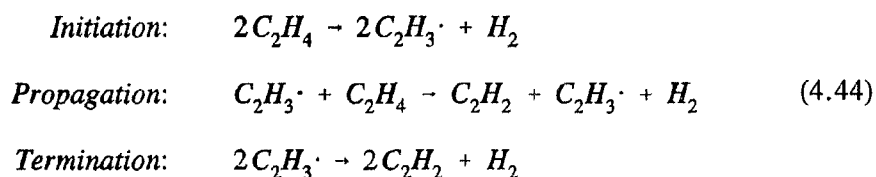
$$\begin{aligned} r_{eff} &= \frac{r_l r_1}{r_1 + r_1 + r_l} \approx \frac{r_l r_1}{r_1} e^{-\Delta E/k_B T} \approx r_l e^{-\Delta E/k_B T}, & r_1 \gg r_1, r_l, \\ &= v_{eff} e^{-E_a/k_B T}; \end{aligned} \quad (4.43)$$

i.e., the Boltzmann probability represents the relative number of attempts by the system, in thermal quasi-equilibrium, having the requisite minimum energy, E_a , to undergo reaction, while the tunnelling rate, as the effective attempt frequency, governs the dynamics of the energy transfer for the decomposition. This is consistent with a slow rate of thermal activation followed by a fast tunnelling step, both much slower than the rate of thermal deactivation. The favourable correlation between the tunnelling rate as the effective prefactor, $r_t = \nu_{eff} \approx 10^4 \text{ s}^{-1}$, and the experimental prefactor, $\nu_{expt} = 10^{6 \pm 2} \text{ s}^{-1}$ [44], argues convincingly for the concerted tunnelling mechanism in the ethylene dehydrogenation reaction. This value for ν_{eff} differs from that of the earlier analysis invoking the SSA, eqn. (4.14), as a result of applying the condition of detailed balance to derive the expression for r_t in eqn. (4.42), rather than approximating it as in eqn. (4.19). The correspondence with the experimental prefactor can be enhanced by approximating the tunnelling prefactor with the vibrational frequency of a C–H bond stretch, 10^{14} s^{-1} , rather than 10^{12} s^{-1} , as in the preceding analysis, to yield $r_t = \nu_t P^{WKB} = \nu_{eff} \approx 10^6 \text{ s}^{-1}$.

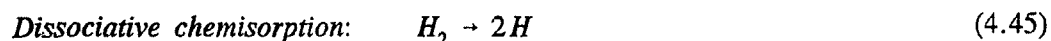
A suggestive point of contact with (unpublished) experimental data [10] is the observation, at temperatures below that requisite for ethylene decomposition, of a product mixture of unreacted ethylene isotopes, $\text{C}_2\text{H}_3\text{D} + \text{C}_2\text{D}_3\text{H} + \text{C}_2\text{H}_2\text{D}_2$, from a reactant mixture of protonated and deuterated ethylenes, $\text{C}_2\text{H}_4 + \text{C}_2\text{D}_4$. The observed H–D exchange can be rationalized with the proposed tunnelling mechanism by postulating HD

(*cf.* H_2 for the normal reaction) and radical hydrocarbon isotopic intermediates, *i.e.*, $C_2H_3\cdot + C_2D_3\cdot + HD$. The requirement for this rationalization is that the rotational frequency of HD, $\nu_{rot}(HD) \sim 10^{12} s^{-1}$ [150], be much greater than the effective prefactor for the reaction, $\nu_{expt} = 10^6 \pm 2 s^{-1}$, which is indeed the case. An additional experimental condition is that the temperature be low enough for the physisorbed HD (or H_2) intermediate to have a residence time long enough for the reverse reaction leading back to reactant ethylenes to be appreciable. An interesting question is whether an analogous isotopic mixture would be found for normal and deuterated acetylenes, which would imply a similar tunnelling mechanism and second-order kinetics for the dehydrogenation of acetylene.

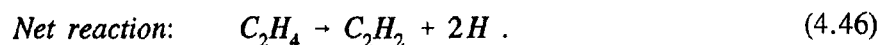
Supported by the above experimental results, the following linear chain mechanism is postulated for the C_2H_4 decomposition reaction:



which, coupled with the dissociative chemisorption of the physisorbed H_2 molecule:



yields the overall conversion:



In this scheme, elimination of the two interior intermolecular H's in a concerted

tunnelling process constitutes the elementary initiation step. Stepwise cleavage would produce a speculated reactive $C_2H_3 \cdot$ radical intermediate, which could then react with other unreacted C_2H_4 's on the surface (in the propagation step) and amongst themselves (termination step). The eventual surface species, C_2H_2 's and coadsorbed H's, then rearrange to their final adsorption sites, to be discussed presently.

3. Final Adsorption Sites of Decomposition Products

The last objective remains to account for the LEED pattern, shown in Figure 4.30, of the final decomposition products, C_2H_2 and coadsorbed H [10], which identifies the acetylene C's in neighbouring threefold sites, with the C–C axis preferentially rotated counterclockwise by an angle of $\phi_c \sim 10^\circ$ with respect to the $[\bar{1}\bar{1}2]$ direction or fourfold bridging μ site of the Ni lattice. The C_2H_2 and H_2 dehydrogenation products of a $Ni_n(C_2H_4)_2$ system, where $n = 30, 51,$ and 72 , are taken to be decoupled and hence treated separately in the investigation of their final adsorption sites. The system is deduced to rearrange in two stages: initial C_2H_2 rotation to the μ site, followed by dissociation of the metastable H_2 to chemisorbed H in the threefold sites, which slightly perturbs the C_2H_2 's from alignment with the μ site. The alternative routes to the final decomposition products, simultaneous H_2 dissociation and C_2H_2 rotation, and dissociative chemisorption of H_2 followed by C_2H_2 rotation, were subsequently investigated to verify the assumed decoupling of the intermediate decomposition products.

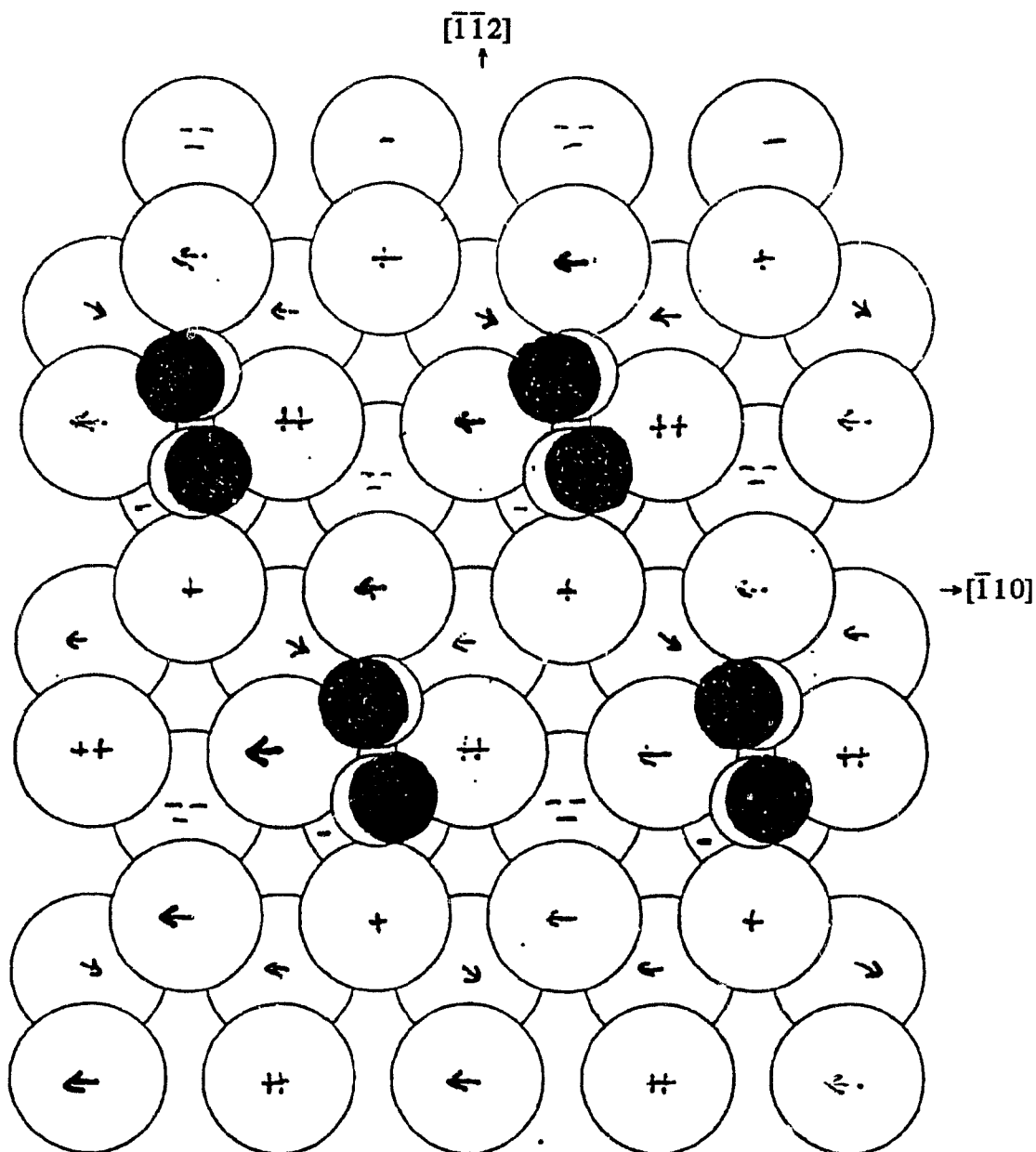


Figure 4.30 Low-energy electron diffraction (LEED) pattern from Ref. [10] of the final decomposition products, C₂H₂ and coadsorbed H, following C₂H₄ dehydrogenation on Ni(111): ○'s are Ni's; ●'s are C's of C₂H₂ observed with the C–C axis rotated counterclockwise by $\phi_c \sim 10^\circ$ from the $[\bar{1}\bar{1}2]$ direction or μ site; ○'s are C's of an ideal C₂H₂ overlayer commensurate with the underlying lattice in the μ binding sites; and the H's are not detectable. The ↑'s, +'s, and -'s indicate the Ni first- and second-layer lateral ($l_{1,2} \leq 0.1 \text{ \AA}$) and buckling ($b_1 \leq 0.04 \text{ \AA}$ and $b_2 \leq 0.07 \text{ \AA}$) reconstructions.

a. $\text{Ni}_{72}(\text{C}_2\text{H}_2)_2$: Rotation of C_2H_2 's about ϕ_C Followed by Dissociative Chemisorption of H_2

As illustrated in Figure 4.31 for a $\text{Ni}_{72}(\text{C}_2\text{H}_2)_2$ system, counterclockwise rotation, $\Delta\phi_C(-)$, of two C_2H_2 molecules from the di- σ ($\Delta\phi_C = 0.0^\circ$) to μ ($\Delta\phi_C = -90.0^\circ$) adsorption sites yields a barrier of $\Delta E_{max} \sim 0.20$ eV and a minimum for the μ site; their cluster layer dependence is depicted in Figure 4.32. Thus, the C_2H_2 's are hypothesized to first rotate (independently) from their orientation after the dehydrogenation step, *i.e.*, $\Delta\phi_C = -21.1^\circ$ from the di- σ site (see Figure 4.24), to the μ site, at an energy cost of $\Delta E \sim 0.11$ eV, which is less than the C_2H_4 rotational barrier, $E_a^{expl} = 0.30$ eV, in its thermally activated decomposition. The H_2 molecules are then assumed to dissociatively chemisorb as H atoms in the threefold sites of the Ni lattice, as occurs in H_2 adsorption on Ni(111) [151], to yield the final decomposition products, acetylene and coadsorbed hydrogen. The presence of H's in the threefold bridging sites of the Ni lattice obstructs C_2H_2 adsorption in the threefold di- σ/π and μ/π sites.

b. $\text{Ni}_{72}[2\text{C}_2\text{H}_2+3\text{H}_2]$: Simultaneous C_2H_2 Rotation and H_2 Dissociation

As an alternative scheme to the final decomposition products, the two components of the system were not treated independently, *i.e.*, the coordinate variables of both the C_2H_2 and physisorbed H_2 molecules were optimized as functions of the rotation angle, $\Delta\phi_C(-)$.

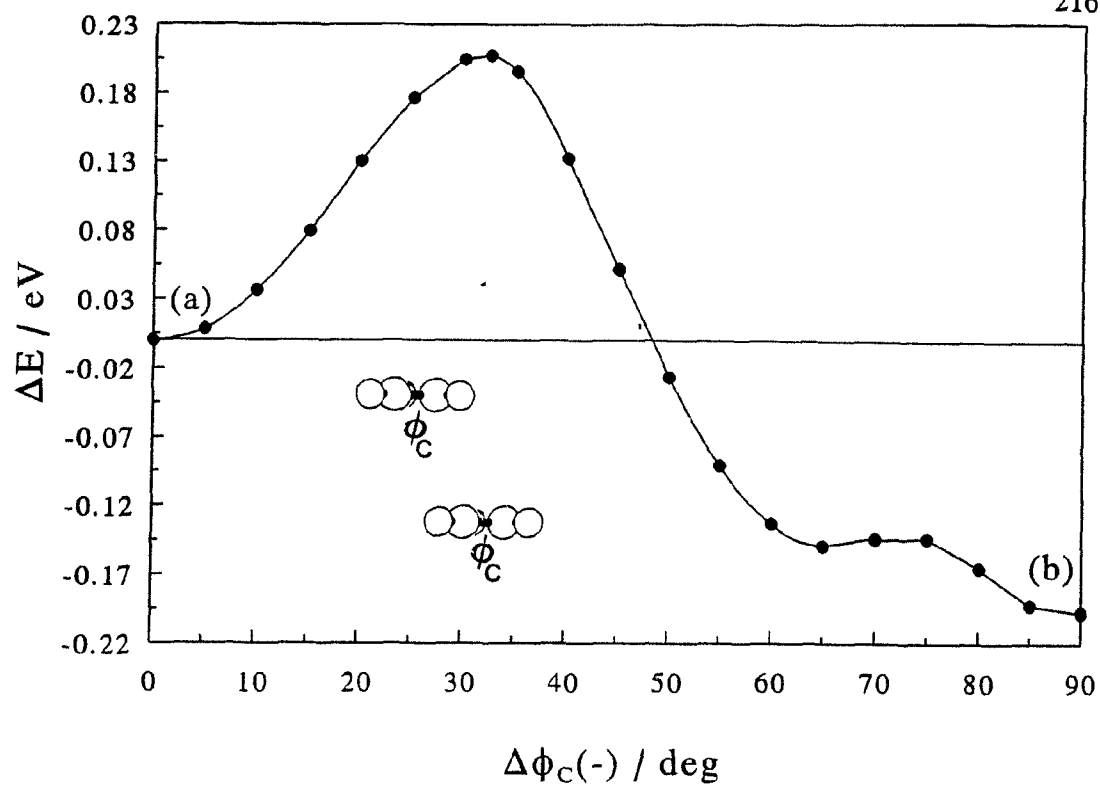
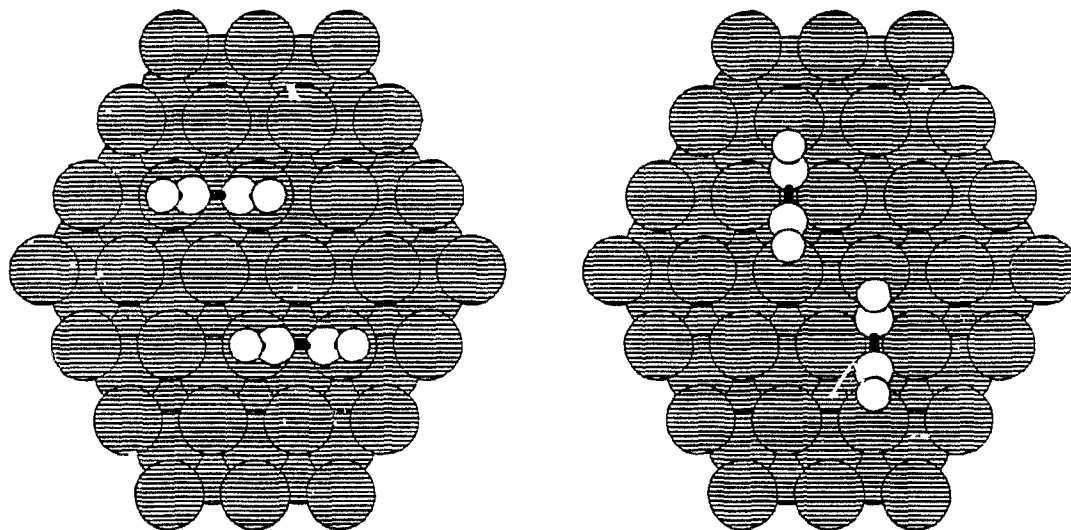
(a) $\Delta\phi_C = 0.0^\circ$ (di- σ site)(b) $\Delta\phi_C = -90.0^\circ$ (μ site)

Figure 4.31 Counterclockwise acetylene rotation for $\text{Ni}_{72}(\text{C}_2\text{H}_2)_2$: ΔE as a function of $\Delta\phi_C$ (-), with optimized structures shown for (a) $\Delta\phi_C = 0.0^\circ$ (di- σ site) and (b) $\Delta\phi_C = -90.0^\circ$ (μ site).

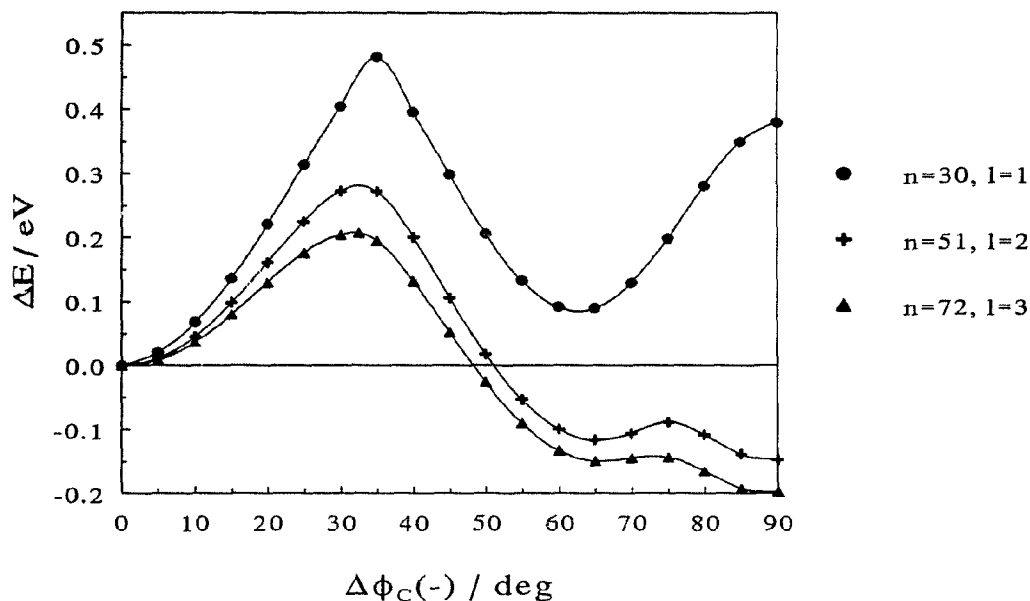


Figure 4.32 Cluster layer dependence of counterclockwise C_2H_2 rotation from the di- σ to μ sites, illustrated in Figure 4.31, for $\text{Ni}_n(\text{C}_2\text{H}_2)_2$, $n = 30, 51$, and 72 ($l = 1 \rightarrow 3$): ΔE as a function of $\Delta\phi_C(-)$.

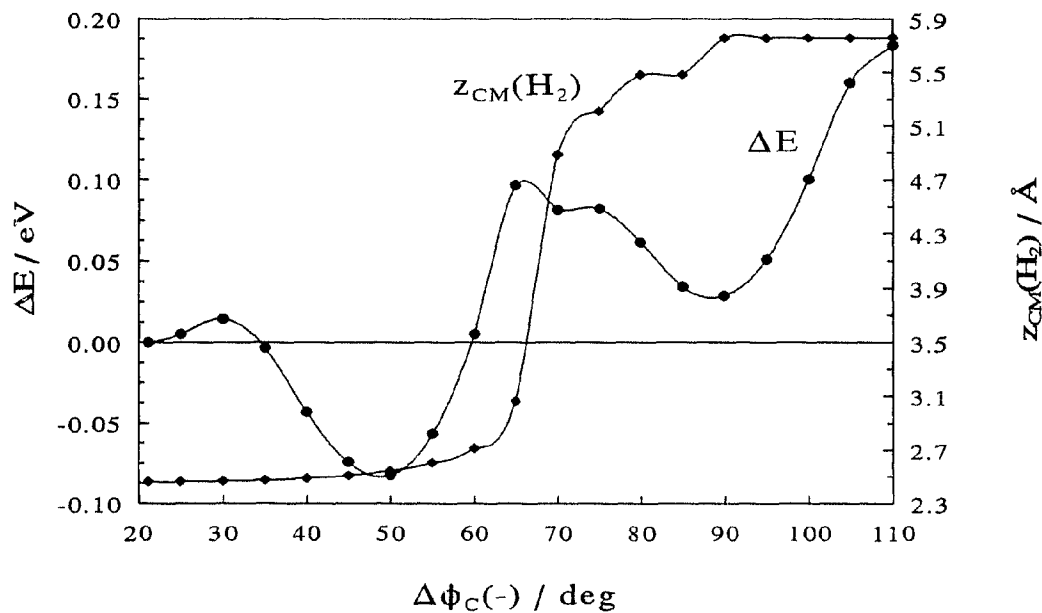


Figure 4.33 Simultaneous counterclockwise C_2H_2 rotation and H_2 optimization following C_2H_4 dehydrogenation of $\text{Ni}_{72}(\text{C}_2\text{H}_4)_2\text{H}_2$ to $\text{Ni}_{72}[2\text{C}_2\text{H}_2+3\text{H}_2]$ from $\Delta\phi_C = -20.0^\circ$ with respect to the di- σ site, *i.e.*, the approximate system configuration of Figure 4.24 (b) following the tunnelling step.

Figure 4.33 shows the results of this calculation for the intermediate decomposition products, $\text{Ni}_{72}[\text{2C}_2\text{H}_2 + 3\text{H}_2]$, from $\Delta\phi_{\text{C}} = -21.1^\circ$, the approximate $\text{Ni}_{72}(\text{C}_2\text{H}_4)_2\text{H}_2$ system configuration, after the tunnelling step, *i.e.*, the orientation of Figure 4.24 (b). Evidently, the H_2 molecule rises off the surface to a height of $z_{\text{CM}}(\text{H}_2) \sim 5.75 \text{ \AA}$ as the C_2H_2 's rotate, effectively decoupling the H_2 from both the C_2H_2 's and the Ni substrate. Optimizing both components together shifts the rotational barrier separating the di- σ and μ sites to $\Delta\phi_{\text{C}} = -65.0^\circ$ from the $[\bar{1}\bar{1}2]$ direction. As the energy cost, again $\sim 0.1 \text{ eV}$, to rotate from $\Delta\phi_{\text{C}} = -21.1^\circ$ to the local minimum at $\Delta\phi_{\text{C}} = -90.0^\circ$ is less than $E_{\text{a}}(\text{C}_2\text{H}_4)$, surmounting this barrier is achievable at the decomposition temperature. The minimum at $\Delta\phi_{\text{C}} = -50.0^\circ$, while deeper than the one at $\Delta\phi_{\text{C}} = -90.0^\circ$, may be escaped by thermal fluctuations, as the well depth is less than $E_{\text{a}}(\text{C}_2\text{H}_4)$. Once the C_2H_2 's have rotated to the μ binding site, perhaps only transiently, the physisorbed H_2 's can readily dissociate to H atoms which chemisorb in the vacant Ni threefold sites. As the calculations of the next section will demonstrate, with the H's thus positioned, the most stable C_2H_2 configuration is then slightly skewed from alignment with the μ site.

c. $\text{Ni}_{72}(\text{C}_2\text{H}_2)_2\text{H}_4$: H_2 Dissociation Followed by C_2H_2 Rotation

Assuming the dissociative chemisorption of isolated H_2 on Ni(111) [151] pertains to the H_2 decomposition intermediate, a $\text{Ni}_{72}(\text{C}_2\text{H}_2)_2\text{H}_4$ system was adopted, whereby the four H's were fixed in their experimental binding, or threefold bridging sites, and the geometries of the two C_2H_2 's were optimized as a function of $\Delta\phi_{\text{C}}(-)$; see Figure 4.34.

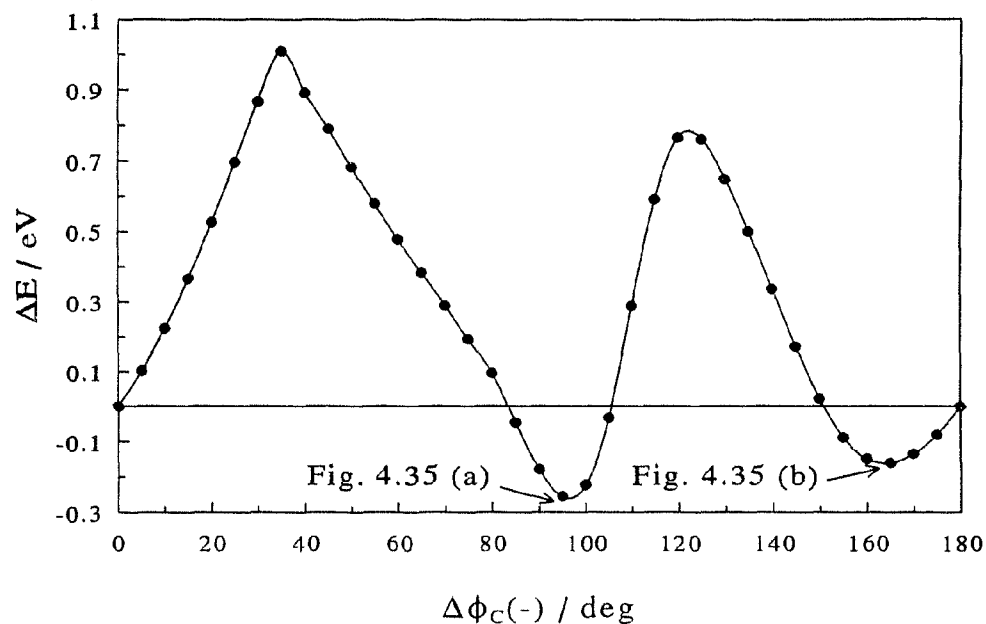
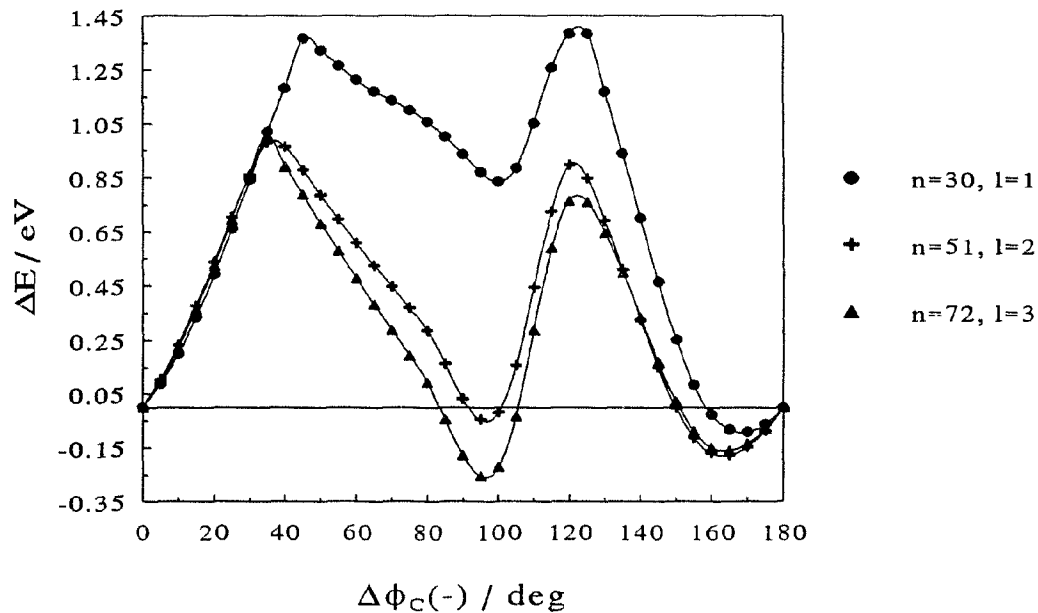
(a) $n = 72, \ell = 3$ (b) $n = 30, 51, \text{ and } 72, \ell = 1 \rightarrow 3$ 

Figure 4.34 Counterclockwise C_2H_2 rotation followed by H_2 dissociation after C_2H_4 dehydrogenation of $Ni_n(C_2H_4)_2$ to $Ni_n(C_2H_2)_2H_4$ for (a) $n = 72; \ell = 3$ and (b) $n = 30, 51, \text{ and } 72; \ell = 1 \rightarrow 3$. Figure 4.35 shows the geometries optimized nearby the two local minima at $\Delta\phi_C = -95.0^\circ$ and -165.0° .

Minima occur at $\Delta\phi_C = -95.0^\circ$ and -165.0° , *i.e.*, angles of -5.0° and 15.0° from the μ and di- σ sites, respectively, with the former more stable by ~ 0.09 eV, in reasonable accord with the LEED results, which estimate a $\sim 10^\circ$ counterclockwise (-) rotation of the C–C axis from alignment with the μ site. The high rotational barrier, ~ 1.0 eV, suggests that the acetylenes first rotate followed by H_2 dissociation, as postulated in Sect. 4.A.3.a, and not vice versa. With the extra H's fixed in the threefold sites, the C_2H_2 's optimize from the μ and di- σ adsorption sites with their C–C axes rotated -5.5° from the $[\bar{1}\bar{1}2]$ and 15.0° from the $[\bar{1}10]$ directions, respectively, corroborating the results obtained by parametrizing $\Delta\phi_C$. The corresponding geometries are illustrated in Figure 4.35, while Table 4.9 lists relevant structural parameters. The conformational similarity between " $Ni_2(C_2H_2)H_2$ " of the $Ni_{72}(C_2H_2)_2H_4$ system and staggered C_2H_6 , transparent if each C of C_2H_2 is viewed as having electron density directed towards a Ni and one of the eliminated H's, is suggestive of sp^3 hybridization, consistent with both the predicted $\Delta r(C-C) = 0.30$ Å and $sp^{2.5}$ hybridization of the *trans*-twisted C_2H_2 in the μ site, as well as the experimental C_2H_2 geometry. The possibility of coadsorbed H contaminants in the experimental conditions perhaps reconciles the apparent discrepancy between the computed and observed C_2H_2 structure and preferred adsorption site.

(a) $\Delta\phi_C = -5.5^\circ$ from the μ site

(b) $\Delta\phi_C = 15.0^\circ$ from the di- σ site

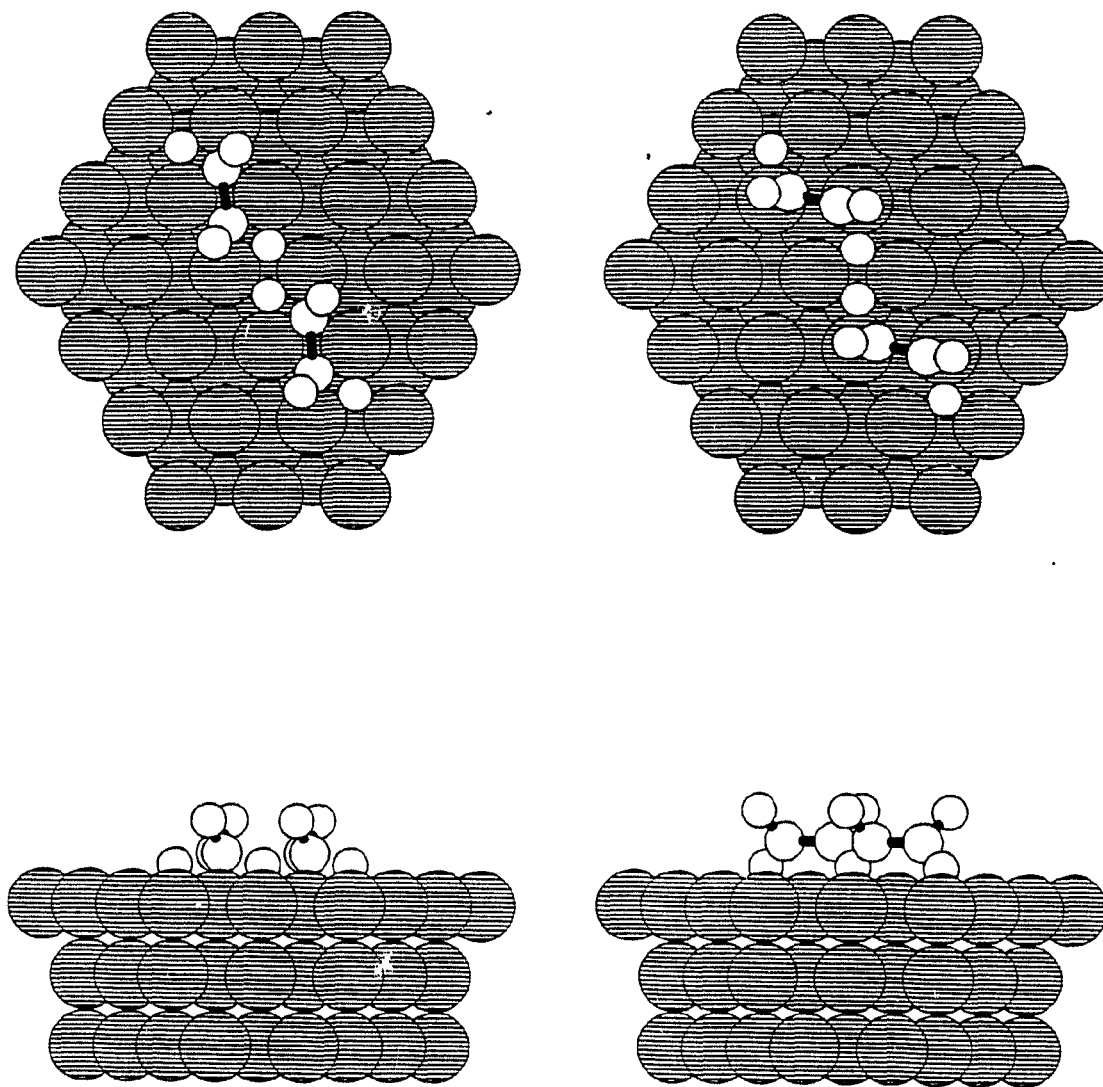


Figure 4.35 Adsorption sites of the final decomposition products, C_2H_2 and coadsorbed H, for $Ni_{72}(C_2H_2)_2H_4$: optimized C_2H_2 geometries with (a) $\Delta\phi_C = -5.5^\circ$ from the μ site, stabler by $\Delta E = 0.09$ eV than (b) $\Delta\phi_C = 15.0^\circ$ from the di- σ site. Two perspectives are shown: view down the surface normal and edge-on parallel to the surface plane.

Table 4.9 Optimized Adsorption Parameters^a for the Ni_n(C₂H₂)₂H₄ Model Systems: $n = 30, 51, 72$; $\ell = 1, 2, 3$

ℓ	$\Delta\phi_{\text{C}}(-)^{\text{b}}$ / deg	$\Delta r(\text{C}-\text{C})^{\text{c}}$ / Å	$\Delta r(\text{C}-\text{H})^{\text{c}}$ / Å	$z(\text{C})^{\text{d}}$ / Å	$\theta_{\text{CCH}}^{\text{e,f}}$ / deg	$\phi^{\text{e,f}}$ / deg
di-σ/di-π (fourfold bridging or μ)						
1	99.3 (9.3)	0.29 ($sp^{2.49}$)	0.00	1.554	64.0	68.0, -68.0
2	95.6 (5.6)	0.28 ($sp^{2.46}$)	-0.02	1.502	63.3	63.7, -63.7
3	95.5 (5.5)	0.30 ($sp^{2.51}$)	-0.02	1.493	64.0	64.7, -64.7
di-σ (twofold aligned bridging)						
1	167.4 (77.4)	0.16 ($sp^{1.93}$)	0.00	1.876	50.8	77.0, -77.0
2	166.7 (76.7)	0.16 ($sp^{1.94}$)	0.00	1.874	51.9	76.4, -76.4
3	165.0 (75.0)	0.16 ($sp^{1.94}$)	0.00	1.868	51.7	77.5, -77.5

^a See structures in Figure 4.35 for the $n = 72$ cluster and *cf.* planar C₂H₂ fragment produced by dehydrogenation step, as depicted in Figure 4.24 (b), left at $\Delta\phi_{\text{C}} = -21.1^\circ$ from the $[\bar{1}\bar{1}2]$ direction, with $\Delta r(\text{C}-\text{C}) = 0.10$ Å, $\Delta r(\text{C}-\text{H}) = 0.01$ Å, and $z(\text{C}) = 1.822$ Å, as documented in Table 4.7

^b Counterclockwise rotation of C-C bond axis from $[\bar{1}\bar{1}2]$ ($[\bar{1}10]$) direction

^{c-f} See footnotes to Table 4.3

4. Cluster Spin-Configuration Dependence of Dehydrogenation Mechanism Results

Following the mode of the analysis given in Chapter 3 (Sect. 3.B.1.d) on the dependence of the adsorption study results on the cluster spin configuration, the proposed dehydrogenation mechanism is analogously scrutinized. Figure 4.36 (a) depicts the cluster spin dependence for the $\text{Ni}_{72}(\text{C}_2\text{H}_4)_2\text{H}_2$ system of the critical configurations as a function of rotation about ϕ_C and shortening of $r(\text{H}-\text{H})$, *i.e.*, $\Delta\phi_C = 0.0^\circ$ and 16.0° and $\Delta r(\text{H}-\text{H}) = 0.640 \text{ \AA}$ and 1.000 \AA . Evidently, the differences in the relative energies, $\Delta E = E(\text{high spin}) - E(\text{low spin})$, are roughly constant for the system configurations as the number of unpaired electrons, s , in the cluster model is varied. Plotted in Figure 4.36 (b), the $r(\text{C}-\text{C})$ values are unaffected by the cluster spin configuration over the range examined. Similarly, the critical configurations for the $\text{Ni}_{72}(\text{C}_2\text{H}_2)_2$ and $\text{Ni}_{72}(\text{C}_2\text{H}_2)_2\text{H}_2$ systems, shown in Figure 4.37 as a function of s , maintain roughly the same differences in ΔE , with the $r(\text{C}-\text{C})$'s varying slightly but insignificantly. These results confirm that the qualitative conclusions of the proposed dehydrogenation mechanism are unaffected by the cluster spin convention, which addresses one potential ambiguity of the theoretical method.

5. Dehydrogenation Mechanism in the Atop Adsorption Site

The same dehydrogenation mechanism was tested for a $\text{Ni}_{37}(\text{C}_2\text{H}_4)_2\text{H}_2$ model system with the C_2H_4 's adsorbed in the alternative, atop site, which, in the adsorption study,

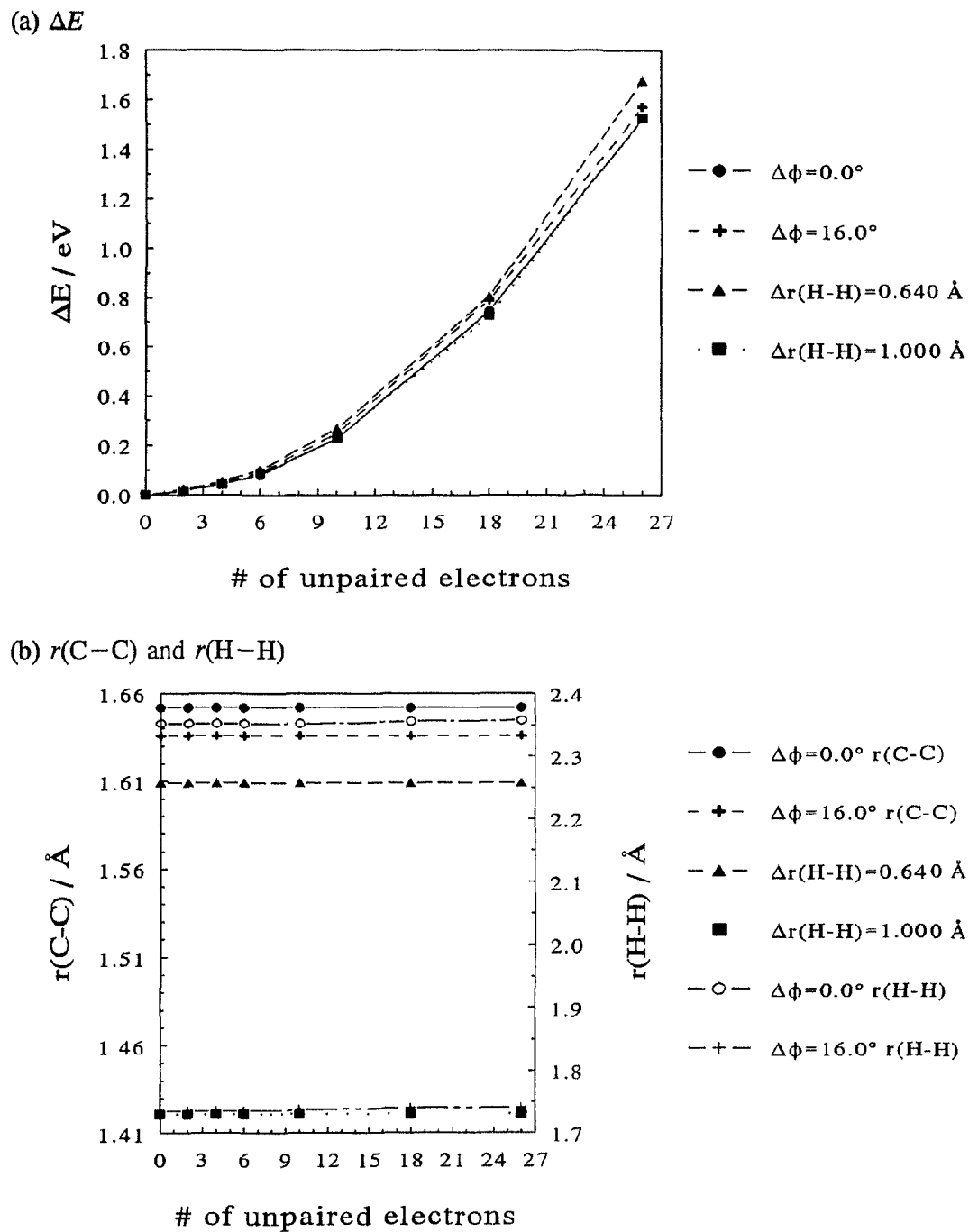


Figure 4.36 Cluster spin-configuration dependence of the critical configurations in the dehydrogenation mechanism for $\text{Ni}_{72}(\text{C}_2\text{H}_4)_2\text{H}_2$, $\Delta\phi_{\text{C}} = 0.0^\circ$ and 16.0° and $\Delta r(\text{H}-\text{H}) = 0.640$ and 1.000 \AA : (a) ΔE and (b) $r(\text{C}-\text{C})$ and $r(\text{H}-\text{H})$ as functions of the number of unpaired electrons, s .

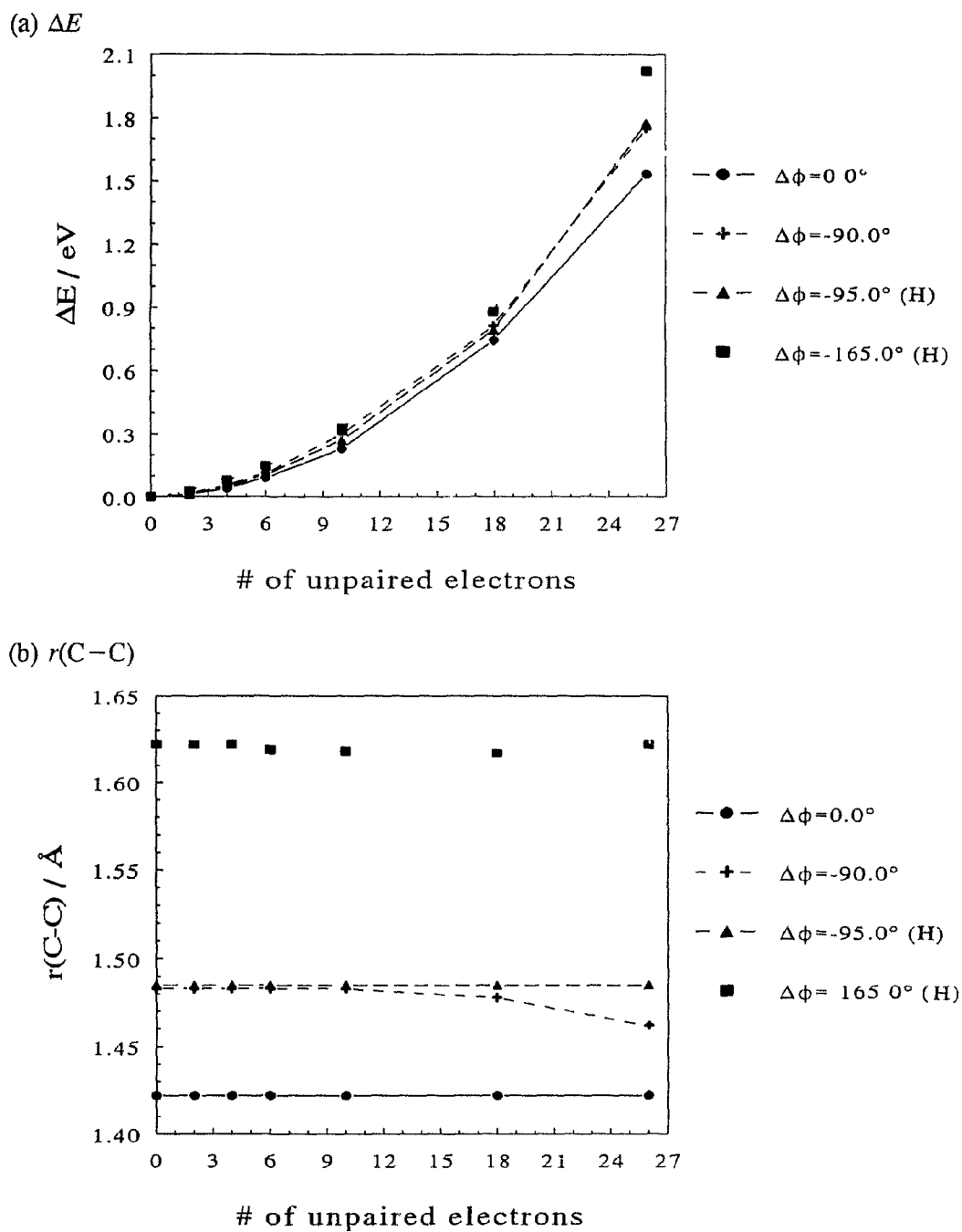


Figure 4.37 Cluster spin-configuration dependence of critical configurations in the adsorption study of the decomposition products for $\text{Ni}_{72}(\text{C}_2\text{H}_2)_2$ ($\Delta\phi_c = 0.0^\circ$ and -90.0°) and $\text{Ni}_{72}(\text{C}_2\text{H}_2)_2\text{H}_4$ ($\Delta\phi_c = -95.0^\circ$ and -165.0°): (a) ΔE and (b) $r(\text{C}-\text{C})$ as functions of s .

gave comparable binding energies to the di- σ -bonded species (see Tables 4.1 and 4.5). As shown in Figure 4.38, concerted rotation of the π -bonded C_2H_4 's about ϕ_C similarly yields a minimum in the intermolecular H-H separation distance, with $r_{min}(H-H) = 1.664 \text{ \AA}$, at an energetic cost of 0.451 eV and a rotation angle of $\Delta\phi_C = 21.0^\circ$, the latter primarily a function of the relative placement of the two C_2H_4 's in a (2×2) overlayer structure. The absence of a concomitant maximum in the relative energy curve, as was observed for di- σ -bonded C_2H_4 (*cf.* Figure 4.22), is attributed to a different bonding interaction, stemming from the altered position of the C_2H_4 's, and hence the C-H bonds, with respect to the surface Ni atoms. While rotation of the di- σ -bonded C_2H_4 's activates a pair of C-H bonds by their interactions with adjacent Ni atoms, rotation of the π -bonded species places a pair of C-H bonds above a single Ni atom, leading to a C-H...M interaction less favourable for C-H bond activation. Parametric shortening of $r(H-H)$ gives the ΔE curve displayed in Figure 4.39. The qualitative correspondence between this curve and that for the reactant di- σ -bonded C_2H_4 's (Figure 4.24) strongly suggests that this decomposition step depends solely on the H-H separation, as expected for a tunnelling mechanism, while the energy barrier of $\Delta E_{max} = 2.300 \text{ eV}$ at $r(H-H) = 1.064 \text{ \AA}$ contrasts with $\Delta E_{max} = 1.674 \text{ eV}$ at $r(H-H) = 1.107 \text{ \AA}$ for di- σ -bonded C_2H_4 on the $n = 30$, $\ell = 1$ cluster (see Table 4.7). The calculated tunnelling parameters, listed in Table 4.8 on p. 199, reveal a tunnelling probability of $P^{WKB} = 7.30 \times 10^{-9}$, one or two orders of magnitude (depending upon the cluster) smaller than that for the di- σ -bonded C_2H_4 's. As well, the calculated $E_a(C_2D_4)$ of 0.91 eV compares less favourably

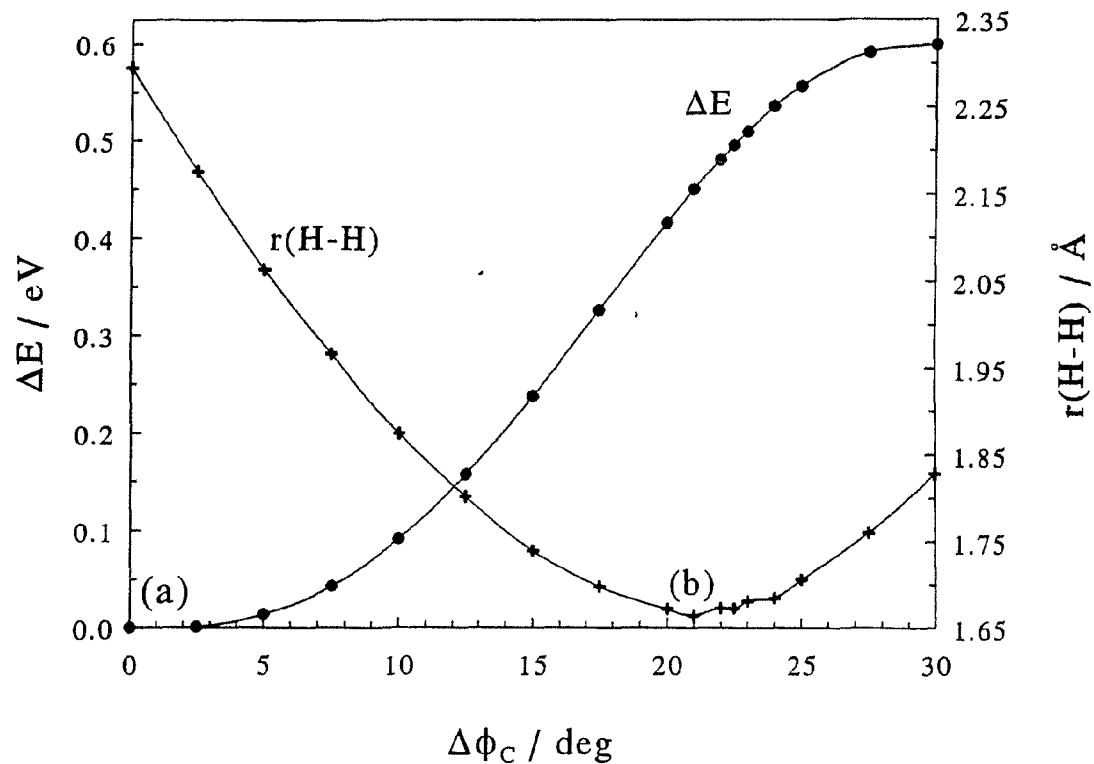
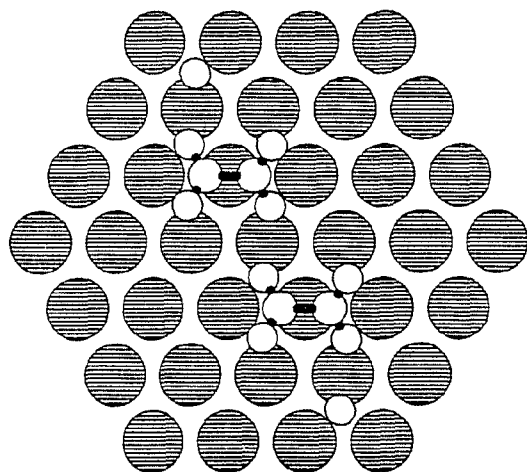
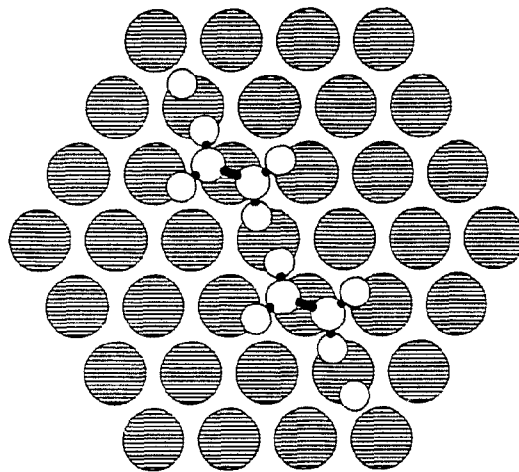
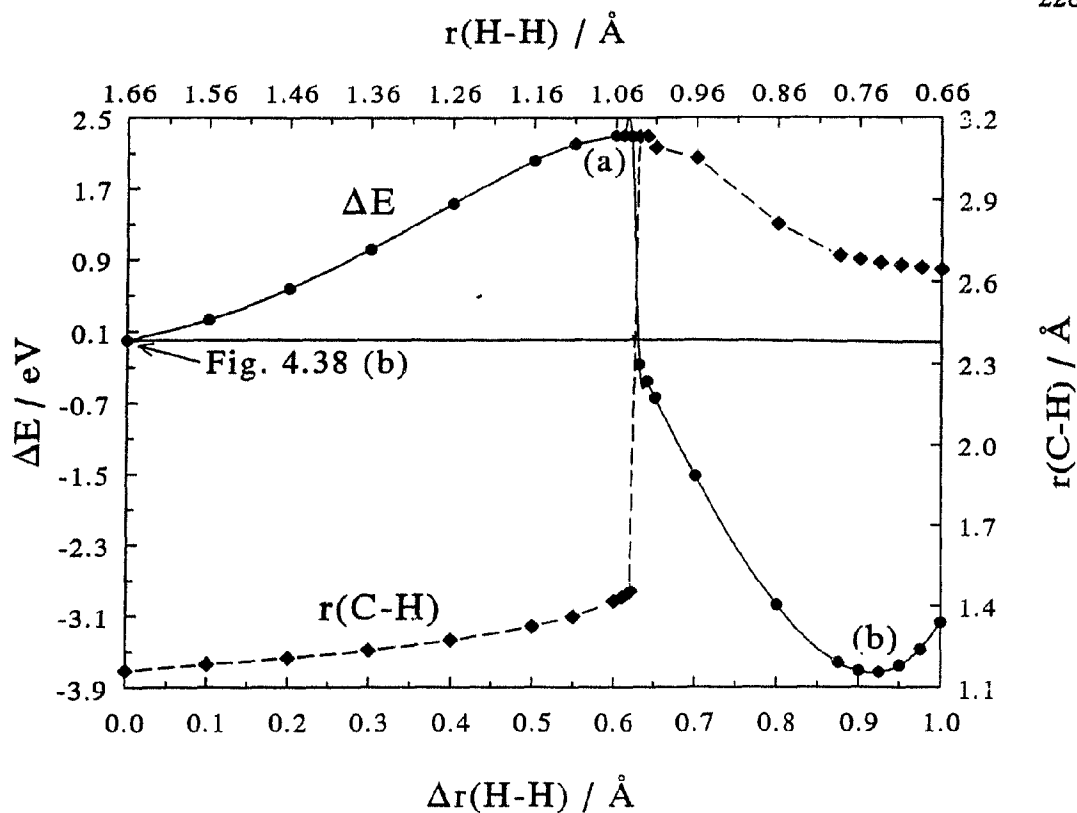
(a) $\Delta\phi_C = 0.0^\circ$ (b) $\Delta\phi_C = 21.0^\circ$ 

Figure 4.38 Initial rotation in the dehydrogenation mechanism for π -bonded C_2H_4 in the atop site of the $\text{Ni}_{37}(\text{C}_2\text{H}_4)_2\text{H}_2$ model system: ΔE and $r(\text{H-H})$ as functions of $\Delta\phi_C$, with optimized structures shown for (a) $\Delta\phi_C = 0.0^\circ$ and (b) $\Delta\phi_C = 21.0^\circ$.



(a) $\Delta r(\text{H}-\text{H}) = 0.600 \text{ \AA}$

(b) $\Delta r(\text{H}-\text{H}) = 0.925 \text{ \AA}$

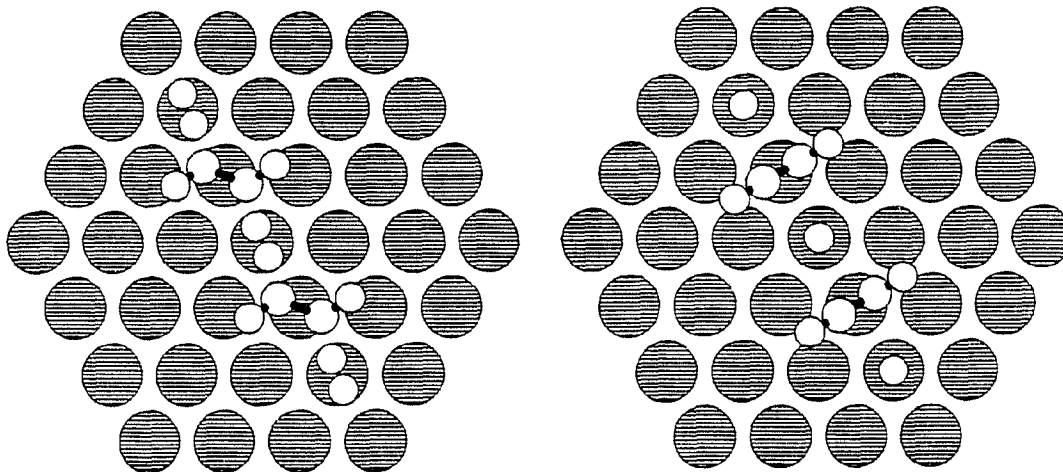


Figure 4.39 Concerted dehydrogenation step for rotated, π -bonded C_2H_4 of $\text{Ni}_{37}(\text{C}_2\text{H}_4)_2\text{H}_2$: ΔE and *trans* $r(\text{C}-\text{H})$ as functions $\Delta r(\text{H}-\text{H})$, with optimized structures shown for (a) $\Delta r(\text{H}-\text{H}) = 0.600 \text{ \AA}$ and (b) $\Delta r(\text{H}-\text{H}) = 0.925 \text{ \AA}$.

with $E_a^{exp}(C_2D_4) = (0.53/0.57 \pm 0.02)$ eV, while the predicted upper bound on the C_2H_4 decomposition temperature for thermal activation to be slower than tunnelling, $T_c = 279$ K, is compatible with $T_{exp} \sim 200$ K. The absence of a rotational barrier and corresponding critical configuration along $\Delta\phi_C$ for the π -bonded C_2H_4 's corroborates the assignment of the twofold aligned bridging site as the preferred adsorption site, as only dehydrogenation of the di- σ -bonded C_2H_4 's yields qualitative behaviour in the computed results consistent with the experimental observations.

6. Comparative Study of the Pt(111)/ C_2H_4 System

Selected calculations were repeated for ethylene adsorption and dehydrogenation on the Pt(111) system, modelled as a low-spin cluster of Pt atoms fixed in their ideal bulk lattice positions ($a_{Pt} = 3.92 \text{ \AA} > a_{Ni} = 3.52 \text{ \AA}$ [120], $nn_{Pt} = 2.77 \text{ \AA}$, $nnn_{Pt} = 4.80 \text{ \AA}$, and $d_{Pt} = 2.26 \text{ \AA}$). As discussed in Chapter 2 (Sect. 2.A.2.b), ethylene on Pt(111) has been shown experimentally to adsorb non-dissociatively at low temperatures ($T \sim 140 - 260$ K) in the di- σ bonding configuration [29], as on Ni(111), but to dehydrogenate at room temperature to the ethylidyne species, $\equiv C-CH_3$ [53]. Hence, a comparative study of the proposed dehydrogenation mechanism was undertaken on Pt(111) to probe, computationally, the uniqueness of the Ni(111) surface towards ethylene dehydrogenation, and thereby verify that the theoretical method can discriminate between dissimilar surfaces. The different results on the Pt(111) cluster model can be ascribed

to the larger Pt lattice constant and hence greater separation distance between adjacent ethylene molecules in the (2×2) overlayer structure, which effectively prohibits a concerted mechanism.

a. Adsorption Sites

Optimization of a single ethylene molecule, in the various adsorption sites considered for the Ni study, on Pt_n clusters, $n = 4$, $\ell = 1$ and $n = 14$, 22, and 30, corresponding to, 1, 2, and 3, respectively, yielded the site stability ordering: di- $\sigma > \mu/\pi$ (hcp) $\sim \mu/\pi$ (fcc) $> \pi > \text{di-}\sigma/\pi$ (hcp) $\sim \text{di-}\sigma/\pi$ (fcc) $> \mu$. The results confirm the assignment of the di- σ configuration as the most favoured site, as was obtained in a previous ASSED-MO study [5]. Two molecules, optimized in a (2×2) overlayer structure on a one-layered Pt₃₀ cluster, maintained the relative site preferences.

b. Dehydrogenation Mechanism

Rotation of two di- σ -bonded C₂H₄'s about ϕ_C produces $r_{min}(\text{H-H}) = 2.235 \text{ \AA}$ at $\Delta\phi_C = 22.5^\circ$, as shown in Figure 4.40 (a), the greater $r_{min}(\text{H-H})$ value over that obtained on the Ni surface being due to the larger a_{Pt} . Despite the absence of a maximum in the ΔE curve at this angle, the parametric shortening of $r(\text{H-H})$ was investigated, nonetheless. The resulting potential energy curve, shown in Figure 4.40 (b), is qualitatively analogous to that obtained on the Ni clusters for both the di- σ and π configurations, again reflecting

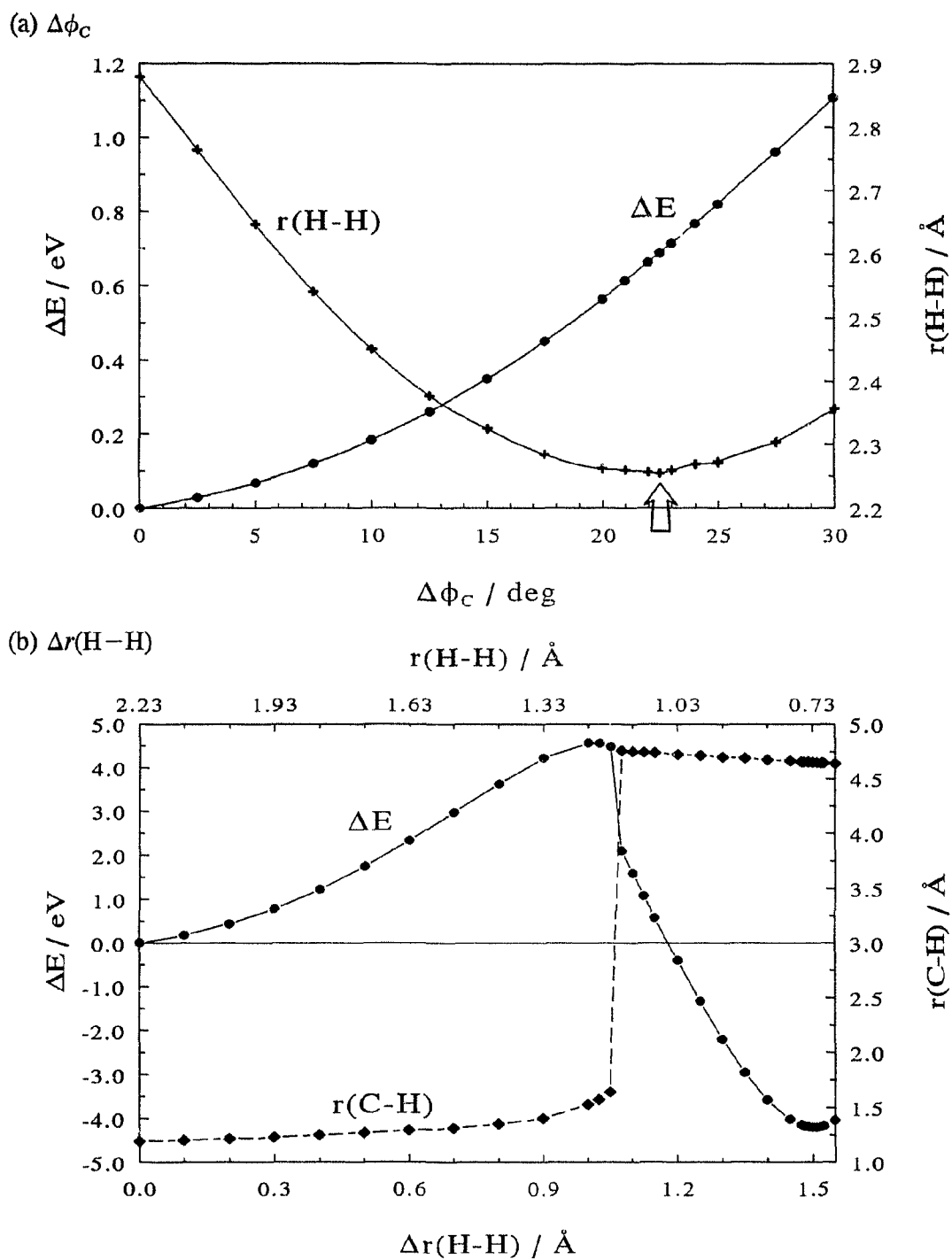


Figure 4.40 Dehydrogenation mechanism for di- σ -bonded C_2H_4 of a $\text{Pt}_{30}(\text{C}_2\text{H}_4)_2\text{H}_2$ model of the $\text{Pt}(111)/\text{C}_2\text{H}_4$ system: (a) ΔE and $r(\text{H-H})$ as functions of $\Delta\phi_C$ and (b) ΔE and *trans* $r(\text{C-H})$ as functions $\Delta r(\text{H-H})$.

the fact that the behaviour observed along this reaction coordinate is basically a function of the H–H internuclear distance. Note, however, the approximate twofold increase in the height and width of the barrier as compared with the Ni results, due to the greater initial $r(\text{H}-\text{H})$. The consequently much reduced H tunnelling probability rationalizes why the same dehydrogenation mechanism does not occur on the Pt(111) surface, corroborating the recent TPRS finding that tunnelling plays an insignificant role in the C–H bond activation of C_2H_4 on Pt(111) [62]. This Pt study, along with the comparative study on Ni for the atop site, suggest the following electronic and structural factors, peculiar to di- σ -bonded C_2H_4 on the Ni(111) surface, that favour the proposed concerted dehydrogenation mechanism: the initial rotational barrier and corresponding critical configuration yielding $r_{\min}(\text{H}-\text{H})$ arise from a favourable C–H...M interaction, which requires a particular C–H bond orientation with respect to the surface and strong overlap between CH σ and σ^* orbitals and unfilled and filled metal d orbitals near ϵ_F ; while the tunnelling step hinges on the Ni lattice constant, which permits the H's to come in close enough proximity to interact with each other following C_2H_4 rotation.

B. DFT Calculations

For comparison, density-functional calculations were initiated for ethylene and acetylene adsorbed on the simplest Ni_n cluster model, $n = 4$, in the same five binding sites considered in the ASED-MO study. Additionally, single-point energy calculations were performed along pertinent coordinate variable changes to approximate the potential

energy curves obtained using the two theoretical methods, DFT and ASED-MO theory. The DFT analysis, however, remains incomplete, and hence the results, while suggestive, are inconclusive.

1. Geometry Optimization of Adsorbate Molecules on a Ni₄ Cluster

a. Ethylene: Ni₄(C₂H₄)

Density-functional results of ethylene adsorbed on Ni₄ are tabulated in Table 4.10, along with the analogous ASED-MO values. An optimized geometry with integral occupation numbers was accomplished for C₂H₄, under a C₂ symmetry constraint, in the di- σ configuration, while for the other sites, geometries with fractional occupation could only be obtained. In agreement with the experimental observation [29], a bond order intermediate between one and two is deduced, as with the ASED-MO method, by comparison of the calculated C–C bond distances for the isolated hydrocarbons, C₂H_x, $x = 2, 4,$ and $6,$ listed in Table 3.2 and plotted in Figure 3.1. The –CH₂ groups counter-rotate slightly in the optimized C₂ symmetry structure, as deduced on the Ni(111) surface [8], though the symmetry of the adsorption site on the Ni₄ cluster should preclude such a distortion.

Table 4.10 Optimized DFT and ASED-MO Adsorption Parameters for $\text{Ni}_4(\text{C}_2\text{H}_4)$ and $\text{Ni}_4(\text{C}_2\text{H}_2)$

Theory	$E_B^a /$ eV	$\Delta r(\text{C}-\text{C})^b /$ Å	$\Delta r(\text{C}-\text{H})^c /$ Å	$z(\text{C})^d /$ Å	$\theta_{\text{CCH}}^{e,f} /$ deg	$\phi^{e,f} /$ deg
C_2H_4						
di-σ:						
DFT	1.732	0.14 ($sp^{2.83}$)	0.01	1.772	115.5, 114.7	25.3, 21.8
ASED-MO	2.038	0.16 ($sp^{2.63}$)	-0.02	1.977	114.2	19.4
C_2H_2						
di-σ:						
DFT	2.788	0.15 ($sp^{2.22}$)	0.03	1.661	128.9	90.0
ASED-MO	1.483	0.10 ($sp^{1.64}$)	0.00	1.897	137.9	90.0
di-σ/π:						
DFT	4.212	0.18 ($sp^{2.38}$)	0.03	1.346	129.5	73.1
ASED-MO	1.574	0.11 ($sp^{1.69}$)	-0.01	1.679	139.3	64.7

^a E_B calculated as in Tables 4.1 and 4.3, *i.e.*, with respect to the isolated-component energies

^b C–C and C–H bond stretches with respect to optimized values of $r(\text{C}-\text{C}) = 1.498$ and 1.324 Å (ASED-MO) and $r(\text{C}-\text{C}) = 1.498$ and 1.324 Å (DFT) for isolated molecules of C_2H_4 and C_2H_2 , respectively

^{c-f} As defined previously in Tables 4.1 and 4.3

b. Acetylene: $\text{Ni}_4(\text{C}_2\text{H}_2)$

SCF-converged results for acetylene from the geometry optimization procedure with integral occupation numbers were obtained only for the di- σ and di- σ/π configurations; for the other sites, only optimized geometries with fractional occupations could be achieved. The di- σ - and di- σ/π -bonded C_2H_2 structural parameters and binding energies, optimized under a C_1 symmetry constraint but yielding complexes of C_{2v} and C_s symmetry, respectively, are listed in Table 4.10, where they are compared with the corresponding ASED-MO results. Note that the C–C bond stretches of $\Delta r(\text{C}–\text{C}) = 0.16$ and 0.18 \AA for the di- σ and di- σ/π sites imply a bond order between one and two, in contrast to the ASED-MO prediction of a bond order between two and three, but in agreement with the experimental conclusion [33,39].

2. Single-Point Energy Calculations along Various Coordinate Variable Changes**a. Elongation of C–H bonds, $\Delta r(\text{C}–\text{H})$**

Single-point energy calculations were performed for both an isolated C_2H_4 molecule and the $\text{Ni}_4(\text{C}_2\text{H}_4)$ system as a function of C–H bond stretch, $\Delta r(\text{C}–\text{H})$, with the C_2H_4 geometry fixed at the optimized di- σ configuration in the latter case. Elongation of both one and a pair of *trans* C–H bonds was investigated and the results compared with both the non-optimized and optimized results obtained using the ASED-MO method. As

Figure 4.41 (a) shows, for an isolated C_2H_4 molecule, the relative energy curves are remarkably similar, both qualitatively and quantitatively; also, the energetic requirement for rupturing two C–H bonds is essentially twice that of breaking one. The relative energy curves for C_2H_4 adsorbed on the Ni_4 cluster deviate, as depicted in Figure 4.41 (b), signifying a divergent treatment of the transition-metal centres by the two methods.

b. Rotation about $\Delta\phi_C$

Rotation about an axis through the centre of the C–C bond and perpendicular to the plane of the cluster, $\Delta\phi_C$, was investigated for both C_2H_4 and C_2H_2 adsorbed on the Ni_4 cluster, with the adsorbate structural parameters fixed at their optimized values in the di- σ sites. Figure 4.42 shows the radical difference between the relative energy changes calculated by the two methods, especially for the $Ni_4(C_2H_2)$ system. Even within the DFT calculations, differences, though slight in comparison with the scale of the graphs, were observed in the calculated energies, depending upon which algorithm was used to enhance SCF convergence, dmixing and smearing, $\alpha + \omega$, or levelshifting, ϵ_{SHIFT} . The truncated DFT curve in the former case reflects its restricted utility in achieving SCF convergence with integral occupation numbers.

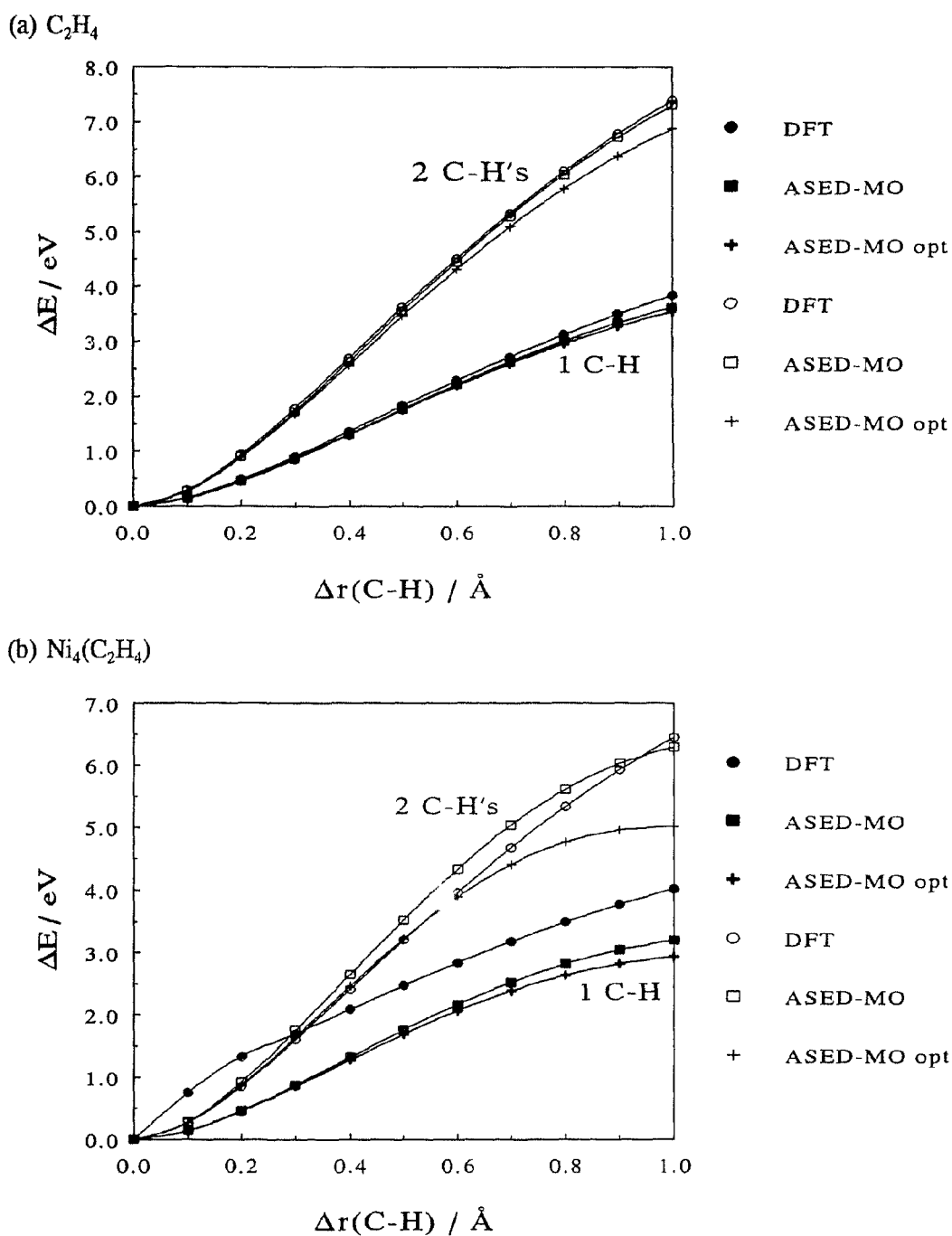


Figure 4.41 Comparative density-functional theoretical (DFT) single-point and ASED-MO single-point and optimized (opt) ΔE 's as functions of single (1 C-H) and concerted *trans* (2 C-H's) C-H bond stretch, $\Delta r(C-H)$, for (a) isolated C_2H_4 and (b) C_2H_4 di- σ -bonded on Ni_4 .

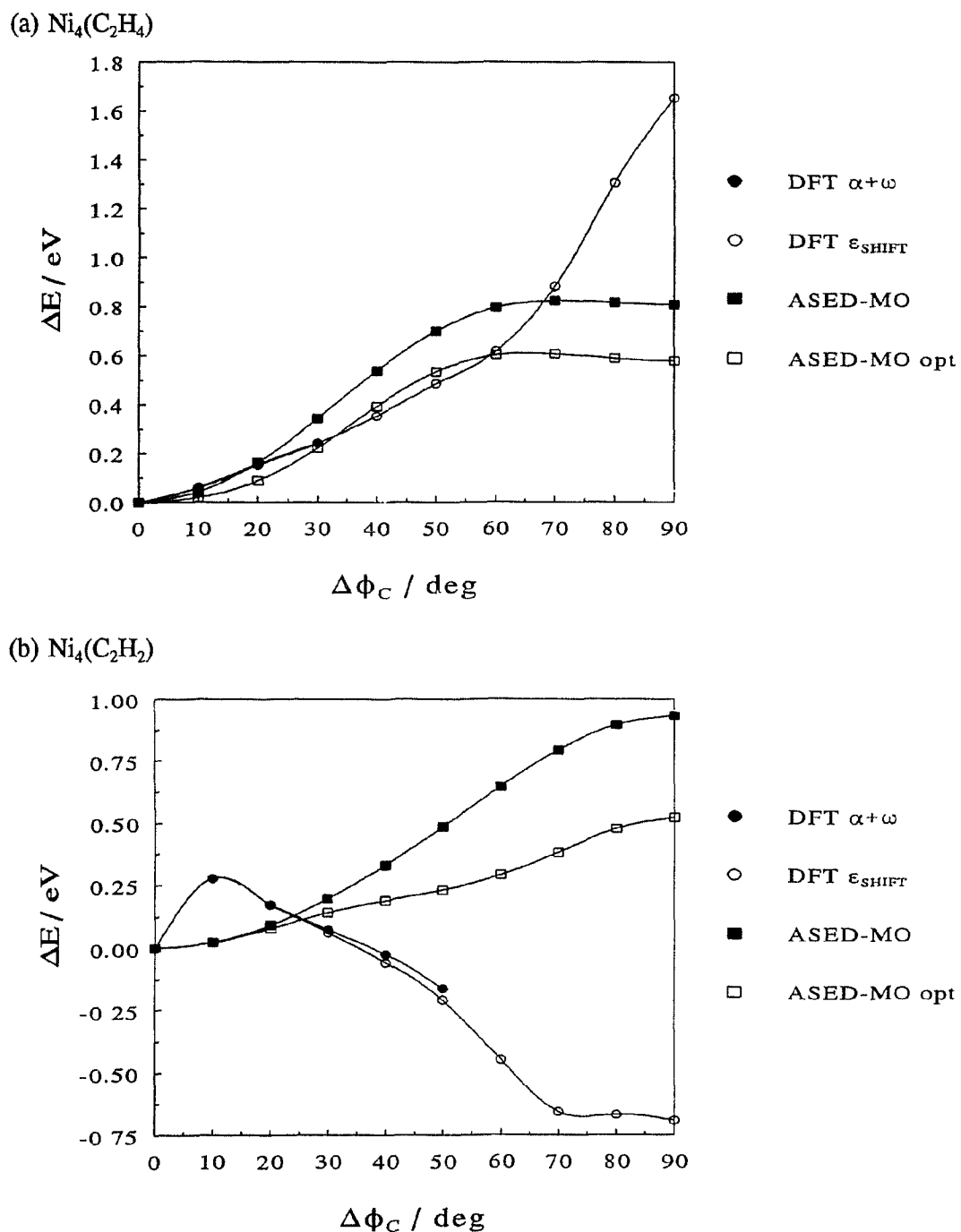


Figure 4.42 Comparative DFT and ASED-MO ΔE 's as functions of $\Delta\phi_C$ for (a) C_2H_4 and (b) C_2H_2 di- σ -bonded on Ni_4 . The DFT single-point ΔE 's implemented two techniques to enhance SCF convergence, damping plus smearing ($\alpha + \omega$) and level shifting (ϵ_{SHIFT}), while ASED-MO single-point and optimized (opt) ΔE 's were computed.

3. Conclusions Based on the DFT Study

The preceding comparative calculations demonstrate that the results stemming from the DFT and ASED-MO methods may deviate. While the ASED-MO results suffer from a one-electron, semiempirical approach, they are based on a more realistic representation of the surface than would be attainable with a more exact *ab initio* method or density-functional theory. The DFT calculations, even using the crudest possible cluster model, were problematic and ultimately abandoned because of convergence difficulties and numerical instabilities. Perhaps with an alternative program, such as Gaussian 92/DFT [152], DGauss [153], or DMol [154], or dedicated time on a much faster computer, examination of the Ni(111)/C₂H₄ system would become tractable at the DFT level, but, at present, only the ASED-MO study was feasible within the computational resources available. However, the cluster analysis of the ASED-MO results, expected to be method-independent within the MO framework, suggests a comparable DFT study, with the minimal, requisite geometry optimizations of two adsorbate molecules on symmetric cluster models broad enough to accommodate both, would be inaccessible, without a simplified treatment of the numerous electrons introduced by the Ni atoms and a solution to the convergence problems associated with the many closely spaced energy levels straddling the ϵ_F .

Chapter 5: CONCLUSIONS

Both C_2H_4 and C_2H_2 adsorption and the mechanism of C_2H_4 dehydrogenation to C_2H_2 on the Ni(111) surface were surveyed with the semiempirical, modified extended-Hückel, ASED-MO method, augmented with preliminary DFT calculations, and coupled with a nonequilibrium, statistical mechanical, master-equation description. While the theoretical and experimental binding sites differ somewhat, the predictions stemming from the analysis of the decomposition reaction are consistent, both internally and with experiment. The proposed fragmentation scheme rationalizing the measured second-order kinetics advances as the slow step, thermally activated rotation of two adjacent C_2H_4 's, while concerted tunnelling of the interior, intermolecular H's from the resultant, transient bimolecular complex yields the decomposition intermediates, physisorbed H_2 and C_2H_2 .

The Ni surface was modelled by rigid, bulk clusters, symmetric about either the centre of a unit cell or an individual atom of the extended lattice, and ranged from $n = 4$ to 80 total atoms, $d = 4$ to 24 top-layer atoms, and $\ell = 1$ to 4 layers. A systematic cluster dependence analysis of the ASED-MO results on n , d , and ℓ revealed that the adsorption site stability ordering and optimized structures for C_2H_2 and C_2H_4 , as well as relative energy and geometrical variable changes along some coordinate parameter, were sensitive to the $(n_1/n_2/.../n_\ell)$ cluster model, the former more than the latter in both cases. Moderately symmetric, three-layered clusters, with a surface layer composed of the chemisorption-bonded Ni's and their nearest neighbours, yielded qualitatively and quantitatively converged results.

In the ASED-MO adsorption study, geometry optimizations of one and two adsorbate molecules, the pairs in their (2×2) LEED structures, yielded the following relative bonding configuration (site) stabilities on the largest, (24/16/16/24) and (30/21/21) cluster models, respectively: for C₂H₄, di-σ (twofold aligned bridging) > π (onefold atop) > μ/π (threefold bridging/atop — hcp) ~ μ/π (fcc) > di-σ/di-π (fourfold bridging or μ) > di-σ/π (threefold triangular or Δ — hcp) ~ di-σ/π (fcc); while for C₂H₂, di-σ/π (hcp) ≥ di-σ/π (fcc) > μ/π (hcp) ≥ μ/π (fcc) ≥ di-σ/di-π > di-σ > π. Both the gas-phase, planar C₂H₄ and linear C₂H₂ species distort upon adsorption, in all sites, with the C–H bonds bent away from the surface and C–C bond lengths elongated, yielding estimated states of hybridization of $sp^{2.3} - sp^{2.6}$ and $sp^{1.1} - sp^{2.0}$, respectively. The C₂H₄ bond order, near- sp^3 hybridization, and di-σ bonding configuration deduced from EELS and PD experiments have been reproduced, while the C₂H₂ bond order and $sp^{2.5} - sp^{2.8}$ hybridization ranges, $r(C-C)$ value, and di-σ/di-π configuration determined from EELS, LEED, and PD studies are incompatible with those calculated, though the di-σ/π configuration was favoured by a LEED/EELS analysis.

In the Ni_n(C₂H₄)₂H₂ model systems implemented in the ASED-MO analysis of the dehydrogenation mechanism, where $n = 30, 51,$ and 72 , corresponding to $\ell = 1 \rightarrow 3$, the two extra H's simulate those of neighbouring C₂H₄'s in the extended overlayer by the constraint of symmetrical equivalence to *trans* H's on the two central C₂H₄'s. Clockwise ethylene rotation from the di-σ site, $\Delta\phi_C$, about an axis through the centre of the C–C bond and perpendicular to the surface, yields a barrier of $\Delta E_{max}^{rot} = 0.38$ eV, comparable to $E_a^{exp} = (0.30/0.31 \pm 0.02)$ eV. Along this initial reaction coordinate, all other

geometrical variables were optimized, under the constraints of equivalent C_2H_4 molecules and local C_2 symmetry. As the C_2H_4 's rotate, the $-CH_2$ groups counter-rotate; their coupled motion, corresponding effectively to a molecular twist about the C–C axis, transports a pair of *trans* H's on each C_2H_4 towards both the surface and an adjacent intermolecular H. The consequential, decreased H–H distance produces a minimum, $r_{min}(H-H) = 1.74 \text{ \AA}$, at $\Delta\phi_C = 16^\circ$, the configuration which yielded ΔE_{max}^{rot} .

As a second reaction coordinate, $r(H-H)$ was parametrically shortened, with all other geometrical variables optimized, subject to the constraints of equivalent C_2H_4 's and local C_1 symmetry, from the bimolecular critical configuration at $r_{min}(H-H)$. A maximum in ΔE as a function of (negative) $\Delta r(H-H)$ signals the rupture of two *trans* C–H bonds per molecule. The minimum in ΔE at $r(H-H) = 0.74 \text{ \AA}$ corresponds structurally to a physisorbed H_2 molecule oriented perpendicularly above the surface, with which it interacts weakly in a chemisorption precursor state. The other decomposition products, planar C_2H_2 fragments, remain slightly rotated from the di- σ site. For computational economy, *i.e.*, to reduce the number of degrees of freedom in the optimizations, the two C_2H_4 's were rotated in unison and a pair of *trans* H's on each C_2H_4 was eliminated in concert, while the elementary steps in the dehydrogenation mechanism likely involve independent rotation of the C_2H_4 's and concerted tunnelling of only the two interior H's.

The calculated WKB transmission coefficient for intermolecular H's to tunnel through the potential barrier along the parametric decrease of $r(H-H)$, $P^{WKB} \approx 10^{-8}$, exceeds by two orders of magnitude the computed Boltzmann probability of thermal activation, $P_{t.a.} \approx 10^{-10}$, in the decomposition reaction of two C_2H_4 's. Thus, for not too disparate

prefactors, the tunnelling process is fast compared with the rate of thermally activated rotation, *i.e.*, $r_t = v_t P^{WKB} > r_{t.a.} = v_{t.a.} P_{t.a.}$ for $v_t \sim v_{t.a.}$. The configuration of critical H–H separation prior to tunnelling and H₂ formation, $r(\text{H–H}) = 1.74 \text{ \AA}$, is proffered as the intermediate, bimolecular complex necessitated by the measured second-order kinetics. The tunnelling mechanism was validated by prediction and comparison with the experimental values of both E_a for C₂D₄ dehydrogenation and the C₂H₄ decomposition temperature for thermal activation to be the slower rate. By explicit solution of the master equations describing the reaction, the effective rate is deduced as the product of a Boltzmann probability, $e^{-E_a/k_b T}$, which reflects the relative number of attempts by the system, in thermal quasi-equilibrium, having the requisite minimum energy, E_a , and the tunnelling rate, as the effective attempt frequency, v_{eff} , which governs the dynamics. The correlation between $v_{eff} = r_t = v_t P^{WKB} \approx 10^4 - 10^6 \text{ s}^{-1}$ ($v_t = 10^{12} - 10^{14} \text{ s}^{-1}$) and $v_{exp} = 10^{6 \pm 2} \text{ s}^{-1}$ strongly supports the concerted tunnelling mechanism.

The decomposition intermediates, C₂H₂ fragments and molecular H₂, rearrange to the final products, atomic H chemisorbed in the threefold sites and C₂H₂'s slightly rotated from the μ site, or $[\bar{1}\bar{1}2]$ direction of the Ni lattice. As revealed by a Ni₇₂(C₂H₂)₂ model system, rotation of the C₂H₂'s about ϕ_C from their orientation after the dehydrogenation step to the μ site is relatively facile. Assuming the dissociative chemisorption of H₂ on Ni(111) pertains to the H₂ intermediate, a Ni₇₂(C₂H₂)₂H₄ system was adopted, whereby the four H's were fixed in their experimental, threefold bridging sites and the geometries of the two C₂H₂'s optimized as a function of $\Delta\phi_C$. Minima at angles of -5° and 15° from the μ and di- σ sites, respectively, the former being more stable, harmonize with the

LEED pattern of the C_2H_4 decomposition products, which identifies the C_2H_2 C's in neighbouring threefold sites, with the C–C axis rotated counterclockwise by $\phi_C \sim 10^\circ$ relative from the μ site. The predicted $\Delta r(C-C) = 0.30 \text{ \AA}$ and $sp^{2.5}$ hybridization of the *trans*-twisted, di- σ /di- π -bonded C_2H_2 are consistent with the experimental C_2H_2 structure.

The peculiarity of the Ni(111) surface towards C_2H_4 reactivity, particularly its second-order dehydrogenation to C_2H_2 , is attributed to the concerted elimination, via tunnelling, of intermolecular H's. The Ni lattice constant and electronic configuration play pivotal roles in the tunnelling step, as demonstrated by calculations for π -bonded C_2H_4 on Ni(111), with its altered adsorbate bonding and position relative to the Ni lattice, and di- σ -bonded C_2H_4 on Pt(111), with its larger crystal lattice constant and hence expanded substrate-atom spacing. Rotation of the di- σ -bonded C_2H_4 's on Ni(111) activates a pair of C–H bonds, which interact with adjacent Ni atoms in two three-centred, two-electron bonds, whereas rotation of the π -bonded species positions a pair of C–H bonds above a single Ni atom, leading to a C–H...M interaction less conducive to C–H bond cleavage, and the larger lattice spacing of Pt(111) precludes the requisite proximity of the intermolecular H's following C_2H_4 rotation.

The density-functional calculations were restricted to the study of single adsorbate molecules on the primitive Ni_4 surface model. The many near-degeneracies close to ϵ_F of the Ni cluster frequently led to oscillatory behaviour in the SCF iterations, rendering convergence with integral occupation numbers difficult. Optimized structures and single-point energies along $\Delta r(C-H)$ and $\Delta\phi_C$ for di- σ -bonded C_2H_4 and C_2H_2 , plus the di- σ/π configuration of C_2H_2 , on Ni_4 were compared with ASED-MO results.

Chapter 6: FURTHER INVESTIGATIONS

Potential extensions of the C_2H_4 dehydrogenation study on Ni(111) include: relaxation of symmetry constraints in the ASED-MO calculations; refinement of either the theory, with DFT, or model, with the ASED-band method; and further elucidation, theoretically and experimentally, of probable reaction intermediates. The analysis also may be expanded to encompass the decomposition mechanisms, of both C_2H_4 and C_2H_2 , on other related systems, *e.g.*, the (111) face of Pd, as well as the (110) and (100) Ni, Pd, and Pt surfaces, to be correlated and contrasted with the present Ni(111) results. Alternatively, the reverse reaction, catalytic hydrogenation of alkynes to alkenes, or alkenes to alkanes, could be explored for a monosubstituted acetylene or ethylene to rationalize the stereospecific *syn* addition. Extensive mapping of the potential energy hypersurface, via computer simulations, *e.g.*, would encourage a fully microscopic, statistical mechanical description of the decomposition kinetics to be entertained.

Alluded to in the discussion of the ASED-MO results, the stepwise versus concerted, *trans* C–H bond cleavage in the dehydrogenation step of the two C_2H_4 's is being examined to verify the proposed linear chain mechanism. Concerted rupture of both pairs of *trans* C–H bonds, while smearing out some of the microscopic details of the mechanism by summing over the elementary steps of the reaction, is much more tractable computationally. The additional degrees of freedom introduced by relaxing the concerted C–H bond cleavage symmetry constraint complicate, and hence protract the calculations considerably. The postulated, physical, stepwise pathway can only now be probed with

the gained mechanistic insight accrued through the concerted elimination analysis. The potential energy curve computed for the net exothermic reaction of C_2H_4 directly to C_2H_2 was essential, however, to the prediction of tunnelling probabilities, as only an overall experimental activation energy for the decomposition was available.

Also being explored is the dehydrogenation of C_2H_2 , the experimental study of which has shown the reaction pathways — and hence, order of the kinetics, dehydrogenation intermediates, and relative ease of C–C and C–H bond scission — to be complicated functions of the adsorbate coverage and temperature. At this initial stage of the analysis, the C_2H_2 's are hypothesized to undergo facile, first-order C–C and C–H bond rupture at low coverages and elevated temperatures to produce methylidyne, $\equiv CH$, and ethynyl, $-C\equiv CH$, which dehydrogenates to C_2 or dissociates to CH and C, the eventual, sole surface species. At higher coverages, the second-order C_2H_4 dehydrogenation mechanism likely pertains for C_2H_2 , *i.e.*, concerted tunnelling, from a bimolecular complex of two rotated C_2H_2 's, of the (interior) intermolecular H's to yield physisorbed H_2 , which subsequently dissociates, and CCH, which decomposes to give a C overlayer. The conversion to and subsequent decomposition of ethylidyne, $-C\equiv CH_3$, at high coverages is also worth probing.

The preliminary density-functional treatment should be continued by completing the geometry optimizations of C_2H_4 and C_2H_2 adsorbed in the various binding sites on the Ni_4 cluster. By comparing with the ASED-MO Ni_4 results, a rough correspondence can then be established between the structural parameters optimized with the two theoretical methods, if they differ systematically. Though discouraged by the existing, comparative

Ni_4 study, an enlarged cluster might vindicate such a correspondence. To this end, the ASED-MO optimized structure for C_2H_4 di- σ -bonded on the Ni_{14} cluster should be adjusted and used as the input configuration in a DFT geometry optimization, if computer resources permit; otherwise, its validity must simply be assumed. Single-point energies of two di- σ -bonded C_2H_4 's on the Ni_{30} cluster, with two additional H's mimicking those of neighbouring C_2H_4 's, can then be computed. By assuming the qualitative invariance to the theoretical method of the potential curves computed with the ASED-MO theory, DFT barrier heights can be deduced from single-point energy calculations of the critical configurations along the reaction coordinates in the dehydrogenation mechanism. The full potential curve, however, is required to predict the tunnelling probabilities.

Divergent to the cluster approach, the superlattice method exploits the two-dimensional, periodic repetition of the adsorption-complex unit cell in applying conventional, surface band-structure techniques to chemisorption problems. Calculations employing the tight-binding band version of the ASED theory for extended systems [155,88] have been initiated to deduce, by comparison with the ASED-MO results, the domain of validity of the cluster model approach, particularly, effects of cluster truncation and lateral adsorbate interactions, for the specific chemical system studied. However, for sub-saturation coverages, the artificial repetition of the unit cell includes more atoms than in reality are affected by the screened adsorbate potential; this problem can be negated somewhat by incorporating enough substrate atoms in the adsorption cell so that adsorbates in neighbouring cells are well-separated. The dehydrogenation mechanism can be investigated with a periodically repeated unit cell containing one C_2H_4 ,

which would react with itself, or two reacting C_2H_4 's, treated as a supermolecule.

As suggestions for future experimental work, H isotopic substitution and exchange reactions and further kinetic studies (via, *e.g.*, TPD, TPSSIMS, and time-resolved HREELS and LID) to identify possible decomposition intermediates in the stepwise dehydrogenation of both C_2H_4 and C_2H_2 , as well as their dependences on adsorbate coverage and temperature, would be valuable in unravelling the microscopic details of the elementary steps in the respective decomposition reactions. A clear asset would be unambiguous structural determinations of both the reactant and product hydrocarbons, with precise C–C and C–H bond distances and orientations relative to the surface. As well, the direct observation of the H decomposition product positions relative to the surface and confirmation of the presence or absence of H contaminants and their potential influences on the hydrocarbon bonding configurations would be welcome. In particular, C_2H_2 adsorption is conjectured to be affected by coadsorbed H: from the adsorption and decomposition studies, C_2H_2 in the rigorous absence of H contaminants is postulated to adsorb in the di- σ/π configuration or Δ binding site, whereas in the presence of chemisorbed H, the di- σ /di- π configuration or μ site is preferred, with the molecule distorting from a planar to a *trans*-twisted species upon the change in adsorption site.

An obvious enhancement of the present research would be to explore decomposition mechanisms on other related surfaces, drawing parallels and divergences to gain insight into the geometric and electronic factors which distinguish their reactivities. Already stressed is the unique ethylene reactivity and second-order decomposition kinetics on the Ni(111) surface, as compared with other fcc surfaces, especially Pt(111) and Pd(111),

which yield the ethynylidyne species, and Ni(100) and Ni(110), which produce vinyl and ethynyl intermediates, respectively. An intimate knowledge of the reaction mechanisms on a particular crystal face for related metals, *e.g.*, the (111) face of the isoelectronic Ni, Pd, and Pt series, and on the varying crystal faces of a single metal, *e.g.*, the (111), (100), and (110) faces of Ni, is prerequisite to tackling salient questions in surface chemistry and physics.

Alternatively desirable is an understanding, at the microscopic level, of the reverse reaction, catalytic hydrogenation of alkynes to alkenes, which proceeds stereospecifically to yield the *syn* addition products, *i.e.*, both H's liberated by the dissociative chemisorption of H₂ add only to the less-hindered side of the double bond. The microscopic reversibility of the elementary steps in the reaction implies that at least some of the steps in the hydrogenation and dehydrogenation reactions differ, as the proposed dehydrogenation mechanism would yield the *anti* elimination products of a substituted alkene. Such a comparative study would illuminate features of the molecular reaction dynamics and chemical reactivity of gas-surface systems, particularly those of fundamental interest in organic synthesis.

Computer simulations could further elucidate the microscopic, dynamical details of the reaction mechanism. By tracing the system's time evolution in phase space via integration of classical (or quantum) equations of motion, molecular dynamics (MD) trajectories yield both equilibrium statistical properties and dynamical information. MD simulations could enhance the adsorption study by sketching out a configurational energy map or clarify aspects of the mechanism by, *e.g.*, directly computing the dynamical

prefactor, which could then be inserted into the master equations arising in the tunnelling analysis. Alternatively, stochastic sampling of the configuration or phase space of the system through Monte Carlo techniques would refine the potential energy hypersurface employed in modelling the reaction dynamics. As well, computer simulations could verify whether the predictions based on quantum chemical calculations, rigorously applicable only at zero temperature, hold for finite temperatures. Thus, the simulations would nicely complement the existing theoretical and experimental work.

The most challenging and potentially fruitful extension of the present work would be to exploit the potential energy surface mapped out for the model heterogeneously catalyzed reaction of ethylene decomposition on Ni(111) to develop a microscopic description, within a nonequilibrium statistical mechanical formalism, of surface reactions involving molecular species. The understanding of time-dependent or dynamical elementary surface processes, such as adsorption, desorption, and diffusion, lags far behind that of static, *i.e.*, equilibrium properties for chemisorption systems, as well as that of physisorption dynamics. Hence, a rewarding direction of future investigation would be to formulate a microscopic theory for chemisorption kinetics, *i.e.*, surface reaction rates via master equations derived from a microscopic Hamiltonian, which allows for relaxation of, and energy transfer between the electronic, vibrational, and rotational degrees of freedom of the adsorbed molecular species and substrate, whereby transition probabilities are extracted in terms of microscopic variables only.

REFERENCES

1. See, *e.g.*, G.A. Somorjai, *Principles of Surface Chemistry*, (Prentice-Hall, Englewood Cliffs, N.J., 1972) and *Chemistry in Two Dimensions: Surfaces* (Cornell University Press, Ithaca, N.Y., 1981).
2. J. Silvestre and R. Hoffmann, *Langmuir* **1** (1985) 621-647.
3. J.C. Bertolini and J. Massardier, in *The Chemical Physics of Solid Surfaces and Heterogeneous Catalysis*, Vol. 3B, D.A. King and D.P. Woodruff, eds. (Elsevier, Amsterdam, 1984), pp. 107-136.
4. N. Sheppard, *Ann. Rev. Phys. Chem.* **39** (1988) 589-644 and B.J. Bandy, M.A. Chesters, D.I. James, G.S. McDougall, M.E. Pemble, and N. Sheppard, *Phil. Trans. R. Soc. Lond. A* **318** (1986) 141-161 review vibrational spectroscopic studies.
5. See, *e.g.*, A.B. Anderson and A.T. Hubbard, *Surf. Sci.* **99** (1980) 384-391 and D.B. Kang and A.B. Anderson, *Surf. Sci.* **155** (1985) 639-652.
6. J.E. Demuth and D.E. Eastman, *Phys. Rev. Lett.* **32** (1974) 1123-1127.
7. L. Hammer and K. Müller, *Prog. Surf. Sci.* **35** (1991) 103-111.
8. J.E. Demuth, H. Ibach, and S. Lehwald, *Phys. Rev. Lett.* **40** (1978) 1044-1047.
9. G. Casalone, M.G. Cattania, F. Merati, and M. Simonetta, *Surf. Sci.* **120** (1982) 171-178.
10. K. Heinz *et al.*, unpublished results.
11. L. Hammer, B. Dötsch, C. Harder and K. Müller, *Vacuum* **41** (1990) 121-125.
12. L. Hammer, B. Dötsch, F. Brandenstein, A. Fricke and K. Müller, *J. Electr. Spec. Rel. Phenom.* **54/55** (1990) 687-696.
13. R.B. Hall, S.J. Bares, A.M. DeSantolo, and F. Zaera, *Vac. Sci. Technol. A* **4** (1986) 1493-1498; F. Zaera and R.B. Hall, *Surf. Sci.* **180** (1987) 1-18.
14. S. Bao, Ph. Hofmann, K.-M. Schindler, V. Fritzsche, A.M. Bradshaw, D.P. Woodruff, C. Casado, and M.C. Asensio, *J. Phys.: Condens. Matter* **6** (1994) L93-L98.
15. See, *e.g.*, K. Christmann, *Introduction to Surface Physical Chemistry* (Springer-Verlag, New York, 1991), and references therein, for a synopsis of methods.

16. D.P. Woodruff, in *The Chemical Physics of Solid Surfaces and Heterogeneous Catalysis*, Vol. 1, D.A. King and D.P. Woodruff, eds. (Elsevier Science, Amsterdam, 1981) pp. 81-181.
17. E. Bauer, in *Interactions on Metal Surfaces*, Vol. 4, R. Gomer, ed. (Springer-Verlag, Berlin, 1975) pp. 225-274.
18. *Methods of Surface Characterization: Vibrational Spectroscopy of Molecules on Surfaces*, Vol. 1, J.T. Yates, Jr. and T.E. Madey, eds. (Plenum Press, New York, 1987).
19. R.F. Willis, A.A. Lucas, and G.D. Mahan, in *The Chemical Physics of Solid Surfaces and Heterogeneous Catalysis*, Vol. 2, D.A. King and D.P. Woodruff, eds. (Elsevier Science, Amsterdam, 1983) pp. 59-163.
20. A. Zangwill, *Physics at Surfaces* (Cambridge University Press, Cambridge, 1988) pp. 244-253.
21. E.W. Plummer, in *Topics in Applied Physics: Interactions on Metal Surfaces*, Vol. 4, R. Gomer, ed. (Springer-Verlag, Berlin, 1975) pp. 143-223.
22. D. Menzel, in *Topics in Applied Physics: Interactions on Metal Surfaces*, Vol. 4, R. Gomer, ed. (Springer-Verlag, Berlin, 1975) pp. 101-142.
23. H.J. Kreuzer and S.H. Payne, in *Dynamics of Gas-Surface Interactions*, C.T. Rettner and M.N.R. Ashfold, eds. (Royal Society of Chemistry, Cambridge, 1991) pp. 220-256.
24. N.W. Ashcroft and N.D. Mermin, *Solid State Physics* (Saunders College, Philadelphia, 1976) pp. 354-364.
25. L. Hammer, T. Hertlein, and K. Müller, *Surf. Sci.* **178** (1986) 693-703.
26. J.E. Demuth, *Surf. Sci.* **76** (1978) L603-L608.
27. M.G. Cattania, M. Simonetta, and M. Tescari, *Surf. Sci.* **82** (1979) L615-L619.
28. S. Lehwald and H. Ibach, *Surf. Sci.* **89** (1979) 425-445.
29. A.M. Baró, S. Lehwald, and H. Ibach, in *Proceedings of the Second International Conference on Vibrations at Surfaces*, Namur, Belgium, 1980, R. Candano, J.-M. Gilles, and A.A. Lucas, eds. (Plenum Press, New York, 1982), pp. 215-230.
30. T.E. Felter and W.H. Weinberg, *Surf. Sci.* **103** (1981) 265-287.

31. J.E. Demuth, *IBM J. Res. Develop.* **22** (1978) 265-276.
32. J.E. Demuth, *Surf. Sci.* **84** (1979) 315-328.
33. J.E. Demuth and H. Ibach, *Surf. Sci.* **85** (1979) 365-378.
34. J.E. Demuth and D.E. Eastman, *Phys. Rev. B* **13** (1976) 1523-1527.
35. R.G. Carr, T.K. Sham, and W.E. Eberhardt, *Chem. Phys. Lett.* **113** (1985) 63-66.
36. J.E. Demuth, *Surf. Sci.* **69** (1977) 365-384.
37. J.C. Bertolini and J. Rousseau, *Surf. Sci.* **83** (1979) 531-544.
38. H. Ibach and S. Lehwald, *J. Vac. Sci. Technol.* **18** (1981) 625-628.
39. S. Bao, Ph. Hofmann, K.-M. Schindler, V. Fritzsche, A.M. Bradshaw, D.P. Woodruff, C. Casado, and M.C. Asensio, *Surf. Sci.* **307** (1994) 722-727.
40. X.-Y. Zhu and J.M. White, *Surf. Sci.* **214** (1989) 240-256.
41. P. Klimesch and M. Henzler, *Surf. Sci.* **90** (1979) 57-64.
42. W. Hasse, H.-L. Günter, and M. Henzler, *Surf. Sci.* **126** (1983) 479-486.
43. A. Morgante, S. Modesti, M. Bertolo, P. Rudolf, and R. Rosei, *Surf. Sci.* **211/212** (1989) 829-836.
44. A. Jakob, M.Sc. thesis, Univ. Erlangen (1992).
45. J.E. Demuth and H. Ibach, *Surf. Sci.* **78** (1978) L238-L244.
46. H. Ibach and S. Lehwald, *J. Vac. Sci. Technol.* **15** (1978) 407-415.
47. P.C. Stair and G.A. Somorjai, *J. Chem. Phys.* **66** (1977) 2036-2044.
48. R.J. Koestner, J. Stöhr, J.L. Gland, and J.A. Horsley, *Chem. Phys. Lett.* **105** (1984) 332-335.
49. H. Ibach, H. Hopster, and B. Sexton, *Appl. Phys.* **14** (1977) 21-24.
50. L.L. Kesmodel, R.C. Baetzold, and G.A. Somorjai, *Surf. Sci.* **66** (1977) 299-320.
51. A.E. Morgan and G.A. Somorjai, *J. Chem. Phys.* **51** (1969) 3309-3320.

52. W.H. Weinberg, H.A. Deans, and R.P. Merrill, *Surf. Sci.* **41** (1974) 312-336.
53. L.L. Kesmodel, L.H. Dubois, and G.A. Somorjai, *Chem. Phys. Lett.* **56** (1978) 267-271; *J. Chem. Phys.* **70** (1979) 2180-2188.
54. P.C. Stair and G.A. Somorjai, *Chem. Phys. Lett.* **41** (1976) 391-393.
55. W.J. Lo, Y.W. Chung, L.L. Kesmodel, P.C. Stair, and G.A. Somorjai, *Solid State Commun.* **22** (1977) 335-337.
56. M.R. Albert, L.G. Sneddon, W. Eberhardt, F. Greuter, T. Gustafsson, and E.W. Plummer, *Surf. Sci.* **120** (1982) 19-37.
57. H. Steininger, H. Ibach, and S. Lehwald, *Surf. Sci.* **117** (1982) 685-698.
58. J.R. Creighton and J.M. White, *Surf. Sci.* **129** (1983) 327-335.
59. T.A. Land, T. Michley, R.J. Behm, J.C. Hemminger, and G. Comsa, *Appl. Phys. A* **53** (1991) 414-417.
60. U. Starke, A. Barbieri, N. Materer, M.A. Van Hove, and G.A. Somorjai, *Surf. Sci.* **286** (1993) 1-14.
61. K.M. Ogle, J.R. Creighton, S. Akhter, and J.M. White, *Surf. Sci.* **169** (1986) 246-266.
62. M. Yata and R.J. Madix, *Surf. Sci.* **328** (1995) 171-180.
63. J.A. Gates and L.L. Kesmodel, *Surf. Sci.* **120** (1982) L461-L467.
64. J.A. Gates and L.L. Kesmodel, *J. Chem. Phys.* **76** (1982) 4281-4286.
65. L.L. Kesmodel and J.A. Gates, *Surf. Sci.* **111** (1981) L747-L754; J.A. Gates and L.L. Kesmodel, *Surf. Sci.* **124** (1983) 68-86.
66. L.L. Kesmodel, G.D. Waddill, and J.A. Gates, *Surf. Sci.* **138** (1984) 464-474.
67. W.T. Tysoe, G.L. Nyberg, and R.M. Lambert, *Surf. Sci.* **135** (1983) 128-146.
68. T.M. Gentle and E.L. Muetterties, *J. Phys. Chem.* **87** (1983) 2469-2472.
69. W. Sesselmann, B. Woratschek, G. Ertl, and J. Küppers, *Surf. Sci.* **130** (1983) 245-258.
70. S. Lehwald, H. Ibach, and H. Steininger, *Surf. Sci.* **117** (1982) 342-351.

71. K. Horn, A.M. Bradshaw, and K. Jacobi, *J. Vac. Sci. Technol.* **15** (1978) 575-579.
72. F. Zaera, D.A. Fischer, R.G. Carr, and J.L. Gland, *J. Chem. Phys.* **89** (1988) 5335-5341.
73. F. Zaera and R.B. Hall, *J. Phys. Chem.* **91** (1987) 4318-1323.
74. J.E. Demuth, *Surf. Sci.* **93** (1980) 127-144.
75. N.J. DiNardo, J.E. Demuth, and Ph. Avouris, *J. Vac. Sci. Technol. A* **1** (1983) 1244-1245; *Phys. Rev. B* **27** (1983) 5832-5835.
76. G. Casalone, M.G. Cattania, M. Simonetta, and M. Tescari, *Surf. Sci.* **62** (1977) 321-325.
77. C.E. Anson, B.J. Bandy, M.A. Chesters, B. Keiller, I.A. Oxtan, and N. Sheppard, *J. Electron Spectrosc. Relat. Phenom.* **29** (1983) 315-316.
78. J.A. Stroschio, S.R. Bare, and W. Ho, *Surf. Sci.* **148** (1984) 499-525.
79. M. Weinelt, W. Huber, P. Zebisch, H.-P. Steinrück, M. Pabst, and N. Rösch, *Surf. Sci.* **271** (1992) 539-554.
80. M. Weinelt, W. Huber, P. Zebisch, H.-P. Steinrück, B. Reichert, U. Birkenheuer, and N. Rösch, *Phys. Rev. B* **46** (1992) 1675-1686.
81. B.J. Bandy, M.A. Chesters, M.E. Pemble, G.S. McDougall, and N. Sheppard, *Surf. Sci.* **139** (1984) 87-97.
82. N.H. March, *Electron Density Theory of Atoms and Molecules* (Academic Press, London, 1992) pp. 273-276.
83. See, e.g., I.N. Levine, *Quantum Chemistry* (Allyn and Bacon, Boston, 1983); D.A. McQuarrie, *Quantum Chemistry* (University Science Books, Mill Valley, CA, 1983); R.G. Parr, *Quantum Theory of Molecular Electronic Structure* (W.A. Benjamin, New York, 1963); and A. Streitwieser Jr., *Molecular Orbital Theory for Organic Chemists* (John Wiley & Sons, New York, 1961).
84. R. Hoffmann, *J. Chem. Phys.* **39** (1963) 1397-1412.
85. M. Wolfsberg and L. Helmholz, *J. Chem. Phys.* **20** (1952) 837-843.
86. A.B. Anderson and R. Hoffmann, *J. Chem. Phys.* **61** (1974) 4545-4559.

87. A.B. Anderson and R. Hoffmann, *J. Chem. Phys.* **60** (1974) 4271-4273; A.B. Anderson, *J. Chem. Phys.* **62** (1975) 1187-1188.
88. K. Nath and A.B. Anderson, *Phys. Rev. B* **41** (1990) 5652-5660.
89. A.B. Anderson and R.G. Parr, *J. Chem. Phys.* **53** (1970) 3375-3376.
90. R.P. Feynman, *Phys. Rev.* **56** (1939) 340-343.
91. B.M. Deb, *Rev. Mod. Phys.* **45** (1973) 22-43.
92. A.B. Anderson, *J. Chem. Phys.* **60** (1974) 2477-2479.
93. R.G. Parr and W. Yang, *Density-Functional Theory of Atoms and Molecules* (Oxford University Press, New York, 1989).
94. W. Kohn and P. Vashishta, in *Theory of the Inhomogeneous Electron Gas*, S. Lundqvist and N.H. March, eds. (Plenum Press, New York, 1983), pp. 79-147.
95. P. Hohenberg and W. Kohn, *Phys. Rev.* **136** (1964) B864-B871.
96. T.L. Gilbert, *Phys. Rev. B* **12** (1975) 2111-2120; E.H. Lieb, *Int. J. Quantum Chem.* **24** (1983) 243-277.
97. W. Kohn and L.J. Sham, *Phys. Rev.* **140** (1965) A1133-A1138.
98. S.H. Vosko, L. Wilk, and M. Nusair, *Can. J. Phys.* **58** (1980) 1200-1211.
99. D.M. Ceperley and B.J. Alder, *Phys. Rev. Lett.* **45** (1980) 566-569.
100. J.C. Slater, *Phys. Rev.* **81** (1951) 385-390.
101. J.P. Perdew and Y. Wang, *Phys. Rev. B* **33** (1986) 8800-8802.
102. A.D. Becke, *Phys. Rev. A* **38** (1988) 3098-3100.
103. J.P. Perdew, *Phys. Rev. B* **33** (1986) 8822-8824, erratum in *Phys. Rev. B* **38** (1986) 7406.
104. A.B. Anderson, *J. Chem. Phys.* **65** (1976) 1729-1734.
105. A.B. Anderson, *J. Am. Chem. Soc.* **100** (1978) 1153-1159.
106. Q. Minglong and C. Barbier, *J. Molec. Catal.* **57** (1989) 165-176.

107. A. Gavezzotti, E. Ortoleva and M. Simonetta, *J. Chem. Soc., Faraday Trans. I*, **78** (1982) 425-436; M. Simonetta and A. Gavezzotti, *J. Molec. Struct.* **107** (1984) 75-86.
108. G.A. Ozin, W.J. Power, T.H. Upton and W.A. Goddard III, *J. Am. Chem. Soc.* **100** (1978) 4750-4760; T.H. Upton and W.A. Goddard III, *J. Am. Chem. Soc.* **100** (1978) 321-323.
109. P.-O. Widmark, B.O. Roos, and P.E.M. Siegbahn, *J. Phys. Chem.* **89** (1985) 2180-2186.
110. N. Rösch and T.N. Rhodin, *Phys. Rev. Lett.* **32** (1974) 1189-1192.
111. P. Guerts and A. van der Avoird, *Surf. Sci.* **102** (1981) 185-206.
112. I. Pápai, J. Mink, R. Fournier and D.R. Salahub, *J. Phys. Chem.* **97** (1993) 9986-9991.
113. M.R.A. Blomberg, P.E.M. Siegbahn, T.J. Lee, A.P. Rendell and J.E. Rice, *J. Chem. Phys.* **95** (1991) 5898-5905.
114. S.A. Mitchell, M.A. Blitz, and R. Fournier, *Can. J. Chem.* **72** (1994) 587-599.
115. A. Gavezzotti and M. Simonetta, *Chem. Phys. Lett.* **48** (1977) 434-438; *Surf. Sci.* **99** (1980) 453-470.
116. H. Kobayashi, S. Yoshida, H. Kato, K. Fukui, K. Tarama, and M. Yamaguchi, *Surf. Sci.* **97** (1980) 329-345.
117. H. Kobayashi, H. Kato, K. Tarama, and K. Fukui, *J. Catal.* **49** (1977) 294-304.
118. X. Xu, N.Q. Wang, and Q.E. Zhang, *J. Molec. Struct.* **247** (1991) 93-106.
119. The "OPASED" program, as modified by R.L.C. Wang, was utilized in all the SED-MO calculations.
120. N.W. Ashcroft and N.D. Mermin, *Solid State Physics* (Saunders College, Philadelphia, 1976) p. 70.
121. A.B. Anderson, *J. Chem. Phys.* **66** (1977) 2173-2175.
122. A.B. Anderson and S.J. Choe, *J. Phys. Chem.* **93** (1989) 6145-6149.
123. D.R. Salahub, R. Fournier, P. Mlynarski, I. Papai, A. St-Amant, and J. Ushio, in *Density Functional Methods in Chemistry*, J.K. Labanowski and J.W. Andzelm, eds. (Springer-Verlag, New York, 1991), pp. 77-100.

124. A. St-Amant and D.R. Salahub, *Chem. Phys. Lett.* **169** (1990) 387-392; A. St-Amant, Ph.D. thesis, U. de Montréal, 1992.
125. deMon User Guide, version 1.0 beta, Biosym Technologies, San Diego, 1992.
126. P.A.M. Dirac, *Proc. Cambridge Phil. Soc.* **26** (1930) 376-385.
127. U. von Barth and L. Hedin, *J. Phys. C* **5** (1972) 1629-1642.
128. B.I. Dunlap, J.W.D. Connolly and J.R. Sabin, *J. Chem. Phys.* **71** (1979) 3396-3402; 4993-4999.
129. H. Sambe and R.H. Felton, *J. Chem. Phys.* **62** (1975) 1122-1126.
130. A.D. Becke, *J. Chem. Phys.* **88** (1988) 2547-2553.
131. P. Pulay, *Chem. Phys. Lett.* **73** (1980) 393-398; *J. Comput. Chem.* **3** (1982) 556-560.
132. V.R. Saunders and I.H. Hillier, *Int. J. Quantum Chem.* **7** (1973) 699-705.
133. R. Carbó, J.A. Hernández, and F. Sanz, *Chem. Phys. Lett.* **47** (1977) 581-583.
134. B.I. Dunlap, *Phys. Rev. A* **25** (1982) 2847-2849.
135. J.P. Perdew and A. Zunger, *Phys. Rev. B* **23** (1981) 5048-5079.
136. K. Nath and A.B. Anderson, *Phys. Rev. B* **38** (1988) 8264-8268.
137. J. Yu and A.B. Anderson, *Surf. Sci.* **254** (1991) 320-328.
138. J. Muilu and T.A. Pakkanen, *Phys. Rev. B* **49** (1994) 11185-11190; *Appl. Surf. Sci.* **75** (1994) 75-82.
139. A. Redondo, W.A. Goddard III, T.C. McGill, and G.T. Surratt, *Solid State Commun.* **21** (1977) 991-994.
140. S.P. Mehandru and A.B. Anderson, *J. Mater. Res.* **5** (1990) 2286-2295; *Surf. Sci.* **248** (1991) 369-381.
141. J.L. Whitten and T.A. Pakkanen, *Phys. Rev. B* **21** (1980) 4357-4367; J.L. Whitten, *Phys. Rev. B* **24** (1981) 1810-1817.
142. See also, e.g., H. Yang and J.L. Whitten, *J. Chem. Phys.* **89** (1988) 5329-5334; *J. Chem. Phys.* **91** (1989) 126-136.
143. R.S. Mulliken, *J. Chem. Phys.* **23** (1955) 1833-1840; 1841-1846.

144. R. Hoffmann, *Rev. Mod. Phys.* **60** (1988) 601-628 and *Solids and Surfaces: A Chemist's View of Bonding in Extended Structures* (VCH, New York, 1988).
145. M.J.S. Dewar, *Bull. Soc. Chim. Fr.* **18** (1951) C71-79; J. Chatt and L.A. Duncanson, *J. Chem. Soc.* (1953) 2939-2947.
146. G. Blyholder, *J. Phys. Chem.* **68** (1964) 2772-2778.
147. R.J. Buenker and S.D. Peyerimhoff, *Chem. Phys.* **9** (1976) 75-89.
148. See, e.g., R.P. Bell, *The Tunnel Effect in Chemistry* (University Press, Cambridge, 1980).
149. See, e.g., H.J. Kreuzer, *Nonequilibrium Thermodynamics and its Statistical Foundations* (Oxford University Press, New York, 1981), pp. 296-321, and H.J. Kreuzer and Z.W. Gortel, *Physisorption Kinetics* (Springer-Verlag, Berlin, 1986), pp. 89-141.
150. G. Herzberg, *Molecular Spectra and Molecular Structure: I. Spectra of Diatomic Molecules* (Robert E. Krieger Publishing Co., Inc., Malabar, Florida, 1989) p. 532.
151. K. Christmann, R.J. Behm, G. Ertl, M.A. Van Hove, and W.H. Weinberg, *J. Chem. Phys.* **70** (1979) 4168-4184.
152. Gaussian 92/DFT, M.J. Frisch, M. Head-Gordon, G.W. Trucks, J.B. Foresman, H.B. Schlegel, K. Raghavachari, M.A. Robb, J.S. Binkley, C. Gonzalez, D.J. Defrees, D.J. Fox, R.A. Whiteside, R. Seeger, C.F. Melius, J. Baker, R.L. Martin, L.R. Kahn, J.J.P. Stewart, S. Topiol, and J.A. Pople, Gaussian, Inc., Pittsburgh, PA (1992).
153. J. Andzelm, E. Wimmer, and D.R. Salahub, in *The Challenge of d and f Electrons: Theory and Computation*, D.R. Salahub and M.C. Zerner, eds. (American Chemical Society, Washington, D.C., 1989), ACS Symposium Series No. 394, pp. 228-245; J.W. Andzelm, in *Density Functional Methods in Chemistry*, J.K. Labanowski and J.W. Andzelm, eds. (Springer-Verlag, New York, 1991) pp. 155-174.
154. B. Delley, *J. Chem. Phys.* **92** (1990) 508-517 and in *Density Functional Methods in Chemistry*, J.K. Labanowski and J.W. Andzelm, eds. (Springer-Verlag, New York, 1991), pp. 101-107. DMol is available commercially from Biosym Technologies, San Diego, CA.
155. K. Nath and A.B. Anderson, *Solid State Commun.* **66** (1988) 277-280.